Spin-orbital entanglement and molecular orbital formation in 4*d* and 5*d* transition metal oxides

von der Fakultät Chemie der Universität Stuttgart zur Erlangung der Würde eines Doktors der Naturwissenschaften (Dr.rer.nat.) genehmigte Abhandlung.

vorgelegt von

Aleksandra Krajewska

aus Gdańsk, Polen

Hauptberichter:	Prof. Dr. Hidenori Takagi
Mitberichter:	Prof. Dr. Thomas Schleid
Mitprüfer:	Prof. Dr. Andreas Köhn

Tag der mündlichen Prüfung: 03/08/2020

Max-Planck-Institut für Festkörperforschung
und
Institut für Funktionelle Materie und Quantentechnologien
Universität Stuttgart

2020

Contents

5 | Acronyms

15 | Chapter 1
Introduction

1.1 Transition metal oxides 15
1.2 Mott insulators with multiple degrees of freedom 16
1.3 Orbital degree of freedom of *d* electrons 17
1.4 Quenching of orbital degree of freedom - orbital ordering 19
1.5 Orbital molecules on a crystalline lattice 22
1.6 Spin-orbital entanglement of *d* electrons 24
1.6.1 $J_{\text{eff}} = 1/2$ Mott insulators 27
1.6.2 $J_{\text{eff}} = 0$ Mott insulators 30
1.7 Case studies for competition between spin-orbit coupling, orbital molecules and crystal field 31

33 | Chapter 2
Methods

2.1 Material synthesis 33
2.1.1 Solid state synthesis 33
2.1.2 High pressure synthesis 34
2.2 Structure determination 35
2.2.1 X-ray diffraction 36
2.2.2 Neutron diffraction 37
2.2.3 Rietveld refinement 40
2.3 Inelastic scattering techniques 41
2.3.1 Resonant Inelastic X-ray Scattering 41

2.4 Physical property measurement techniques 45
2.4.1 Magnetism 45
2.4.2 Transport 46
2.4.3 Thermodynamics 47
2.5 Muon spin rotation 49
2.5.1 Band structure calculations 52
2.6 Co-authorship 53

Chapter 3

55 Pressure-driven collapse of $J_{\text{eff}} = 1/2$ state in β-Li_2IrO_3

3.1 Introduction 55
3.1.1 Kitaev model 55
3.1.2 $J_{\text{eff}} = 1/2$ pseudospin on honeycomb lattice 56
3.1.3 Candidate Kitaev materials 59
3.1.4 Tuning of Kitaev materials 65
3.1.5 Target material: hyperhoneycomb iridate β-Li_2IrO_3 66
3.2 Methods 69
3.2.1 Sample preparation 69
3.2.2 Time of flight neutron diffraction under pressure 70
3.2.3 Resonant inelastic x-ray scattering under pressure 72
3.2.4 Band structure calculations 73
3.3 Results 73
3.3.1 Dimerisation under pressure 73
3.3.2 Destruction of the $J_{\text{eff}} = 1/2$ state under pressure 77
3.3.3 Formation of molecular orbitals in the Ir_2 units under pressure 79
3.4 Discussion 81
3.5 Conclusion 83

Chapter 4

85 $In_2Ir_2O_7$—a nearly pure $J_{\text{eff}} = 1/2$ Mott insulator

4.1 Introduction 85

4.1.1 Properties of pyrochlore iridates 86
4.1.2 Topological semimetal in pyrochlore iridates 90
4.1.3 Validity of $J_{\text{eff}} = 1/2$ state in the limit of strong non-cubic crystal field 93
4.2 Methods 94
4.2.1 Sample preparation 94
4.2.2 Powder x-ray diffraction and analysis 94
4.2.3 Resonant inelastic x-ray scattering 94
4.2.4 Band structure calculations 95
4.3 Results 95
4.3.1 New pyrochlore iridate with frustrated magnetism 95
4.3.2 Reduced trigonal crystal field in $In_2Ir_2O_7$ despite larger IrO_6 distortion 98
4.3.3 Nearly pure $J_{\text{eff}} = 1/2$ state in $In_2Ir_2O_7$ 101
4.4 Discussion 103
4.4.1 Influence of intersite hopping 103
4.4.2 Effect of short-range and long-range crystal field 105
4.4.3 *A*-O bond-covalency-induced $J_{\text{eff}} = 1/2$ state 108
4.5 Conclusion 110
Chapter 5
113 Ru_2O molecule formation in $In_2Ru_2O_7$
5.1 Introduction 113
5.1.1 $J_{\text{eff}} = 0$ pseudospin and excitonic magnetism 113
5.1.2 Molecular orbital formation in ruthenates 115
5.1.3 Competition between phases in a new pyrochlore ruthenate tuned by *A*-O covalency 117
5.2 Methods 118
5.2.1 Sample preparation 118
5.2.2 Single crystal x-ray diffraction and analysis 119
5.2.3 Powder x-ray diffraction and analysis 119
5.2.4 Time of flight neutron powder diffraction and analysis 120
5.2.5 Structure determination 122

5.2.6 Resistivity at high temperatures 123
5.2.7 Resonant inelastic x-ray scattering 123
5.2.8 Muon Spin Rotation 124
5.2.9 Band structure calculations 124
5.2.10 Energy Dispersive X-ray spectroscopy in the SEM mode 124
5.3 Results 125
5.3.1 Weakly distorted pyrochlore lattice at room temperature 125
5.3.2 Spin-orbital entangled singlet state in $In_2Ru_2O_7$ at room temperature 128
5.3.3 Multiple phase transitions 136
5.3.4 Non-magnetic ground state 139
5.3.5 Formation of Ru_2O trimers at low temperatures 140
5.3.6 Molecular orbital formation within the Ru_2O units at low temperatures 144
5.3.7 The role of the In-O network 149
5.4 Discussion 152
5.5 Conclusion 155
Chapter 6
157 Conclusion
Appendix A
159 Structural aspects
Appendix B
167 Band structure calculations of pyrochlore iridates $A_2Ir_2O_7$
171 References

Acronyms

(Z)FC	(zero) field-cooled
AC	alternating current
AFM	antiferromagnetic
AIAO	all-in–all-out
ARPES	angle-resolved photoemission spectroscopy
BR	branching ratio
CCR	closed-cycle refrigerator
CF	crystal field
D	dimension, dimensional
DAC	diamond anvil cell
DC	direct current
DFT	density functional theory
DOF	degree of freedom
DOS	density of states
DSC	differential scanning calorimetry
EDX	energy dispersive x-ray
FM	ferromagnetic
FWHM	full width at half maximum
GKA	Goodenough-Kanamori-Anderson
GSAS	General Structure Analysis System

HRPD	High resolution powder neutron diffractometer
I	insulator
INS	inelastic neutron scattering
IS	inversion symmetry
ISIS	Rutherford Appleton Laboratories, ISIS, STFC
JT	Jahn-Teller
LDA	local density approximation
M	metal
MIT	metal-to-insulator transition
MPMS	magnetic property measurement system
PDF	pair distribution function
PPMS	physical property measurement system
PSD	position sensitive detector
QSL	quantum spin liquid
REXS	resonant elastic x-ray scattering
RIXS	resonant inelastic x-ray scattering
SEM	scanning electron microscopy
SG	space group
SM	semimetal
SOC	spin-orbit coupling
SPring-8	Super Photon ring-8 GeV, Japan Synchrotron Radiation Research Institute
SQUID	Superconducting QUantum Interference Device
TM	transition metal
TMO	transition metal oxide

TRS	time-reversal symmetry
WSM	Weyl semimetal
XMCD	x-ray magnetic circular dichroism
XR(P)D	x-ray (powder) diffraction
ZF	zero-field
ZTA	zirconia toughened alumina
μSR	muon spin rotation

Zusammenfassung

Übergangsmetalloxide weisen eine Vielzahl exotischer Phänomene auf, unter anderem Supraleitung oder kolossalen Magnetwiderstand. Diese Phänomene sind in der Regel durch das Zusammenspiel von Ladungs-, Spin- und Orbitalfreiheitsgraden der korrelierten Elektronen im Kristallgitter getrieben. Mott-Isolator-Übergangsmetalloxide mit teilweise gefüllten und entarteten d-Orbitalen bieten die Grundlage für exotische elektronische Zustände wie zum Beispiel Orbitalordnung, die Bildung von Molekülorbitalen und die Verschränkung von Spin und Bahndrehimpuls. Der Einfluss all dieser Effekte ist besonders in 4d- und 5d-Systemen interessant, da viele Wechselwirkungen, die diese Mechanismen steuern, aufeinandertreffen und dieselbe Größenordnung besitzen. In 4d- und 5d-Materialien sind die d-Orbitale räumlich weiter ausgedehnt als im Vergleich zu 3d-Orbitalen. Dies führt zu einer reduzierten Elektronenkorrelation U und damit kleineren Hundschen Kopplung J_{H}, gleichzeitig aber zu erhöhtem „Intersite-Hopping“ t. Ein nichtkubisches Kristallfeld hat zudem für die größeren d-Orbitale einen größeren Effekt. Am wichtigsten ist, dass aufgrund der schwereren Kerne in 4d und 5d-Elementen die Spin-Bahn-Kopplung in der Größenordnung von Hunderten meV liegt und mit den anderen Wechselwirkungen konkurriert. Der Wettbewerb der verschiedenen Wechselwirkungen in den schweren Übergangsmetallmaterialien kann durch Variation von Temperatur, Druck oder chemische Substitution abgestimmt werden. In dieser Thesis werden drei Materialien im Zusammenhang mit der Konkurrenz zwischen Spin-Bahn-Kopplung, Molekülorbitalbildung und nicht-kubischem Kristallfeld untersucht.

β-Li_2IrO_3 ist ein Kitaev-Material mit Honigwabenstruktur welches einen Spin-Bahn verschränkten $J_{\mathrm{eff}} = 1/2$-Zustand bei Umgebungsbedingungen aufweist. Bei hohem hydrostatischem Druck wird der $J_{\mathrm{eff}} = 1/2$-Magnetismus unterdrückt und es findet ein struktureller Übergang statt. β-Li_2IrO_3 besteht aus kantenverknüpften IrO_6-Oktaedern. Bei hohem Druck schrumpft das Kristallgitter, und das dadurch größere direkte „d-d-Hopping“ über die gemeinsame Kante, konkurriert wahrscheinlich mit dem ansonsten dominierenden indirekten „d-p-d-Hopping“. Mittels Neutronenbeugung, RIXS und Bandstrukturberechnungen stellen wir fest, dass bei hohem Druck der $J_{\mathrm{eff}} = 1/2$-Zustand kollabiert und sich Ir_2-Dimere mit Molekülorbitalen bilden. Somit kann der Effekt von Spin-Bahn-Kopplung und Molekülorbitalbildung in t_{2g}-Systemen durch Druck beeinflusst und abgestimmt werden. Dieser Wettbewerb zwischen Dimerbildung und Magnetismus Spin-Bahn gekoppelter Momente scheint ein universelles Merkmal der Kitaev-Materialien zu sein.

Starke nichtkubische Kristallfelder können auch den Spin-Bahn verschränkten $J_{\text{eff}} = 1/2$-Zustand stören. Pyrochlor-Iridate enthalten trigonal komprimierte Oktaeder und das trigonale Kristallfeld ist bis zu 0.3 eV groß, mehr als halb so groß wie die Spin-Bahn-Kopplung. Während Pyrochlor-Iridate als Plattform für nicht-triviale topologische Zustände dienen, ist der Magnetismus und die Robustheit des $J_{\text{eff}} = 1/2$-Zustandes in Pyrochlor-Iridaten mit starker trigonaler Verzerrung weitgehend unerforscht. Mit der Hochdruck-Synthesetechnik haben wir ein neues Pyrochlor-Iridat $In_2Ir_2O_7$ mit der bisher größten trigonalen Verzerrung der IrO_6-Oktaeder unter den Pyrochlor-Iridaten entdeckt. Überraschenderweise beherbergt $In_2Ir_2O_7$ im Gegensatz zu anderen Pyrochlor-Iridaten und trotz des größten nichtkubischen Kristallfeldes einen nahezu puren $J_{\text{eff}} = 1/2$-Zustand. Unsere Bandstrukturberechnungen deuten darauf hin, dass „Intersite-Hopping“, welches bei anderen Pyrochlorid-Iridaten recht groß ist, eine zentrale Rolle bei der Vermischung der J_{eff}-Zustände spielt. Was $In_2Ir_2O_7$ jedoch einzigartig macht, ist die kovalente In-O-Bindung welche die Ir-5d/O-2p-Hybridisierung reduziert. Dies unterdrückt das „Intersite-Hopping“ und die Vermischung der $J_{\text{eff}} = 1/2$- und $J_{\text{eff}} = 3/2$-Zustände. Daher ist eine kovalente A-O-Bindung ein mögliches Rezept für die Stabilisierung eines nahezu reinen Spin-Bahn verschränkten Zustands.

Für Ruthenate mit d^4-Konguration wird vorhergesagt, dass sie einen $J_{\text{eff}} = 0$-Zustand beherbergen und exzitonischen Magnetismus über angeregte $J_{\text{eff}} = 1$-Zustände aufweisen könnten. Viele Ruthenate bilden jedoch Molekülorbitale aus und diejenigen, die dies nicht tun, z.B. Pyrochlorruthenate, werden als $S = 1$-Magnete diskutiert, bei denen der orbitale Freiheitsgrad durch große Verzerrung ausgelöscht oder zumindest unterdrückt ist. Ein Pyrochlorruthenat $Tl_2Ru_2O_7$ bildet jedoch einen exotischen nichtmagnetischen Grundzustand mit Orbitalordnung. Der besondere Zustand von $Tl_2Ru_2O_7$ unter den Pyrochlorruthenaten wird im Zusammenhang mit der kovalenten Tl-O-Bindung diskutiert. Angesichts des Einflusses der kovalenten In-O-Bindung auf den elektronischen Zustand in $In_2Ir_2O_7$ und des wahrscheinlich ähnlichen Charakters der Tl-O- und In-O-Bindungen, wurde ein neues Pyrochlorruthenat $In_2Ru_2O_7$ synthetisiert. $In_2Ru_2O_7$ ist ein einzigartiges Pyrochlorruthenat, das sowohl einen Spin-Bahn verschränkten Grundzustand als auch Molekülorbitale aufweist. Bei hohen Temperaturen spaltet und vermischt das nichtkubische Kristallfeld zwar die J_{eff}-Zustände, aber es kann den Bahndrehimpuls nicht vollständig auslöschen, und ein Spin-Bahn verschränkter Singulett-Grundzustand wird realisiert. Mit abnehmender Temperatur durchläuft $In_2Ru_2O_7$ mehrere Strukturübergänge, die die elektronische Struktur weitgehend verändern, und der Spin-Bahn verschränkte Singulett-Zustand kollabiert. Das Kristallgitter verzerrt sich stark, und einige Ru-O-Ru-Winkel nehmen von $\sim 125^\circ$ auf fast $\sim 160^\circ$ zu - nahe an die Ru-O-Ru 180°-Bindungsgeometrie. Infolgedessen bilden sich quasi-isolierte nichtmagnetische Ru_2O-Einheiten auf dem Pyrochlor-Gitter. Diese dienen als erstes Beispiel eines nichtmagnetischen

„Orbitalmoleküls“, an dem auch das O^{2-} Anion beteiligt ist. Es wird angenommen, dass das unterschiedliche Verhalten von $In_2Ru_2O_7$ im Vergleich zu anderen Pyrochlorruthenaten durch die Bindungsdisproportionierung des kovalenten In-O-Netzwerks verursacht wird.

Diese Arbeit zeigt, dass Übergangsmetallverbindungen, bei denen eine starke Spin-Bahn-Kopplung mit den anderen elektronischen Parametern konkurriert, eine Vielzahl exotischer elektronischer Phasen aufweisen. Durch die Wahl der Elektronenzahl, des kristallinen Gitters und der Energieskala der verschiedenen Wechselwirkungen kann der Grundzustand zwischen Spin-Bahn verschränkten Zuständen, Orbitalordnungen oder „Orbitalmolekülen“ getrieben werden. Die *A*-O-Kovalenz des konstituierenden nichtmagnetischen Kations hat sich als ein wichtiger Faktor bei der Stabilisierung sowohl der Spin-Bahn verschränkten Zustände als auch der „Orbitalmolekül“-Phasen erwiesen. Die Erforschung und Synthese neuer Materialien unter Berücksichtigung dieses Faktors dient als spannender Ansatz für die Entdeckung neuer exotischer elektronischer Phasen.

Abstract

Transition metal oxides exhibit a variety of exotic phenomena such as superconductivity or colossal magnetoresistance. Those phenomena are usually driven by interplay of charge, spin and orbital degrees of freedom of correlated electrons on a crystalline lattice. Mott insulating transition metal oxides with partially filled d orbitals host orbital degeneracy, which is a source of exotic electronic states such as orbital ordering, molecular orbital formation and spin-orbital entanglement. The competition between those effects becomes interesting in $4d$ and $5d$ systems as many interactions, which govern those mechanisms, meet on the same energy scale. In $4d$ and $5d$ materials the d orbitals are more spatially extended as compared to $3d$ orbitals, which results in reduced correlation U and hence Hund's coupling J_{H} as well as enhanced intersite hopping t. Non-cubic crystal field also has more drastic consequences for the large d orbitals. Most importantly, due to heavier nuclei in $4d$ and $5d$ elements spin-orbit coupling is of the order of hundreds of meV and competes with the other interactions. The subtle competition of various energy scales in heavy-transition-metal materials can be tuned by varying temperature, pressure or chemical substitution. In this thesis, three materials are investigated in context of competition between spin-orbit coupling, molecular orbital formation and non-cubic crystal field.

β-Li_2IrO_3 is a honeycomb-based Kitaev material with a spin-orbital entangled $J_{\mathrm{eff}} = 1/2$ state at ambient conditions. At high pressures, the $J_{\mathrm{eff}} = 1/2$ magnetism is suppressed and a structural transition takes place. β-Li_2IrO_3 comprises edge-sharing IrO_6 octahedra. At high pressures, the crystalline lattice shrinks and the direct d-d hopping across the edge likely competes with the otherwise dominant indirect d-p-d hopping. With neutron diffraction, RIXS and band structure calculations we find that at high pressures the $J_{\mathrm{eff}} = 1/2$ state collapses and Ir_2 dimers with molecular orbital formation emerge. Therefore, the competition between spin-orbit coupling and molecular orbital formation in t_{2g} systems can be tuned by pressure. Such competition between dimers and spin-orbital entangled magnetism seems to be a universal feature of Kitaev materials.

Strong non-cubic crystal field also can disturb the spin-orbital entangled $J_{\mathrm{eff}} = 1/2$ state. Pyrochlore iridates contain trigonally compressed octahedra and the trigonal crystal field is as large as 0.3 eV which is more than half of the spin-orbit coupling magnitude. While pyrochlore iridates serve as a platform for non-trivial topological states, the magnetism and validity of the $J_{\mathrm{eff}} = 1/2$ state is unexplored in pyrochlore iridates in the limit of large trigonal

distortion. With high pressure synthesis technique, we discovered a new pyrochlore iridate $In_2Ir_2O_7$ with the largest trigonal distortion among pyrochlore iridates. Surprisingly, $In_2Ir_2O_7$ hosts a nearly pure $J_{\text{eff}} = 1/2$ state in contrast to other pyrochlore iridates and despite the largest non-cubic crystal field. Our band structure calculations indicate that intersite hopping plays a central role in mixing of the J_{eff} states, which is quite large in other pyrochlore iridates. However, what makes $In_2Ir_2O_7$ unique is the covalent *A*-O bond, which in turn reduces Ir-5*d*/O-2*p* hybridisation. This suppresses the intersite hopping and $J_{\text{eff}} = 1/2$-$J_{\text{eff}} = 3/2$ mixing. Therefore, the covalent *A*-O bond is one possible recipe for stabilising a nearly pure spin-orbital entangled state.

Ruthenates with d^4 configuration are predicted to host a $J_{\text{eff}} = 0$ state and exhibit excitonic magnetism via excited $J_{\text{eff}} = 1$ states. However, many ruthenates undergo molecular orbital formation, and those that do not, for example pyrochlore ruthenates, are discussed to be $S = 1$ magnets where the orbital degree of freedom is quenched by large distortion. However, one pyrochlore ruthenate $Tl_2Ru_2O_7$ forms an exotic non-magnetic ground state with orbital ordering. The distinct state of $Tl_2Ru_2O_7$ among pyrochlore ruthenates is discussed to be related to Tl-O covalency. Given the likely similar character of Tl-O and In-O bonds and the impact of In-O covalency on the electronic state identified in $In_2Ir_2O_7$, we synthesised a new pyrochlore ruthenate $In_2Ru_2O_7$. $In_2Ru_2O_7$ is a unique pyrochlore ruthenate that represents both spin-orbital entangled and molecular orbital limits. At high temperatures, while the non-cubic crystal field splits and mixes the J_{eff} states, it fails to fully quench orbital moments, and a spin-orbital entangled singlet is identified as the ground state. With decreasing temperature, $In_2Ru_2O_7$ undergoes several structural transitions which largely modify the electronic structure and the spin-orbital entangled singlet state collapses. The crystalline lattice strongly distorts, and some Ru-O-Ru angles increase from $\sim 125^\circ$ to nearly $\sim 160^\circ$, which brings the Ru-O-Ru link close to the 180° bond geometry. As a result, semi-isolated non-magnetic Ru_2O units form on the pyrochlore lattice, serving as a first example of a non-magnetic orbital molecule involving the O^{2-} anion on top of pyrochlore lattice. The distinct behaviour of $In_2Ru_2O_7$ as compared to other pyrochlore ruthenates is believed to be caused by the bond disproportionation of the covalent In-O network.

This thesis demonstrates that transition metal compounds, where strong spin-orbit coupling competes with the other electronic parameters, offer a plethora of exotic electronic phases. By selection of electron count, crystalline lattice and energy scales one can tune the ground state between spin-orbital entangled states, orbital ordering or orbital molecules. *A*-O covalency of constituent non-magnetic cation has been proven to be an important player in stabilisation of both spin-orbital entangled and orbital molecule phases. Exploration and synthesis of new materials, with taking this factor into account, serves as an exciting approach for stabilising new exotic electronic phases.

Chapter 1

Introduction

1.1 Transition metal oxides

Transition metal oxides (TMOs) contain the elements from the *d*-block of the periodic table of elements and their behaviour is governed by the partially filled *d* orbitals. Spatially compact *d* orbitals lead to large electron-electron repulsion and hence most transition metal oxides fall into a class of *strongly correlated* materials. Such localised *d* electrons feature charge, spin and orbital degrees of freedom (DOF), which couple with each other and to the crystalline lattice. The electron correlations operate with other energy scales on the crystalline lattice, which leads to a variety of exotic phenomena, such as high-temperature superconductivity in cuprates [1], metal-insulator transitions in vanadates [2], colossal magnetoresistance in manganites [3–5], quantum critical behaviour [6] and many more. These phenomena exhibit high susceptibility to external tuning, such as by doping, pressure, strain or magnetic field. In the most prominent class of TMOs, the layered perovskite cuprates, superconductivity emerges upon hole or electron doping [1] and a variety of other phases emerge depending

	I	II	III	IV	V	VI	VII	VIII	IX	X	XI	XII	XIII	XIV	XV	XVI	XVII	XVIII
1	1 H																	2 He
2	3 Li	4 Be											5 B	6 C	7 N	8 O	9 F	10 Ne
3	11 Na	12 Mg											13 Al	14 Si	15 P	16 S	17 Cl	18 Ar
4	19 K	20 Ca	21 Sc	22 Ti	23 V	24 Cr	25 Mn	26 Fe	27 Co	28 Ni	29 Cu	30 Zn	31 Ga	32 Ge	33 As	34 Se	35 Br	36 Kr
5	37 Rb	38 Sr	39 Y	40 Zr	41 Nb	42 Mo	43 Tc	44 Ru	45 Rh	46 Pd	47 Ag	48 Cd	49 In	50 Sn	51 Sb	52 Te	53 I	54 Xe
6	55 Cs	56 Ba	57-71 La-Lu	72 Hf	73 Ta	74 W	75 Re	76 Os	77 Ir	78 Pt	79 Au	80 Hg	81 Tl	82 Pb	83 Bi	84 Po	85 At	86 Rn
7	87 Fr	88 Ra	89-103 Ac-Lr	104 Rf	105 Db	106 Sg	107 Bh	108 Hs	109 Mt	110 Ds	111 Rg	112 Cn	113 Nh	114 Fl	115 Mc	116 Lv	117 Ts	118 Og

■ *Figure 1.1.* The periodic table of elements.

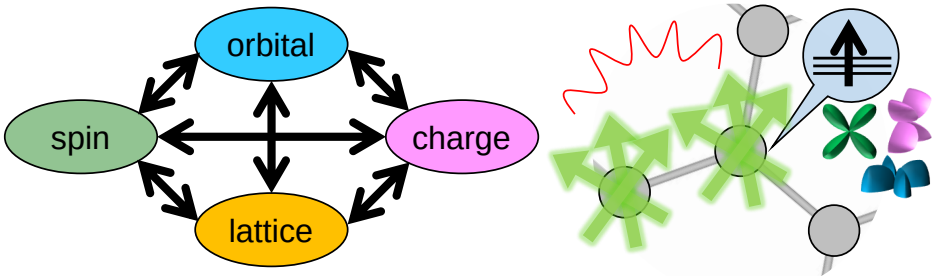

■ *Figure 1.2.* A cartoon illustrating the interplay of charge, spin and orbital degree of freedom on the crystalline lattice.

on temperature and the level of doping [7]. In perovskite manganites, tuning the level of hole doping leads to a variety of charge, orbital- or spin-ordered phases [4]. Those exotic physical properties and their sensitivity to external perturbations, as well as appreciable abundance and relatively uncomplicated synthesis of many TMOs, has generated a wealth of research activity in strongly correlated materials for industrial applications as well as basic understanding of physical phenomena.

1.2 Mott insulators with multiple degrees of freedom

The behaviour of many metallic transition metal compounds can be understood within the framework of the Fermi liquid theory, where the effects of electron-electron interactions are embedded in the concept of "quasiparticles", which can be treated like electrons with parameters modified by the interactions [8]. However, in many transition metal oxides the interactions between electrons lead to a breakdown of the Fermi liquid picture. This originates from the fact that d orbitals are much more spatially compact as compared to s and p orbitals comprising the valence states of simple metals (Fig. 1.3(a)). The consequences of the electron-electron repulsion can be understood by considering a system with one electron per site. Electron hopping, which is necessary for formation of a band, to a site already occupied by another electron costs Coulomb repulsion energy U as shown in Fig. 1.3(b). This can be expressed in terms of the Hubbard model [9]:

$$H = -t \sum_{\langle ij \rangle, \sigma} c^{\dagger}_{i\sigma} c_{j\sigma} + U \sum_{i} n_{i\uparrow} n_{i\downarrow} \tag{1.1}$$

where t is the hopping integral between neighbouring sites i and j with spin σ, $c^{\dagger}_{i\sigma}$ and $c_{i\sigma}$ are the creation and annihilation operators, respectively, and $n_{i\uparrow}$ is the electron density operator, where $n_{i\sigma} = c^{\dagger}_{i\sigma} c_{i\sigma}$. The first term describes the electron hopping from site to site which leads to formation of an energy band (the kinetic term), while the second term describes

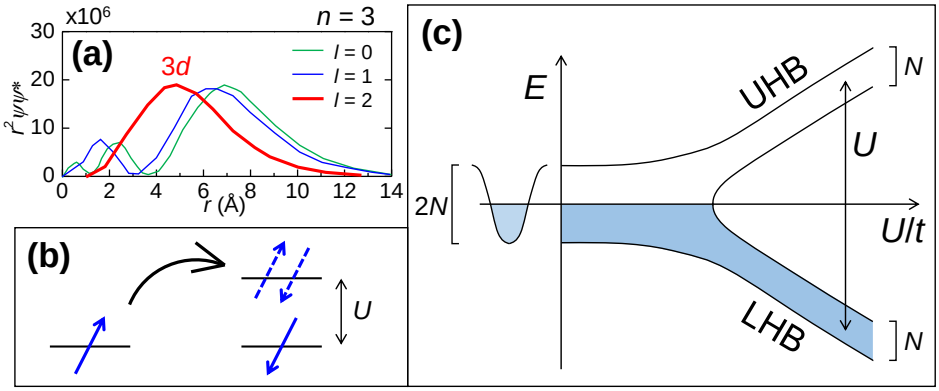

■ *Figure 1.3.* (a) The probability density distribution of the hydrogen electron for principal quantum number $n = 3$. $r^2\psi\psi^* dr$ corresponds to the probability of finding the electron in the spherical shell of thickness dr at a distance r from the nucleus. Reproduced from Ref. [12]. (b) Hopping of an electron from one site to another costs U due to electron-electron repulsion. (c) Diagram of the energy bands in the Hubbard model in eq. 1.1 as a function of the strength of electron-electron repulsion U. UHB, LHB and N correspond to upper- and lower-Hubbard band and number of states, respectively. Reproduced from Ref. [13].

the Coulomb repulsion of electrons at the same site (the correlation term). Bandwidth W is proportional to t. In Fig. 1.3(c), if one starts from non-interacting regime, that is, $U = 0$, the system is metallic. Above a critical value of U/t (where $U \gg W$), the system undergoes a metal-to-insulator transition (MIT), where a gap opens. The higher-lying empty and the lower-lying full band are referred to as the upper Hubbard band and lower Hubbard band, and the insulator produced is called a *Mott* or a *Mott-Hubbard* insulator [10]. The MIT as a function of U/t is called a Mott transition [11], and in general the most interesting phenomena occur in the vicinity of that transition. The transition depends on the details of the system such as band structure, electron filling fraction or other external forces.

Therefore in Mott insulators the charge degree of freedom of d electrons is quenched. However, the localised electrons feature other degrees of freedom, namely, spin and orbital. The spin DOF usually dominates the low-energy excitations of Mott insulators and gives rise to a variety of exotic magnetic properties. The orbital degree of freedom is associated with the different possible occupation of the five-fold d orbital manifold discussed in the next section.

1.3 Orbital degree of freedom of *d* electrons

In TMOs, the transition metal ions are often surrounded by an octahedron of oxygen atoms, which is denoted as BO_6 octahedron shown in (Fig 1.4(b)). The originally 5-degenerate d orbitals with angular momentum $l = 2$; $l^z = 2, 1, 0, -1, -2$ are subject to a cubic crystal field

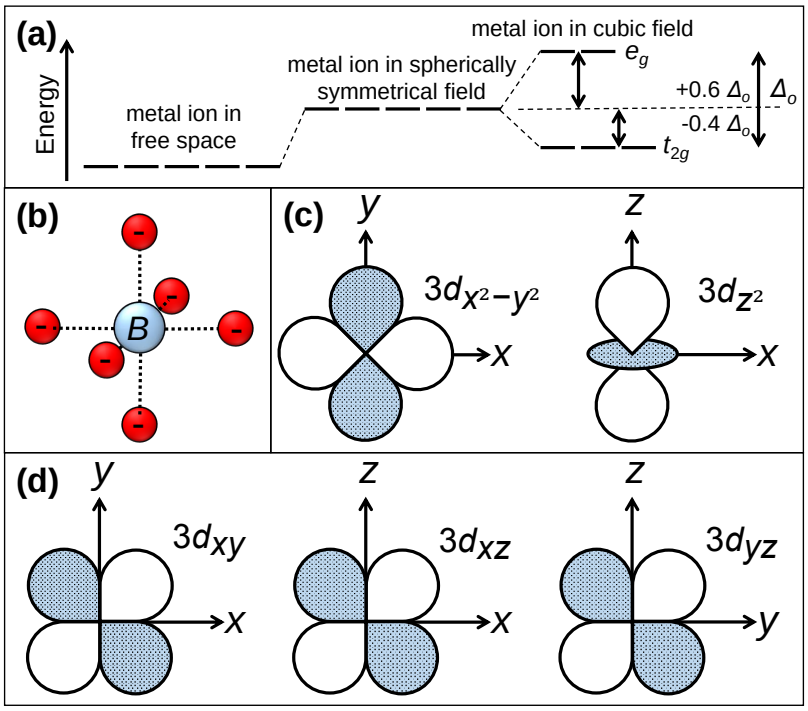

■ *Figure 1.4.* (a) The splitting of d orbitals under cubic crystal field Δ_O generated by ligands in octahedral coordination shown in (b). (b) The transition metal B surrounded by octahedral arrangement of point charges originating from O^{2-} anions. (c) t_{2g} orbitals. (d) e_g orbitals.

and are split into triply-degenerate t_{2g} and doubly-degenerate e_g manifolds, which point away from and towards the ligands, respectively. The energy of the lower triplet is $-\frac{2}{5}\Delta_O = -4\,\mathrm{Dq}$ while the energy of the higher-lying doublet is $+\frac{3}{5}\Delta_O = +6\,\mathrm{Dq}$ as shown in Fig 1.4(a). The resulting wavefunctions can be expressed as linear superpositions of $|l, l^z\rangle$:

$$t_{2g}: \begin{cases} d_{xy} = -\frac{i}{\sqrt{2}}(|2,2\rangle - |2,-2\rangle) \\ d_{xz} = -\frac{1}{\sqrt{2}}(|2,1\rangle - |2,-1\rangle) \\ d_{yz} = \frac{i}{\sqrt{2}}(|2,1\rangle + |2,-1\rangle) \end{cases} \quad e_g: \begin{cases} d_{3z^2-r^2} \sim d_{z^2} = |2,0\rangle \\ d_{x^2-y^2} = \frac{1}{\sqrt{2}}(|2,2\rangle + |2,-2\rangle) \end{cases} \tag{1.2}$$

Those are depicted in Fig 1.4(c) and (d). For an isolated ion, the orbital momentum l is quenched for e_g states. It is clear that d orbitals are highly anisotropic, and should therefore be very sensitive to the lattice geometry.

► d orbitals on a crystalline lattice

Properties of TMOs largely depend on the arrangement and connectivity of the constituent atoms, that is, the crystal structure. Known crystal structures can generally be considered as arrangements of building blocks of simple metal oxide polyhedra, such as BO_6 octahedra. The most common type of BO_6 connectivity is corner-sharing with 180° B-O-B bonds and

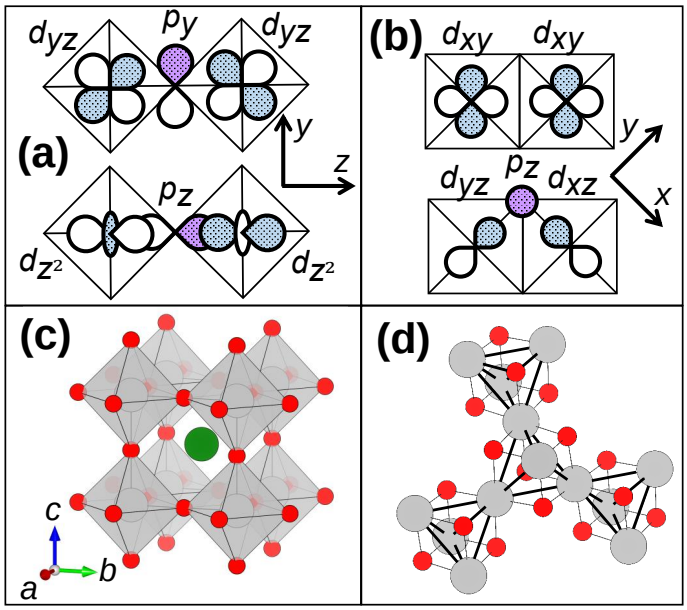

■ *Figure 1.5.* (a) Examples of orbital overlap in the corner-sharing geometry. (b) Examples of orbital overlap in the edge-sharing geometry. (c) The perovskite structure. The grey, green and red spheres correspond to the magnetic *B*, the constituent *A* and O atoms, respectively. (d) A fragment of the spinel structure. The grey and red spheres correspond to the magnetic *B* and O atoms. The *B* atoms form a frustrated pyrochlore lattice.

edge-sharing with 90° *B*-O_2-*B* bonds shown in Fig. 1.5(a) and (b). In the former, the hopping of electron from one transition metal ion to another occurs via the O 2*p* orbitals (indirect *d*-*p*-*d* hopping), while in the latter the hopping through direct overlap of *d* orbitals (direct *d*-*d* hopping) and the one mediated by O 2*p* orbitals (indirect *d*-*p*-*d* hopping) through the 90° path are possible. One of the best known, as well as versatile, structures hosting octahedral corner-sharing network is a simple perovskite ABO_3 shown in Fig. 1.5(c), which consists of corner-sharing BO_6 octahedra intercalated by constituent cations [14]. For edge-sharing BO_6, a prominent structure is that of a spinel AB_2O_4 which hosts a geometrically frustrated pyrochlore network of *B* cations. A brief review of crystal structures can be found in Appendix A. As will be discussed below, the polyhedral connectivity as well as global lattice geometry on which the anisotropic *d* orbitals operate, play a critical role in fostering the properties of TMOs.

1.4 Quenching of orbital degree of freedom - orbital ordering

d levels which are neither full nor half-filled host orbital degeneracy which must be lifted upon reaching zero temperature. Such systems can gain energy by breaking cubic (or other) symmetry of the BO_6 octahedron and reducing the electrostatic repulsion between the *d*

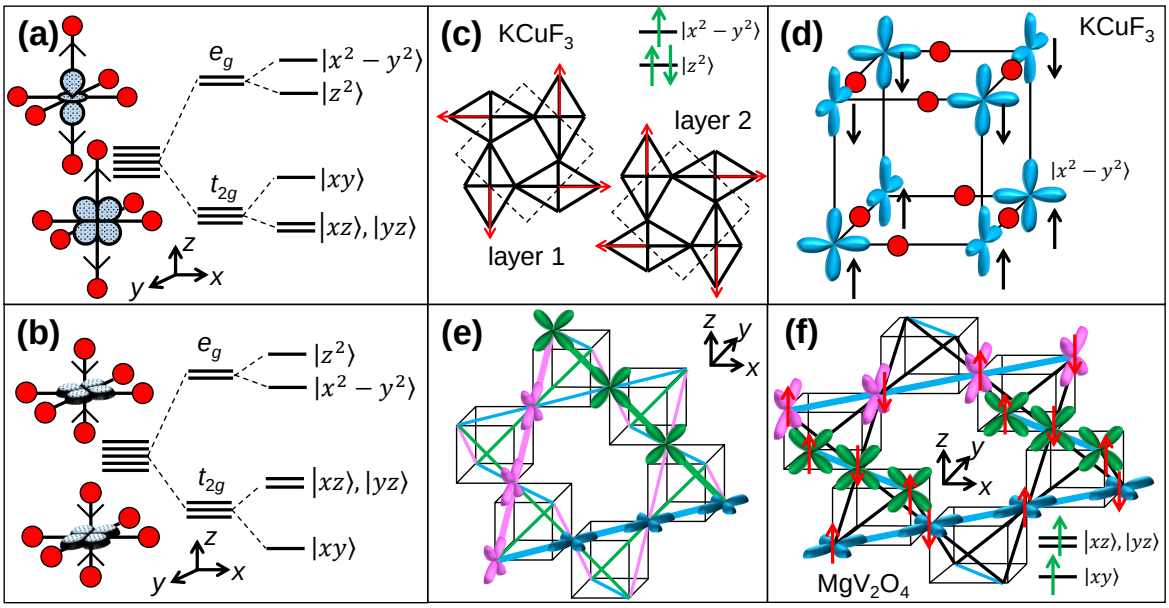

■ *Figure 1.6.* Splitting of d levels due to tetragonal elongation (a) and compression (b) of BO_6 octahedra with the stabilised orbitals shown. (c) The cooperative JT distortion in perovskite $KCuF_3$. The red arrows show the local z axis for each BO_6 octahedron. (d) The spin-orbital order in the perovskite $KCuF_3$. (e) The one-dimensional nature of the spinel structure. The three t_{2g} orbitals and the bonds relevant for their direct overlap are shown in the same colours: d_{xy}, d_{xz} and d_{yz} have direct d-d overlap along chains running in the (110)/($\bar{1}$10), (101)/($\bar{1}$01) and (011)/(0$\bar{1}$1) directions, respectively. (f) The spin-orbital order in the spinel MgV_2O_4. d_{xy} orbital is occupied on each site. On the bottom fragment only d_{xy} orbitals are shown, while on the top fragment only d_{xz}, d_{yz} orbitals are shown.

electrons and negatively charged O atoms. This stabilises a particular orbital and is called the Jahn-Teller (JT) effect [15]. The ions which have an electron configuration allowing the Jahn-Teller distortion are called Jahn-Teller active. Such phenomenon on the crystalline lattice where the BO_6 octahedra collectively distort and stabilise certain orbitals (orbital order) is termed a cooperative Jahn-Teller effect. One of the simplest and most prominent types of distortion is tetragonal, where one of the three local axes becomes unique by either compression or elongation with respect to the other two axes. In Fig. 1.6(a), if an isolated BO_6 octahedron is tetragonally elongated, the d_{xz} and d_{yz} as well as d_{z^2} are lower in energy within the t_{2g} and e_g manifolds, respectively. Fig. 1.6(b) shows the case of tetragonal compression, where both t_{2g} and e_g states split and d_{xy} as well as $d_{x^2-y^2}$ is stabilised, respectively. Whether the system picks compression or elongation depends on the electron count, orbital filling and the lattice geometry.

Let us first examine an isolated BO_6 octahedron with partially filled e_g orbitals, for example perovskite $KCuF_3$ which contains Cu^{2+} with d^9 configuration. One hole with orbital degeneracy resides within the e_g manifold. Locally, energy is gained and degeneracy is

lifted by tetragonal elongation, where the d_{z^2} orbital is stabilised and fully occupied with the hole now residing in the $d_{x^2-y^2}$ orbital. The cooperative distortion on the crystalline lattice occurs at high temperatures and produces tetragonally elongated CuF_6 octahedra with the local z axes perpendicular to each other for all nearest neighbours, which is illustrated in Fig. 1.6(c). It follows from the Goodenough-Kanamori-Anderson (GKA) rules that large and small overlaps of orbitals between neighbouring cations produces antiferromagnetic (AFM) and ferromagnetic (FM) coupling, respectively [16–18]. This produces long-range magnetic order at low temperatures with FM layers within the *ab* plane due to weak overlap that are coupled antiferromagnetically due to strong overlap along *c* in Fig. 1.6(d).

In e_g systems, typically the JT cooperative distortion takes place at high temperatures, while the long-range magnetic order governed by the orbital configuration emerges at low temperatures [13]. While such phenomena are also found in the partially-filled t_{2g} systems, it is more complicated due the remaining unquenched orbital degeneracy of the d_{xz}, d_{yz} doublet following the JT distortion. In some cases, the JT-driven orbital order takes place at higher temperatures and is followed by long-range magnetic order which additionally quenches the remaining orbital degree of freedom at lower temperatures. In systems with a geometrically frustrated lattice, quenching of spin and orbital DOF may be coupled to relieve the magnetic frustration. Such intertwined spin- and orbital orders are indeed observed in vanadate spinels such as MgV_2O_4 with V^{3+} ion and d^2 electron count [19, 20]. The spinel structure illustrated in Fig. 1.6(e) can be seen as a combination of three types of 1D chains along which direct overlap of d_{xy}, d_{xz} or d_{yz} orbitals is most favoured. With decreasing temperature, MgV_2O_4 undergoes a structural transition with tetragonal compression and orbital order. The proposed orbital ordering pattern is that the d_{xy} orbital is filled on all V^{3+} ions while d_{yz} and d_{xz} orbitals are filled in the alternate chains running along (110) and $(1\bar{1}0)$ directions, respectively (Fig. 1.6(f)). The orbital ordering pattern of AV_2O_4 spinels (A = Mg, Zn, Cd) has not been fully clarified yet and several scenarios and underlying mechanisms have been proposed so far [20–24].

As discussed above, partially-filled t_{2g} orbitals may exhibit complex behaviour due to residual unquenched orbital degree of freedom. In fact, vanadate perovskites AVO_3 with d^2 configuration stabilise several spin-orbital ordered patterns depending on the A cation and temperature [25]. Similarly to the vanadate spinels, the orbital ordering and spin ordering take place separately with decreasing temperature. Interestingly, perovskite $LaTiO_3$ with d^1 configuration does not undergo a clear JT-type distortion and exhibits only very weak tilting of TiO_6 octahedra [26]. It has been discussed that the coupling of the t_{2g} states to the lattice is very weak and strong orbital fluctuation takes place [27].

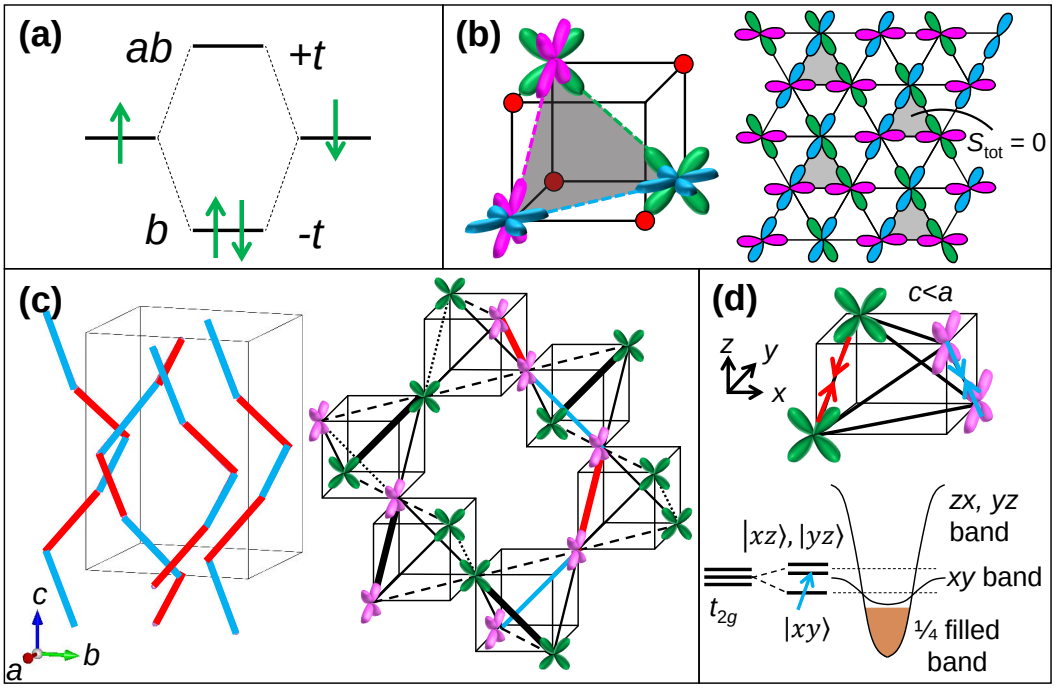

■ *Figure 1.7.* (a) Hopping t between two sites forms bonding (b) and antibonding ab molecular orbitals. (b) Orbital order found in $LiVO_2$ [28]. The three colours of t_{2g} orbitals represent d_{xy}, d_{xz} and d_{yz} orbitals. Left: fragment of $LiVO_2$ lattice showing edge-sharing V-O-V links and the t_{2g} orbital overlap between sites. Right: The orbital pattern with only the triangular lattice of V atoms shown. The total spin of each trimer is S_{tot} = "1 + 1 + 1" = 0. (c) Orbital order found in $MgTi_2O_4$. Left: the helical dimerised chains of Ti atoms [29], where the blue and red lines correspond to long and short dimer bonds, respectively. Right: the orbital order [29–31] with one helical chain marked. (d) One possible explanation of the observed orbital order. Top: the tetragonal compression brings d_{xz} and d_{yz} orbitals closer together. Bottom: the overlapping d_{xz} and d_{yz} orbitals form a broad band, while the d_{xy} orbital forms a narrow empty band located above the Fermi level. The resulting (d_{xz},d_{yz})-derived band is 1/4 full, and leads to a Peierls distortion in forms of tetramerisation.

1.5 Orbital molecules on a crystalline lattice

JT-assisted orbital order is not common in t_{2g} systems as compared to e_g systems and is often complicated once it occurs [13]. It appears that orbital-degenerate t_{2g} materials prefer yet another way of releasing orbital entropy [32]. The t_{2g} orbitals point away from the ligands comprising the anion cage and in some lattice geometries, such as face- or edge-sharing (the latter shown in Fig. 1.5(b)), a direct overlap of d orbitals between neighbouring sites is favoured. While in some cases orbital preference is inherent from the low-dimensionality of the crystal structure such as face-sharing octahedra forming trimers in $Ba_4Ru_3O_{10}$ [33], the system may form strong covalent bonds between transition metal ions via distortion of an otherwise isotropic lattice. Often such a structural transition is accompanied by a metal-to-insulator

transition and a sharp drop in magnetisation, which below the transition temperature is suppressed to nearly zero. This is associated with a formation of a non-magnetic state with a cluster-like motif of transition metal ions. The non-magnetic cluster-like state can be viewed as a molecular orbital formation of d electrons, i.e. "orbital molecule" [34]. The molecular orbital formation stems from strong overlap for hopping t and thus "metallicity" within the molecular cluster, where bonding and antibonding molecular orbitals are formed and the electrons from the molecule sites fill the molecular orbitals (Fig. 1.7(a)), usually rendering a band insulator. We note that the formation of a molecular orbital is distinct from spin-singlet state in a strong electron repulsion U limit. In a spin-singlet state, the d electrons are localised at each site and the non-magnetic state generates a spin singlet-triplet gap. On the other hand, for the orbital molecules, the transition metal ions form covalent bonding-antibonding molecular orbitals and the electrons are delocalised along the bond.

Non-magnetic orbital molecules are common in transition metal compounds, where the formation of metal-metal dimers is found, such as in rutile VO_2 [35], or spinels $MgTi_2O_4$ [29] and $CuIr_2S_4$ [36]. In some cases, even larger molecular clusters can be formed, such as trimers in triangular lattice of $LiVO_2$ [28], tetramers in layered CaV_4O_9 [37] or even heptamers in spinel AlV_2O_4 [38] (however, recently it was discussed that tetramers and trimers are formed instead [39]). The global arrangement of the molecular clusters on top of the crystalline lattice can sometimes be easily rationalised, for example in 2-dimensional $LiVO_2$ with triangular lattice of V^{3+} ions with d^2 electron count. As illustrated in Fig. 1.7(b), $LiVO_2$ comprises corner-sharing VO_6 octahedra and hence the V-O_2-V link favours the direct overlap of t_{2g} orbitals. 2 electrons per site require that each site participates in two strong bonds, and conveniently, for each site two t_{2g} have large overlap along two V-V bonds. As such, at low temperatures isolated trimers form, where orbital ordering of three sublattices occurs and each V site participates in two strong bonds with molecular orbital formation.

On the other hand, the spinel $MgTi_2O_4$ with pyrochlore lattice of Ti^{3+} with d^1 electron count shows a complicated dimer pattern which can be viewed as dimerised helical chains running along the crystallographic c axis as depicted in Fig. 1.7(c). The complicated pattern can be accounted for with the Kugel-Khomskii model [40] (which couples the spin and orbital degrees of freedom) and magnetoelastic coupling considerations [30, 31] for the cubic crystal structure without dimer formation. On the other hand, a band approach proposed by Ref. [41] with already applied tetragonal compression utilises the Peierls instability [30, 31], which is illustrated in Fig. 1.7(d). The tetragonal compression stabilises d_{xy} orbital, while as the other two t_{2g} orbitals move closer to each other, they form a broad band which crosses the narrow d_{xy} band. Therefore the d_{xz}-d_{yz} bands are quarter-filled. In the metallic picture, the Peierls instability would trigger a dimerisation pattern of n^{th} periodicity for $d^{1/n}$ electron

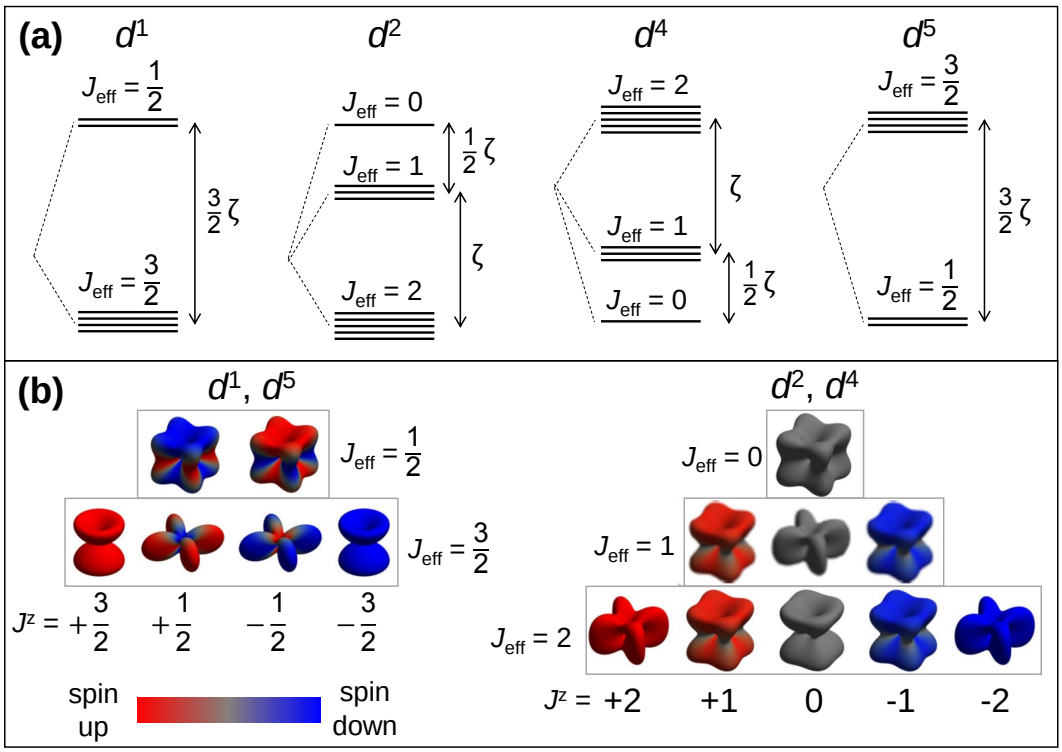

■ *Figure 1.8.* (a) Lowest energy spin-orbital entangled states for ions with d^1, d^2, d^4 and d^5 electron configuration for 10 Dq = ∞ and $J_H \gg \lambda_{SOC}$ (*LS* coupling limit). (b) Orbital shapes for all levels shown in (a). The radial part of the individual single particle wavefunctions was integrated and the remaining angular distribution is shown as a surface plot. The coloured surface indicates spin polarisation. The images were created by Dr. Jiří Chaloupka and are used here with his permission.

filling of a band [42, 43]. Indeed, along the 1D chain direction every fourth Ti-Ti bond is dimerised, which is consistent with 1/4-filled band and tetramerisation. If charge degree of freedom is added on a frustrated lattice, the generated pattern can be even more complicated. $CuIr_2S_4$ spinel with $Ir^{3.5+}$ oxidation state and $d^{5.5}$ electron count undergoes a simultaneous charge order and spin singlet/molecular orbital formation with orbital order accompanied by a structural distortion. The complicated pattern of Ir-Ir dimers is discussed to form an octamer [36].

1.6 Spin-orbital entanglement of *d* electrons

When t_{2g} orbitals are partially filled, another interaction, spin-orbit coupling (SOC), may dominate the electronic structure. Spin-orbit coupling is a relativistic effect stemming from the motion of the electron around the nucleus, which entangles the spin $\boldsymbol{S}$ and orbital $\boldsymbol{L}$ angular momenta into total angular momentum $\boldsymbol{J} = \boldsymbol{S} + \boldsymbol{L}$. The strength of spin-orbit coupling

ζ for outer electrons scales with the atomic number Z as $\zeta \sim Z^2$. In the $3d$-based TMOs discussed so far, spin-orbit interaction is of the order of tens of meV, which is small compared to other parameters, such as Hund's coupling J_{H} or non-cubic crystal field, and can therefore be treated as a perturbation while $\boldsymbol{S}$ and $\boldsymbol{L}$ remain good quantum numbers of the Hamiltonian. However, this is not the case for $4d$ and $5d$ elements, where ζ can be as large as 0.5 eV and is of the order of Coulomb repulsion $U \sim 1-2$ eV and electron hopping $t \sim 1$ eV. Therefore, spin-orbital entanglement becomes one of the dominant energy scales in $4d$- and $5d$-based TMOs which governs the energy level splitting and competes with the JT and molecular orbital degeneracy-lifting mechanisms.

The spin-orbit interaction can be expressed as follows:

$$H_{\mathrm{SOC}} = \sum_i \zeta_i \boldsymbol{l}_i \cdot \boldsymbol{s}_i \tag{1.3}$$

where ζ, $\boldsymbol{l}$ and $\boldsymbol{s}$ are the strength of spin-orbit interaction, orbital angular momentum and spin angular momentum, respectively, for an electron i. The spin-orbital entangled $\boldsymbol{J}$ can be formed by starting from two limits: the Russell-Saunders (LS) scheme and jj scheme. If $\zeta \gg J_H$, that is, when the strength of spin-orbit interaction for each electron exceeds that of the electrostatic interaction between them, the jj scheme applies. The orbital $\boldsymbol{l}$ and spin $\boldsymbol{s}$ angular momenta combine for each electron individually as $\boldsymbol{j}_i = \boldsymbol{l}_i + \boldsymbol{s}_i$, rendering a lower-lying $j_{\mathrm{eff}} = 3/2$ quartet and an upper-lying $j_{\mathrm{eff}} = 1/2$ doublet which are split by $3/2\zeta$. The produced energy levels are then filled with individual electrons and their respective $\boldsymbol{j}_i$ combine to give a total angular momentum of the atom, $\boldsymbol{J} = \sum_i \boldsymbol{j}_i$. If $\zeta \ll J_H$, that is, when the electrostatic interaction between electrons is stronger than the spin-orbit interaction in each of them, the LS scheme applies. First, the total spin and orbital moments are summed for the atoms, $\boldsymbol{S} = \sum_i \boldsymbol{s}_i$ and $\boldsymbol{L} = \sum_i \boldsymbol{l}_i$. Then, the total orbital and spin momenta combine to produce the total angular momentum $\boldsymbol{J}$, and the splitting between individual energy levels depends on the electron filling. The spin-orbit coupling scheme then takes the form:

$$H_{\mathrm{SOC}} = \lambda_{\mathrm{SOC}} \boldsymbol{L} \cdot \boldsymbol{S} \tag{1.4}$$

where λ_{SOC} is the total spin-orbit coupling composed of the ζ_i of individual electrons and for the same shell $\zeta_i = \zeta$:

$$\lambda_{\mathrm{SOC}} = \pm \frac{\zeta}{2S} \tag{1.5}$$

where + and − apply for less-than-half-filled and more-than-half filled shells, respectively. In reality, no material locates strictly in the jj or LS coupling limit, however naïvely, jj coupling should be more relevant to the heavier atoms such as Ir, while LS coupling might more accurately describe the lighter Ru atoms. In this section we discuss the LS coupling for convenience.

4d and 5d orbitals are more spatially extended as compared to 3d which renders Hund's coupling smaller than the cubic crystal field splitting 10 Dq and stabilises low spin states with only t_{2g} manifold occupied for d^n, $n \leq 6$ electron count. According to the Hund's rule, there can be total spin $S = 1/2$ (d^1 and d^5), $S = 1$ (d^2 and d^4) and spin $S = 3/2$ (d^3) configurations. All configurations except orbital singlet d^3 (which will not be discussed here) host three-fold orbital degeneracy. By examining how $\boldsymbol{L}$ operates on the t_{2g} states (for the $|l, l^z\rangle$ notation) and comparing the matrix elements $\langle t_{2g}|\boldsymbol{L}|t_{2g}\rangle$ to those of p orbitals $\langle p|\boldsymbol{L}|p\rangle$ ($L = 1$), one finds the relation $\boldsymbol{L}_{t_{2g}} = -\boldsymbol{L}_p$ [44]. Therefore one can consider an effective orbital moment $L_{\text{eff}} = 1 = -L_{\text{p}}$. The effective orbital moment reverses third Hund's rule, such that $\boldsymbol{S}$ and $\boldsymbol{L}$ are parallel and antiparallel for less- and more-than-half-filled t_{2g} manifold, respectively. In Fig. 1.8(a), for d^1, d^2, d^4 and d^5 configurations $J_{\text{eff}} = 3/2$, $J_{\text{eff}} = 2$, $J_{\text{eff}} = 0$ and $J_{\text{eff}} = 1/2$ states, respectively, are stabilised [45].

The magnetic moment $\boldsymbol{M} = 2\boldsymbol{S} - \boldsymbol{L}_{\text{eff}}$ and for d^1 configuration $\boldsymbol{M} = 0$ and the Landé factor $g_{\text{J}} = 0$, rendering $J_{\text{eff}} = 3/2$ non-magnetic. The g_{J} factors deviate from the spin-only value $g_{\text{S}} = 2$, which is a manifestation of orbital magnetism, for example for $J_{\text{eff}} = 2$ $g_{\text{J}} = 1/2$ and for $J_{\text{eff}} = 1/2$ $g_{\text{J}} = -2$. Fig. 1.8(b) illustrates the electron wavefunction shapes for all of the J_{eff} states. The $J_{\text{eff}} = 1/2$ wavefunction has an isotropic shape. On the other hand, the d^1 and d^2 ions are Jahn-Teller active: $J_{\text{eff}} = 3/2$ and $J_{\text{eff}} = 2$ have varying orbital shapes for different values of J^z and hence are susceptible to distortions. It must be noted that the LS coupling scheme for d^n ions presented in Fig. 1.8 relies on several approximations, such as 10 Dq $= \infty$ and $J_{\text{H}} \gg \lambda_{\text{SOC}}$. Real materials locate between the LS and jj coupling limit which would modify the local multiplet structure and the observed excitations. In addition, a finite mixing between t_{2g} and e_g states should take place and split the $J_{\text{eff}} = 2$ states.

The spin-orbital entangled states are expected to produce exotic electronic states depending on the d electron count and type of lattice. For d^1 and d^2 ordered double perovskites with $J_{\text{eff}} = 3/2$ and $J_{\text{eff}} = 2$ states, respectively, emergence of multipolar order was predicted [46, 47]. Due to the spin-orbital entanglement of the J_{eff} state, the magnetic and electric interactions can involve coupling of higher-order multipoles such as charge quadrupoles and magnetic octupoles. The interactions between J_{eff} pseudospins may lead to multipolar order, or a spin-orbital liquid state might be realised in a specific type of lattice [48, 49]. The d^4 configuration with the magnetically inactive $J_{\text{eff}} = 0$ state opens up a possibility of excitonic magnetism which can lead to exotic ground states on a honeycomb lattice [50]. The d^5 configuration with $J_{\text{eff}} = 1/2$ state is the most explored and established system so far, as a plethora of novel electronic states is predicted such as Kitaev spin liquid [51], Weyl semimetal [52] or topological Mott insulator [53]. The d^4 and d^5 configurations are the focus of this thesis and are discussed in more detail below.

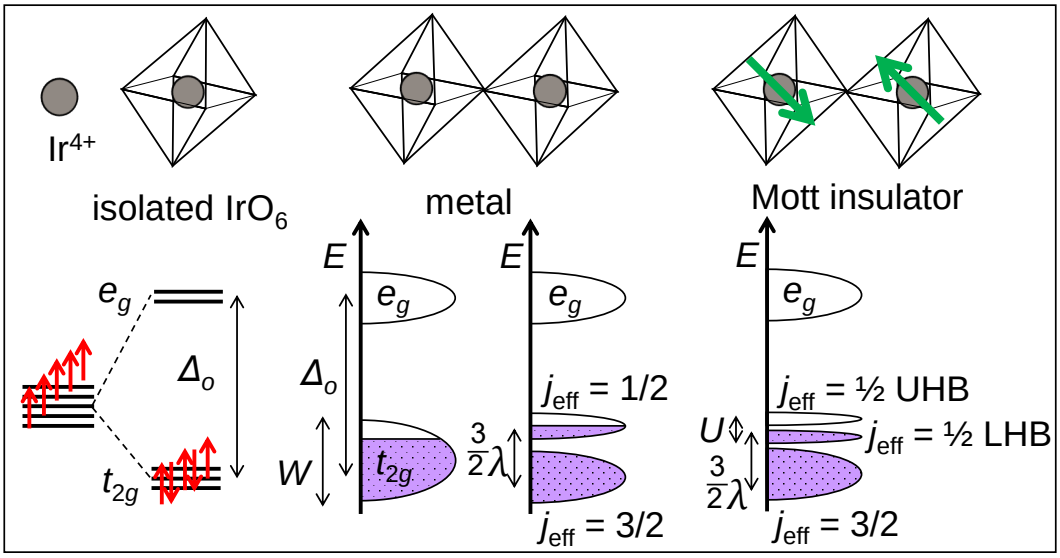

■ *Figure 1.9.* The evolution of Ir 5*d* states from free Ir^{4+} ion to complex iridium oxide such as Sr_2IrO_4. The cubic crystal field (Δ_o) locates all five electrons in the t_{2g} manifold. In a crystalline lattice, a t_{2g} band is formed, and correlation U is not large enough to overcome the bandwidth W and open a gap. Instead, large spin-orbit coupling λ splits the t_{2g} band into $j_{\text{eff}} = 3/2$ and half-filled $j_{\text{eff}} = 1/2$ bands. Finally, moderate correlation U splits the $j_{\text{eff}} = 1/2$ manifold into an upper Hubbard and a lower Hubbard bands (UHB and LHB, respectively) and produces a Mott insulator, such as found in Sr_2IrO_4.

1.6.1 $J_{\text{eff}} = 1/2$ Mott insulators

t_{2g}^5 configuration renders a one-half pseudospin by starting both from *LS* and *jj* limits. The spin-orbital entangled $J_{\text{eff}} = 1/2$ wavefunction is composed of quantum superposition of d_{xy}, d_{xz} and d_{yz} orbitals with complex components:

$$|J_{\text{eff}} = 1/2, J^z_{\text{eff}} = +1/2\rangle = (1/\sqrt{3})(|d_{xy}, \uparrow\rangle + |d_{yz}, \downarrow\rangle + i\,|d_{xz}, \downarrow\rangle), \tag{1.6}$$

$$|J_{\text{eff}} = 1/2, J^z_{\text{eff}} = -1/2\rangle = (1/\sqrt{3})(|d_{xy}, \downarrow\rangle - |d_{yz}, \uparrow\rangle + i\,|d_{xz}, \uparrow\rangle), \tag{1.7}$$

where $|J_{\text{eff}} = 1/2, J^z_{\text{eff}} = +1/2\rangle$ and $|J_{\text{eff}} = 1/2, J^z_{\text{eff}} = -1/2\rangle$ correspond to up and down pseudospin, respectively. As the $J_{\text{eff}} = 1/2$ wavefunction comprises equal superposition of all three t_{2g} orbitals, it exhibits a remarkably isotropic shape as shown in Fig. 1.8(a). The gyromagnetic factor $g_J = -2$ giving a magnetic moment of $1\,\mu_B$ which is of the same magnitude as for spin-only $S = 1/2$. The negative sign of g_J is a signature of unquenched orbital moment which renders the interactions between $J_{\text{eff}} = 1/2$ pseudospins extremely sensitive to the local lattice geometry [51, 54].

The $J_{\text{eff}} = 1/2$ state was first identified in a layered perovskite Sr_2IrO_4. In this structure, the 3*d* and 4*d* analogues, namely Sr_2CoO_4 [55] and Sr_2RhO_4 [56] are metallic. Naïvely, the 5*d* analogue Sr_2IrO_4 would be expected to host a metallic state as well due to even more extended

5d orbitals. In contrast, Sr_2IrO_4, as well as many other complex iridium oxides, is found to be insulating. Sr_2IrO_4 comprises tilted IrO_6 octahedra within the layered perovskite lattice and shows insulating behaviour [57] with a magnetic transition at $T = 240\,\mathrm{K}$ [58]. The origin of this unexpected insulating state can be understood by considering the spin-orbit coupling and moderate electron correlation. In the band picture without SOC and U one finds a partially filled t_{2g} band of width W as shown in Fig. 1.9. In a typical scenario for 3d TMOs, $U \gg W$ and a gap opens. However, for 4d and 5d compounds, the correlation is weaker due to spatially extended d orbitals and modest U cannot open a gap. However, the large SOC of the order of $\sim 0.4\,\mathrm{eV}$ in Sr_2IrO_4 splits the t_{2g} band and forms a distinct half-filled $j_{\mathrm{eff}} = 1/2$ band, and consequently the $j_{\mathrm{eff}} = 1/2$ band is narrow enough to be split by moderate correlation U into UHB and LHB, producing a spin-orbit "assisted" Mott insulator. In the case of Sr_2RhO_4, the SOC is about three times smaller than that of Sr_2IrO_4. As a result, the SOC-produced $j_{\mathrm{eff}} = 1/2$ and $j_{\mathrm{eff}} = 3/2$ bands are not well separated, resulting in a broad t_{2g} band which is still too wide to be split by the weak correlation, giving a metallic state. Therefore, the large SOC is key for understanding the Mott insulating state of Sr_2IrO_4 and other complex iridium oxides. The validity of this scenario and the $J_{\mathrm{eff}} = 1/2$ state has been directly probed with angle-resolved photoemission spectroscopy (ARPES) [59] and REXS at Ir L_3 and L_2 edge [54].

Interestingly, the essential ingredients for high-temperature superconductivity in cuprates are believed to be spin one-half Heisenberg AFM on a 2D square lattice in the parent compounds [60] and strong exchange couplings [61], and Sr_2IrO_4 is a material that also comprises those components [62]. Therefore, it has been predicted that Sr_2IrO_4 could be tuned towards superconductivity with doping (left of Fig. 1.10) [63–65]. Indeed, a pseudogap opens in Sr_2IrO_4 upon electron doping [66], however further evidence of the possible superconductivity is lacking. Nevertheless, experimental verification of a spin-orbital entangled one-half pseudospin motivated research activity on $J_{\mathrm{eff}} = 1/2$ materials with lattices other than quasi-2D layered perovskite. $J_{\mathrm{eff}} = 1/2$ honeycomb and pyrochlore lattices are of broad interest due to possible realisation of novel electronic states. For example, materials with $J_{\mathrm{eff}} = 1/2$ pseudospin are predicted to be realisation of condensed-matter-analogues of exotic particles relevant to high-energy physics such as Majorana or Weyl fermion.

Jackeli and Khaliullin proposed that Ir^{4+} ions with $J_{\mathrm{eff}} = 1/2$ state in edge-sharing geometry embedded in a quasi-2D honeycomb lattice is a possible realisation of Kitaev quantum spin liquid (QSL) [51]. Kitaev QSL is a novel type of QSL based on ferromagnetic anisotropic couplings, which is exactly solvable if one maps electrons into Majorana fermions with bond-dependent interactions (middle of Fig. 1.10). Material candidates for realisation of Kitaev QSL called "Kitaev materials" are α, β-A_2IrO_3 honeycomb-based compounds as well as α-$RuCl_3$. While the importance $J_{\mathrm{eff}} = 1/2$ spin-orbital entangled state and bond-dependent ferromag-

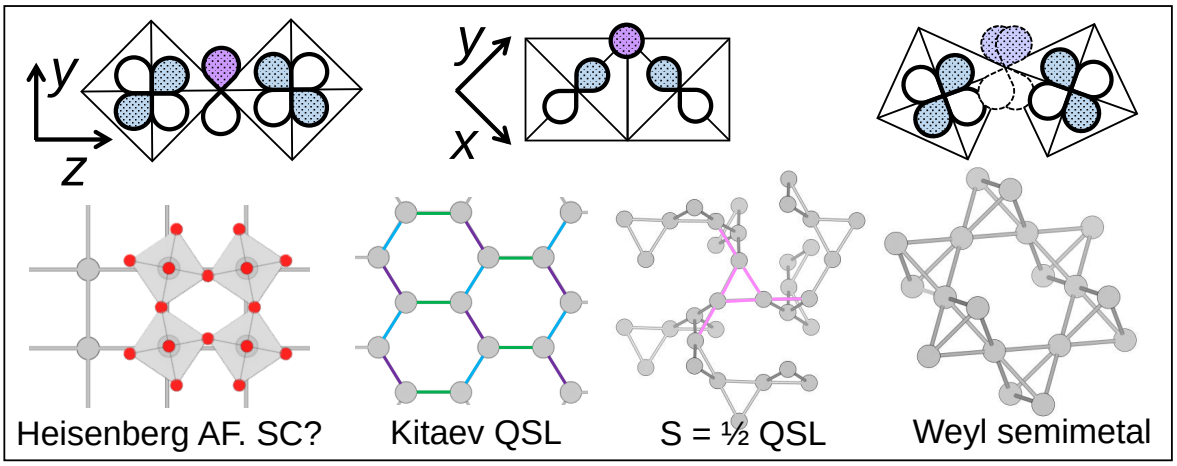

■ *Figure 1.10.* Zoo of $J_{\text{eff}} = 1/2$ complex iridium oxides. The bottom part shows the lattice of Ir atomsvonly. Left: 180° corner-sharing geometry embedded in a quasi-2D square lattice renders Heisenberg-like pseudospin one-half antiferromagnet. Superconductivity (SC) is predicted upon doping. Middle: 90° edge geometry embedded in a quasi-2D honeycomb lattice, for which Kitaev QSL is predicted, and in a hyperkagome lattice, a 3D lattice with triangular motif which a $S = 1/2$ quantum spin liquid candidate. Right: $\sim$ 130° corner-sharing geometry embedded in pyrochlore lattice, for which Weyl semimetal is predicted.

netic exchange has been established in Kitaev materials, the pure Kitaev QSL state remains to be identified [67]. Substantial efforts have been made in tuning these systems towards a QSL with doping and application of pressure or magnetic field. Surprisingly, in search for a QSL a competing state of molecular orbital has been identified under high pressure. The nature of the pressure-induced state in the 3D Kitaev material β-Li_2IrO_3 is explored in chapter 3.

Interestingly, it appears that another edge-sharing Ir^{4+}-based oxide shows competition between QSL and molecular orbital phases. In hyperkagome $Na_4Ir_3O_8$ (middle of Fig. 1.10, refer to Appendix A for detail on crystalline lattice), the geometrical frustration prevents the system from ordering and likely stabilises a QSL state of localised $S = 1/2$ moment despite strong AFM interaction [68]. Upon doping with 1/3 of holes per Ir site with removal of some Na sites, $Na_3Ir_3O_8$ becomes semimetallic [69]. The semimetallic state is proposed to arise from competition of molecular orbital formation within the Ir_3 triangles and spin-orbit coupling [69].

Another common polyhedral corner-sharing Ir-O-Ir link with $\sim$ 130° geometry is found in geometrically frustrated pyrochlores (Appendix A). Pyrochlore iridates are expected to realise an exotic Weyl semimetal (WSM) state for intermediate correlation strength [52]. Pyrochlore iridates $A_2Ir_2O_7$ show an MIT as a function of the ionic radius of A and hence evidence promising tunability. However, no clear evidence of WSM has been identified to date despite exhaustive studies in the metallic regime of pyrochlore iridates [70]. IrO_6 octahedra

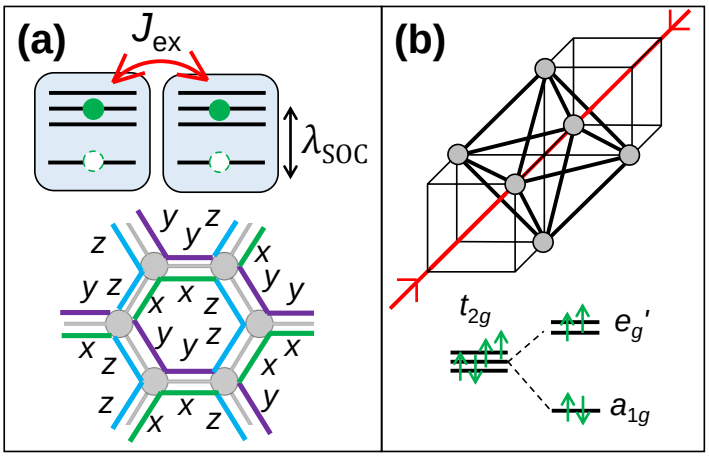

■ *Figure 1.11.* (a) Top: a cartoon illustrating magnetic coupling between excited states. Bottom: 1D bond-dependent couplings of triplon states on a honeycomb lattice are denoted with different colours. (b) Strong trigonal compression (top) quenches the orbital degeneracy of a t_{2g}^4 configuration. The red line is the compression axis along which the new z' axis in the trigonal coordinate system lies.

comprising the Ir pyrochlore lattice are strongly trigonally distorted, such that the trigonal crystal field is of the order of SOC. The impact of the trigonal distortion on the spin-orbital entangled $J_{\text{eff}} = 1/2$ state has not been greatly addressed, and its impact on the local electronic states as well as intersite hopping is investigated in a new material $In_2Ir_2O_7$ in chapter 4.

1.6.2 $J_{\text{eff}} = 0$ Mott insulators

The $J_{\text{eff}} = 1/2$ state can give rise to a variety of exotic electronic phases on different types of lattices. Another route for a novel ground state is $J_{\text{eff}} = 0$ state with t_{2g}^4 configuration. Not much exciting physics emerges from a non-magnetic singlet, however if the magnetic coupling between the excited states can overcome the excitation gap, the excited $J_{\text{eff}} = 1$ moments are expected to form a long-range magnetic order called "excitonic condensate" (Fig. 1.10(a)). In addition, if one maps the $J_{\text{eff}} = 1$ triplet into three "triplons" with bond-dependent interactions on a honeycomb lattice, exotic spin liquid state may be realised [50].

Some candidate $J_{\text{eff}} = 0$ $5d$-based materials have been reported to show singlet magnetism, implying that the gap between $J_{\text{eff}} = 0$ and $J_{\text{eff}} = 1$ states is too large to allow for the condensation of the excited states. Therefore, a $4d$ ion such as Ru^{4+} could be a promising candidate for excitonic magnetism. However, several ruthenates, such as honeycomb Li_2RuO_3 and pyrochlore $Tl_2Ru_2O_7$, form non-magnetic molecular clusters at low temperatures. On the other hand, ruthenates that do show long-range magnetic order, for example other pyrochlore ruthenates, have not been discussed in the context of excitonic magnetism. Instead, it has been

suggested that the orbital degree of freedom is quenched by trigonal or tetragonal distortion rendering a spin-only $S = 1$ moment. In the absence of SOC, trigonal compression splits the t_{2g} states into lower-lying a_{1g} singlet and upper-lying e'_g doublet, where 4-electron filling gives an orbital singlet (${a_{1g}}^2{e'_g}^2$ configuration) as shown in Fig. 1.10(b). Exciton condensation of a d^4 material was only discussed in a layered perovskite ruthenate recently [71, 72], suggesting that the orbital magnetism can survive despite distortion. In addition, the dimerisation in Li_2RuO_3 can be suppressed by ion substitution of Li with Ag [73], which indicates that spin-orbital entangled states compete not only with the non-cubic crystal field, but with molecular orbital formation as well. Therefore, ruthenates with t_{2g}^4 configuration are an interesting platform for competition of orbital molecule and spin-orbital entangled states, which is explored in a new material $In_2Ru_2O_7$ presented in chapter 5.

1.7 Case studies for competition between spin-orbit coupling, orbital molecules and crystal field

Orbital degeneracy is a source of exotic electronic states such as orbital ordering, molecular orbital formation and spin-orbital entanglement. The competition between these effects becomes interesting in 4*d* and 5*d* systems as many interactions, which govern these mechanisms, meet on the same energy scale. In 4*d* and 5*d* materials the *d* orbitals are more spatially extended as compared to 3*d* orbitals, which results in reduced correlation U and hence Hund's coupling J_H as well as enhanced intersite hopping t. Non-cubic crystal field also has more drastic consequences for the large *d* orbitals. Most importantly, due to large atomic numbers in 4*d* and 5*d* elements spin-orbit coupling is of the order of hundreds of meV and competes with the other interactions. In this thesis, three materials are investigated in the context of competition between spin-orbit coupling, molecular orbital split and non-cubic crystal field.

β-Li_2IrO_3 is a honeycomb-based spin-orbital entangled $J_{\text{eff}} = 1/2$ magnet at ambient conditions. At high pressures, the magnetic order is suppressed and a structural transition takes place. β-Li_2IrO_3 comprises edge-sharing IrO_6 octahedra. At high pressures, the crystalline lattice shrinks and orbital overlap is enhanced. The direct *d*-*d* hopping likely competes with the otherwise dominant indirect *d*-*p*-*d* hopping at high pressures. With neutron diffraction, RIXS and band structure calculations, we address the impact of the structural transition on the electronic state of β-Li_2IrO_3 as well as the validity of the $J_{\text{eff}} = 1/2$ state. We find that at high pressures the $J_{\text{eff}} = 1/2$ state collapses and Ir–Ir dimers with molecular orbital formation emerge. Therefore, the competition between spin-orbit coupling and molecular orbital formation in t_{2g} systems can be tuned by pressure.

A strong non-cubic crystal field can also disturb the spin-orbital entangled $J_{\text{eff}} = 1/2$ state.

Pyrochlore iridates contain trigonally compressed octahedra and the trigonal crystal field is as large as 0.3 eV which is more than half of the spin-orbit coupling magnitude. While pyrochlore iridates serve as a platform for non-trivial topological states, the magnetism and validity of the $J_{\mathrm{eff}} = 1/2$ state is unexplored in pyrochlore iridates with large trigonal distortion. Utilising high pressure synthesis, we discovered a new pyrochlore iridate $In_2Ir_2O_7$ with the largest trigonal distortion among pyrochlore iridates. We find that In-O bond covalency suppresses intersite hopping of Ir d electrons and as a result induces a nearly pure $J_{\mathrm{eff}} = 1/2$ state despite large compression of IrO_6 in contrast to other pyrochlore iridates. Here it is demonstrated that the A-O bond covalency of the constituent cation can induce a pure spin-orbital entangled state.

Ruthenates with d^4 configuration are predicted to host a $J_{\mathrm{eff}} = 0$ state and exhibit excitonic magnetism via excited $J_{\mathrm{eff}} = 1$ states. However, many ruthenates undergo molecular orbital formation, and those that do not, for example pyrochlore ruthenates, are discussed to be $S = 1$ magnets due to large trigonal distortion silencing the orbital degree of freedom ($a_{1g}^2 e_g'^2$ configuration). However, one pyrochlore ruthenate $Tl_2Ru_2O_7$ forms a non-magnetic ground state with orbital ordering. The distinct state of $Tl_2Ru_2O_7$ among pyrochlore ruthenates is discussed to be related to Tl-O covalency. Given the likely similar character of Tl-O and In-O bonds (Fig. 1.1) together with the impact of In-O covalency on the electronic state identified in $In_2Ir_2O_7$, we synthesised a new pyrochlore ruthenate $In_2Ru_2O_7$. $In_2Ru_2O_7$ is a unique pyrochlore ruthenate that represents both spin-orbital entangled and molecular orbital limits. At high temperatures, despite the large non-cubic crystal field, $In_2Ru_2O_7$ stabilises a likely non-magnetic spin-orbital entangled singlet state. With decreasing temperature, the singlet state collapses due to large distortion of In-O network which in turn sparks distortion of the Ru-O network. On top of the Ru pyrochlore lattice, semi-isolated Ru_2O units with molecular orbital formation emerge. While In-O covalency stabilises a spin-orbital entangled state in $In_2Ir_2O_7$, it suppresses the spin-orbit coupling effect in $In_2Ru_2O_7$ at low temperatures and favours an orbital molecule state instead.

Chapter 2

Methods

2.1 Material synthesis

2.1.1 Solid state synthesis

Polycrystalline materials studied in the scope of this thesis are synthesised mostly by a solid state synthesis method shown in Fig. 2.1. For enhancement of the reaction and maximisation of the reagent surface contact, powders of reagents are thoroughly ground in an agate mortar such that the size of the particles is of the order of tens of micrometers, and are subsequently pressed into a pellet with a pressure of $\sim$ 10 MPa, which is then heated. Usually, impurity levels can be reduced by repeated grinding and calcination cycles.

Single crystal growths of β-Li_2IrO_3 and $In_2Ru_2O_7$ were performed by employing a flux method using a halide salt comprising the same A = Li or In cation as the target compounds to avoid contamination. Further details are discussed in the relevant chapters.

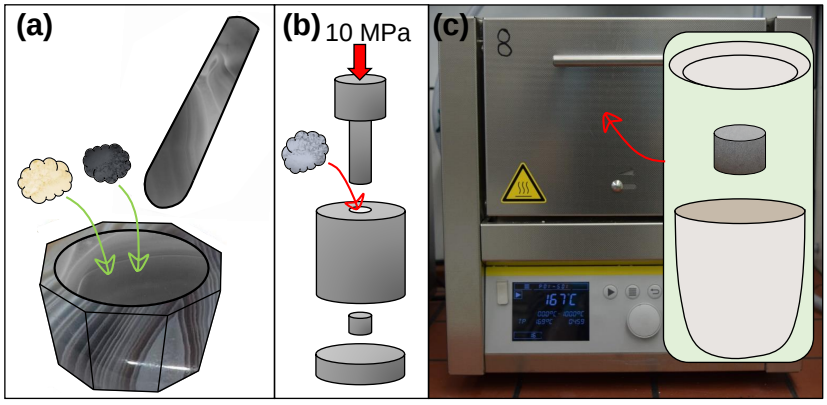

■ *Figure 2.1.* (a) The powders of the reagents are mixed using an agate mortar. (b) The mixture is pressed into a pellet using a tungsten carbide 6 mm die. (c) The pressed pellet is placed into a Al_2O_3 crucible and into a box furnace used for calcination.

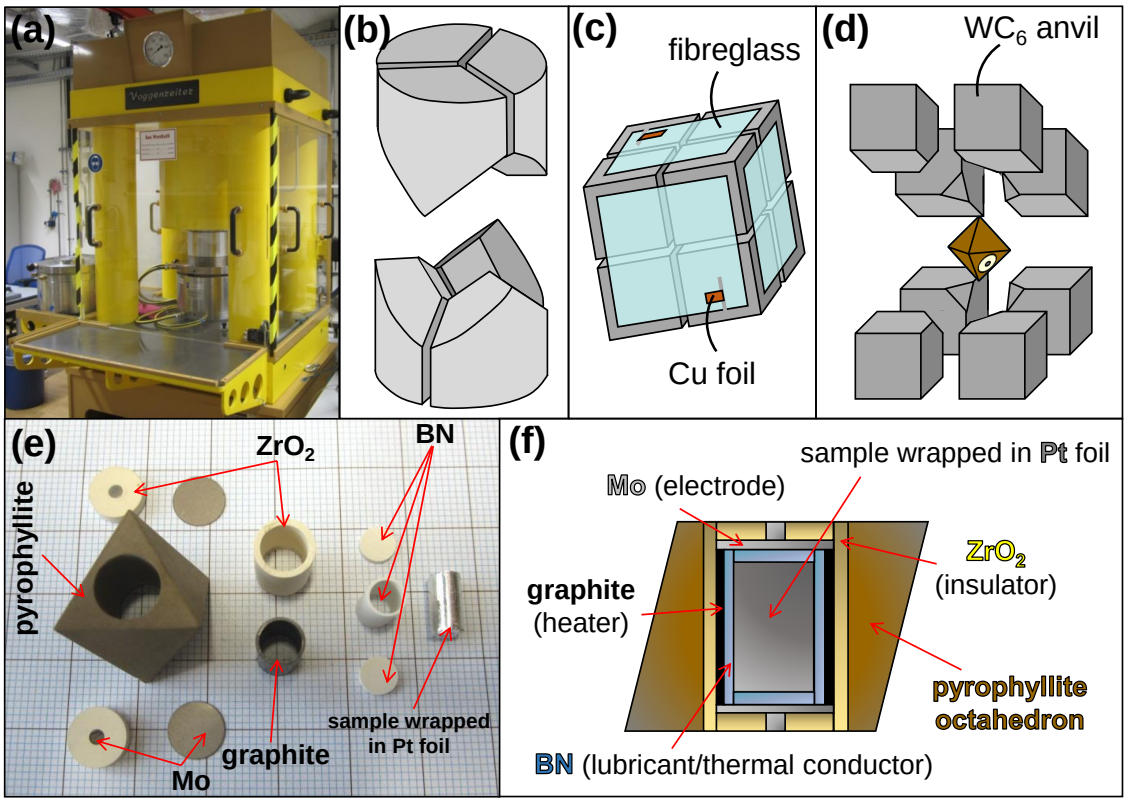

■ *Figure 2.2.* High pressure and high temperature synthesis set up. The Walker module has a water cooling system. (a) The Voggenreiter press station. (b) The stainless steel wedges located inside the Walker module which transform the uniaxial pressure generated by the press into octahedral pressure applied to the WC_6 cubes. (c) The WC_6 assembly surrounding the sample cell. The eight cubes are held together by fibreglass sheets and have slices of copper foil attached for electrical contact across the desired direction. (d) The octahedral sample cell that is placed between the eight WC_6 cubes with truncated corners. (e) Parts of a high pressure cell used for synthesis. (f) Diagram of a cross section of a high pressure cell.

2.1.2 High pressure synthesis

In order to access new materials beyond the tolerance factor determined for $A_2B_2O_7$ pyrochlore lattice [74], high pressure synthesis depicted in Fig. 2.2 was employed. For generating isotropic pressure, a multi-anvil Walker module [75] was used, which transforms uniaxial pressure generated by the 1000 tonne hydraulic press into 8-directional pressure that acts on an octahedral sample cell. Well mixed powders of reagents are placed in a platinum foil capsule. After the target pressure is achieved, the capsule is heated by flowing current through the graphite cylinder via the molybdenum electrodes as shown in Fig. 2.2(e) and (f). The sample is electrically isolated from the graphite cylinder by a capped boron nitride cylinder. After the

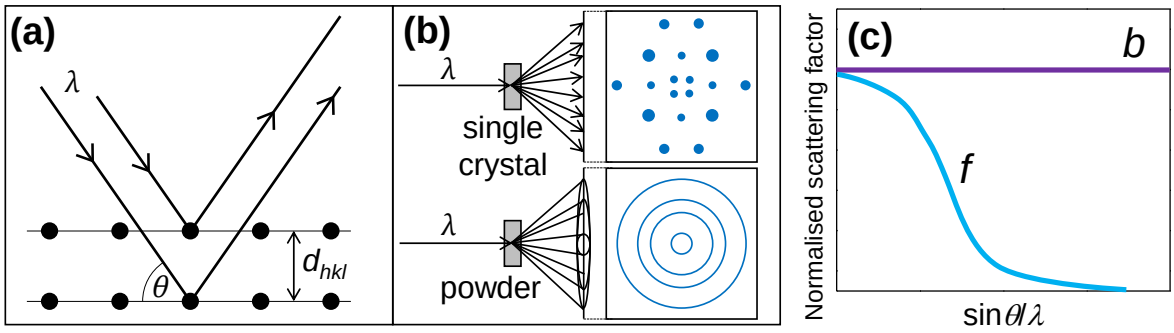

■ *Figure 2.3.* (a) Diagram illustrating the Bragg's law. (b) Differences between diffraction patterns from single crystal (top) and polycrystalline (bottom) samples. (c) Comparison neutron b and x-ray f form factor dependence on 2θ.

heating period is completed, the sample is quenched by manually switching off the current. Then, the pressure is slowly decreased down to ambient pressure over 10 hour period.

2.2 Structure determination

Since atoms are periodically arranged in a crystalline lattice, radiation diffracted off these atoms with a wavelength comparable to the interatomic spacing interacts constructively or destructively. The periodic arrangements can be described in terms of equally-spaced planes denoted by the Miller indices hkl with spacing between the planes d_{hkl}. One can then arrive at the Bragg's condition illustrated in Fig. 2.3(a):

$$2d_{hkl} \sin\theta = n\lambda, \tag{2.1}$$

where d_{hkl}, θ, n and λ is interatomic spacing denoted by the Miller indices h, k and l, glancing angle, a positive integer (usually fixed as 1) and the wavelength of the incident wave, respectively. At certain glancing angles the constructive interference occurs producing high intensity points known as Bragg peaks, and from equation 2.1 the individual d_{hkl} can be indexed. The observed Bragg peak position and intensity contains information on the crystal symmetry, unit cell size and atomic positions, from which the crystal structure can be deduced. Therefore, diffraction is one of the most common techniques used for structure determination.

Single crystal samples produce a two-dimensional pattern related to the orientation of the crystal with respect to the indicent beam as shown in Fig. 2.3(b). In polycrystalline samples, such orientation can be no longer fixed and an average of superpositions of all possible orientations, where combinations of waves scattered off the symmetry equivalent Miller indices produce so-called Debye-Scherrer cones. This results in a set of rings in a diffraction

pattern due to overlap of diffraction peaks and thus loss of all information on orientation. Usually, the obtained 2D pattern of rings is linearised and the data analysed data is a function of intensity vs angle (2θ).

Diffraction techniques used in this thesis involved time-of-flight neutron diffraction and laboratory x-ray diffraction (XRD). While both techniques utilise the same principle outlined above, there are some fundamental differences between the two. X-ray beams scatter from the electronic charge in the crystal, while neutrons scatter via nuclear and magnetic interactions with the atomic nuclei and spin density of the sample, respectively. Neutron diffraction allows for precise determination of lighter elements in contrast to x-ray diffraction. On the other hand, some elements are strongly neutron absorbing, and in general neutron experiments require larger sample sizes and longer counting times since the interactions of neutrons with the nuclei of the atom are weak. In this thesis, low-resolution x-ray diffraction has been mostly used in the laboratory for phase identification after synthesis, while the high resolution x-ray diffraction has been used for structure determination of newly discovered compounds $In_2Ir_2O_7$ and $In_2Ru_2O_7$. Neutron diffraction was used for precise determination of the positions of the light atoms in the high pressure study of β-Li_2IrO_3 and for structural phases identified in $In_2Ru_2O_7$.

2.2.1 X-ray diffraction

While there are many synchrotron-based x-ray techniques, x-ray diffraction is also easily available in a laboratory setting as compared with neutron sources. A diffraction pattern can be collected in a few minutes or hours, and therefore XRD is a convenient technique for fast phase identification and quality verification. The scattering cross-section of x-rays is proportional to Z^2, where Z is the atomic number. As a result, the form factor drops off rapidly for light atoms and the diffraction data is dominated by the heavier atoms comprising the crystalline lattice. The form factor f is also dependent on the scattering vector $\boldsymbol{q}$ as

$$\boldsymbol{q} = \frac{4\pi \sin\theta}{\lambda} \tag{2.2}$$

and hence $f \sim \sin\theta/\lambda$, which leads to a decrease in observed intensity with increasing 2θ as illustrated in Fig. 2.3(c). The scattered x-ray wave is a superposition of all the scattered waves from individual electrons and the phase shift of scattered x-rays increases with 2θ as shown in (Fig. 2.3(c)).

The instrument used for phase identification in samples studied in this thesis was Bruker D2 Phaser x-ray diffractometer with $Cu_{K\alpha}$ radiation unless specified otherwise.

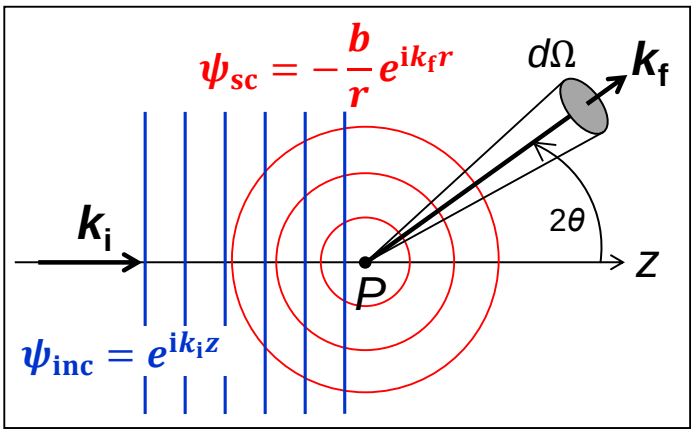

■ *Figure 2.4.* Scattering of a plane wave of neutrons (Ψ_{inc}, blue) of a point scatterer into a spherical wave (Ψ_{sc}, red) into solid angle dΩ.

2.2.2 Neutron diffraction

In contrast to x-rays, charge neutral neutrons do not scatter strongly off the electron density of a material and instead weakly interact with the atomic nuclei via the nuclear interaction. This allows precise determination of atomic positions as the true position of atomic nuclei, instead of the shape of the electron cloud, is probed. In addition, the size of atomic nuclei (10^{-5} Å) is orders of magnitude smaller than the typical wavelength of thermal neutrons used in diffraction experiments ($\sim$ 1 Å). Therefore, in neutron scattering experiments the atomic nuclei can be approximated as point scatterers and scattered neutrons take the form of spherically symmetric waves. One can express the incident neutrons as a plane wave [76]:

$$\psi_{inc} = \exp(i\boldsymbol{k}_i z), \tag{2.3}$$

where the wavevector $\boldsymbol{k}_i$ is aligned along z. In Fig. 2.4, the spherically symmetric scattered wave at a distance r from the nucleus can be written as:

$$\psi_{sc} = -\frac{b}{r}\exp(i\boldsymbol{k}_f r), \tag{2.4}$$

where b is the scattering length (fm) which expresses the neutron scattering strength of atoms. In Fig. 2.4, b is independent of atomic number and is nearly random with respect to the atomic number Z. Therefore, with neutron diffraction one can locate light atoms precisely as well as distinguish between elements with similar atomic number.

For elastic scattering, the fundamental quantity measured is the differential scattering cross section expressed as $d\sigma/d\Omega$, which is the number of neutrons per second scattered into the solid angle dΩ measured as a function of momentum transfer $\boldsymbol{k}_i - \boldsymbol{k}_f$. One can derive the

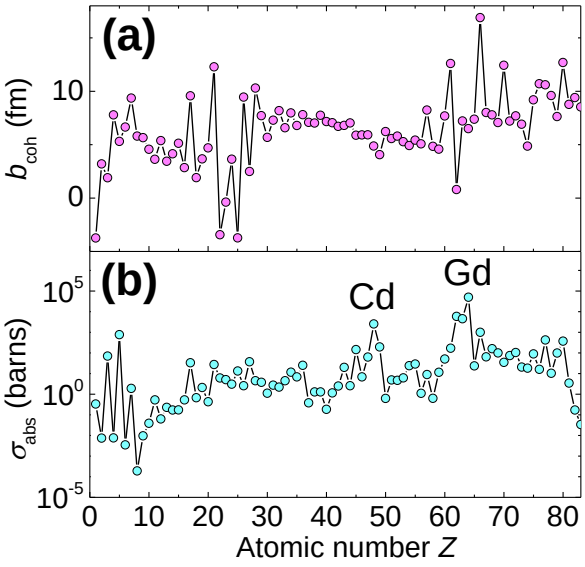

■ *Figure 2.5.* Coherent scattering lengths b_{coh} (a) and absorption cross sections σ_{abs} (b) for naturally occurring elements [77].

relationship:

$$\frac{d\sigma_{tot}}{d\Omega} = |\psi_{sc}|^2 r^2 \tag{2.5}$$

where σ_{tot} is the total scattering cross section expressed in units of barns. For scattering of a single nucleus, $|\psi_{sc}|^2 = b^2/r^2$ and hence

$$\sigma_{tot} = 4\pi b^2. \tag{2.6}$$

Different isotopes have their characteristic b as the scattering interaction between the neutron and the nucleus is a resonance phenomenon that can be characterised as a "compound nucleus" with the σ_{tot} derived above. However, real systems often contain a mixture of isotopes which gives rise to coherent and incoherent scattering. Since the interaction of neutrons with atomic nuclei depends not only on the energy but also on the type of isotope, such mixture of isotopes in a material generates incoherent scattering of neutrons, and the corresponding total, coherent and incoherent scattering cross sections become:

$$\sigma_{tot} = 4\pi\overline{b^2}, \tag{2.7}$$

$$\sigma_{coh} = 4\pi\overline{b}^2, \tag{2.8}$$

$$\sigma_{incoh} = 4\pi(\overline{b^2} - \overline{b}^2). \tag{2.9}$$

Some isotopes have a large incoherent scattering cross section. In addition, some naturally occurring elements (mixtures of isotopes) are strongly neutron-absorbing, for example Cd

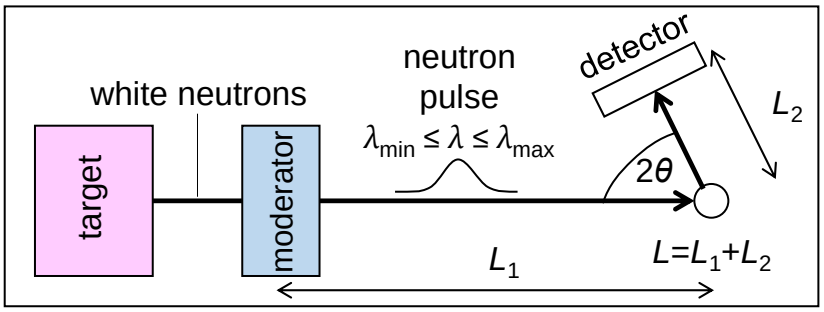

■ *Figure 2.6.* Schematic time of flight neutron diffractometer geometry. The total path length is $L = L_1 + L_2$.

and Gd, or Ir and In studied in this thesis. In some cases, enrichment with an isotope with the smallest absorption cross sections σ_{abs} within the element has to be employed in material synthesis. The coherent scattering length b_{coh} and σ_{abs} are shown in Fig. 2.5. Structural refinement programmes for neutron diffraction data contain the corresponding scattering parameters for individual isotopes as well as averages for elements (according to abundance).

► Time of flight technique

Most diffraction experiments, especially in a laboratory setting, employ angle-dispersive techniques, where the energy of the incoming beam is fixed, and one accesses a range of d_{hkl} spacings by varying the scattering angle in the Bragg's law in eq. 2.1. Another method is energy-dispersive mode, where the scattering angle is fixed and the incoming beam contains a range of wavelengths. This approach is most commonly used in facilities with spallation sources, where beams are generated in pulses in order to avoid time contamination of a signal. This approach exploits the wave-particle duality and the Broglie relation $\lambda = h/p$ which is then combined with Brag's law $2d_{hkl}\sin\theta = n\lambda$. One can express the momentum p as a product of mass m and velocity v and time of flight t over the path L one obtains:

$$\lambda = h/mv = 2d_{hkl}\sin\theta \quad (n = 1) \tag{2.10}$$

$$ht/mL = 2d_{hkl}\sin\theta \tag{2.11}$$

$$t = \frac{1}{h}2mLd_{hkl}\sin\theta \tag{2.12}$$

Note that time of flight t is directly proportional to d_{hkl}.

The basic setup of a time-of-flight neutron diffractometer is shown in Fig. 2.6. First a beam of neutrons with broad energy is produced from the target, which is then narrowed by passing through a moderator, where neutrons undergo multiple collisions with atoms held at a constant temperature. If desired, the neutrons may finally pass through a monochromator or choppers to further decrease the energy range. The neutrons scattered off the sample

are measured with a detector at an angle 2θ. The resolution function for a time of flight instrument is:

$$\frac{\Delta d}{d} = \left(\left(\frac{\Delta L}{L} \right)^2 + \left(\frac{\Delta t}{t} \right)^2 + (\Delta\theta \cot\theta)^2 \right)^{1/2} \tag{2.13}$$

And hence the higher the scattering angle, the higher the resolution. In this thesis, high-resolution neutron powder diffraction on HRPD at ISIS was utilised for structural study on $In_2Ru_2O_7$. A moderate resolution powder diffractometer PEARL was utilised for structural study on β-Li_2IrO_3 at high pressures.

2.2.3 Rietveld refinement

Overlapping reflections in powder patterns are problematic which makes it difficult to extract the F_{hkl} structure factors (proportional to intensity, $I_{\text{hkl}} \sim |F_{\text{hkl}}|^2$). This can be overcome with a computational fitting method implemented by Rietveld [78]. Intensity $y_{i,\text{obs}}$ at each point i of a parameter (such as t, d spacing, 2θ angle) is calculated from the relation:

$$y_{i,\text{calc}} = \sum_{hkl} K_i \phi(2\theta_i - 2\theta_{hkl}) + y_{i,\text{bkg}} \tag{2.14}$$

where K_i contains numerous corrections (geometric, absorption, multiplicity, preferred orientation, etc.), ϕ is a normalised function that describes the shape of a diffraction peak which is centred at the reflection position $2\theta_{hkl}$ and $y_{i,\text{bkg}}$ is a background term. The model parameters, such as unit cell parameters, atomic positions, isotropic atomic displacement, background coefficients, profile parameters, sample displacement and a zero offset, are typically refined in order to minimise the difference between the model and observed data points with a least squares fits.

$$D = \sum_i (w_i (y_{i,\text{obs}} - y_{i,\text{calc}}))^2 \tag{2.15}$$

where w_i is the inverse of the total observed intensity at point i. The weighted residual for the Rietveld refinement R_{wp} is defined as:

$$R_{\text{wp}} = \left(\frac{D}{\sum_i w_i (y_{i,\text{obs}})^2} \right)^{1/2} \tag{2.16}$$

Another commonly used parameter expressing quality of fit is χ^2:

$$\chi^2 = \left(\frac{R_{\text{wp}}}{R_{\text{exp}}} \right)^2 \tag{2.17}$$

where R_{exp} is the expected R-factor dependent on the counting statistics [79].

The neutron powder diffraction data were refined with the Rietveld method by using GSAS [80] programme, while the x-ray powder diffraction data was refined with TOPAS6 [81]. Images of crystal structures presented in this thesis were generated with VESTA [82].

2.3 Inelastic scattering techniques

The only spectroscopic technique presented in this thesis is resonant inelastic x-ray scattering (RIXS). As shown in Fig. 2.7(d), depending on the energy resolution, one can probe a variety of excitations, such as lattice, magnetic or local *d*-*d* excitations. TMOs host a variety of orbital-ordered, spin-orbital entangled or orbital molecule states. RIXS is a key technique for elucidating the nature of those exotic states as the excitation structure provides information on the local orbital manifold structure. In this thesis, we are mostly concerned with $\boldsymbol{q}$-averaged *d*-*d* excitations.

2.3.1 Resonant Inelastic X-ray Scattering

Resonant inelastic x-ray scattering (RIXS) is a powerful technique for investigation of magnetic, charge and orbital orders via excitation [83] which requires synchrotron radiation. RIXS is a two step process that allows transfer of both energy and momentum to the sample (Fig. 2.7(b)). By tuning the incident x-ray beam to the resonant energy for absorption in a specific element, one can select sensitivity towards specific types of order, such as magnetic, orbital or charge. Here no $\boldsymbol{q}$-dependence is discussed as this thesis concerns polycrystalline samples.

Fig. 2.7(a) illustrates the two-step photon-in photon-out process of RIXS. First, the incident beam is tuned to match the energy of core orbital $\rightarrow$ valence orbital excitation, for example excitation from core $2d$ orbitals to valence $4/5d$ orbitals in Ru/Ir. The intermediate state with a core hole is highly unstable and is annihilated by an electron from the valence band such that the final state $|f\rangle$ is different from the initial state $|i\rangle$. Accordingly, one can probe atomic excitations within the local electronic state manifold. The energy gain/loss and momentum transfer of the scattered x-ray beam is typically evaluated with a spherically-bent diced crystal analyser (Fig. 2.9) which operates on Bragg's law and can provide energy resolution below 200 meV [84].

Fig. 2.7(b) shows energies for various absorption "edges" depending on the atomic number Z. K, L and M denote excitations from core shells with the principal quantum number $n = 1$, 2 and 3 to the valence shells, respectively. Both hard and soft x-ray energy ranges have well established techniques, however the intermediate range of x-ray beams around 1 keV to 2 keV are problematic as in that energy range the attenuation from air is large and the energy

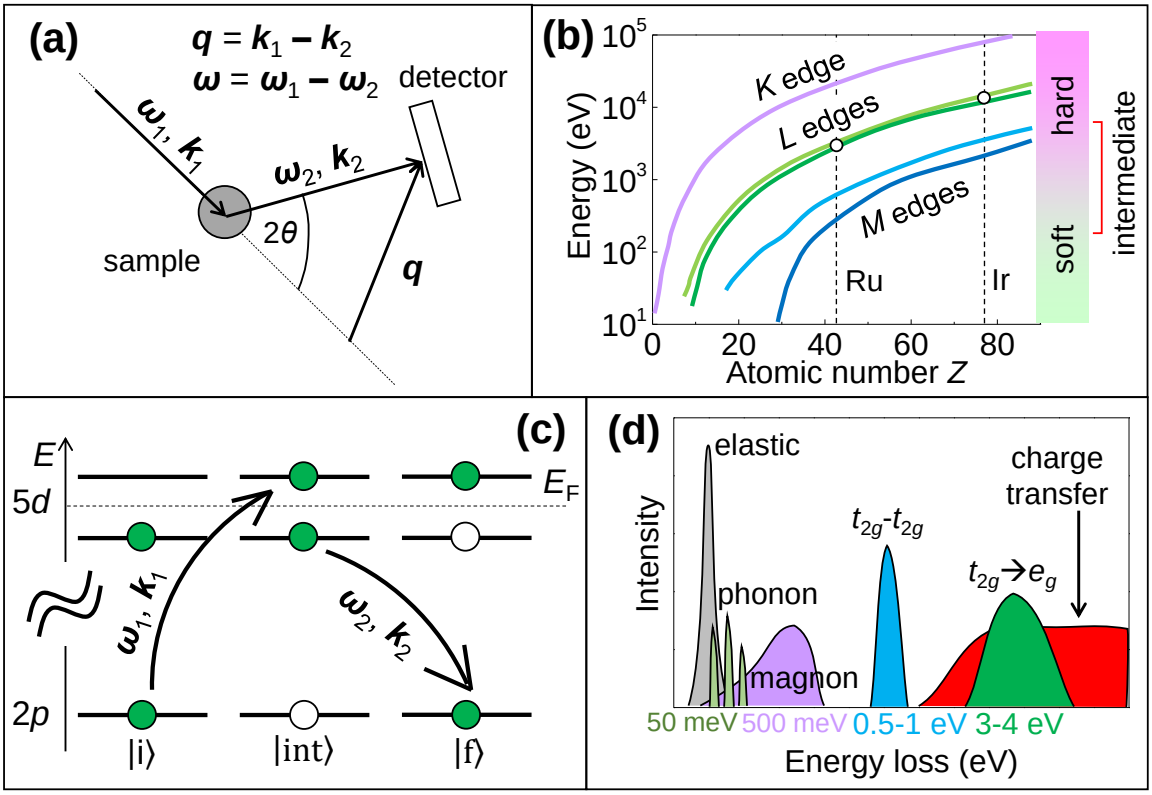

■ *Figure 2.7.* (a) A schematic diagram of the "photon-in photon-out" process. Incident photon with energy ω_1 and momentum $\boldsymbol{k}_1$ is absorbed by the sample and a photon is emitted with with energy ω_2 and momentum $\boldsymbol{k}_2$. The detector at an angle 2θ measures both the energy ω and momentum $\boldsymbol{q}$ transfers. (b) Energy of K, L and M absorption edges as a function of atomic number Z. Reproduced and modified from Ref. [83]. (c) Illustration of the two-step RIXS process. In the first step (initial state $|i\rangle$), the incident beam energy matches that of an excitation from a core shell to the valence shell (absorption edge shown in (b)), and thus a core electron is promoted to the valence band (intermediate state $|int\rangle$). The final step involves annihilation of the core hole by another lower-lying electron (final state $|int\rangle$). In REXS, $|i\rangle$ and $|f\rangle$ are identical, why in RIXS they are not. (d) RIXS spectrum expected for 4*d* and 5*d* TMOs. Usually the t_{2g} manifold is split by spin-orbit coupling and/or non-cubic crystal field.

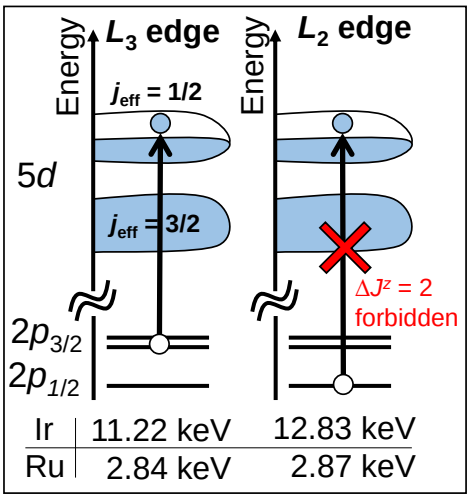

■ *Figure 2.8.* Schematic diagram of Ir L_3 and L_2 edges with the absorption energies for Ir^{4+} *only* in the *jj* picture. Bottom: Ir and Ru L_3 and L_2 absoprtion energies.

resolution for the available Bragg reflections is limited, hence the experimental activity in the intermediate x-ray energy RIXS was quite low until recently [72].

Ir and Ru atoms are of interest here as the orbital states concerning these atoms are studied in the compounds presented in this thesis. The L edge of Ir atom falls within the convenient hard x-ray energy range and hence is widely used for studying orbital magnetism of complex iridum oxides. As depicted in Fig. 2.8, $j_{\text{eff}} = 1/2$ state comprises exclusively $j_{5/2}$ ($d_{5/2}$) states, while $j_{\text{eff}} = 3/2$ is a mixture of both $j_{5/2}$ ($d_{5/2}$) and $j_{4/2}$ ($d_{4/2}$) states. $p_{1/2} \rightarrow j_{5/2}$ excitation (L_2 edge) is forbidden by electric dipole selection rules [85] and should show no resonant enhancement as compared to the $p_{3/2} \rightarrow j_{5/2}$ one (L_3 edge). Hence, Ir RIXS is performed utilising the L_3 edge, and the lack of resonant enhancement at the L_2 edge in resonant elastic x-ray scattering (REXS) is commonly exploited as a probe of spin-orbital entangled $j_{\text{eff}} = 1/2$ state [54, 86–90].

On the other hand, Ru absorption edges fall into inconvenient energy ranges: K edge is rather high in energy and can damage ceramic samples, while L and M edges fall into the intermediate x-ray energy range and hence are difficult to explore experimentally. However, recently, Gretarsson *et al.* has developed a Ru L edge intermediate RIXS (IRIXS) where nearly the entire incident beam path is under vacuum to avoid attenuation from air and advanced focusing techniques for achieving high intensity are used (Fig. 2.9) [72].

More detail on the RIXS measurements presented in this thesis is outlined in respective chapters.

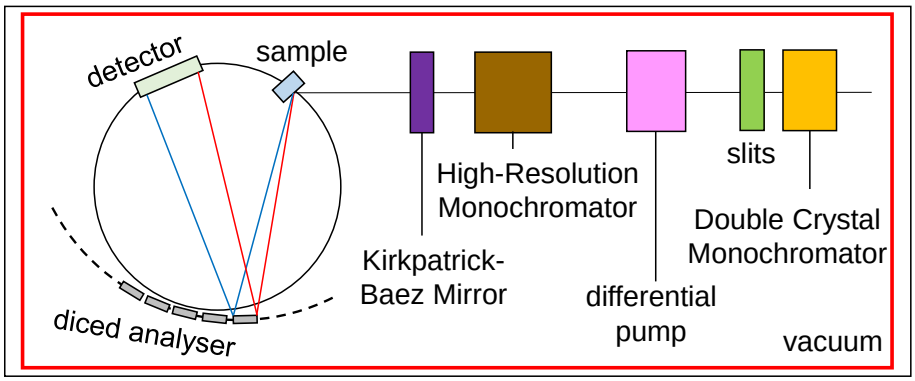

■ *Figure 2.9.* A schematic of the spectrometer with the position of the sample, the spherically bent diced analyser and the detector are shown. The layout showing the monochromators and focusing mirrors is that of IRIXS at DESY [72].

▸ Theoretical interpretation of the RIXS spectra

The RIXS spectra of low temperature $In_2Ir_2O_7$ and room temperature $In_2Ru_2O_7$ were theoretically interpreted by employing a standard single-ion Hamiltonian for t_{2g}^5 and t_{2g}^4 configuration ($L_{\text{eff}} = 1$), respectively, which includes intra-ionic Coulomb interaction, spin-orbit coupling and trigonal crystal field. e_g states were excluded under the assumption that $10\,\text{Dq} \gg J_{\text{H}}$. The Coulomb interaction is accounted for with the parameters U, U' and J_{H} (under the approximation $U' = U - J_{\text{H}}$) in a form of a Kanamori Hamiltonian [91]:

$$H_{\text{C}} = U \sum_{m} n_{m\uparrow} n_{m\downarrow} + U' \sum_{m \neq m'} n_{m\uparrow} n_{m'\downarrow} + (U' - J_{\text{H}}) \sum_{m<m',\sigma} n_{m\sigma} n_{m'\sigma} - J_{\text{H}} \sum_{m \neq m'} d^{\dagger}_{m\uparrow} d_{m\downarrow} d^{\dagger}_{m'\downarrow} d_{m'\uparrow} + J_{\text{H}} \sum_{m \neq m'} d^{\dagger}_{m\uparrow} d^{\dagger}_{m\downarrow} d_{m'\downarrow} d_{m'\uparrow} \quad (2.18)$$

The first three terms correspond to electron density-density (n) interactions: interactions between electrons with opposite spins in the same orbital (U), electrons with opposite spins in different orbitals (U') and parallel spins in different orbitals ($U' - J_{\text{H}}$). m is the orbital label and σ denotes spin (fixed identical between orbitals in the third term). The two latter terms describe inter-orbital Hund's coupling interactions with electron creation and annihilation operators (d and $d^{\dagger}$, respectively). The spin-orbit coupling Hamiltonian is expressed as follows:

$$H_{\text{SOC}} = \zeta \sum_{i} \boldsymbol{l}_i \cdot \boldsymbol{s}_i \quad (2.19)$$

where ζ is the atomic spin-orbit coupling and $\boldsymbol{l}_i$ and $\boldsymbol{s}_i$ are the orbital and spin angular momenta vectors for individual electrons, respectively. The single-ion anisotropy for trigonal

distortion is described as follows:

$$H_{\text{tri}} = \Delta \sum_i (l^z)^2 \tag{2.20}$$

where l^z refers to the z component of the orbital angular momentum in the trigonal coordinate system and Δ is the trigonal crystal field, where $\Delta < 0$ refers to compression. The total Hamiltonian is the sum of the above:

$$H_{\text{total}} = H_{\text{C}} + H_{\text{SOC}} + H_{\text{tri}} \tag{2.21}$$

which is diagonalised in order to obtain the energy levels and multi-electron wavefunctions of Ir^{4+} and Ru^{4+} ions which are then compared to and fit with a least-squares method to observed RIXS peak positions using Python 3 [92]. The L, S, J, L^z, S^z and J^z expectation values were obtained using Quanty [93].

2.4 Physical property measurement techniques

2.4.1 Magnetism

In order to elucidate the magnetic behaviour and magnetic transitions of the materials studied here, magnetometry measurements were performed by utilising the Superconducting Quantum Interference device (SQUID) based Quantum Design Magnetic Property Measurement System (MPMS). The MPMS utilises the motion of the sample through a superconducting second-order gradient coil which creates a current in the coil, which generates superconducting currents (shown Fig. 2.10(a)). The gradient coil is connected to a SQUID, which converts the current into voltage as a function of the sample position [94]. Accordingly, such voltage is proportional to the magnetisation of the sample. An example of a raw scan from a sample measured in this thesis is shown in Fig. 2.10(b). A correctly positioned sample should generate a maximum value of the voltage at the centre of the coils, which is located at 2 cm, and is the case in Fig. 2.10(b). The MPMS can be operated in a direct current (DC) or alternating (AC) mode. DC magnetisation measurement involves oscillating sample in a static magnetic field, while AC magnetisation uses an oscillating magnetic field on a static sample. In this thesis, only the DC susceptibility was measured, and for linear magnetisation with magnetic field one may assume that the magnetisation of the sample is directly proportional to the applied field H via the magnetic susceptibility χ:

$$\boldsymbol{M} = \chi \boldsymbol{H} \tag{2.22}$$

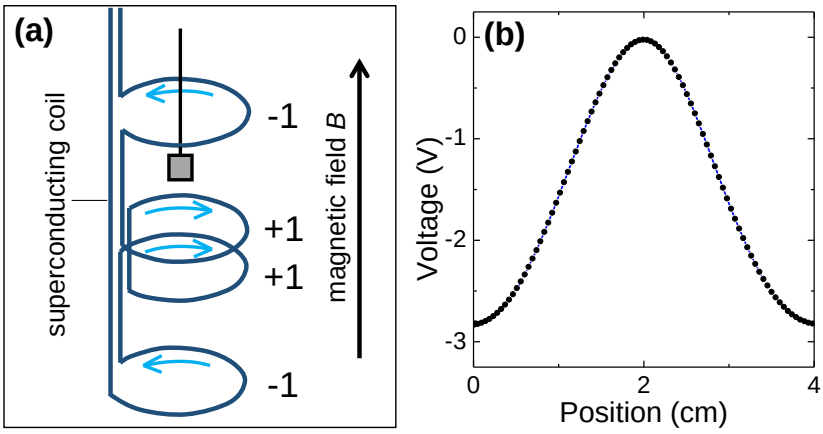

■ *Figure 2.10.* (a) The second-order gradient coil employed in the MPMS. The grey square represents the sample. Reproduced from Ref. [94]. (b) Sample position scan showing raw voltage.

For non-interacting spins in the paramagnetic regime the magnetic susceptibility follows the Curie-Weiss law:

$$\chi = \frac{C}{T - \theta_{\mathrm{CW}}} \tag{2.23}$$

where C is the Curie constant and θ_{CW} is the Weiss constant. From the former, the size of the local effective magnetic moment can be extracted ($\mu_{\mathrm{eff}} = \sqrt{8C}$), while the latter indicates the sign (AFM or FM) and strength of spin-spin correlations.

In a typical magnetic susceptibility $\chi(T)$ measurement, 30 mg to 100 mg of powder sample was packed into plastic foil and placed in a plastic straw. For enhancement of data statistics, two scans per temperature point were performed. Built-in MPMS software MultiVu was used for automatic processing and corrections to the data. The contributions from the core diamagnetism [95] and the diamagnetic signal of the plastic foil, in which the samples were packed, were subtracted manually.

2.4.2 Transport

Transport measurements are an important tool in identifying insulating or metallic behaviour as well as phase transitions. At normal temperatures, the resistivity of semiconductors is dominated by thermally activated charge carriers, which is described with the following expression:

$$\rho = \rho_0 \exp(-E_a/k_B T) \tag{2.24}$$

where at high temperatures the activation energy E_a should be close to the true charge gap, while at low temperatures E_a mostly reflects the impurity levels.

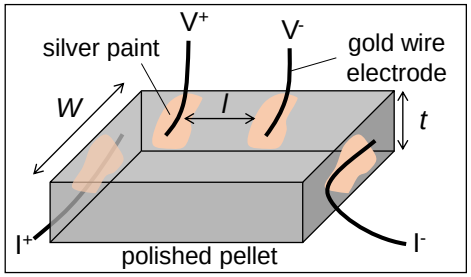

■ *Figure 2.11.* The four-probe resistivity measurement setup. The hard-pressed powder sample is polished into a flat cuboid shape.

Resistivity of pressed powder pellets was measured with the four-probe technique shown in Fig. 2.11. Two electrodes are used for passing current through the sample, while the second pair is used for estimating the voltage gradient. Thin gold wires are used as electrodes and are attached to the pellet surface with silver paint. By applying the current and recording the voltage gradient, using Ohm's law one can estimate the resistance R:

$$R = \rho \frac{l}{Wt} \tag{2.25}$$

where ρ is resistivity and l, W and t are distance between voltage electrodes, sample width and thickness, respectively, as illustrated in Fig. 2.11. We note that the resistivity of a hard-pressed pellet may be about an order of magnitude higher than that of a single crystal due to grain boundaries. The DC resistivity of polycrystalline samples was measured with Quantum Design Physical Property Measurement System (PPMS).

2.4.3 Thermodynamics

Specific heat

Specific heat provides an estimate of degrees of freedom and their energy scales and therefore heat capacity measurement is a useful probe for identifying a phase transition and its nature. The specific heat C, which comprises lattice, electronic, nuclear and magnetic contributions, is proportional to the product of temperature and the temperature derivative of entropy:

$$C = T \frac{\delta S}{\delta T} \tag{2.26}$$

The most common method for extracting specific heat is the relaxation method employed for the PPMS by Quantum Design, which was utilised in this thesis. Fig. 2.12(a) shows a typical setup used for materials studied here. The sample is mounted on the sample stage with grease (addenda) which provides good thermal coupling with the thermometer and heater below.

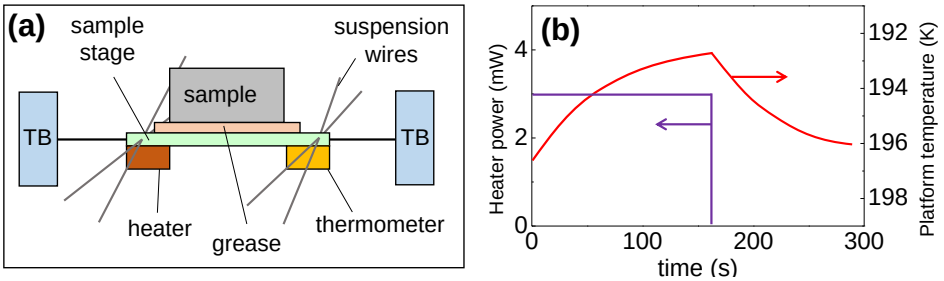

■ *Figure 2.12.* (a) Heat capacity measurement setup. The polished hard-pressed pellet of known mass is mounted on the suspended with wires sample stage with Apiezon N grease. Underneath the stage a heater and a thermometer are attach and both are connected to thermal baths (TB). (b) Typical raw scan from the PPMS. A heat pulse is applied to reach higher temperature (set by ΔT) and the platform temperature increases. Once the set temperature is reached, the heater power is terminated and the platform temperature relaxes back to the heat bath temperature with a characteristic relaxation rate related to the specific heat of the sample.

The measurement proceeds as follows. A set amount of heater power is used to increase the temperature of the sample of known mass by known ΔT value for a certain length of time. Once the target temperature is reached, the sample relaxes back to the heat bath temperature while the thermal relaxation is measured ($A \exp(-t/\tau)$, where τ is the relaxation rate). Then, the temperature of the sample platform can be modelled as:

$$C_{\text{total}} \frac{\delta T}{\delta t} = -K_{\text{w}}(T - T_{\text{b}}) + P(t) \tag{2.27}$$

where C_{total} is the combined heat capacity of the sample and the sample platform, K_{w} is the thermal conductivity between the sample and the link to the thermal bath, T_{b} is temperature of the whole setup within the sample platform and $P(t)$ is the heater power. The sample heat capacity can be extracted by subtraction of that of the addenda.

Specific heat of polycrystalline samples was measured with Quantum Design Physical Property Measurement System (PPMS).

Differential scanning calorimetry

Differential scanning calorimetry (DSC) monitors heat effects associated with phase transitions and chemical reactions as a function of time and temperature. In contrast to the specific heat relaxation technique described above, DSC monitors the exchange of heat between the sample and the system. As a result, one can estimate the entropy associated with first-order phase transitions through the evaluation of latent heat. Identifying the amount of entropy released across a phase transition is useful, because one can estimate what DOF are involved

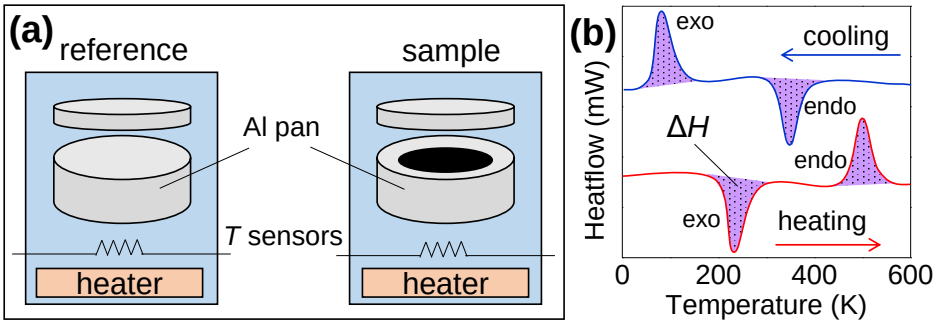

■ *Figure 2.13.* (a) The differential scanning calorimetry experiment setup. (b) A cartoon illustrating expected features generated by first-order phase transitions, that is, a clear peak-like anomaly and reversibility. "exo" and "endo" denote exothermic and endothermic transitions, respectively.

as the entropy should amount to $\sim R\ln(\Omega)$, where R is the gas constant and Ω is the number of DOF (for example, $\Omega = 2S + 1$ for spin DOF).

DSC measurement is performed at constant pressure and two samples, a reference and the target material, are subject to the same rate of temperature change. From the difference of heat flow (in mW) between the two samples is obtained, from which the enthalpy and entropy change can be deduced for the measured material. The two samples are placed in two aluminium pans and heated/cooled under inert conditions as illustrated in Fig 2.13(a). Fig 2.13(b) demonstrates expected signal for endothermic and exothermic first-order phase transitions.

DSC data of polycrystalline $In_2Ru_2O_7$ samples was collected using Mettler Toledo DSC with liquid nitrogen cooling system at Rutherford Appleton Laboratory.

2.5 Muon spin rotation

Muon spin rotation or relaxation (μSR) is an non-destructive magnetic-field-sensitive implantation technique which involves bombardment of a sample with positive spin-polarised muons and tracking of their directional decay. Positive muons are spin 1/2 particles with the direction of spin and momentum fixed opposite to each other and are produced with two-body decay of pions. Some of fundamental properties of muons are listed in Table 2.1 and compared with those of an electron and a proton. For stationary pions, the emergent muons are intrinsically nearly 100 % polarised. Upon implantation in the investigated material, muons thermalise and occupy usually an interstitial site in the crystalline lattice until they decay (muon lifetime is 2.2 µs). Muons are extremely sensitive to small magnetic field (0.1 m T or $10^{-3}\,\mu_B$) and can distinguish between static and slowly fluctuating ones. Not only are

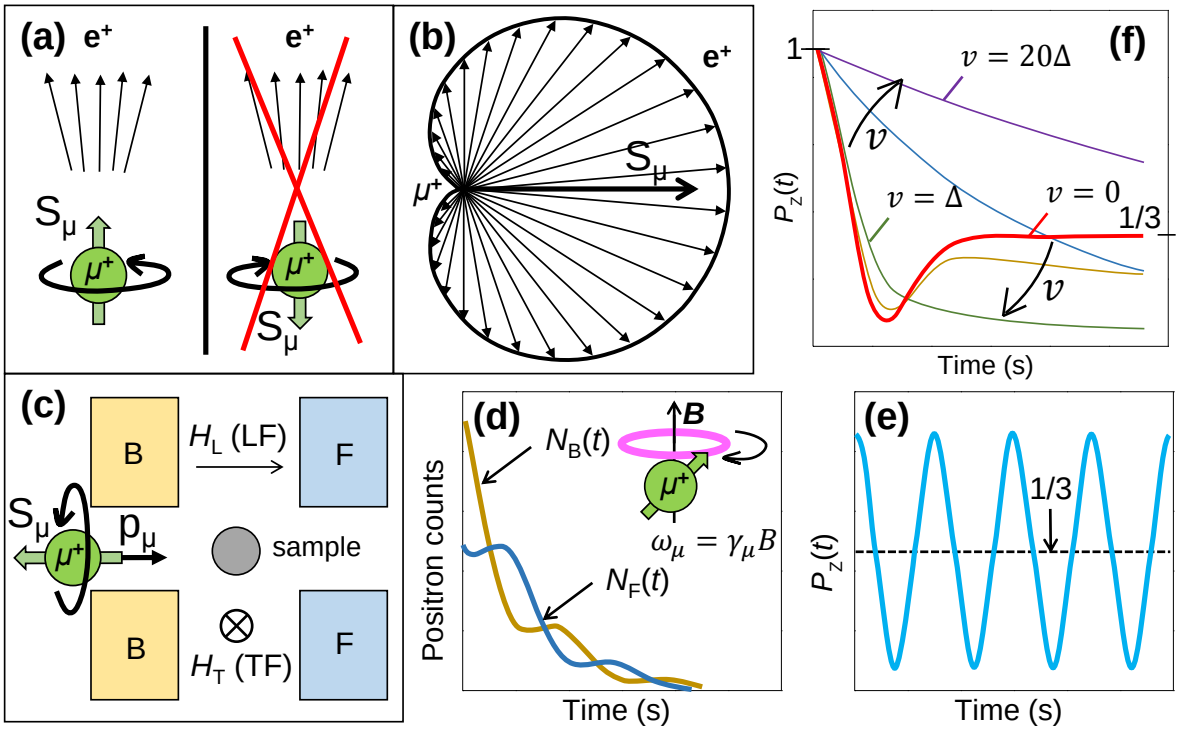

■ *Figure 2.14.* (a) Upon reflection with a mirror plane the muon spin is reversed. However, the decay on the left hand side of the mirror plane is only ever observed due to parity violation, and hence the positrons are always emitted along the direction of the muon spin. (b) The asymmetry of the muon for highest energy muons with respect to the initial muon spin polarisation. (c) A typical experimental set-up used in μSR experiments for zero-, longitudinal-, and transverse-field configurations (ZF, LF and TF, respectively). The sample is placed between forward (F) and backward (B) detector banks. The muon stopping in the sample is influenced by the local and/or external magnetic field and produces positrons upon decay which are counted with the detectors. (d) The number of positrons detected in the F and B detectors in a static homogeneous magnetic field. Upper right corner: muon precessing about the applied/local magnetic field with the Larmor frequency ω_μ. (e) The asymmetry function of a polycrystalline sample, where the oscillation averages at 1/3 (muon decay has been subtracted). (f) The relaxation function for muon hopping or spin fluctuation rate ν. Red curve corresponds to the ZF-Kubo-Toyabe function in eq. 2.31 with $\nu = 0$. ν increases from 0 from the red, yellow, green, blue to the purple curve. (a)-(e) reproduced and modified from Ref. [96].

■ *Table 2.1.* Fundamental properties of the muon compared to those of an electron and a proton. e and p are an electron and a proton, respectively. m_p, m_e, μ_p and γ are proton mass, electron mass, proton spin and gyromagnetic ratio, respectively.

Particle	Charge	Spin	Mass	Moment	$\gamma/2\pi$ (kHz G^{-1})	Lifetime (μs)
e	$\pm e$	1/2	m_e	$657\mu_p$	2800	∞
μ	$\pm e$	1/2	$207m_e \sim (1/9)m_p$	$3.18\mu_p$	13.5	2.19
p	$\pm e$	1/2	m_p	μ_p	4.26	∞

muons conveniently nearly fully spin-polarised, the muon decay has preferred direction as well - one of the particles emerging from the three-body decay, positrons, are largely emitted along the direction of the muon spin due to parity violation (Fig. 2.14(a) and (b)) [97]. Hence, one can track the direction of the muon spin as a function of time with position-sensitive positron detectors and obtain information on the local magnetic fields inside the material of interest.

The muon asymmetry, which gives measure of the muon spin polarisation as a function of time, in zero-field configuration is defined as:

$$A(t) = \frac{N_B(t) - N_F(t)}{N_B(t) + N_F(t)} \tag{2.28}$$

where $A(t)$, $N_B(t)$ and $N_F(t)$ are time dependent muon asymmetry and the number of positron counts in the backward and forward detector banks, respectively. In a presence of a magnetic field, muon will precess about it with Larmor frequency, which depends on the magnetic field:

$$\omega_\mu = \gamma_\mu B \tag{2.29}$$

where ω_μ and γ_μ is the Larmor frequency and muon gyromagnetic ratio, respectively. In the zero-field configuration, if a material undergoes long-range magnetic order, a clear oscillation in the muon asymmetry signal should be observed as shown in Fig. 2.14(e). In the presence of a magnetic field, a polycrystalline sample (or a sample with randomly distributed magnetic fields) show averaging in the oscillations expressed as:

$$P_z(t) = \frac{1}{3} + \frac{2}{3}\cos(\omega_\mu t) \tag{2.30}$$

where $P_z(t)$ is the asymmetry quantified along the z axis. Real, especially polycrystalline, materials, have a Gaussian distribution of the local magnetic fields of width Δ/γ_μ, and therefore the muons will progressively dephase, which can be expressed with a Kubo-Toyabe function:

$$P_z(t) = \frac{1}{3} + \frac{2}{3}\exp(\Delta^2 t^2/2)(1 - \Delta^{t^2}) \tag{2.31}$$

which at large time t averages at 1/3. Kubo-Toyabe function (red curve in Fig. 2.14(f)) can be therefore understood as a superposition of many functions shown in Fig. 2.14(e) of different B, with the width Δ within those.

The oscillations could also be damped by dynamic effects, for example fluctuating magnetic moments due to spin liquid behaviour, fluctuating nuclear spins, fluctuating impurity spins, or thermally-activated hopping of muons between interstitial sites. One can define all dynamic events with a fluctuation rate ν. At values $\nu < \Delta$, the fluctuation suppresses the 1/3 tail of the Kubo-Toyabe curve. At $\nu = \Delta$, the curve shows a Lorentzian-like shape, and for high values of ν a Gaussian shape is obtained. In general, fluctuations are enhanced at high temperatures, and hence a cross-over from $\nu \sim \Delta$ to $\nu \gg \Delta$ limits with increasing temperature is seen in systems with fluctuating moments (intrinsic or impurity). This cross-over can be described with a simple "stretched" exponential:

$$P_z(t) = Ae^{-(\lambda t)^{\beta}} \tag{2.32}$$

where A is the initial asymmetry and λ is the relaxation rate. The larger the fluctuation rate υ, the slower the relaxation rate.

In this thesis, ZF-μSR was utilised in distinguishing between long-range antiferromagnetic order (oscillation) and a non-magnetic state (no oscillation) with little consideration for the spin dynamics. Muon spin rotation/relaxation data have been collected for $In_2Ru_2O_7$ polycrystalline samples in order to distinguish between a non-magnetic molecular orbital state and long-range magnetic order. ZF-μSR data have been collected on the ARGUS spectrometer at the ISIS Muon Facility, Rutherford Appleton Laboratory.

2.5.1 Band structure calculations

Band structure calculations for the experimentally determined crystal structures presented in this thesis were performed within the local density approximation (LDA) [98] to the density functional theory (DFT) [99, 100] using the linear muffin-tin orbital (LMTO) [101] method implemented in the PY LMTO code [102] with the combined correction terms taken into account. To examine the influence of spin-orbit coupling on the electronic structure, fully relativistic and scalar relativistic calculations were performed. The fully relativistic treatment is achieved by solving the four-component Dirac equation inside an atomic sphere and, thus, includes the kinematic relativistic effects (Darwin and mass velocity terms) as well as spin orbit coupling. The effect of spin–orbit coupling is clarified by calculating the J-resolved density of states (DOS) where $J = l \pm 1/2$ is the total angular momentum for the spherically symmetric $5d$ states. The J_{eff}-resolved states are assigned by analysis of the wavefunction components of the J-resolved states. The value of spin-orbit coupling estimated from calculations for

$In_2Ir_2O_7$ and β-Li_2IrO_3 was $\zeta = 0.58\,eV$. In the scalar relativistic treatment, the spin-orbit coupling is neglected but the kinematic relativistic effects are taken into account.

2.6 Co-authorship

The work presented in this thesis is a result of collaborative research. While I was the principal investigator of the three projects presented in this thesis, I received valuable contributions and assistance from a number of colleagues, as outlined below.

- High pressure neutron diffraction experiment on β-Li_2IrO_3 was performed by Dr. Tomohiro Takayama, Dr. Alexandra Gibbs and I with technical support from the PEARL beamline scientists Dr. Craig Bull and Dr. Nick Funnel. Structural analysis was performed by me with the support of Dr. Alexandra Gibbs.

- High pressure RIXS experiment on β-Li_2IrO_3 was performed by Dr. Tomohiro Takayama and I with technical support from the SPring-8 beamline scientists Dr. Hirofumi Ishii, Dr. Nozomu Hiraoka, Dr. Kenji Ishii and Dr. Hitoshi Yamaoka.

- RIXS experiment on $In_2Ir_2O_7$ was performed by Dr. Tomohiro Takayama and Dr. Kenji Ishii.

- RIXS experiment on $In_2Ru_2O_7$ was performed by Dr. Joel Bertinshaw, Dr. Hlynur Gretarsson, Marian Blankenhorn and I. RIXS experiment on $Y_2Ru_2O_7$ was performed by Dr. Joel Bertinshaw and Dr. Hlynur Gretarsson.

- ZF-μSR experiment on $In_2Ru_2O_7$ was performed by Dr. Tomohiro Takayama and I with technical support from the μSR beamline scientists Dr. Isao Watanabe and Dr. Dita Puspita Sari.

- Neutron diffraction experiment on $In_2Ru_2O_7$ was performed by Dr. Tomohiro Takayama, Dr. Alexandra Gibbs and I with technical support from the HRPD beamline scientist Dr. Alexandra Gibbs. Structural analysis was performed by me with the support of Dr. Alexandra Gibbs.

- Single crystal x-ray diffraction experiments and structural analysis on $In_2Ru_2O_7$ crystals was performed by Dr. Jürgen Nuss.

- Powder x-ray diffraction experiments and structural analysis on $In_2Ru_2O_7$ was performed by Dr. Sebastian Bette.

- Powder x-ray diffraction experiments and structural analysis on $In_2Ir_2O_7$ was performed by Christine Stefani and Prof. Dr. Robert Dinnebier, respectively.
- High temperature resistivity measurements on $In_2Ru_2O_7$ were performed by Dr. Tomohiro Takayama and I with equipment constructed by Dr. Tomohiro Takayama.
- All band structure calculations presented in this thesis were performed by Dr. Alexander Yaresko. Figures which contain band dispersion were created by Dr. Alexander Yaresko.
- Kanamori Hamiltonians were written by Marian Blankenhorn. Fitting of RIXS data of $In_2Ru_2O_7$ was performed by Marian Blankenhorn.
- EDX experiments on $In_2Ru_2O_7$ crystals were performed by Sabine Prill-Diemer and Viola Duppel.
- High temperature MPMS measurements were performed by Eva Büchner.
- The abstract of this thesis was translated from English to German language by Marian Blankenhorn.

Chapter 3

Pressure-driven collapse of $J_{\text{eff}} = 1/2$ state in β-Li_2IrO_3

3.1 Introduction

Honeycomb-based iridates with spin-orbital entangled $J_{\text{eff}} = 1/2$ pseudospins serve as potential realisation of a Kitaev QSL, a spin-liquid with anisotropic ferromagnetic interactions on a honeycomb lattice. However, most of the real materials undergo long-range magnetic order [67]. While Kitaev materials are found to be robust $J_{\text{eff}} = 1/2$ magnets with dominant bond-dependent ferromagnetic coupling, it has been discussed that the magnetic order is stabilised due to the presence of other magnetic couplings. This has motivated attempts to drive the system towards a QSL by tuning the magnetic interactions with chemical modification or application of magnetic field or pressure. Here, we investigate the effect of high pressure on the electronic structure of β-Li_2IrO_3 which is reported to undergo a structural transition at ~ 4 GPa. We find that short Ir-Ir bonds with molecular orbitals are formed and the $J_{\text{eff}} = 1/2$ state collapses at high pressure.

We first describe the Kitaev model and candidate materials in section 3.1. The methods employed in this work are outlined in section 3.2. We describe the modulated hyperhoneycomb structure and the implications on the electronic structure of β-Li_2IrO_3 in section 3.3. Finally, we discuss the implication of our results in section 3.4.

The content presented in this chapter has been previously published in Ref. [103].

3.1.1 Kitaev model

The Kitaev model attracts great interest in the condensed matter community as it is one of the few microscopic models that can be exactly analytically solved and it hosts both gapped and gapless spin liquid phases [104]. The Kitaev model involves $S = 1/2$ on a honeycomb

lattice interacting via nearest-neighbour bond-dependent ferromagnetic coupling:

$$H = -\sum_{\langle ij \rangle_\gamma} J_\gamma S_i^\gamma S_j^\gamma \tag{3.1}$$

where J_γ is the ferromagnetic coupling between site i and j sharing a bond with index γ and the S_i^γ is the Ising spin. When treating the $S = 1/2$ classically, the ground state will be extensively degenerate, where the degeneracy is related to the number of ways of arranging the satisfied bonds, that is, bonds where the corresponding spins are aligned along the easy axis as depicted in Fig. 3.1(a). Quantum mechanically, the ground state is a superposition of all the classically-described configurations and is a quantum spin liquid state (QSL). The Kitaev QSL is distinct from other QSLs as it is based on Ising rather than Heisenberg spins.

The Kitaev model can be solved exactly by mapping each spin operator into four Majorana fermion operators. The Majorana fermion is its own antiparticle and carries half degrees of freedom of a conventional fermion. In short, such fractionalisation of the spin into a fermionic form results in a ground state comprising itinerant and localised Majorana fermions, where the former forms a gapless Dirac dispersion, while the latter forms a flux-free gapped state. When interactions along all bonds are of comparable magnitude, that is $J_x \sim J_y \sim J_z$, a Majorana metal with Dirac dispersion is formed, giving a gapless state. When substantial anisotropy is present and one of the J_γ dominates such that it is greater than the sum of the other two, the system becomes a gapped spin liquid with Abelian topological order. The gapless state can become gapped upon the application of magnetic field and transform into a more exotic spin liquid state with Ising-type topological order, which is discussed to be relevant for applications in quantum computing [105]. The Kitaev model, due to its relative simplicity generating exotic electronic properties, is of great interest in condensed matter physics and has inspired a search for its realisation in real materials in the context of new spin liquid systems, long-sought experimental discovery of Majorana fermions and experimental probing of fractionalisation. For more details on Kitaev model and materials, refer to Ref. [67, 104, 106–108].

3.1.2 $J_{\text{eff}} = 1/2$ pseudospin on honeycomb lattice

Initially the Kitaev model was considered strictly a toy model as $S = 1/2$ spins do not exhibit the Ising anisotropy necessary for realisation of the bond-dependent coupling. It has been proposed, however, that the interaction anisotropy can be achieved via a *pseudospin* expected in Mott insulators with strong spin-orbit coupling and t_{2g}^5 configuration [51]. The t_{2g}^5 configuration can be achieved in materials hosting transition metal ions, such as Ir^{4+} or Ru^{3+}, coordinated by octahedral arrangements of ligands, where the d orbitals become split into t_{2g}

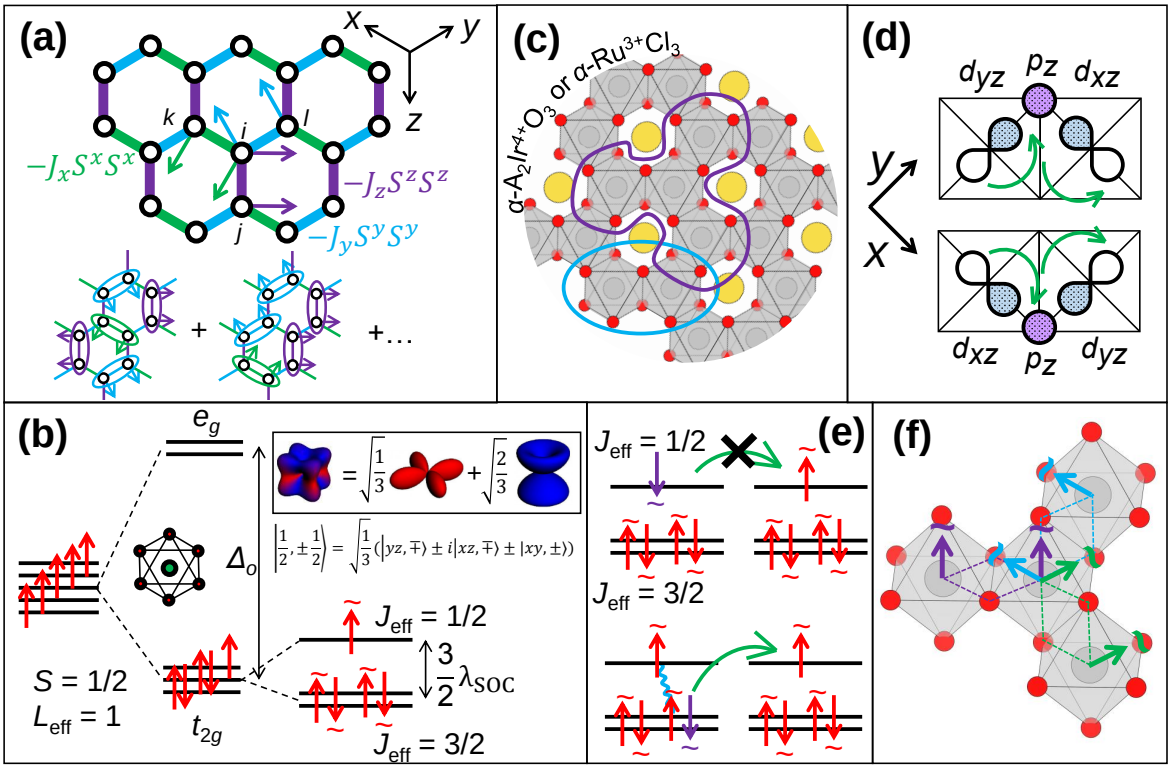

■ *Figure 3.1.* (a) Schematic of the interactions in the Kitaev honeycomb model. The Ising spins S^γ interact along the orthogonal directions are x, y and z along the honeycomb bonds, rendering frustration as evident from site i. At the bottom, examples of arrangements of the ferromagnetic spin pairs is shown. (b) The emergence of $J_{\text{eff}} = 1/2$ pseudospin in the t_{2g}^5 electron configuration in the jj coupling limit. The wavefunction of the $J_{\text{eff}} = 1/2$ state is visualised in the upper right corner. Partially reproduced from Ref. [51]. The arrow with ˜ symbol represents a pseudospin. (c) The structure of the honeycomb layers of Kitaev candidate materials with IrO_6 or $RuCl_6$ octahedra shown. The blue line corresponds to the region shown in (d), and the purple line highlights the region pictured in (f). (d) The two d-p-d hoppings between the d_{yz} and d_{xz} orbitals comprising the $J_{\text{eff}} = 1/2$ state have opposite sign and interact destructively and cancel each other out. (e) Top: the antiferromagnetic coupling of $J_{\text{eff}} = 1/2$ pseudospin does not take place as it cancels out due to considerations shown in (d). Bottom: the ferromagnetic coupling stabilised by hopping between $J_{\text{eff}} = 1/2$ and $J_{\text{eff}} = 3/2$ states favoured by Hund's coupling (blue curve) between two unpaired spins. (f) The Kitaev-like interactions resulting from (d) shown on the edge-sharing octahedra comprising the lattice shown in (c).

and e_g manifolds by about 3.5 eV, locating all five electrons in the t_{2g} manifold as $J_H \ll \Delta_O$ as shown in Fig. 3.1(b). The t_{2g} manifold can be treated as triply degenerate p manifold rendering effective orbital angular momentum $-L_{\text{eff}} = -1 = L$ [45].

The spin-orbital entangled 1/2 pseudospin can be reached by starting from two limits. If $\lambda_{\text{SOC}} \gg J_H$, in the jj limit the orbital l and spin s angular momenta combine for each electron individually, rendering a fully occupied $j_{\text{eff}} = 3/2$ quartet and a half-filled $j_{\text{eff}} = 1/2$ doublet. If $\lambda_{\text{SOC}} \ll J_H$, in the LS limit the total orbital $L_{\text{eff}} = 1$ and spin $S = 1/2$ momenta combine to give a ground state $J_{\text{eff}} = 1/2$ doublet and the next excited state $J_{\text{eff}} = 3/2$ quartet. In both limits, the ground state is the $J_{\text{eff}} = 1/2$ doublet, and the gap between the doublet and the quartet is equal to $(3/2)\lambda_{\text{SOC}}$. In reality, no material locates strictly in the jj or LS coupling limit, however naïvely, jj coupling should be more relevant to the heavier Ir^{4+} case, while LS coupling might more accurately describe the lighter Ru^{3+}. In a crystalline lattice a half-filled $J_{\text{eff}} = 1/2$ band is formed, which is then split by moderate U rendering the material a Mott insulator [54] (see section 1.6.1).

The $J_{\text{eff}} = 1/2$ wavefunction comprises equal superposition of the d_{xy}, d_{yz} and d_{zx} orbitals yielding an isotropic shape as shown in Fig. 3.1(b). The gyromagnetic factor g_J = -2 gives a magnetic moment of 1 μ_{B} which is of the same magnitude as for spin-only $S = 1/2$. The negative sign of g_J is a signature of unquenched orbital moment which renders the interactions between $J_{\text{eff}} = 1/2$ pseudospins sensitive to the local lattice geometry [51, 54].

One possible realisation of a honeycomb lattice of transition metal (TM) ions is a hexagonal arrangement of edge-sharing octahedra, for example IrO_6 or $RuCl_6$ found in layered materials such as α-Li_2IrO_3 or α-$RuCl_3$ shown in Fig. 3.1(c). Due to the sizeable hybridisation of oxygen p orbitals with the spatially extended 4d and 5d orbitals, d-p-d hopping can be initially considered as the dominant hopping process. In the Ir-O_2-Ir or Ru-Cl_2-Ru edge-sharing 90° bond geometry, there are two equivalent paths of ligand-mediated d-p-d hopping as depicted in Fig. 3.1(d). If one maps the $J_{\text{eff}} = 1/2$ into its d_{xy}, d_{xz} and d_{yz} components, it becomes apparent that the d-p-d hopping does not conserve the orbital component. Moreover, due to the complex components of the $J_{\text{eff}} = 1/2$ wavefunction, the two possible paths are of opposite sign and interfere destructively, and hence the conventional antiferromagnetic Heisenberg term effectively vanishes [51]. What is left is the bond-dependent ferromagnetic Ising term with easy axes perpendicular to the Ir-O−2-Ir plane, which involves hopping of electrons from the $J_{\text{eff}} = 3/2$ to $J_{\text{eff}} = 1/2$ favoured by J_H shown in Fig. 3.1(e). This ferromagnetic Ising coupling corresponds to the Kitaev model as evident in Fig. 3.1(f), where the easy axis is perpendicular to the Ir-O_2-Ir bond plane.

3.1.3 Candidate Kitaev materials

Due to the theoretical prediction of realisation of the Kitaev QSL in honeycomb TM compounds, there has been extensive research effort to pin down Kitaev physics in honeycomb-based materials which are summarised in Table 3.1. The first explored materials were 2D-honeycomb systems such as α-Li_2IrO_3, Na_2IrO_3 and α-$RuCl_3$, however they all exhibit long-range magnetic order, which sparked the search for alternative materials. Second-generation 2D-honeycombs were produced by ion exchange [109–113], where the inter-layer Li ions in α-Li_2IrO_3 are replaced by A' = H, Ag or Cu ions, while the intra-layer Li ions inside the honeycomb remain intact, rendering a chemical formula $A'_3LiIr_2O_6$. While A' = Ag or Cu orders magnetically, $H_3LiIr_2O_6$ was found to host quantum spin liquid ground state, however the nature of the QSL state has not been clarified yet [113]. Another group of second-generation 2D-honeycombs was explored, where all Li ions are replaced with divalent cations such as A' = Zn and Mg giving a chemical formula $A'IrO_3$, and which too exhibit magnetic order. Since the Kitaev model has been expanded to three dimensions where a QSL is also expected [114], 3D analogue materials have also been explored [67]. The hyperhoneycomb β-Li_2IrO_3, which locally has the same structure as the 2D honeycomb, has appeared as a new platform for Kitaev magnetism however it orders magnetically as well [115]. Therefore, no pure Kitaev QSL has been identified up to date as shown in Table 3.1. The reason for this is that there are many additional interactions and structural aspects one has to take into account to accurately describe the behaviour of the Kitaev candidate materials. Nevertheless, the honeycomb-based iridium and ruthenium compounds are still called "Kitaev materials" because, despite the additional interactions destabilising the potential Kitaev QSL state, the $J_{\text{eff}} = 1/2$ magnetism is alive and the strength of the ferromagnetic bond-dependent coupling appears dominant, as discussed below.

- Crystal structure

Crystal structures of candidate Kitaev materials comprise honeycomb layers of transition metal ions surrounded by edge-sharing octahedra of anions. The honeycomb layers are intercalated by A cations such as A = Li, Na, Ag, Cu, H, Mg or Zn. Kitaev materials adopt a range of crystal symmetries as those depend on the chemical composition and the stacking of the honeycomb layers. The first generation of Kitaev materials are derivatives of the rocksalt structure (Appendix A) and crystallise in a monoclinic structure with space group $C2/m$ shown in Fig. 3.2(a-c). Both Ir and A ions have octahedral coordination and all IrO_6 and AO_6 octahedra are edge-sharing. In Fig. 3.2(e), there are two symmetrically inequivalent types of Ir-Ir bonds, where 1/3 of bonds runs along the b crystallographic axis (Z, C_{2h} point symmetry), while the other 2/3 of bonds are located in the ab plane (X, Y, C_i point symmetry). The low symmetry allows for distortions from the ideal rocksalt-derived lattice, where the IrO_6

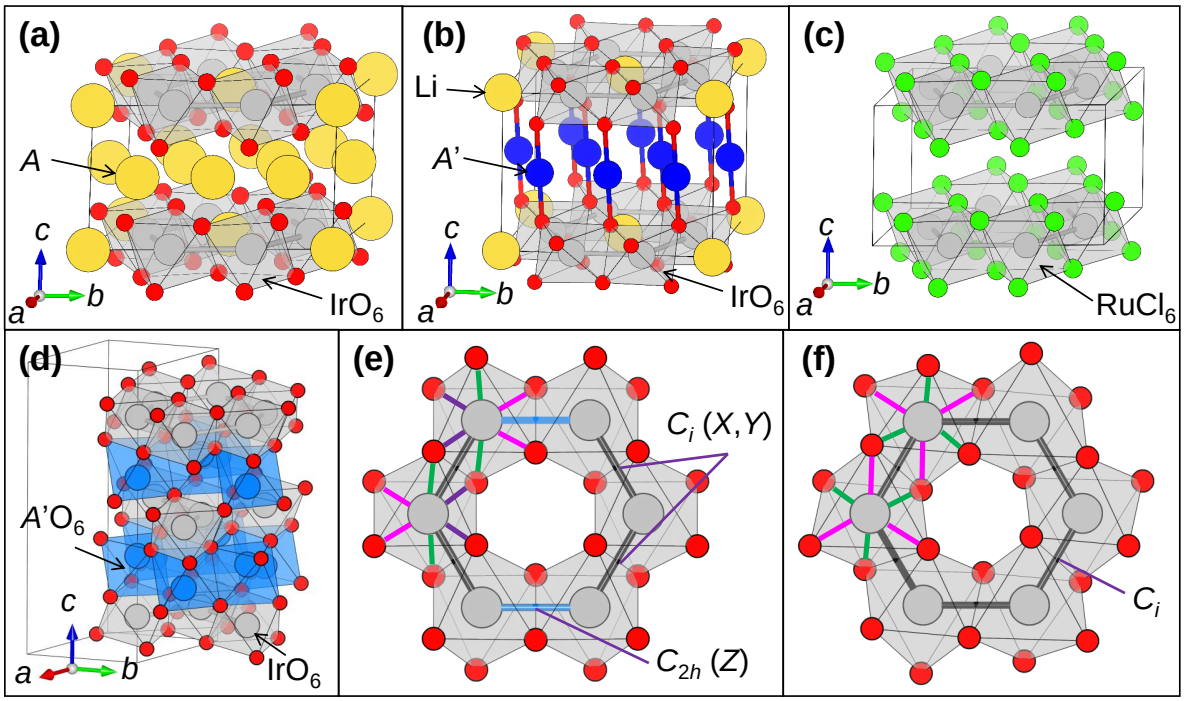

■ *Figure 3.2.* (a) The crystal structure of α-A_2IrO_3 2D Kitaev materials, where a = Li, Na. (b) The crystal structure of the second generation 2D Kitaev materials retaining the $C2/m$ symmetry. The cations separating the 2D layers are exchanged, while the Li ions inside the honeycomb remain intact, giving a chemical formula α-$A'_3LiIr_2O_6$, where A' = H, Ag, Cu. (c) The crystal structure of α-$RuCl_3$. (d) The crystal structure of the second generation 2D Kitaev materials adapting the $R\bar{3}$ symmetry. The cations between and inside the honeycomb layers are removed, and the newly intercalated cations form a buckled honeycomb lattice between the IrO_3 honeycomb layers, giving a chemical formula of $A'IrO_3$, where A' = Mg, Zn. (e) The local geometry in α-Li_2IrO_3, Na_2IrO_3 and α-$RuCl_3$ with only IrO_6/$RuCl_6$ octahedra are shown. Ir-O-Ir/Ru-Cl-Ru angles are about 95°. The Ir-Ir/Ru-Ru bond that lies along the c axis has C_{2h} point symmetry (blue), while the other two bonds have C_i point symmetry (black). The point symmetry of IrO_6 octahedra is C_2 and equivalent Ir-O/Ru-Cl bonds are shown in the same colours. (f) The local geometry in $MgIrO_3$ and $ZnIrO_3$, where only IrO_6 octahedra are shown. Ir-O-Ir angles are about 92°. All Ir-Ir bonds are equivalent and have C_i point symmetry. The point symmetry of the IrO_6 octahedra is C_3 and equivalent Ir-O bonds are shown in the same colours.

■ *Table 3.1.* Summary of physical properties of known Kitaev materials. S. G. is space group, LRO is long-range order, T_m is the ordering temperature, μ_{eff} is the effective magnetic moment, θ_{CW} is the Curie-Weiss constant and AFM is antiferromagnetic. *ab*, *a*, *b* and *b* notation corresponds to quantities extracted from measurements performed with magnetic field aligned along the crystallographic plane or axis. Table reproduced and modified from Ref. [67].

Material	S.G.	T_m(K)	$\mu_{\text{eff}}(\mu_B)$	θ_{CW}(K)	LRO	Ref.
2D honeycomb materials						
α-Li_2IrO_3	$C2/m$	15	1.50(*ab*), 1.58(*b*)	5(*ab*), −250(*b*)	spiral	[116–118]
Na_2IrO_3	$C2/m$	15	1.81(*ab*), 1.94(*b*)	−176(*ab*), −40(*b*)	zigzag	[116, 119–121]
$H_3LiIr_2O_6$	$C2/m$	—	1.60	−105	spin liquid	[113]
Cu_2IrO_3	$C2/m$	2.7	1.93	−110	AFM or spin glass	[111]
$Cu_3LiIr_2O_6$	$C2/m$	15	2.1	−145	AFM	[110]
$Ag_3LiIr_2O_6$	$R\bar{3}m$	12	1.77	—	AFM	[109]
$ZnIrO_3$	$R\bar{3}$	47	1.73	−48	AFM	[112]
$MgIrO_3$	$R\bar{3}$	32	1.73	−67	AFM	[112]
α-$RuCl_3$	$C2/m$	7	2.33(*ab*), 2.71(*b*)	40(*ab*), −216(*b*)	zigzag	[122]
3D honeycomb materials						
β-Li_2IrO_3	$Fddd$	38	1.50(*a*), 1.80(*b*), 1.97(*b*)	−90(*a*), 13(*b*), 22(*c*)	spiral	[115, 123]
γ-Li_2IrO_3	$Cccm$	40	1.6	40	spiral	[124]

octahedra are weakly distorted and mostly trigonally compressed, while the Ir-O-Ir angles deviate from the 90° value. α-$RuCl_3$ on the other hand, has no intercalating cations (Fig. 3.2(c)) and its distortions of $RuCl_6$ octahedra are of a smaller degree than those found in iridates. The second generation Kitaev materials produced by ion exchange crystallise in two types of structures. Those retaining $C2/m$ symmetry have A' cations forming O-A'-O dumbbell bonds as depicted in Fig. 3.2(b) or O-H like bonds found in $H_3LiIr_2O_6$. Materials where all Li ions in α-Li_2IrO_3 are replaced by half the amount of divalent cations adopt an ilmenite structure with space group $R\bar{3}$, which is a derivative of the corundum structure hosting edge-sharing octahedra in the *ab* plane and face-sharing octahedra along the *c* axis shown in Fig. 3.2(d). The A' cations form a buckled honeycomb lattice between the Ir honeycomb layers. As shown in Fig. 3.2(f), all Ir-Ir bonds are equivalent and have C_i point symmetry. The crystal structures of the three-dimensional analogues will be discussed in later sections.

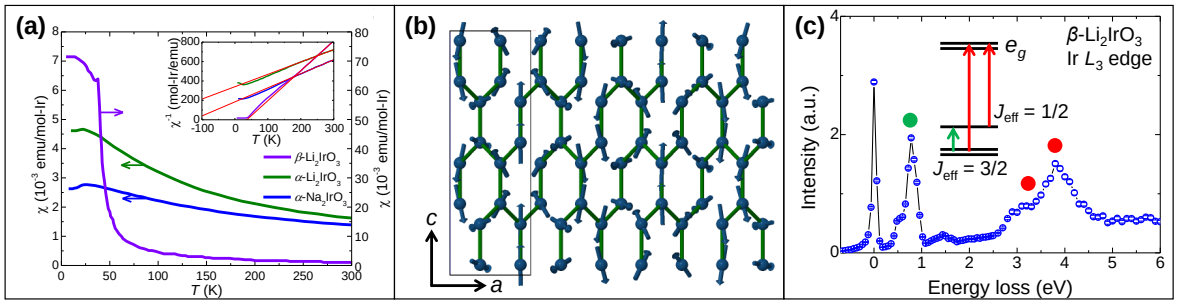

■ *Figure 3.3.* (a) Temperature dependent magnetic susceptibilities of polycrystalline β-Li_2IrO_3 [115], α-Li_2IrO_3 [119] and Na_2IrO_3 [119]. The inset shows inverse magnetic susceptibilities where the red solid lines denote the Curie-Weiss fit. (b) The incommensurate spiral magnetic structure on the hyperhoneycomb sub-lattice of β-Li_2IrO_3 created with Jmol [125] using the magnetic unit cell reported in [123]. (c) RIXS spectrum of polycrystalline β-Li_2IrO_3 obtained at BL11XU at SPring-8 (unpublished). The feature at $\sim$ 0 eV is the elastic peak, while those at $\sim$ 0.7 eV and $\sim$ 3.5 eV correspond to the $J_{\text{eff}} = 3/2 \rightarrow J_{\text{eff}} = 1/2$ and $t_{2g} \rightarrow e_g$ excitations, respectively.

▶ $J_{\text{eff}} = 1/2$ state and its magnetism

The Kitaev materials shown in Table 3.1 are Mott insulators and display localised moment magnetism, where $\mu_{\text{eff}} \sim 1.5\,\mu_B$ to $3\,\mu_B$, close to the idealised value predicted for $J_{\text{eff}} = 1/2$ or spin-only $S = 1/2$. The negative Curie-Weiss constants θ_{CW} indicate the presence of antiferromagnetic couplings, contrary to the expected positive value induced by ferromagnetic exchange, implying that the Kitaev exchange is not the only relevant one as discussed above. However, if the nearest neighbour antiferromagnetic Heisenberg exchange was dominant, a simple Néel order on the bipartite honeycomb lattice would likely be observed (Fig 3.4(d)), and that is not the case. The Kitaev materials adopt a variety of magnetic structures, such as zigzag or spiral (example shown in Fig. 3.3(b)) implying sthat other interactions, such as possibly the Kitaev one, are non-negligible. In addition, the anisotropic character of the magnetic interactions is manifested in the anisotropic magnetic susceptibility and the corresponding extracted values of θ_{CW} observed for example in α-Li_2IrO_3, Na_2IrO_3, α-$RuCl_3$ and β-Li_2IrO_3 shown in Table 3.1.

The relevance of spin-orbit coupling and J_{eff}-physics is evidenced in RIXS experiments on honeycomb iridates at the Ir L_3 edge, where low-energy excitations located at $\sim$ 0.7 eV emerge [126], see Fig. 3.3(c). Those should correspond to the $J_{\text{eff}} = 3/2 \rightarrow J_{\text{eff}} = 1/2$ excitations and should be of the magnitude of $(3/2)\lambda_{\text{SOC}}$, which indicates the value of spin-orbit coupling of Ir to be $\sim$ 0.4 eV. In addition, a splitting of that excitation peak of the order of $\sim$ 100 meV is observed in α-Li_2IrO_3 and Na_2IrO_3. Therefore the trigonal crystal field resulting from trigonal compression of the IrO_6 octahedra is non-negligible in honeycomb iridates, however still smaller than λ_{SOC}, and hence the J_{eff}-description should still remain

valid. The $J_{\text{eff}} = 3/2 \rightarrow J_{\text{eff}} = 1/2$ excitation has been also observed in α-$RuCl_3$ [127], where it is accordingly smaller (0.2 eV) as compared to those reported iridates due to smaller spin-orbit coupling of Ru atom. Moreover, evidence of bond-directional interactions inferred from the azimuthal angle dependence of diffuse magnetic x-ray scattering of Na_2IrO_3 [128], and from the $\boldsymbol{q}$-dependence of excitations obtained with inelastic neutron scattering in α-$RuCl_3$ [127], was identified.

Another experimental verification of the "J_{eff}"-ness of the electronic ground state is x-ray absorption spectroscopy (XAS), where the expectation value of the spin-orbit operator $\langle \boldsymbol{L} \cdot \boldsymbol{S} \rangle$ is directly proportional to the ratio of intensity between the L_3 ($2p_{3/2} \rightarrow 5d$) and L_2 ($2p_{1/2} \rightarrow 5d$) absorption edges called the branching ratio, BR $= L_3/L_2$ [129, 130]. In the absence of spin-orbit coupling, that is, $\langle \boldsymbol{L} \cdot \boldsymbol{S} \rangle = 0$, BR $= 2$ which is due to the twice larger number of states in $2p_{3/2}$ as compared to $2p_{1/2}$. In a variety of iridates BR is reported to range from 4 to 6 [85, 86], which has been discussed as evidence for the spin-orbital entangled $J_{\text{eff}} = 1/2$ state. However, the BR should be evaluated with caution as it can be affected by other effects such as hybridisation.

Additional magnetic couplings

The original microscopic model proposed for the realisation of a Kitaev QSL involves nearest-neighbour anisotropic *d-p-d* hopping on an *undistorted* honeycomb lattice with 90° geometry [51]. Firstly, the C_{2h} symmetry of an unit of two IrO_6 or $RuCl_6$ octahedra allows two additional nearest-neighbour terms [132]:

$$H = \sum_{\langle ij \rangle_\gamma} J\boldsymbol{S}_i \cdot \boldsymbol{S}_j - KS_i^\gamma S_j^\gamma + \Gamma(S_i^\alpha S_j^\beta + S_i^\beta S_j^\alpha) \tag{3.2}$$

where S_i^γ and $S_i^{\alpha(\beta)}$ denote the in-plane and out of plane components with respect to the edge-sharing bond plane, respectively. J is the isotropic Heisenberg coupling inherent from direct *d-d* hopping, K is the Kitaev coupling, and Γ is the symmetric anisotropic coupling, which are depicted in Fig 3.4(a), (b) and (c), respectively. In the earliest discussed models with additional interactions, Kitaev-type and Heisenberg-type nearest-neighbour couplings were considered, and that was found to already dramatically shrink the spin liquid parameter space [133]. The pure Heisenberg-Kitaev (H-K) model can only account for the experimentally observed zigzag order in Na_2IrO_3 if the ferromagnetic Heisenberg and antiferromagnetic Kitaev couplings are considered [131] (Fig 3.4(d)). This has motivated further expansion and inclusion of more parameters in the model: the observed zigzag and spiral magnetic orders can be explained either by adding interactions further than nearest-neighbour interactions [134] (Fig 3.4(e)) or considering the off-diagonal Γ term [132].

The low symmetry of the honeycomb materials allows for distortions from the ideal rocksalt-derived lattice. In Fig 3.2(e), only one bond in the $C2/m$ 2D honeycomb has C_{2h} point

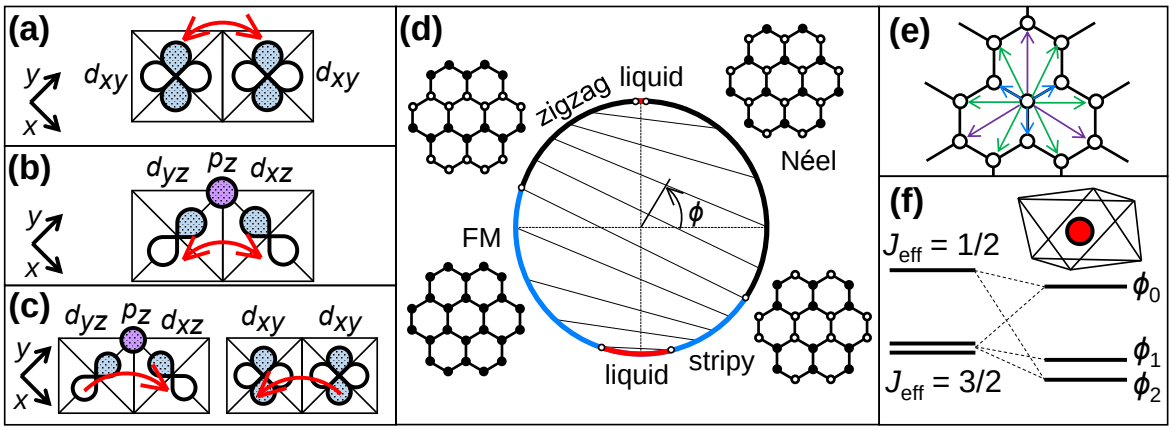

■ *Figure 3.4.* (a) Direct *d-d* hopping which gives rise to the isotropic Heisenberg term. (b) *d-p-d* hopping which gives rise to the anisotropic Kitaev term shown also in Fig 3.1(d). (c) A combination of *d-d* and *d-p-d* hopping gives rise to the symmetric off-diagonal term. (d) Magnetic phase diagram for the Heisenberg-Kitaev model. $J = \cos\phi$ and $K = \sin\phi$. Open and solid circles correspond to up and down spins. Reproduced from Ref. [131]. (e) Further than nearest-neighbour interactions on a honeycomb lattice, where blue, green and violet arrows denote J_1, J_2 and J_3, respectively. (f) The effect of trigonal compression of TM octahedron on the local electronic J_{eff} states producing three doublets in the single ion anisotropy description. The $J_{\text{eff}} = 3/2$ quartet splits into two doublets, ϕ_1 and ϕ_2, and the ($J_{\text{eff}} = 1/2$)-derived state is ϕ_0. ϕ_0 and ϕ_2 are mixtures of the original $J_{\text{eff}} = 1/2$ and $J_{\text{eff}} = 3/2$ states. In the 2D honeycomb Kitaev materials, the trigonal compression axis is usually perpendicular to the honeycomb plane.

group symmetry, while the other two contain only an inversion centre, which should allow for additional exchange paths. In the case of the hyperhoneycomb exemplified by β-Li_2IrO_3 with space group *Fddd* shown in Fig 3.6, one of the bonds has D_2 point symmetry which forbids the off-diagonal exchange, however since it lacks an inversion centre it allows the antisymmetric Dzyaloshinskii-Moriya coupling. The other two bonds possess inversion symmetry only, similar to the case of $C2/m$. In addition, the local distortions of IrO_6 or $RuCl_6$ octahedra should modify the local electronic states as demonstrated in Fig 3.4(f) [135]. Overall, the point symmetry of bonds lower than C_{2h}, distorted octahedra and interactions with further neighbours allow for new exchange couplings and/or modify the initially considered ones, for example lead to imperfect cancellation of the Heisenberg *d-p-d* antiferromagnetic coupling discussed in section 3.1.2 or induce substantial mixing of $J_{\text{eff}} = 1/2$ and $J_{\text{eff}} = 3/2$ states. While such distortions are small, they might be sufficient to push the system away from a QSL and contribute to stabilisation of long range magnetic order.

In addition, the two-dimensional Kitaev materials suffer from stacking faults [136, 137] which when large can affect the ordering temperature or even turn the system into a spin glass, implying that the magnetic interactions are not truly two-dimensional. For α-$RuCl_3$, which

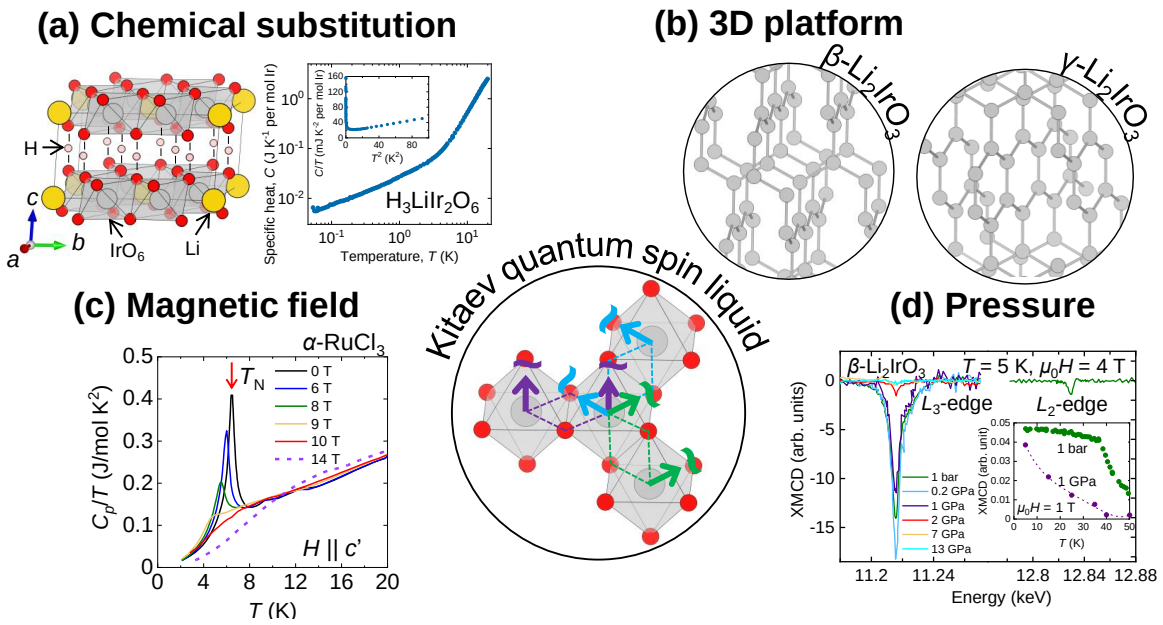

■ *Figure 3.5.* Possible routes to Kitaev QSL. (a) Chemical substitution. Newly reported $H_3LiIr_2O_6$ does not exhibit magnetic order down to the lowest temperature. Reproduced from Ref. [113]. (b) New 3D platforms with Ir sub-lattices of β, γ-Li_2IrO_3. (c) Magnetic field. The magnetic ordering of α-$RuCl_3$ is supressed by application of magnetic field as evident from the specific heat. Reproduced from Ref. [142]. (d) Pressure. The net ferromagnetic moment of β-Li_2IrO_3 is suppressed as evident from x-ray magnetic circular dichroism (XMCD). Reproduced from Ref. [115].

exhibits a three-dimensional zigzag order, there is a variance in reported ordering temperatures and crystal structures due to difference in stacking faults and synthesis conditions [122, 138–141]. Overall, there are plenty of additional interactions and deviations from the ideal Kitaev model that may push the honeycomb systems towards magnetic order.

3.1.4 Tuning of Kitaev materials

Despite the presence of long-range magnetic order, other magnetic couplings and distortions, the Kitaev materials remain robust $J_{\text{eff}} = 1/2$ magnets with sizeable anisotropic magnetic interactions. Moreover, in a model considering J, K and Γ, a spin liquid still exists for certain parameter values [106, 132]. As a result, there have been extensive efforts to tune those interactions in order to bring the system towards the Kitaev QSL by applying external perturbations such as magnetic field or pressure, or exploring new material platforms other than recent chemically-modified $H_3LiIr_2O_6$ or 3D β, γ-Li_2IrO_3 (Fig. 3.5(a) and (b)).

In some Kitaev materials, the magnetic order is suppressed in presence of external magnetic field: the zigzag magnetic order in α-$RuCl_3$ [139] (Fig. 3.5(c)) and the incommensurate spiral

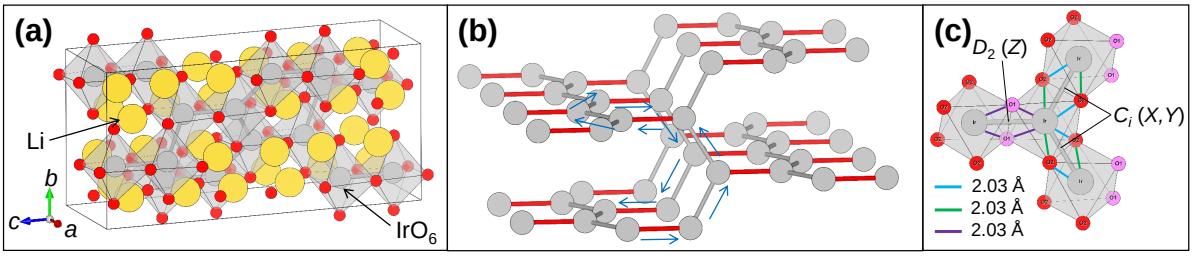

■ *Figure 3.6.* (a) The crystal structure of hyperhoneycomb β-Li_2IrO_3. (b) The hyperhoneycomb network of Ir atoms in (a). The Z bonds (red) which run along the crystallographic c axis, connect the 1D zigzag chains of X, Y bonds (grey). The blue arrows indicate a decagon loop. (c) The local geometry in β-Li_2IrO_3. Ir-O-Ir angles are about 94°, and the Ir-Ir bond that lies along b has D_2 point symmetry.

magnetic order in β, γ-Li_2IrO_3 [115, 143–145] are quenched under applied magnetic field of $\sim$ 7 T in-plane (ab) and $\sim$ 3 T along the crystallographic b axis, respectively. While the 3D iridates have not been receiving much attention in this regard, there has been extensive activity regarding the field-induced spin liquid state in α-$RuCl_3$ [139, 142, 146–148]. For example, signatures of Majorana physics have been observed such as half-integer thermal Hall effect [148, 149], which have been discussed in relevance to the Kitaev QSL.

Another way of tuning the magnetic couplings is application of external pressure, which was first attempted in β-Li_2IrO_3 due to its apparent dominant ferromagnetic interactions inferred from θ_{CW} and hence likely proximity to the Kitaev QSL [115].

3.1.5 Target material: hyperhoneycomb iridate β-Li_2IrO_3

The Kitaev model is based on the three-fold coordination of each magnetic site and the bond-dependent Ising interactions. This can be realised not only in a 2D honeycomb lattice, but in a 3D lattice as well, and hence the Kitaev model can be extended to 3 dimensions [114]. This discovery sparked research activity in 3D analogues of first-generation Kitaev materials with strong spin-orbit coupling, t_{2g}^5 configuration and edge-sharing octahedra.

▶ Crystal structure

The first reported 3D analogue of 2D Kitaev materials is hyperhoneycomb β-Li_2IrO_3, a high temperature polymorph of α-Li_2IrO_3, discovered by Takayama *et al.* [115]. β-Li_2IrO_3 crystallises in an orthorhombic structure with space group *Fddd* (No. 70) and consists of the same edge-sharing LiO_6 and IrO_6 octahedra building blocks as α-Li_2IrO_3 as shown in Fig. 3.6(a). While the local environment of each Ir site is the same as that found in 2D honeycombs, that is, each site has three nearest neighbours connected with the Ir-O_2-Ir link (Fig. 3.6(c)), the Ir atoms arrange in a 3D fashion and generate a 3D network named “hyperhoneycomb”. To understand this 3D network, one can view the 2D honeycomb structure shown in Fig. 3.2(e)

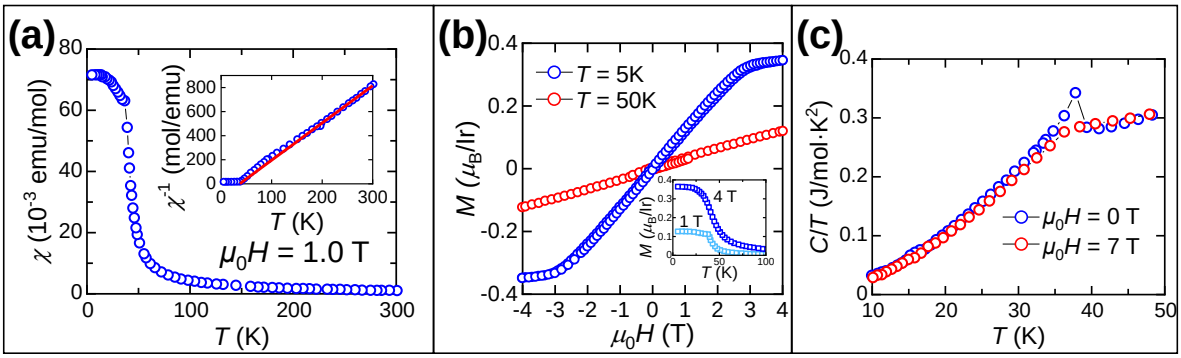

■ *Figure 3.7.* (a) Temperature-dependent magnetic susceptibility of β-Li_2IrO_3. The red line in the inset shows the Curie-Weiss fit. (b) Field-dependent magnetisation of β-Li_2IrO_3. The inset shows the temperature-dependent magnetisation at different magnetic fields. (c) Temperature-dependent heat capacity of β-Li_2IrO_3 at different fields. (a)-(c) are reproduced from Ref. [115].

as an arrangement of 1D zigzag chains (X, Y bonds) in the ab plane connected by links running along the b axis (z bonds). Those 1D zigzag chains are then stacked along the b crystallographic axis in the $Fddd$ structure, alternating in orientation between $a + b$ and $a - b$, and connected to each other with the Z bonds running along the b crystallographic axis as demonstrated in Fig. 3.6(b). The resulting hyperhoneycomb network features ten-site decagon loops. The local environment of each Ir atom and the Ir-Ir and Ir-O bond lengths are quite similar to those found in α-Li_2IrO_3 or Na_2IrO_3 and all Ir-Ir bond angles are $\sim 120°$ (Fig. 3.6(a)). The Ir-Ir bond symmetry remains except for the one running along the $Fddd$ b axis, which is D_2 without an inversion centre.

► Physical properties

β-Li_2IrO_3 is an insulator and its temperature dependence of magnetic susceptibility shown in Fig. 3.7(a) indicates $\mu_{\text{eff}} \sim 1.6\,\mu_B$, which is close to the ideal value expected for $J_{\text{eff}} = 1/2$ or $S = 1/2$ and implies a formation of a $J_{\text{eff}} = 1/2$ moment [115]. The presence of a spin-orbit exciton as evidenced in RIXS shown in Fig. 3.3(c) supports the $J_{\text{eff}} = 1/2$ magnetism. The positive Curie-Weiss temperature of $\theta_{CW} \sim 40\,\text{K}$ points to the dominance of ferromagnetic couplings. An antiferromagnetic ordering occurs at $\sim 40\,\text{K}$ as evident from the kink in magnetic susceptibility and a peak in heat capacity depicted in in Fig. 3.7(a) and (c). The magnetic ordering in β-Li_2IrO_3 has been identified as an incommensurate one with non-coplanar, counter-rotating spirals of spins with a propagation vector of $(0.57, 0, 0)$ [123] shown in Fig. 3.3(b). The small amount of entropy associated with the transition is of the order of a few % of Rln2 indicating frustration [115]. In addition, this frustration suggests that the magnetic couplings present in β-Li_2IrO_3 are larger than the Curie-Weiss temperature, where likely the greater ferromagnetic interaction is partially cancelled by a competing antiferromagnetic

one, bringing the system close to a ferromagnetic state. Below its ordering temperature, that is, below $\sim 40\,\text{K}$, β-Li_2IrO_3 undergoes a metamagnetic transition at $\mu_0 H = 2.8\,\text{T}$ as shown in Fig. 3.7(b). At $\mu_0 H = 4\,\text{T}$, the field-induced moment is $\sim 0.35\,\mu_\text{B}$ indicating approximately full polarisation and the peak in heat capacity vanishes [115, 145]. The $J_{\text{eff}} = 1/2$ magnetism, instability towards ferromagnetism, frustration and theoretical classification of the observed magnetic order in proximity to the spin liquid phase in the parameter space place β-Li_2IrO_3 in the vicinity of a Kitaev QSL state [150]. Therefore, β-Li_2IrO_3 provides a playground for tuning the system towards Kitaev QSL using external perturbations such as pressure.

- Effect of pressure

  The magnetic-field-induced ferromagnetic moment of β-Li_2IrO_3 measured with x-ray magnetic circular dichroism (XMCD) at the $L_{2,3}$ edge increases with decreasing temperature at $\mu_0 H = 4\,\text{T}$ and shows a kink at T_m of $\sim 40\,\text{K}$ as shown in Fig. 3.5(d). With increasing pressure however, the XMCD signal at the L_3 edge decreases until it completely vanishes between 2 GPa and 7 GPa, all while the system remains insulating [115]. The vanishing net ferromagnetic moment could imply a collinear antiferromagnetic long range order or a QSL state. Detailed experimental investigation showed the suppression of long-range order above $\sim 2\,\text{GPa}$ was further evidenced by magnetic susceptibility and muon spin rotation measurements [151] as shown in Fig. 3.8(a) and (b). These promising experimental results motivated the first theoretical investigation of pressure-tuned interactions in a Kitaev material β-Li_2IrO_3, where it was found with DFT calculations that under high pressure the lattice is compressed anisotropically and the anisotropic symmetric term Γ becomes dominant, rendering strong magnetic frustration and yet another type of QSL [152]. A microscopic model considering pressurised and strained honeycomb and hyperhoneycomb lattices was also investigated and it was found that the Kitaev term is much more enhanced as compared to the Heisenberg term under strain. On the other hand, the off-diagonal term becomes larger than the other two under pressure [153], which is consistent with the DFT study in Ref. [152]. However, XMCD and resonant magnetic x-ray scattering demonstrated that $J_{\text{eff}} = 1/2$ magnetism might be no longer relevant as a significant drop in the branching ratio (BR) concomitant with the drop of the net ferromagnetic moment was observed [154]. The branching ratio is indicative of the strength of the spin-orbit coupling, however it can be affected by other factors such as hybridisation. Nevertheless, at ambient pressure the BR ~ 4.5, which at a pressure above 2 GPa drops down to ~ 3, indicative of suppression of spin-orbit coupling and modification of the $J_{\text{eff}} = 1/2$ state. Moreover, it is found that with further pressure increase β-Li_2IrO_3 undergoes a structural transition and adopts a monoclinic $C2/c$ structure above $\sim 4\,\text{GPa}$. While it was recognised that 1/3 of the Ir-Ir bonds become shorter than the others, the impact of the structural change on the electronic structure was not investigated [154]. Understanding of

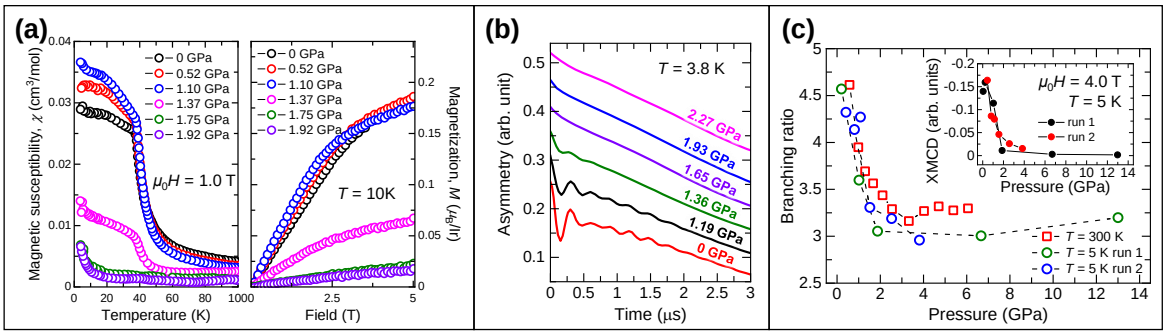

■ *Figure 3.8.* Reported properties of β-Li_2IrO_3 under hydrostatic pressure. (a) Left: Magnetic susceptibility of β-Li_2IrO_3 as a function of temperature at different pressures. Right: $M(H)$ curve at different pressures measured at $T = 10$ K. Reproduced from Ref. [151]. (b) Time-dependent ZF-μSR spectrum of of β-Li_2IrO_3 at $T = 3.5$ K at different pressures. Reproduced from fitting of ZF-μSR data in Ref. [151]. (c) Pressure-dependent branching ratio, which is the ratio of intensities at L_3 and L_2 edge defined as $\text{BR} = I_{L_3}/I_{L_2}$ and is a measure of the expectation value of the angular part of spin-orbit coupling $\langle \boldsymbol{L} \cdot \boldsymbol{S} \rangle$. If $\langle \boldsymbol{L} \cdot \boldsymbol{S} \rangle = 0$, BR = 2. If $\langle \boldsymbol{L} \cdot \boldsymbol{S} \rangle \neq 0$, BR > 2. Reproduced from Ref. [154]. The error bars are omitted.

the driving force of the structural transition might provide important insight into competing interactions that appear dominant at high pressures, and hence aid the understanding of the tuning of Kitaev materials. Here, the changes occurring in β-Li_2IrO_3 under hydrostatic pressure are investigated with neutron diffraction for tracking structural changes including movement of light atoms, and RIXS together with band structure calculations for elucidating the changes occurring in the electronic structure.

3.2 Methods

3.2.1 Sample preparation

An isotope-enriched powder sample for the neutron diffraction experiment was prepared by solid state reaction using powders of $^7Li_2CO_3$ (Sigma Aldrich, isotope enrichment 99 %) and ^{193}Ir (Isoflex, isotope enrichment 98.5 %):

$$^7Li_2CO_3 + {}^{193}\text{Ir} \xrightarrow[\text{air}]{1100\,^\circ\text{C}} (1-x)\,(\alpha\text{-}{}^7Li_2{}^{193}IrO_3) + x\,(\beta\text{-}{}^7Li_2{}^{193}IrO_3) + CO_2\uparrow \xrightarrow[\text{air}]{1150\,^\circ\text{C}} y\,(\beta\text{-}{}^7Li_2{}^{193}IrO_3) \tag{3.3}$$

β-Li_2IrO_3 is the high-temperature polymorph of Li_2IrO_3 [117], and hence long annealing at a temperature of 1150 °C with regrinding rendered nearly pure β-Li_2IrO_3 as demonstrated in Fig. 3.9. The magnetic susceptibility shows an antiferromagnetic transition in agreement with Ref. [115]. Single crystals of β-Li_2IrO_3 used in the RIXS experiment were obtained by a flux method with LiCl, for detail see Ref. [115].

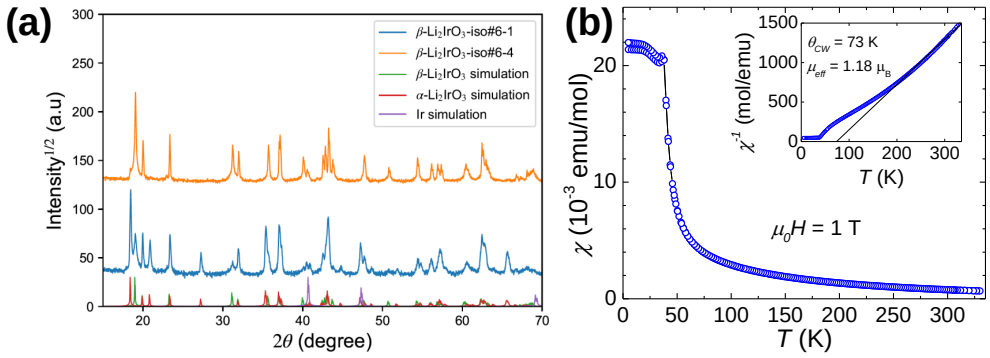

■ *Figure 3.9.* Evaluation of the β-Li_2IrO_3 sample used in the neutron diffraction experiment. (a) Powder x-ray diffraction patterns of polycrystalline β-Li_2IrO_3-iso#6 batch after first (6-1) and fourth (6-4) round of annealing at 1150 °C collected with Cu-$\kappa\alpha$ radiation at room temperature and compared to simulation patterns. (b) Magnetic susceptibility of β-Li_2IrO_3-iso#6. The black solid line in the inset represents Curie-Weiss fit in the range between 220 K to 300 K.

3.2.2 Time of flight neutron diffraction under pressure

In order to track the structural changes occurring in β-Li_2IrO_3 at high pressure, including light atom positions, neutron diffraction via the time-of-flight technique at PEARL, ISIS (Fig 3.10(a)) was employed [155]. The isotope-enriched sample of β-$^7Li_2^{193}IrO_3$ was prepared in order to minimise the neutron absorption cross-section (Table 3.2). A Paris-Edinburgh press with zirconia toughened alumina (ZTA) anvils and null-scattering Ti-Zr gaskets for achieving pressures below 5 GPa at room temperature was used. For more detail on the high pressure neutron diffraction method, visit Ref. [155]. NaCl powder was mixed with the polycrystalline sample to serve as a pressure marker, and deuterium-substituted methanol-ethanol mixture (4:1 ratio by volume) was utilised as a hydrostatic pressure medium. The hydrostatic pressure experienced by the sample and pressure marker mixture was determined by refinement of the unit cell parameter of NaCl with using third-order Birch-Murnaghan isothermal equation of state [156]:

$$P(V) = \frac{3B_0}{2}\left[\left(\frac{V_0}{V}\right)^{\frac{7}{3}} - \left(\frac{V_0}{V}\right)^{\frac{5}{3}}\right]\left[1 + \frac{3}{4}(B_0' - 4)\left[\left(\frac{V_0}{V}\right)^{\frac{2}{3}} - 1\right]\right], \tag{3.4}$$

where P is pressure, V_0 is the reference (ambient pressure) volume, V is the pressure-dependent volume, B_0 is the bulk modulus and B_0' is the derivative of the bulk modulus. For NaCl at room temperature, $B_0 = 23.5$ GPa and $B_0' = 5.35$ GPa [157]. V_0 was determined from the diffraction pattern obtained at the lowest pressure of 0.0018 GPa. The hydrostatic pressure achieved with a given hydraulic press load is shown in Fig 3.10(b).

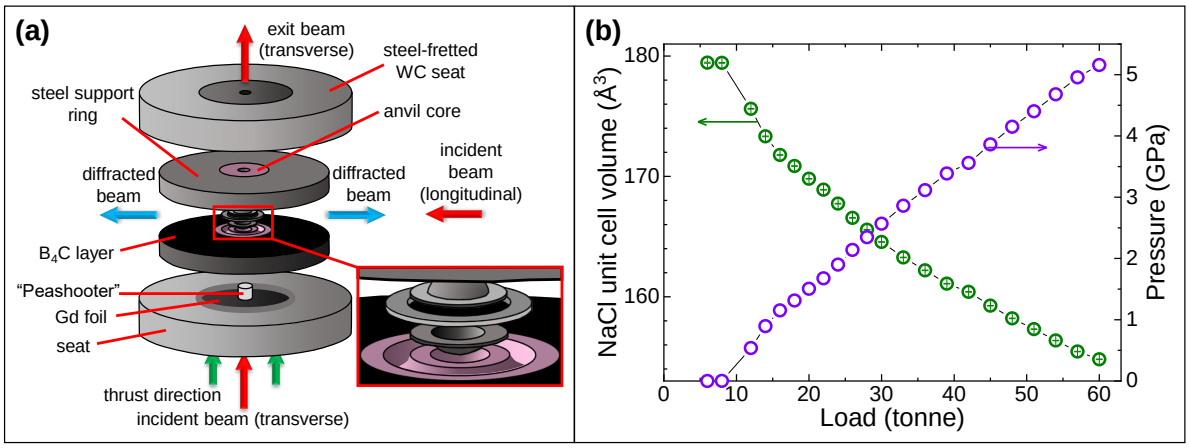

■ *Figure 3.10.* (a) The sample environment in the PEARL instrument at ISIS. Sandwiched tungsten carbide (WC) and ZTA anvils, both coated with boron, oppose the null-scattering Ti-Zr gaskets (grey elements shown in the red box), into which the powder sample was loaded. The diffracted beam is always measured in the horizontal plane, which is indicated by the blue arrows. Reproduced from Ref. [155]. (b) The decrease of NaCl unit cell volume V with increasing hydraulic press load and the corresponding hydrostatic pressure determined using Equation 3.4.

■ *Table 3.2.* Neutron scattering lengths b and cross sections σ for thermal neutrons. b is given in fm and σ is given in barns. All values are taken from Ref. [77] unless specified otherwise.

Isotope	Concentration(%)	b_{coh}	b_{inc}	σ_{coh}	σ_{inc}	σ_{tot}	σ_{abs}
Li	—	−1.90	—	0.454	0.92	1.37	70.5
^{6}Li	7.5	$2.00 - 0.261i$	$-1.89 + 0.26i$	0.51	0.46	0.97	940(4)
^{7}Li	92.5	−2.22	−2.49	0.619	0.78	1.4	0.0454
Ir	—	10.6	—	14.1	0(3)	14(3)	425(2)
^{191}Ir	37.3	12.1 [159]	—	—	—	—	940(4)
^{193}Ir	62.7	9.71 [159]	—	—	—	—	111(5)
O	—	5.803	—	4.232	0.0008	4.232	0.00019
^{16}O	99.762	5.803	0	4.232	0	4.232	0.0001
^{17}O	0.038	5.78	0.18	4.2	0.004	4.2	0.236
^{18}O	0.2	5.84	0	4.29	0	4.29	0.00016

The collected neutron diffraction data was reduced, normalised and corrected using Mantid [158], where the neutron attenuation by the ZTA anvil and Ti-Zr gasket was accounted for [155]. Rietveld analysis of the neutron diffraction data was performed with the GSAS programme [80].

3.2.3 Resonant inelastic x-ray scattering under pressure

The electronic structure under pressure was investigated by recording RIXS excitation spectra up to pressures of $\sim$ 7 GPa measured at Ir L_3 edge at BL12XU beamline at SPring-8. For application of pressure a diamond anvil cell (DAC) was used as shown in Fig 3.11. The pressure was controlled by four screws holding the two diamond anvils opposite each other. A beryllium gasket was used in order to minimise the attenuation of the incident and scattered x-ray beams, and Mo gasket cover with slits was used to minimise background scattering. A crystal of β-Li_2IrO_3 of a size of $\sim$ 50 µm was used and loaded in the DAC with Fluorinert (FC70:FC-77=1:1 mixture by volume) as a pressure medium and a ruby ball as a pressure marker. The pressure dependence R_1 line in ruby fluorescence is defined as [160]:

$$P = \frac{A}{B}[(\lambda/\lambda_0)^B - 1](\text{GPa}) \tag{3.5}$$

where P is pressure, $A = 1905$ and $B = 5$ are least-squares fit parameters, λ_0 and λ are the ambient pressure and pressure-dependent wavelengths of the R_1 line, respectively. The pressure achieved in the RIXS experiment is shown in Fig. 3.11(e). Fluorinert is reported to lose hydrostaticity as a pressure medium above pressures of $\sim$ 1 GPa. Therefore the shift between the two emission lines R_1 and R_2 together with the FWHM of R_1 were evaluated in Fig. 3.11(f). The $R_1 - R_2$ does not change significantly with increasing pressure, however FWHM is larger than 0.5 nm (value for He gas, the most hydrostatic pressure medium known) and increases with pressure, which could indeed imply some hydrostaticity loss. Nevertheless, the non-hydrostaticity cannot account for the drastic changes in RIXS spectra shown below.

The energy of the incident x-ray beam was tuned to 11 215 eV ($2p_{3/2} \rightarrow 5d(t_{2g})$ excitation) by using a Si(111) double crystal monochromator and four-bounce Si (440) high resolution monochromator, which was then focused with a Kirkpatrick-Baez mirror. π-polarised x-rays were used for minimising Thompson scattering and the scattering angle was fixed to 90° in planar geometry. The scattered x-ray beam was analysed with a diced and spherically bent Si(844) analyser. The total energy resolution was $\sim$ 100 meV as determined from the FWHM of the elastic line. After each pressure load, which required removal of the DAC from the RIXS geometry, the single crystal of β-Li_2IrO_3 was located by monitoring the intensity of the Ir L_α emission line ($3d \rightarrow 2p_{3/2}$ excitation) with a spherically bent Ge(733) analyser. The RIXS spectra were measured at an unknown $\boldsymbol{q}$, and since honeycomb iridates α-Li_2IrO_3 and Na_2IrO_3 do not show appreciable $\boldsymbol{q}$-dependence of the d-d excitations [126], it is expected that the obtained RIXS spectra represent the key features of the d-d excitations in β-Li_2IrO_3.

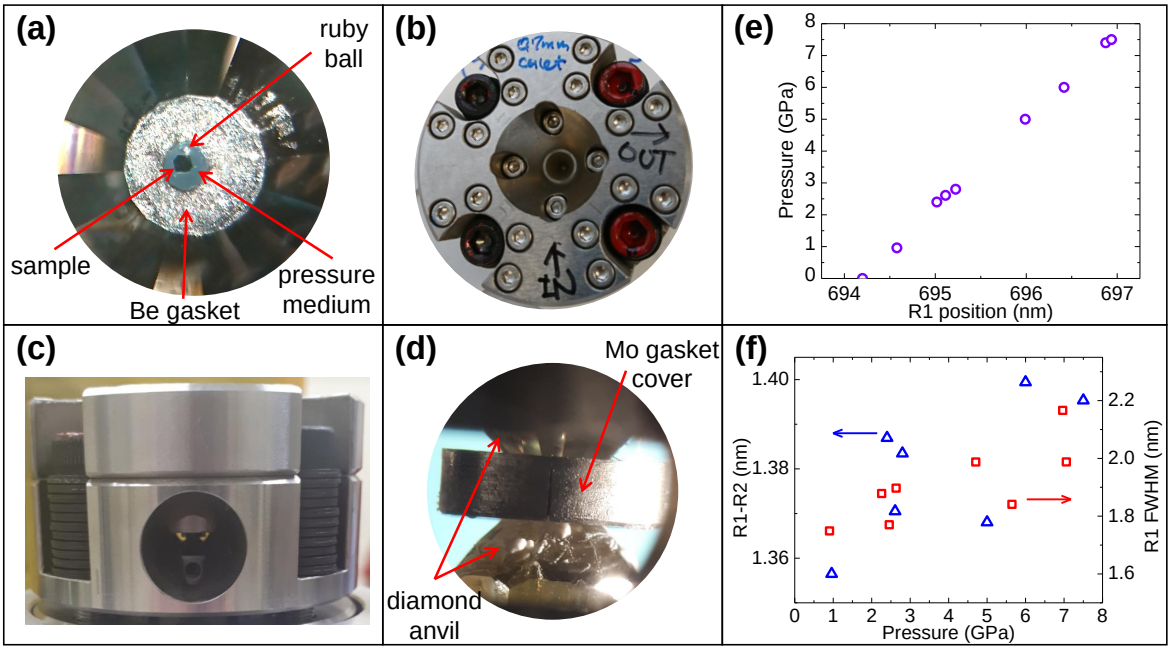

■ *Figure 3.11.* Experimental details of the RIXS experiment performed on the single crystal of β-Li_2IrO_3. (a) The view of the sample space surrounded by the Beryllium (Be) gasket with the sample and the ruby ball visible. (b) The top view of the DAC showing the direction of the incoming (IN) and scattered (OUT) beam. (c) The side view of the DAC. (d) The view of the Be gasket with a slit permitting transmission of scattered x-ray beam from the sample only. (e) The pressure experienced by the sample evaluated from the shift of the R_1 ruby emission line. (f) Evaluation of the hydrostaticity of the fluorinert pressure medium.

3.2.4 Band structure calculations

The LDA band structure calculations were performed using the method described in chapter 2.5.1 and the crystal structures obtained from the neutron diffraction experiment at pressures of 0 GPa and 4.4 GPa.

3.3 Results

3.3.1 Dimerisation under pressure

Neutron diffraction patterns of β-Li_2IrO_3 obtained at pressures of 0 GPa, 2.6 GPa and 4.4 GPa are presented in Fig 3.12(a), (b) and (c) and the corresponding crystal structures determined with Rietveld refinement are shown in Table 3.3. The structure parameters obtained at $P =$ 0 GPa are slightly different than those obtained with single crystal x-ray diffraction reported in Ref. [115], however they give qualitatively the same result. At ambient pressure, β-Li_2IrO_3

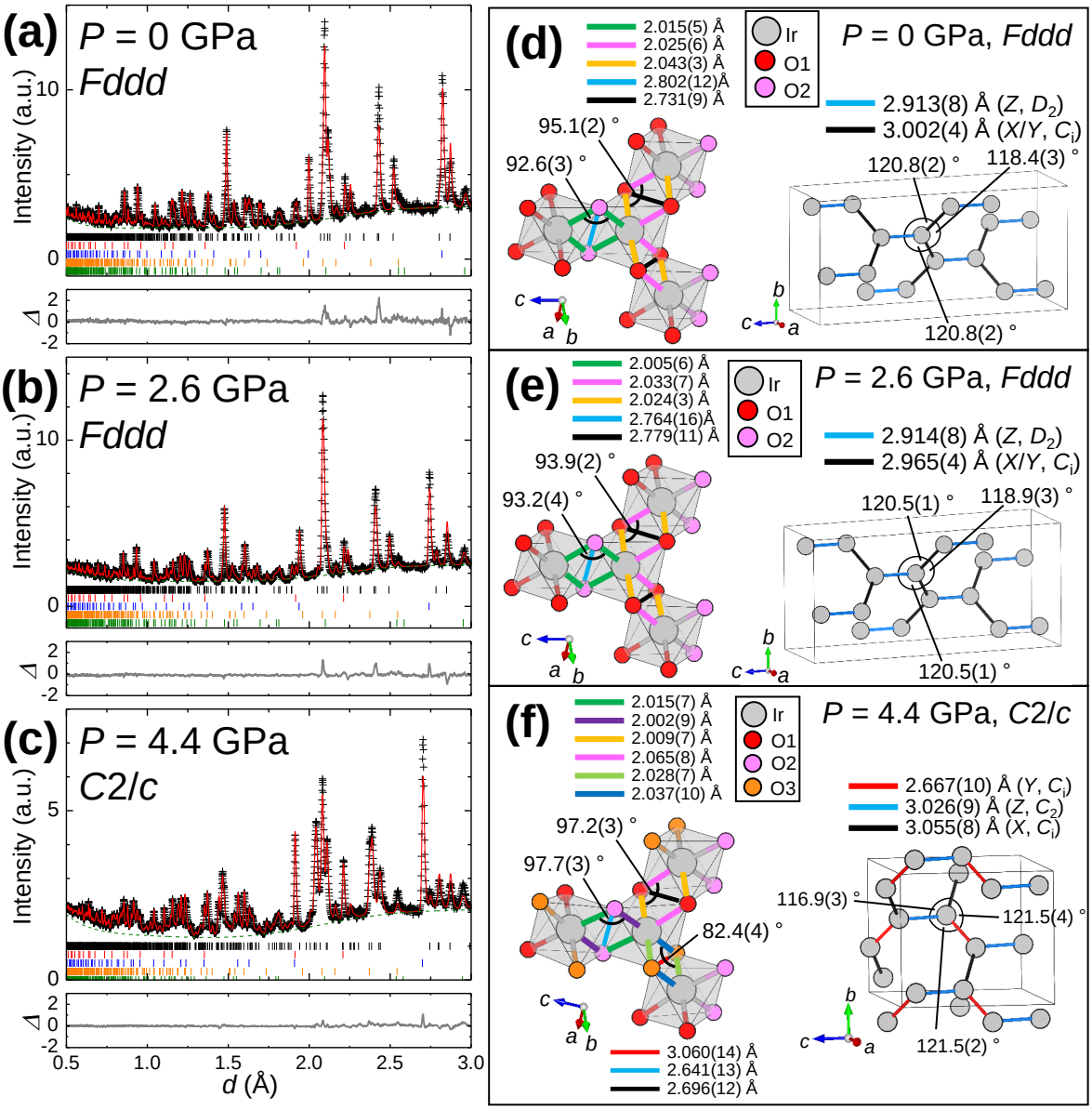

■ *Figure 3.12.* Structural changes occurring in β-Li_2IrO_3 under hydrostatic pressure inferred from neutron diffraction patterns observed at $P = 0$ GPa ((a) and (d)), 2.6 GPa ((b) and (e)) and 4.4 GPa ((c) and (f)). In (a), (b) and (c) the black crosses, red line, dashed green line and grey line correspond to the observed pattern, the Rietveld fit profile, the fitted Chebyshev background and the difference curve between observed and calculated profiles, respectively. The black, red, blue, orange and green bars represent reflection positions of β-Li_2IrO_3, Ir, NaCl, Al_2O_3 and ZrO_2, respectively. The significant intensity mismatch at higher d-spacings largely originates from the anvil components, Al_2O_3 and ZrO_2, as evident from the labelled reflections, most likely due to the modelling of the peak profiles of those components under high pressure being imperfect. (d), (e) and (f) depict changes occurring in Ir-O bond lengths and the Ir hyperhoneycomb network with Ir-Ir bond symmetry indicated. The edge-sharing O-O bonds have the same colour as their corresponding Ir-Ir bond.

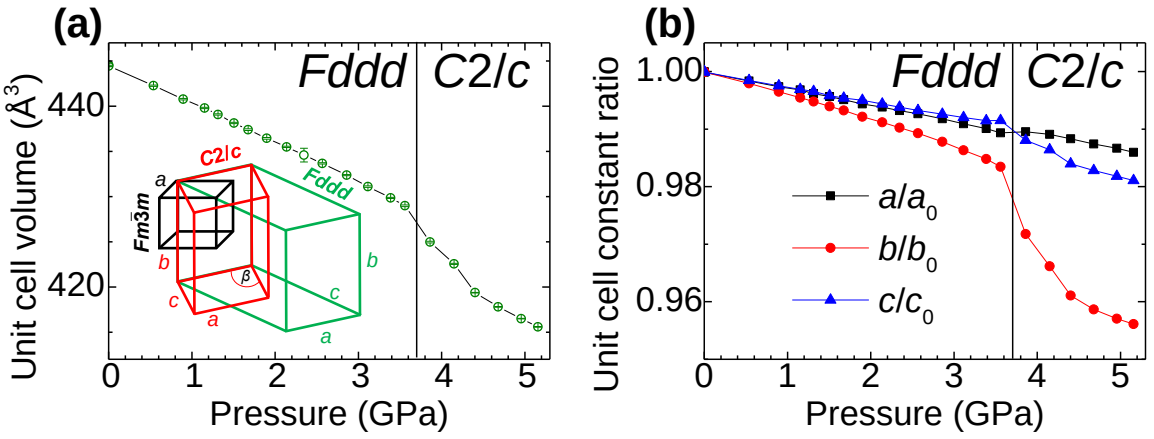

■ *Figure 3.13.* Pressure-dependent lattice parameters of β-Li_2IrO_3. In both (a) and (b) the ambient pressure *Fddd* phase has been converted to a $C2/c$ superstructure and hence its volume is decreased by a factor of 2. (a) Unit cell volume of β-Li_2IrO_3 under pressure. At around 3.7 GPa a sharp drop is observed. The inset shows the relationship between the parent rocksalt structure, ambient pressure orthorhombic *Fddd* structure, and the high pressure monoclinic $C2/c$ structure as defined by the basis shown in Table 3.3. (b) Ratio of lattice parameters normalised with respect to the ambient pressure ones showing anisotropic lattice contraction.

adopts an orthorhombic *Fddd* structure. As depicted in Fig 3.12(d), the IrO_6 octahedra are edge-sharing, and each Ir site has three nearest neighbours. While there is one unique Ir Wyckoff site, the hyperhoneycomb network consists of two types of symmetrically inequivalent Ir-Ir bonds: one that runs along the crystallographic c axis and has D_2 point symmetry (Z), and the two degenerate ones forming a zigzag chain which run along $a + b$ and $a - b$ directions and have C_i point symmetry (X, Y). The angle between all Ir-Ir bonds is $\sim 120°$, the Ir-Ir bonds lengths are on average ~ 2.95 Å and the Ir-O-Ir angles are between $\sim 91°$ and $\sim 96°$. For a better comparison of pressure-dependence of the two structures shown in Fig 3.13, the *Fddd* structure has been transformed into the low symmetry $C2/c$ structure following a group-subgroup transformation (basis shown in Table 3.3). With increasing pressure, the β-Li_2IrO_3 unit cell shrinks (Fig 3.13(a)), where b axis, which is related to the direction of the zigzag chains (X, Y bonds), contracts more rapidly as evident in Fig 3.13(b). Consequently, at $P = 2.6$ GPa shown in Fig 3.13(e), the lengths of X, Y bonds decrease more (~ 1.2 %) than that of the Z bond (~ 0.03 % and within the error bar), resulting in X, Y and Z bond lengths being more isotropic.

With further increase of pressure, a structural transition occurs sharply at $P_s \sim 3.7$ GPa. The ambient pressure orthorhombic *Fddd* structure transforms into a monoclinic $C2/c$ structure with the unit cell volume reduced by a factor of 2 as shown in Fig 3.13(a). In the $C2/c$ symmetry, the X and Y bonds are no longer equivalent. In Fig 3.12(f), the Z bond bridging the

■ *Table 3.3.* Refined structural parameters of β-Li_2IrO_3 obtained at pressures of 0 GPa, 2.6 GPa and 4.4 GPa from diffraction patterns shown in Fig 3.12. g and U_{iso} correspond to the site occupancy and the isotropic atomic displacement parameter, respectively. U_{iso} was constrained to be identical for the same elements residing on different Wyckoff sites. R_{wp} and χ^2 are refinement quality indices. a, b, c and β are unit cell parameters.

$P = 0$ GPa, *Fddd* (No. 70), Z = 16. $R_{\text{wp}} = 0.0381$ and $\chi^2 = 1.619$ for 13 refined parameters.
$a = 5.9055(4)$ Å, $b = 8.4559(5)$ Å, $c = 17.8046(12)$ Å.

Atom	Site	x	y	z	g	U_{iso} (Å^2)
Li1	16g	1/4	1/4	0.0556(6)	1	0.0022(11)
Li2	16g	1/4	1/4	0.8707(7)	1	=Li1
Ir	16g	1/4	1/4	0.70656(21)	1	0.0047(4)
O1	16e	0.8622(10)	1/4	1/4	1	0.00539(35)
O2	32h	0.6371(10)	0.36602(35)	0.03797(23)	1	=O1

$P = 2.6$ GPa, *Fddd* (No. 70), Z = 16. $R_{\text{wp}} = 0.0309$ and $\chi^2 = 2.556$ for 13 refined parameters.
$a = 5.8639(4)$ Å, $b = 8.3601(5)$ Å, $c = 17.6882(10)$ Å.

Atom	Site	x	y	z	g	U_{iso} (Å^2)
Li1	16g	1/4	1/4	0.0605(7)	1	0.0158(16)
Li2	16g	1/4	1/4	0.8717(9)	1	=Li1
Ir	16g	1/4	1/4	0.70773(28)	1	0.0117(4)
O1	16e	0.8607(13)	1/4	1/4	1	0.00871(27)
O2	32h	0.6339(14)	0.3673(4)	0.04022(26)	1	=O1

$P = 4.4$ GPa, $C2/c$ (No. 15), Z = 8. $R_{\text{wp}} = 0.0242$ and $\chi^2 = 2.804$ for 25 refined parameters.
Basis with respect to *Fddd* : [1,0,0], [0,1,0], [-1/2,0,1/2] with origin shift [5/4,5/4,3/2].
$a = 5.8386(4)$ Å, $b = 8.1301(5)$ Å, $c = 9.2245(7)$ Å, $\beta = 106.658(5)^\circ$.

Atom	Site	x	y	z	g	U_{iso} (Å^2)
Li1	8f	0.2567(35)	0.6453(19)	0.2445(22)	1	0.0078(13)
Li2	8f	0.9353(29)	0.6216(23)	0.5980(16)	1	=Li1
Ir	8f	0.4239(7)	0.3846(5)	0.0788(5)	1	0.00492(34)
O1	8f	0.9027(12)	0.3619(6)	0.5829(9)	1	=O1
O2	8f	0.7270(10)	0.3893(8)	0.2518(7)	1	0.00491(31)
O3	8f	0.4056(12)	0.3665(6)	0.5848(8)	1	=O1

X, Y zigzag chains increases in length by a factor of ~ 4 %, while the X and Y bonds increase and decrease by a factor of ~ 3 % and ~ 10 %, respectively (as compared to 2.6 GPa phase). Effectively, the X, Y zigzag chains comprise alternating short and long Ir-Ir bonds. In addition, along the short Y links, the Ir-O-Ir angles decrease significantly and the two oxygen atoms bridging the IrO_6 octahedra move further apart from each other as compared to those along

Z or X links, as depicted in Fig 3.12(f).

The difference between the longest and the shortest bonds is of the order of $\sim 13\,\%$, and it is comparable to the difference found in honeycomb ruthenate Li_2RuO_3 with dimer and molecular orbital formation [161, 162]. The pattern of dimers found in Li_2RuO_3 is herringbone, and β-Li_2IrO_3 adopts a 3D version of that pattern as evident in Fig 3.12(f). The Y bond length of 2.667(10) Å is even shorter than that found in metallic Ir (~ 2.71 Å [163]), implying formation of Ir_2 dimers in the zigzag chains. This is in contrast to the theoretical prediction of dimer formation along the Z bond in the absence of SOC [164]. To verify the electronic structure reconstruction and the relevance of the $J_{\text{eff}} = 1/2$ state associated with drastic structural change under pressure in form of Ir_2 dimer formation, RIXS measurement and band structure calculations were performed as shown below.

3.3.2 Destruction of the $J_{\text{eff}} = 1/2$ state under pressure

RIXS spectra under pressure collected at room temperature are presented in Fig 3.14(a). The pressure was determined from the R_1 ruby emission line shown in Fig 3.14(b). The pressure in the DAC exhibited slight instability as it increased and decreased with measurement time. Nevertheless, each measurement comprises x-ray emission data strictly above or below the P_s. For simplicity, each measurement will be referred to with its pressure determined after the RIXS scan.

The bottom panel of Fig 3.14(a) shows Ir L_3 edge RIXS spectrum of a reference polycrystalline sample of β-Li_2IrO_3 at ambient pressure and room temperature (also displayed in Fig 3.3(c)). Except for the elastic peak at 0 eV, two clear features are observed at ~ 0.7 eV and ~ 3.5 eV, which correspond to $J_{\text{eff}} = 3/2 \rightarrow J_{\text{eff}} = 1/2$ and $t_{2g} \rightarrow e_g$ excitations, respectively. The spin-orbit exciton confirms the predominant $J_{\text{eff}} = 1/2$ character of β-Li_2IrO_3. The RIXS spectrum from the single crystal at $P = 0.9$ GPa is similar to that observed in powder, which confirms that there should be no sizeable q-dependence of the d-d excitations. When the pressure is increased to $P = 3.1$ GPa, the spin-orbit exciton remains, evidencing that despite the suppression of long-range magnetic order at around 1 GPa to 2 GPa [151], the $J_{\text{eff}} = 1/2$ state remains relevant. However, with the given resolution it is difficult to determine whether subtle changes in intensity or excitation energy take place. In the honeycomb α-Li_2IrO_3, which also shows dimerisation at high pressures [165], the intensity and energy of the spin-orbit exciton decreases at pressures below P_s which is discussed to be a signature of electronic structure modification caused by lattice deformation below P_s [166].

At a pressure of 6.0 GPa, that is, above the structural transition, a drastic change occurs in the excitation spectra. The spin-orbit exciton observed at ~ 0.7 eV at lower pressures vanishes, and instead, a broad continuum stretching from 0.3 eV to 2 eV appears. In addition, on the

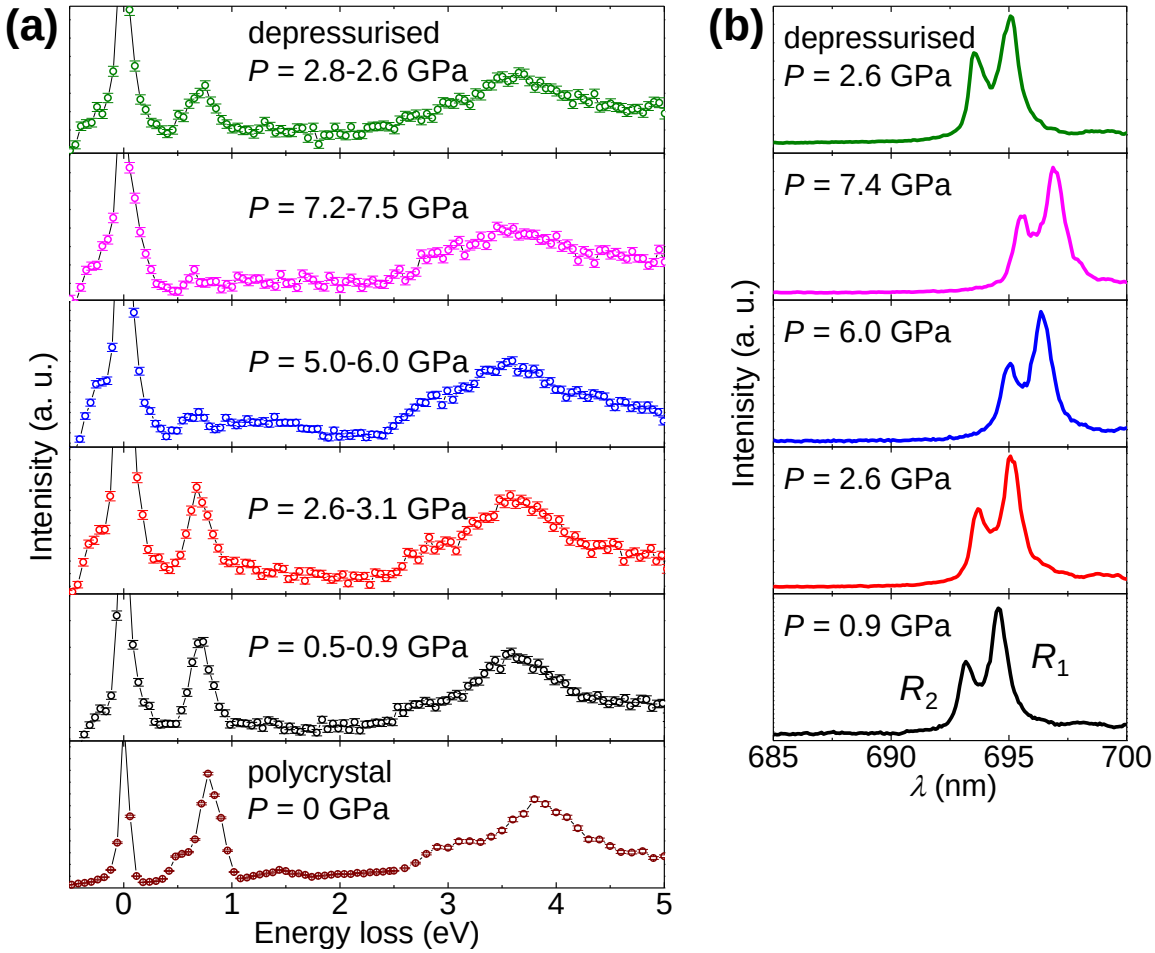

■ *Figure 3.14.* (a) RIXS spectra of β-Li_2IrO_3 under pressure collected at room temperature. In addition, RIXS spectra of polycrystalline sample at ambient pressure (bottom) and of single crystal sample depressurised from 7.5 GPa to 2.6 GPa (top) were recorded. The pressure range associated with each spectrum denotes the pressure recorded before and right after the measurement. (b) The ruby fluorescence spectra from the ruby ball located inside the sample space of the DAC corresponding to some of the pressure points measured in (a).

low-energy side of the $t_{2g} \rightarrow e_g$ excitation a shoulder at ~ 2.8 eV emerges. When the pressure in the DAC is decreased to below P_s, the peak at ~ 0.7 eV is recovered as shown in the top panel of Fig 3.14(a), evidencing that the modification of the RIXS spectra at high pressures is not due to damage or decomposition of the sample due to x-ray irradiation or reaction with the pressure medium. The disappearance of the spin-orbit exciton above ~ 3 GPa implies that the $J_{\text{eff}} = 1/2$ local electronic state is destroyed in the high pressure phase.

3.3.3 Formation of molecular orbitals in the Ir_2 units under pressure

The electronic structure calculations for the ambient pressure and the high pressure phases of β-Li_2IrO_3 are shown in the partial density of states (DOS) shown in Fig 3.15(a), (c) and (b), (d), respectively. On-site Coulomb U was not incorporated, and for the $Fddd$ phase a metallic state is produced with and without spin-orbit coupling. In Fig 3.15(a) and (b) the spin-orbit coupling is not incorporated. The top and bottom panels show the partial DOS projected onto O $2p$ and Ir $5d$ states, where substantial hybridisation between those is evident. In Fig 3.15(c) and (d), the spin-orbit coupling is included in the calculation. The top panel shows DOS of Ir $5d$ states projected onto $J = 5/2$ ($J_{5/2}$) and $J = 3/2$ ($J_{3/2}$) states, while the bottom panel depicts Ir t_{2g} orbitals resolved into $J_{\text{eff}} = 1/2$ and $3/2$ characters. The pure $J_{\text{eff}} = 1/2$ wave function comprises only the $J_{5/2}$ states and $J_{\text{eff}} = 3/2$ wave function consists of both $J_{5/2}$ and $J_{3/2}$.

We begin by considering the band calculation results for the ambient pressure phase without and with spin-orbit coupling. The bottom panel of Fig 3.15(a) shows that in the $Fddd$ ambient pressure phase wihout spin-orbit coupling, the states between ~ -1.5 eV and ~ 0.25 eV comprise the t_{2g} manifold giving a metallic state, while the states between ~ 3 eV and ~ 4 eV are the e_g ones. The t_{2g} (1), (2) and (3) are degenerate states comprising combination of d_{xy}, d_{xz} and d_{yz} states due to the weak distortion of the IrO_6 octahedra. In Fig 3.15(c), when spin-orbit coupling is incorporated in the band structure calculations, the DOS of the $Fddd$ phase are strongly affected. Spin-orbit coupling splits the degenerate t_{2g} states into the half-filled $J_{\text{eff}} = 1/2$ band located at ± 0.25 eV and the $J_{\text{eff}} = 3/2$ band located between ~ -1.5 eV and ~ -0.5 eV. The states near E_{F} comprise mostly $J_{5/2}$, and hence $J_{\text{eff}} = 1/2$, states, which is consistent with the $J_{\text{eff}} = 1/2$ magnetism observed in β-Li_2IrO_3. Since a metallic state is obtained for the $Fddd$ phase with spin-orbit coupling, incorporation of U would be necessary to gap the $J_{\text{eff}} = 1/2$ band, which is consistent with β-Li_2IrO_3 being a Mott insulator.

The structural transition has great impact on the electronic structure which is evident from the DOS of the $C2/c$ phase without spin-orbit coupling. In Fig 3.15(b) an insulating result is obtained. The local axes are defined such that the d_{xz} orbitals point along the shortest Ir-Ir bond (Fig 3.15(e)). While there are two (t_{2g})-derived orbitals that remain nearly degenerate

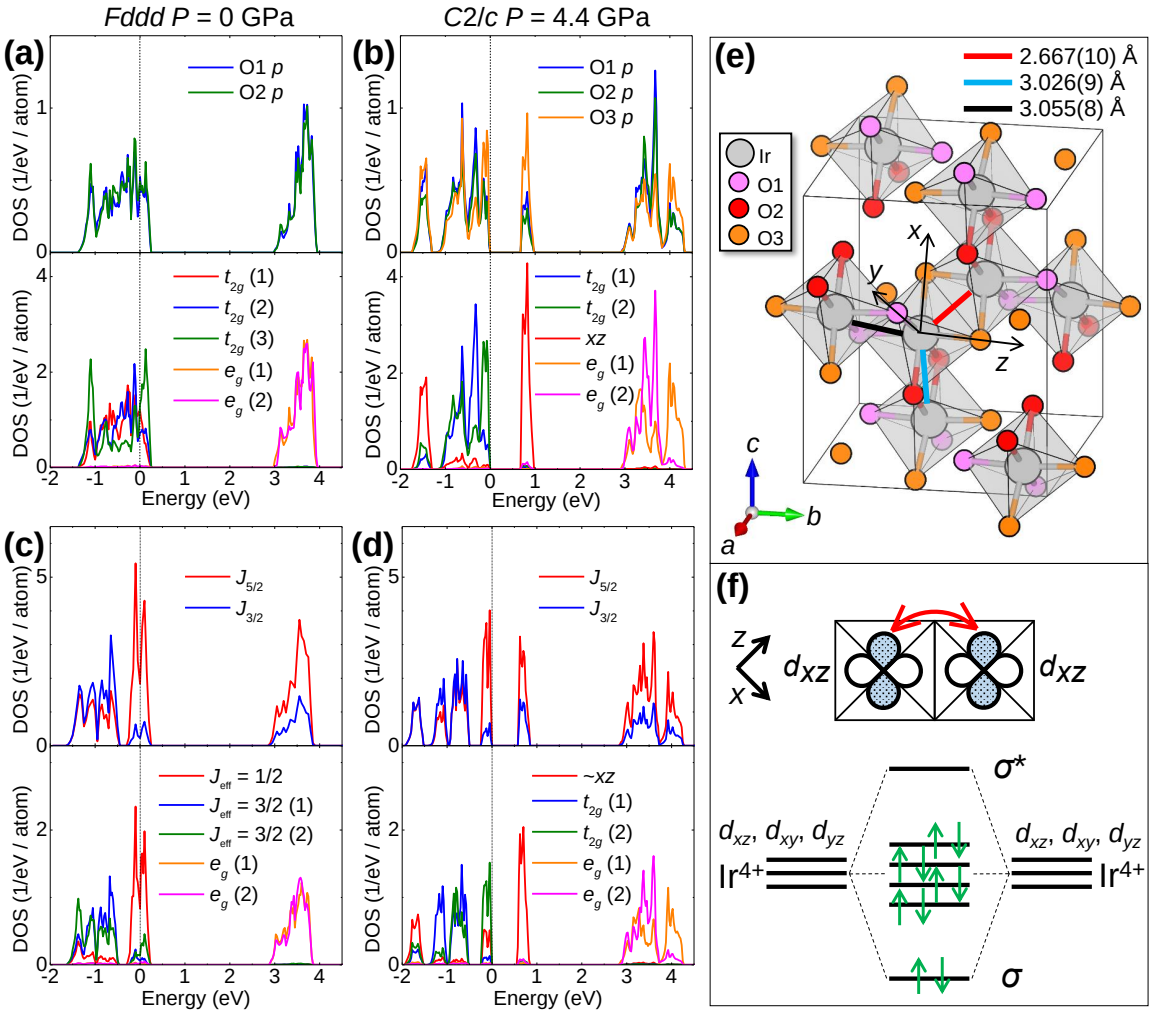

■ *Figure 3.15.* Calculated DOS for Ir 5*d* states for the ambient pressure structure ((a) and (c)) and the high pressure structure ((b) and (d)) of β-Li_2IrO_3 with ((c) and (d)) and without ((a) and (b)) spin-orbit coupling. The Fermi level E_F is indicated by dashed black lines. The e_g (1) and (2) states correspond to d_{z^2} and $d_{x^2-y^2}$ states, respectively. In (a) and (b), the top and bottom panels show the O 2*p* and Ir 5*d* states, respectively. The t_{2g} (1), (2) and (3) states correspond to three degenerate orbitals which all comprise combinations of d_{xy}, d_{xz} and d_{yz} due to the weak distortion of the IrO_6 octahedra. In (c) and (d), the top panels illustrate DOS resolved into $J_{5/2}$ and $J_{3/2}$ full *d* orbital states, while the bottom panels illustrate DOS with t_{2g} states resolved into $J_{\text{eff}} = 1/2$ and $J_{\text{eff}} = 3/2$ states. In (c), the $J_{\text{eff}} = 3/2$ (1) and (2) states comprise mostly $|J_{\text{eff}} = 3/2, J^z_{\text{eff}} = \pm 1/2\rangle$ and $|J_{\text{eff}} = 3/2, J^z_{\text{eff}} = \pm 3/2\rangle$, respectively. In (d), t_{2g} (1) and (2) represent spin-orbital entangled d_{xy} and d_{yz} states. The d_{xz} orbital points along the Ir_2 dimer as depicted in (e). (e) The $C2/c$ high-pressure structure of β-Li_2IrO_3 showing the IrO_6 octahedra only. The local x, yz axes correspond to the ones used in (a), (b), (c), (d). (f) Top: the primary direct *d*-*d* hopping mechanism between d_{xz} orbitals along the shortest Ir_2 bonds. Bottom: a diagram showing bonding and antibonding molecular orbital formation due to the hopping depicted above as observed in (d).

just below the Fermi level E_F, the d_{xz} orbital becomes split by ~ 2.4 eV implying bonding and anti-bonding molecular orbital formation. This suggests the destruction of the $J_{\text{eff}} = 1/2$ state and molecular orbital formation along the Ir_2 dimers. In addition, in the top panel of Fig 3.15(b), the O3 $2p$ states appear dominant over other oxygen atom states at the anti-bonding band at ~ 0.8 eV, which might be consistent with the O3 atoms bridging the Ir_2 dimers. Moreover, the e_g states are split due to the strong distortion of the IrO_6 octahedra which appears to be manifested by the broadening of the $t_{2g} \rightarrow e_g$ excitation at high pressure observed in RIXS (Fig 3.14(a)).

In contrast to the $Fddd$ phase, incorporation of spin-orbit coupling does not show appreciable impact on the DOS of the $C2/c$ phase shown in Fig 3.15(d). The gap remains robust, and the bonding and antibonding states located at ~ -1.8 eV and ~ 0.8 eV, respectively, hold much of the d_{xz} character. Therefore, the J-state description is no longer convenient, evidencing that the spin-orbit coupling is not the energy scale governing the local electronic states. Instead, the direct hopping t between d orbitals dominates. Since the (d_{xy},d_{yz})-derived orbitals remain nearly degenerate in Fig 3.15(b), those become entangled and split by spin-orbit coupling as seen in the t_{2g}(1) and (2) states in Fig 3.15(d).

The molecular orbital formation can be understood by considering direct d-d hopping between d orbitals along the Ir_2 dimers. The d_{xy} and d_{yz} orbitals point away from the shortest Ir-Ir bond, and hence are full and inactive, while the d_{xz} orbital which points along that bond is half full on each Ir site. The direct d-d hopping between d_{xz} orbitals renders bonding σ and anti-bonding $\sigma*$ molecular orbital states. As a result, a molecular orbital scheme shown in Fig 3.15(f) is obtained. Two Ir sites contribute 5 d electrons each, filling the σ molecular orbital and the non-bonding (d_{xy}, d_{yz})-derived orbitals, giving a band insulator, which is consistent with the result in Fig 3.15(b) and (d). Incorporation of spin-orbit coupling entangles and splits the non-bonding orbitals. The presence of several filled bands between ~ -2 eV and ~ 0 eV in Fig 3.15(d) may account for the broad continuum stretching up to ~ 2 eV observed in RIXS (Fig 3.14(a)).

3.4 Discussion

The destruction of the $J_{\text{eff}} = 1/2$ state and molecular orbital formation under pressure evidences the competition between the spin-orbital entanglement and hopping-induced dimerisation in β-Li_2IrO_3. The spin-orbital entanglement dominates and overcomes the direct hopping, stabilising the $J_{\text{eff}} = 1/2$ state at ambient pressure. With increasing pressure , the anisotropic lattice distortion enhances direct d-d hopping in 1/3 of the Ir-Ir bonds, aiding the dimerisation and molecular orbital formation. The competition between spin-

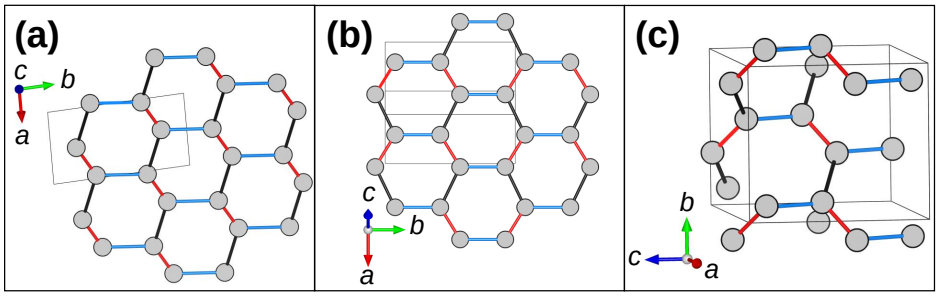

■ *Figure 3.16.* Examples of types of dimer pattern adopted in honeycomb systems with edge-sharing octahedra. The Z bonds of the respective ambient pressure structures are shown in blue, while the X and Y bonds are shown in black and red, where the red bond corresponds to the dimer. (a) Ladder pattern found in α-Li_2IrO_3 and α-$RuCl_3$. (b) Herringbone pattern found in Li_2RuO_3. (c) The 3D-analogue of a herringbone pattern found in β-Li_2IrO_3.

orbital entanglement and dimerisation is also supported theoretically, where it was found that in the absence of SOC, dimer formation should occur along the Z-type (symmetrically unique) Ir-Ir bond in β-Li_2IrO_3 [152] or Ru-Ru bonds α-$RuCl_3$ under pressure [164]. Indeed, this competition seems to be universal in honeycomb-based 4*d* and 5*d* materials with edge-sharing octahedra, including Kitaev materials. However, none of the Kitaev materials form dimers along the Z bonds, but rather the X or Y bonds. α-Li_2IrO_3 [165], α-$RuCl_3$ [167] and α-$MoCl_3$ ($4d^3$ with dimers along the Z bonds) [168] form a ladder pattern shown in Fig 3.16(a), while β-Li_2IrO_3 [161, 162] adopts a 3D version (Fig 3.16(c)) of the herringbone pattern shown in Fig 3.16(c) adopted by Li_2RuO_3 ($4d^4$). While the Kitaev (d^5 electron count) materials form molecular orbitals under pressure, Li_2RuO_3 and α-$MoCl_3$ readily dimerise at low temperatures and ambient pressure.

The dimerisation in β-Li_2IrO_3 occurs at $P_s \sim 3.7$ GPa at room temperature, however suppression of magnetic order is reported at pressures below ~ 2 GPa as seen in μSR and magnetic susceptibility [151] as well as in XMCD [115, 154] (Fig 3.8). Initially those results were interpreted as purely electronic effects due to lattice deformation, albeit without symmetry breaking, since the structural transition occurs only at higher pressures at room temperature. Recently Veiga *et al.* investigated the structural changes occurring in β-Li_2IrO_3 at high pressures and low temperatures, and it has been found that a structural transition takes place $P_s \sim 1.5$ GPa at $T = 50$ K [169]. In addition, the authors reported new structural phases at $T = 50$ K. With increasing pressure, $Fddd$ transforms into monoclinic $P2_1/n$ above ~ 1.5 GPa, where only 1/6 of the Ir-Ir bonds dimerise, which can be interpreted as a "precursor" to the fully dimerised high pressure phase [169]. With further increasing pressure above ~ 1.5 GPa, the fully dimerised $C2/c$ phase coexists with a *dimerised Fddd* phase, where in the latter the Z bond is the shortest one [169], which is interestingly in agreement with the theoretical

prediction [152]. Finally above $\sim$ 6 GPa, β-Li_2IrO_3 comprises pure dimerised $C2/c$ phase. Therefore, the pressure-induced suppression of magnetic order at high and low pressures and temperatures in β-Li_2IrO_3 can be associated with formation of molecular orbitals in Ir_2 dimers or dimer "precursors".

3.5 Conclusion

β-Li_2IrO_3 undergoes Ir_2 dimer formation at a pressure of $\sim$ 4 GPa, where the spin-orbital entangled $J_{\text{eff}} = 1/2$ state breaks down. Instead, pressure-enhanced direct *d-d* hopping between d_{xz} orbitals on neighbouring Ir sites generates bonding and anti-bonding molecular orbitals. Other honeycomb systems with edge-sharing octahedra, a geometry which favours direct *d-d* hopping that competes with the *d-p-d* hopping, also show dimer formation, often despite sizeable spin-orbit coupling. Therefore, the competition between spin-orbital entanglement and molecular orbital formation is universal in the honeycomb-based iridates and ruthenium chloride.

Chapter 4

$In_2Ir_2O_7$—a nearly pure $J_{\text{eff}} = 1/2$ Mott insulator

4.1 Introduction

The honeycomb network with edge-sharing octahedra discussed in chapter 3 provides a route for frustration via competing bond-dependent ferromagnetic couplings of $J_{\text{eff}} = 1/2$ pseudospins. Another route for frustration in interactions between $J_{\text{eff}} = 1/2$ states is a geometrically frustrated lattice, such as the pyrochlore lattice found in $A_2Ir_2O_7$. In recent years, pyrochlore iridates have been receiving a lot of attention as interplay between U and λ_{SOC} taking place on a frustrated lattice is expected to produce novel electronic states such as a *Weyl semimetal* (WSM) state with long-range all-in-all-out magnetic order [52]. The properties of pyrochlore iridates depend on the ionic radius of the A site which controls the Ir 5*d* bandwidth, through which the system is driven from metallic to insulating regime with decreasing size of A and increasing trigonal compression of IrO_6. While there has been considerable effort made towards identifying a WSM, little attention has been given to pyrochlore iridates in the strongly insulating limit, in particular the relevance of the $J_{\text{eff}} = 1/2$ in the large distortion limit. We discovered a new pyrochlore iridate $In_2Ir_2O_7$ with the smallest A ion and largest trigonal compression. Surprisingly, $In_2Ir_2O_7$ realises an almost pure $J_{\text{eff}} = 1/2$ state, while other pyrochlore iridates show strong mixing of $J_{\text{eff}} = 1/2$ and $J_{\text{eff}} = 3/2$ characters. We find distinct electronic structure of $In_2Ir_2O_7$ can be rationalised by the effect of the A-O bond covalency.

In section 4.1 we introduce the family of pyrochlore iridates and predicted exotic electronic states. In section 4.2 we outline the methods used in this work. We describe the physical properties of new pyrochlore iridate $In_2Ir_2O_7$ and the electronic structure elucidated with band structure calculations in section 4.3. In section 4.4, we discuss the implications of intersite hopping in pyrochlore iridates and the influence of In-O bond covalency on the electronic state of $In_2Ir_2O_7$.

The content presented in this chapter has been previously published in Ref. [170].

4.1.1 Properties of pyrochlore iridates

- **Distortion-tuned bandwidth**

  Pyrochlore iridates crystallise in the cubic $Fd\bar{3}m$ structure with a unit cell parameter $a \sim 10$ Å consisting of two interpenetrating pyrochlore networks of A and Ir cations (Fig. 4.1(a)). There exist two degrees of freedom in the crystal structure of pyrochlore iridates with chemical formula $A_2Ir_2O_7$: lattice parameter a and O1 x fractional coordinate, where both are scaled by the ionic size of the A cations r_A (refer to Appendix A for more detail). With decreasing r_A, the IrO_6 trigonal compression increases (as O1 x increases) and the Ir-O-Ir angles decrease as illustrated in Fig. 4.1(b). Small Ir-O-Ir angles reduce the hopping between the neighbouring Ir sites, which decreases the t_{2g} bandwidth. Accordingly, the electronic state and physical properties of pyrochlore iridates evolve with r_A [171, 172]. As shown in Fig. 4.1(d), for the largest reported r_A in the pyrochlore iridate family, $Pr_2Ir_2O_7$ is metallic down to the lowest temperatures [173, 174]. With decreasing r_A through to A = Nd, Sm and Eu, the system undergoes a metal-to-insulator transition with decreasing temperature and exhibits long-range magnetic order (Fig. 4.1(c) and Fig. 4.3(a)). Upon further reduction of the size of the A cation to Y or Lu, the system is insulating up to room temperature, while the magnetic ordering takes place only at low temperatures. We can now add the newly discovered pyrochlore iridate $In_2Ir_2O_7$ to this phase diagram. The onset of long range magnetic order T_m is suppressed for small r_A, which is expected as T_m should be scaled by the exchange interaction J_{ex} which should be proportional to the bandwidth.

- **$J_{eff} = 1/2$ state and the effect of trigonal distortion**

  The relevance of the $J_{eff} = 1/2$ state to pyrochlore iridates can be verified with RIXS experiments at Ir the L_3 edge. Similarly to honeycomb-based iridates (chapter 3), in A = Pr, Eu and Y pyrochlore iridates excitations around 1 eV are observed [85, 175] (Fig. 4.2(a)). In perfect cubic symmetry, one would expect one excitation within the t_{2g} manifold, that is the $J_{eff} = 3/2 \rightarrow J_{eff} = 1/2$ excitation. However, the Ir sites have D_{3d} symmetry and IrO_6 octahedra are trigonally compressed, which would lead to splitting of the $J_{eff} = 3/2$ states and their mixing with the $J_{eff} = 1/2$ states. Indeed, two distinct peaks are observed below 1.5 eV in all three compounds, and the splitting is of the order of 0.5 eV, about 2 times larger than those found in honeycomb-based iridates [126]. Therefore, the trigonal crystal field experienced by Ir atoms in pyrochlore iridates is significantly stronger than that found in the honeycomb analogues. Such a large trigonal crystal field should induce substantial mixing of the $J_{eff} = 3/2$ states with the $J_{eff} = 1/2$ ones, and that has indeed been observed in LDA band structure

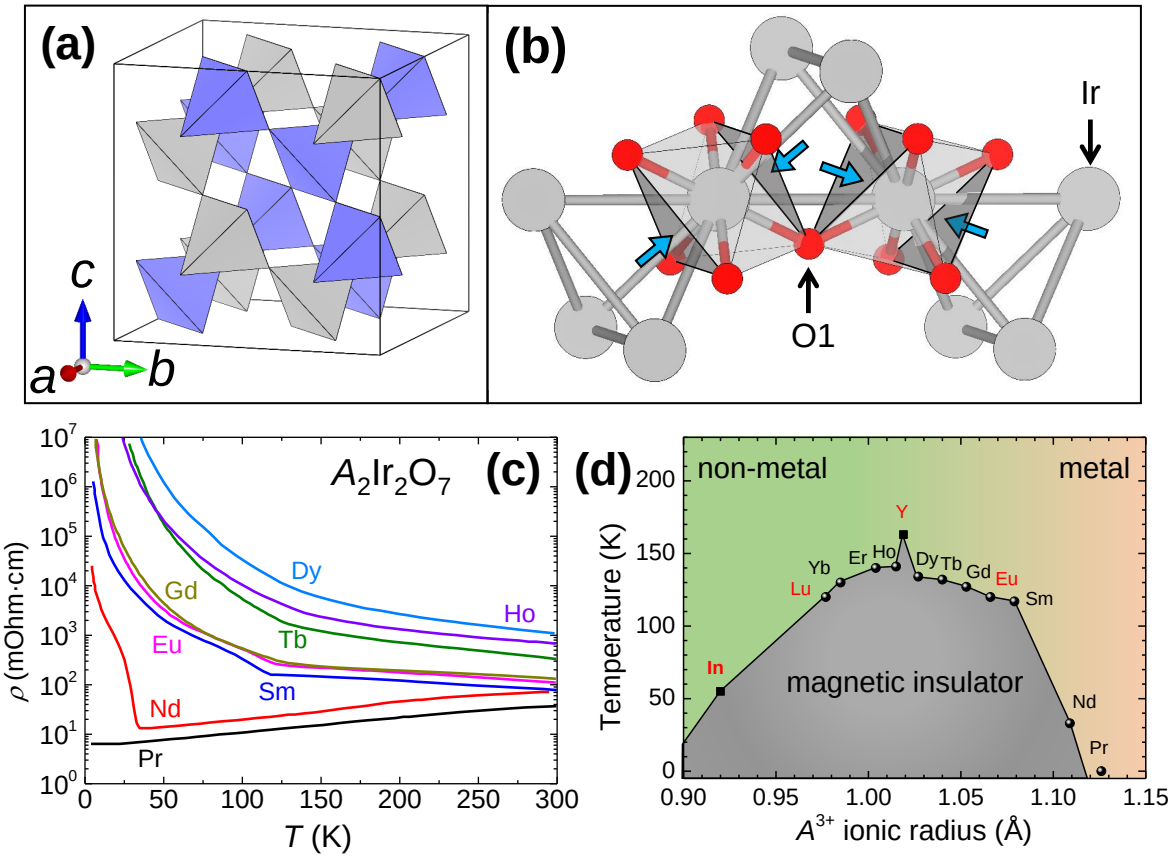

■ *Figure 4.1.* (a) The $Fd\bar{3}m$ unit cell showing two interpenetrating networks of Ir (grey) and A (purple) corner-sharing tetrahedra in the $A_2Ir_2O_7$ pyrochlores. (b) The geometry of the $Ir_2(O1)_6$ network. The axis of the trigonal compression is aligned with the local (111) directions of the Ir tetrahedra. The trigonal compression and the Ir-O-Ir angle depends on the O1 x fractional coordinate. (c) Temperature-dependent electrical resistivities $\rho(T)$ of $A_2Ir_2O_7$ for A = Pr, Nd, Sm, Eu, Gd, Tb, Ho and Dy. Figure reproduced from Ref. [172]. (d) Phase diagram for the pyrochlore iridates $A_2Ir_2O_7$ based on transport and magnetometry measurements as a function of the A^{3+} ionic radius. Circles and squares denote the transition temperature T_m. The A^{3+} cations that do not host any magnetic moment are shown in red colour, while the non-lanthanide A^{3+} cations are denoted by squares. A = In, the new member of the pyrochlore iridate family, is shown in bold. Figure reproduced and modified from Ref. [70, 172].

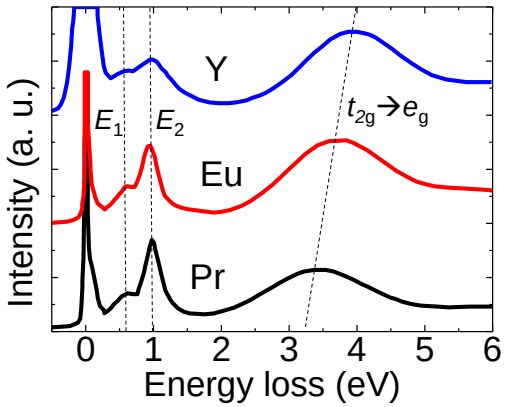

■ *Figure 4.2.* (a) RIXS spectra of $Pr_2Ir_2O_7$, $Eu_2Ir_2O_7$ [85] and $Y_2Ir_2O_7$ [175]. The E_1 and E_2 excitations correspond to the excitations from the split $J_{eff} = 3/2$ states to the $J_{eff} = 1/2$ state. Note that the data is reproduced from cumulative fits of RIXS spectra in Ref. [85, 175].

of $Y_2Ir_2O_7$ [176]. However, in the single ion approximation, the $|J_{eff} = 3/2, J^z_{eff} = \pm 3/2\rangle$ state remains pure and does not mix with the other two doublets as shown in Fig. 4.8(b). On the other hand, the band structure calculation in Ref. [176] shows that a sizeable weight of $|J_{eff} = 3/2, J^z_{eff} = \pm 3/2\rangle$ component emerges near the Fermi level, which indicates that other mechanisms could play a role in the character of the local electronic state.

▶ $J_{eff} = 1/2$ moment on pyrochlore lattice

Except for $Pr_2Ir_2O_7$, pyrochlore iridates are Mott insulators and show localised moment magnetism. In the magnetisation of pyrochlore iridates, a sharp anomaly appears at low temperatures [171, 172] (Fig. 4.3(a)), which correspond to long-range magnetic order as evidenced by a muon precession frequency developing below T_m [177–180] and anomalies in specific heat [171, 172]. The effective magnetic moment μ_{eff} of Ir^{4+} is not widely reported as most pyrochlore iridates host magnetically active A cations which make the Curie-Weiss fitting and extraction of μ_{eff} non-trivial. For non-magnetic A = Y and Lu, the μ_{eff} is $\sim 1.9\,\mu_B$ and $\sim 1.4\,\mu_B$ [170], respectively, which is close to the ideal value for $J_{eff} = 1/2$ or spin-only $S = 1/2$. The Curie-Weiss temperature θ_{CW} is $\sim -1200\,K$ and $\sim -725\,K$ for A = Y and Lu, respectively, which indicates dominant antiferromagnetic exchange and frustration.

Nearest neighbour Heisenberg antiferromagnetic exchange yields a spin liquid on a pyrochlore lattice in both classical [181] and quantum limits [182]. However, in the $Fd\bar{3}m$ $A_2Ir_2O_7$, the Ir-Ir bond has C_{2v} symmetry, which lacks inversion and introduces the antisymmetric Dzyaloshinskii-Moriya (DM) interaction. One can express the interactions between classical spins on the pyrochlore lattice as follows:

$$H = J \sum_{\langle ij \rangle} \boldsymbol{S}_i \cdot \boldsymbol{S}_j + \sum_{\langle ij \rangle} \boldsymbol{D}_{ij} \boldsymbol{S}_i \times \boldsymbol{S}_j, \tag{4.1}$$

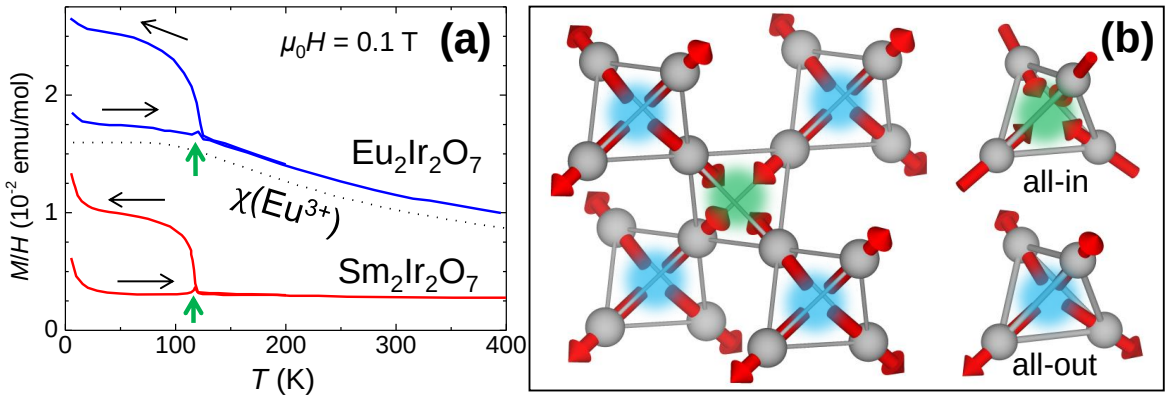

■ *Figure 4.3.* (a) Temperature dependent magnetic susceptibilities $M/H(T)$ of $A_2Ir_2O_7$ for A = Eu and Sm for applied magnetic fields of 0.1 T. The black arrows denote zero-field-cooling (→) and field-cooling (←) curves. The dotted line corresponds to the calculated contribution from the Van Vleck susceptibility of Eu^{3+} ion with $\lambda = 375$ K. The green arrows denote the magnetic transition temperature T_m. Figure reproduced from Ref. [172]. (b) All-in-all-out order on the pyrochlore lattice.

where J and $\boldsymbol{D}_{ij}$ are the isotropic antiferromagnetic Heisenberg and antisymmetric DM coupling between classical spins $\boldsymbol{S}_i$ and $\boldsymbol{S}_j$ on neighbouring sites i and j such as Ir nearest neighbours. In addition, spin-orbit coupling is large in pyrochlore iridates, and as the strength of the DM interaction is scaled by spin-orbit coupling [183], it should be relevant in these materials. The symmetry of the Ir tetrahedron is T_d and by using Moriya's rules [183] one can fix the orientation of a DM vector along one of the Ir-Ir bonds as illustrated in Fig. 4.4(a). However, it is not possible to determine the sign of a DM vector from symmetry arguments. The vectors on the other bonds can be obtained by applying T_d symmetry operations (while keeping in mind that the DM vector is a *cross product* of $\boldsymbol{S}_i$ and $\boldsymbol{S}_j$) which gives two possible configurations for positive and negative $\boldsymbol{D}$, which are referred to as "direct" and "indirect", respectively [184] (Fig. 4.4(b)). It is convenient to transform the Ir pyrochlore network into a new Bravais lattice where one whole Ir terahedron is a lattice point, or a "simplex" (as the one shown in Fig. 4.4(a)). Then, minimising equation 4.1 would give AIAO magnetic order for $\boldsymbol{D} > 0$ and non-coplanar and orthogonal magnetic orders for $\boldsymbol{D} < 0$ [185]. Fixing the magnetic order on one tetrahedron determines the configuration for the whole unit cell. In the AIAO magnetic order, which is shown in Fig. 4.3(b), spins align with the local (111), $(1, -1, -1)$, $(-1, -1, 1)$ and $(-1, 1, -1)$ (or equivalent) directions in the Ir tetrahedron, where all spins point either towards or away from the centre of the tetrahedron. The AIAO order is a $\boldsymbol{q} = 0$ order which breaks time-reversal symmetry, but not inversion symmetry, and it is discussed to be an essential ingredient for the Weyl semimetal state.

Pyrochlore iridates show ZFC-FC hysteresis in magnetisation, where small ferromagnetic

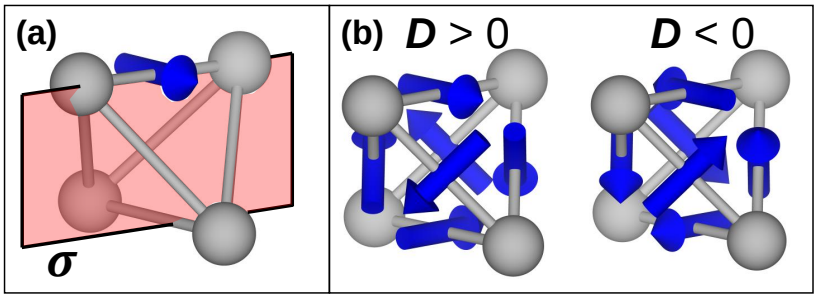

■ *Figure 4.4.* (a) The Ir tetrahedron has T_d point symmetry. One of the mirror planes shown in red determines the orientation of a DM vector shown in blue. (b) Two possible $\boldsymbol{D}$ configurations depicting the DM interaction on the pyrochlore lattice. Left and right are referred to as "direct" and "indirect", respectively. Reproduced from Ref. [184]

moment develops below T_m in the FC curve as illustrated in Fig. 4.3(a). For the AIAO magnetic order, two types of configurations related by time-reversal symmetry exist: all-in-all-out and all-out-all-in (AOAI) and the domain walls between those host a ferromagnetic moment [186–188], which could account for the small magnetic moment below T_m. $Eu_2Ir_2O_7$ and $Sm_2Ir_2O_7$ indeed realise the AIAO magnetic order as evidenced by resonant elastic x-ray scattering (REXS) [189] and magnon dispersions inferred from RIXS [190–192].

4.1.2 Topological semimetal in pyrochlore iridates

The Weyl semimetal is a solid-state analogue of Weyl fermions in high-energy physics. Weyl fermions emerge as solutions of the Weyl equation, which is a massless limit of the Dirac equation for relativistic fermions. As such, Weyl fermions are massless spin-1/2 particles and can be described with two-component wavefunctions in contrast to the four-component Dirac spinors. The equation can be separated such that the solutions are left- and right-handed spinors, i.e. they have a definite *chirality* [193].

In a Weyl semimetal, the Weyl fermions arise as low-energy excitations in linearly dispersing bands that intersect in a node called the Weyl point [193]. The nodal Weyl points imply that the spectrum of the Weyl semimetal is gapless. In the absence of either time-reversal symmetry (TRS) or crystal inversion symmetry (IS) the two chiralities are non-degenerate and the Weyl points split in momentum space. In the special case that both TRS and IS are preserved, there is only a single Weyl point which is equivalent to the Dirac semimetal (right side of Fig. 4.5(c)). On the surface, the projections of bulk Weyl nodes on the surface are connected by open curves called the "Fermi arcs" (left side of Fig. 4.5(c)). One of the important consequences of the WSM band structure is chiral anomaly, which occurs when simultaneously applied nonorthogonal electric and magnetic fields induce population imbalance

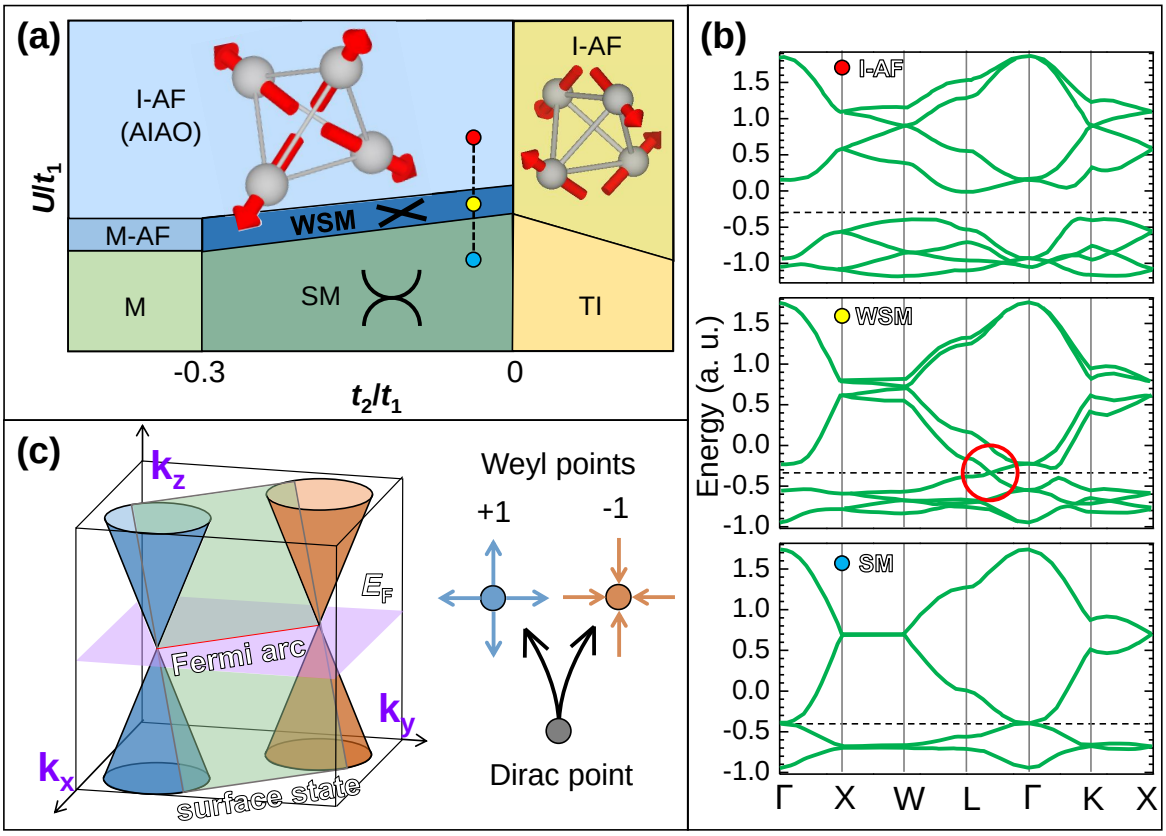

■ *Figure 4.5.* (a) Mean-field phase diagram of the Hubbard model in equation 4.2. The shaded regions show stabilised phases as a functions of U/t_1 and t_2/t_1: metal (M), insulating antiferromagnet (I-AF) with all-in-all-out order (AIAO), metallic antiferromagnet (M-AF), semimetal (SM), Weyl semimetal (WSM), topological insulator (TI). The I-AF phase in the positive t_2/t_1 limit corresponds to non-coplanar magnetic order where the spins are perpendicular to the local [111] Ir tetrahedron directions. The regions in blue have AIAO magnetic order. The three coloured circles connected with dashed lines correspond to the band structures shown in (b). Reproduced from Ref. [70]. (b) The evolution of the electronic structure as U increases as marked by the coloured circles in (a), from top to bottom: I-AF, WSM and SM. The Weyl point along the Γ-L direction is shown with a red circle. Dashed lines denote the Fermi level and the energy is given in arbitrary units. Reproduced from Ref. [70]. (c) Left: Weyl cones in three dimensions, where blue and orange colours indicate opposite chirality. The two Weyl cones are connected by chiral edge states (denoted as surface states shown in green). The Weyl points are connected by a Fermi arc. Reproduced from Ref. [52]. Right: Splitting of the Dirac point due to TRS or IR breaking into two Weyl points with opposite chirality (±).

of the two Weyl valleys with opposite chirality. The chiral anomaly is predicted to lead to negative magnetoresistance and exotic properties such as nonlocal transport and optical properties [193, 194]. The Fermi arcs are unique to the WSM state and hence are accepted as the experimental evidence of a WSM. Fermi arcs have been observed with surface-sensitive ARPES in non-centrosymmetric (broken IS) arsenides and phosphides [195–197]. Another route for WSM is breaking time-reversal symmetry.

Pyrochlore iridates were the first proposed materials to realise the WSM state via time-reversal symmetry breaking in AIAO magnetically ordered state with use of LDA+U DFT calculations [52]. This result was reproduced by phenomenological Hubbard model [198, 199]. All studies claim that the essential ingredients for realising a WSM state in $A_2Ir_2O_7$ is AIAO order of Ir moments and not too excessive correlations. Ref. [70] studied a minimal nearest-neighbour Hamiltonian:

$$H = \sum_{\langle ij \rangle} c_i^\dagger (t_1 + i t_2 \boldsymbol{d}_{ij} \cdot \boldsymbol{\sigma}) c_j + \frac{U}{2} \sum_i (n_i - 1)^2 \tag{4.2}$$

where the first and second terms are the kinetic and mean-field Hubbard terms, respectively. U is Coulomb repulsion, t_1 and t_2 are hopping parameters defined as combinations of direct and oxygen-mediated hoppings, $\boldsymbol{\sigma}$ is a vector of Pauli matrices acting on the pseudospin, $\boldsymbol{d}_{ij}$ is a real vector aligned along the opposite bond on the tetrahedron between i, j sites, $c_i^\dagger$ and c_j are electron creation and annihilation operators, respectively and n_i is spin density operator at site i for different possible spin configurations.

The resulting electronic structure as a function of direct hopping and correlation is illustrated in the phase diagram in Fig. 4.5(a). For some certain parameter range of direct hopping and weak correlation, the pyrochlore iridates realise a semimetallic state with quadratic band touching (bottom panel of Fig. 4.5(b)). With increasing correlation, the Ir moments become localised and AIAO magnetic order takes place and splits the degenerate bands into non-degenerate Weyl nodes with opposite chiralities with a total of four pairs (middle panel of Fig. 4.5(b)). With further increasing of U, the Weyl nodes migrate across the Brillouin zone closer to each other to finally annihilate, which generates a gapped phase with AIAO magnetic order shown in the top panel of Fig. 4.5(b).

$Pr_2Ir_2O_7$ with the largest r_A seems to realise the semimetallic phase as it is a bad metal with low carrier concentration [200], which implies a semimetallic state. Indeed, quadratic band touching has been identified by ARPES [173]. While for other pyrochlore iridates the magnetically active A^{3+} cations appear to interact weakly with the Ir^{4+} and order or freeze at temperatures lower than T_m [178], the Pr^{3+} $4f$ magnetic moments are reported to play an important role in the low energy properties and are discussed to exhibit chiral spin-liquid behaviour [174, 200, 201].

With decreasing r_A through to A = Nd, Eu Sm and Eu, and thus naïvely decreasing the bandwidth and increasing correlation, the system undergoes a metal to insulator transition with AIAO ordering. In both $Nd_2Ir_2O_7$ and $Eu_2Ir_2O_7$ a charge gap emerges below T_m [202, 203], suggesting that the two compounds locate in the large U/t_1 region of the phase diagram in Fig. 4.5(a). Accordingly, it has been discussed that correlation in pyrochlore iridates is too large and topologically trivial state is stabilised in the insulating phase [176, 204]. Nevertheless, $Nd_2Ir_2O_7$ and $Eu_2Ir_2O_7$ show indications of a semimetallic or narrow-gap semiconductor state in the high-temperature metallic regime as inferred from optical conductivity [203, 205] and quadratic band touching similar to that of $Pr_2Ir_2O_7$ identified in ARPES [206]. Therefore, even though $Nd_2Ir_2O_7$ and $Eu_2Ir_2O_7$ are insulators, there exists a chance these compounds could be tuned towards a WSM state. Indeed, the MIT is suppressed by application of pressure [202, 207] or doping with Rh [203]. However, ARPES measurements, essential for identification of a WSM state, are lacking.

Attempts to stabilise a WSM state in $Nd_2Ir_2O_7$ with external magnetic field have also been reported [207–209]. When the magnetic field is applied along the [001] crystallographic direction, an insulator to semimetal transition occurs, while the AIAO order of Nd^{3+} moments switches to 2-in-2-out configuration above $\sim 10\,T$. On the other hand, when the magnetic field is applied along the [111] crystallographic direction, a 3-in-1-out configuration is stabilised. The phase with 2-in-2-out configuration is discussed to realise a nodal-line semimetal state [207, 209], while the 3-in-1-out phase is suggested to generate yet another type of WSM phase [209].

4.1.3 Validity of $J_{eff} = 1/2$ state in the limit of strong non-cubic crystal field

Pyrochlore iridates appear to be an exciting platform for exploration of quantum magnetism, Weyl semimetal and related phases according to theoretical predictions and recent experimental observations under pressure and magnetic field. The AIAO magnetic order has been established for $A_2Ir_2O_7$ with relatively large A cations such as Eu or Sm, however the strongly distorted region of the phase diagram has not been investigated in that context so far. In addition, a general understanding of the electronic structure of pyrochlore iridates has been lacking, especially with respect to the influence of large trigonal crystal field on the character of the $J_{eff} = 1/2$ states. The magnitude of the trigonal crystal field appears to be comparable ($\sim 0.3\,eV$) to that of spin-orbit coupling ($\sim 0.4\,eV$). While the pioneering DFT study in principle takes such aspects into account [52], the tight-binding models do not [70]. The role of $J_{eff} = 3/2$ states mixing into the $J_{eff} = 1/2$ band could play an important role in the properties of pyrochlore iridates. In addition, in the large trigonal distortion limit, the $J_{eff} = 1/2$ description could be invalid. It is therefore of interest to explore new pyrochlore

iridates in the large trigonal crystal field limit and examine the validity of $J_{eff} = 1/2$ character. In search of new pyrochlore iridates with large trigonal distortion, we discovered a new, most distorted pyrochlore iridate $In_2Ir_2O_7$.

4.2 Methods

4.2.1 Sample preparation

The polycrystalline samples of $In_2Ir_2O_7$ were obtained by a high-pressure synthesis technique (section 2.1.2). Powders of In_2O_3 (Alfa Aesar, 99.994 % metal basis) and IrO_2 (Tanaka Kikinzoku, 86 wt.% Ir content) were mixed and ground in stoichiometric molar ratios, and sealed in a platinum-foil ampoule. The ampoule was heated at 1500 °C for 30 minutes under pressure of 6 GPa in a cubic anvil press, and quenched to room temperature.

4.2.2 Powder x-ray diffraction and analysis

X-ray powder diffraction data of the powdered $In_2Ir_2O_7$ sample were collected at room temperature with a Stoe Stadi-P transmission diffractometer (primary beam Johann-type Ge(111) monochromator for Ag-$K\alpha_1$-radiation, Mythen-1K PSD) in Debye-Scherrer geometry with the sample sealed in a glass capillary of 0.5 mm diameter (Hilgenberg, glass No. 50). The powder pattern was recorded for 24 h in the 2θ-range from 2 to 9° with a step width of 0.02°. The sample was spun during measurement for better particle statistics. Rietveld refinement was performed with TOPAS6 [81].

4.2.3 Resonant inelastic x-ray scattering

The resonant inelastic x-ray scattering (RIXS) measurement was performed on a polycrystalline pellet of $In_2Ir_2O_7$ at BL11XU beamline of SPring-8. The energy of incident x-rays was tuned at 11.215 eV, which is about 3 eV below the peak energy of the white line in the x-ray absorption spectrum at the Ir L_3-edge. This energy corresponds to the excitation of Ir $2p_{3/2}$ to $5d\ t_{2g}$. The incident x-ray beam was monochromised by a double-crystal Si(111) monochromator and a secondary Si(844) four-crystal monochromator. The scattering angle (2θ) was fixed at 90° and π-polarised incident x-rays were used in order to minimise the elastic scattering. The scattered x-rays were analysed by a diced and spherically-bent Si(844) crystal. The measurement was performed at 7 K and the total energy resolution, evaluated by the elastic scattering of amorphous thin tape, was about 50 meV. The least squares fitting of the RIXS spectrum of $In_2Ir_2O_7$ was performed using a method described in section 2.3.1.

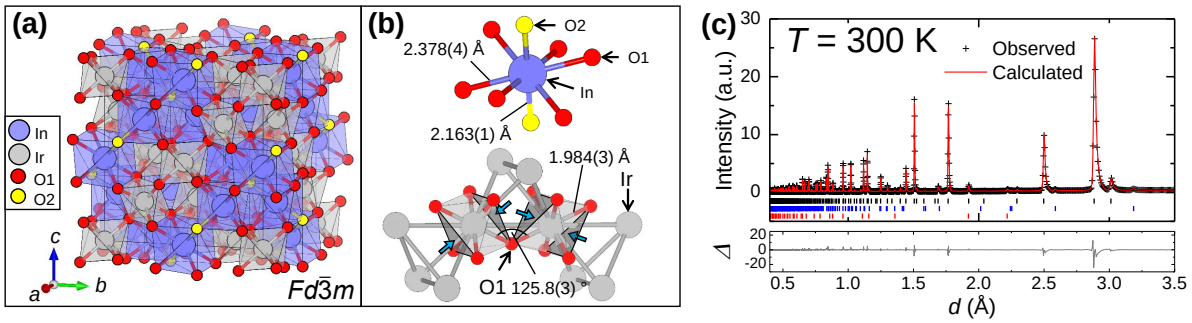

■ *Figure 4.6.* The crystal structure of $In_2Ir_2O_7$. The O2 atoms, which coordinate the In atoms only, are shown in yellow. (a) The $Fd\bar{3}m$ unit cell. (b) Top: the local environment of the In atom showing six long In-O1 and two short In-O2 bonds. Bottom: the local environment of Ru atoms on top of the pyrochlore lattice. The blue arrows indicate the direction of the trigonal compression. In pyrochlore iridates, the trigonal compression axis runs along the (111)-like directions of the Ir tetrahedron. (c) Rietveld analysis of XRD pattern of polycrystalline $In_2Ru_2O_7$ collected with Ag-$K\alpha_1$ radiation at room temperature. The black crosses, red line and grey line represent the observed pattern, the calculated profile and the difference curve between the observed and calculated profiles, respectively. The blue, red and black bars correspond to reflection positions of $In_2Ir_2O_7$, IrO_2 and Ir, respectively.

4.2.4 Band structure calculations

The LDA band structure calculations were performed using the method described in section 2.5.1 and the crystal structures obtained from the x-ray diffraction experiment.

4.3 Results

4.3.1 New pyrochlore iridate with frustrated magnetism

The $In_2Ir_2O_7$ sample was stable in air and it consisted of $In_2Ir_2O_7$ (97.81(10) wt.%), IrO_2 (1.26(8) wt.%) and Ir (0.93(5) wt.%) as determined by Rietveld analysis, shown in Fig. 4.6(c). $In_2Ir_2O_7$ crystallises in the cubic pyrochlore structure with the space group $Fd\bar{3}m$ (Fig. 4.6(a)). As expected from the smallest cation radius of In^{3+} of 0.92 Å, $In_2Ir_2O_7$ has the smallest unit cell constant of 9.9884(4) Å, the largest trigonal compression of IrO_6 octahedra and the smallest Ir-O-Ir angle of 125.8(3)° among reported pyrochlore iridates (Fig. 4.6(b)). The refined structural parameters are displayed in Table 4.1. As discussed in chapter 1, the degree of trigonal distortion in cubic pyrochlores can be parameterized by the x fractional coordinate of the O1 atom. $x_c = 5/16$ corresponds to the case of a regular IrO_6 octahedron, which produces an Ir-O-Ir angle of $\sim 141°$. $x > x_c$ corresponds to trigonal compression and an Ir-O-Ir angle smaller than $\sim 141°$, commonly found in pyrochlore iridates. $x = 0.3405(5)$ for $In_2Ir_2O_7$ yields the largest trigonal compression and the smallest Ir-O-Ir angle of 125.8(3)° among pyrochlore

■ *Table 4.1.* Refined structural parameters of $In_2Ir_2O_7$ at room temperature. The space group is $Fd\bar{3}m : 2$ (No. 227) and $Z = 8$. The lattice constant a is 9.9884(4) Å. g corresponds to occupancy. The isotropic displacement parameter U_{iso} converged to 0.0(1) Å for all atoms. $R_{wp} = 0.0562$ and $\chi = 1.99$ for 6 refined parameters.

Atom	Site	x	y	z	g
In	$16d$	1/2	1/2	1/2	1
Ir	$16c$	0	0	0	1
O1	$48f$	0.3405(5)	1/8	1/8	1
O2	$8b$	3/8	3/8	3/8	1

iridates. This implies that $In_2Ir_2O_7$ has relatively small $5d$ bandwidth and represents the insulating limit of the family of pyrochlore iridates.

$In_2Ir_2O_7$ shows insulating behaviour as evident from the resistivity measurement shown in Fig. 4.7(a), which is consistent with the expected small bandwidth due to the small Ir-O-Ir angle. The Arrhenius fit displayed in the inset of Fig. 4.7(a) shows that the activation energy around room temperature is $\sim$ 100 meV, which is comparable to those of strongly insulating Ir oxides such as Ba_2IrO_4 and α-Li_2IrO_3 [116, 210]. Magnetic susceptibility $M/H(T)$ in Fig. 4.7(b) shows a Curie-Weiss behaviour on cooling from high temperatures. The magnetic response originates from the $5d$ electrons of Ir^{4+} as In^{3+} is non-magnetic. The Curie-Weiss fit between 350 K and 600 K shown in the inset of Fig. 4.7(b) yields an antiferromagnetic $\theta_{CW} = -443(7)$ K and an effective magnetic moment μ_{eff} of 1.72(1) μ_B. The effective moment is close to that of $J_{eff} = 1/2$ (or $S = 1/2$) state with $|g| = 2$, which implies that the admixture of $J_{eff} = 3/2$ and other states is not appreciably large. The Curie-Weiss temperature of $|\theta_{CW}| \sim 450$ K may represent the strength of exchange coupling, which is smaller than those of other insulating pyrochlore iridates such as $Y_2Ir_2O_7$ ($\sim$ 1180 K) and $Lu_2Ir_2O_7$ ($\sim$ 725 K) [170]. This likely reflects the smaller intersite hopping t expected in the strongly distorted Ir-O network, since the exchange coupling J_{ex} is scaled by t^2 as $J_{ex} \sim t^2/U$.

At $T_m = 55$ K, an anomaly accompanying a hysteresis between the field-cooling and the zero-field-cooling measurement is observed. The history-dependent contribution originates from a weak ferromagnetic moment of $\sim 10^{-4}$ μ_B. In the specific heat $C(T)$ shown in Fig. 4.7(c), we observe a clear jump at the onset temperature of the weak ferromagnetic moment, evidencing that the magnetic anomaly does not originate from a impurity ferromagnetic phase but represents a bulk magnetic transition. Similar behaviour was observed in other pyrochlore iridates such as $Y_2Ir_2O_7$, where an AIAO magnetic ordering of iridium moments takes place at T_m [211]. The small moment below T_m in pyrochlore iridates is discussed to originate from the AIAO domain boundaries [186–188]. This suggests that $In_2Ir_2O_7$ also adopts the AIAO

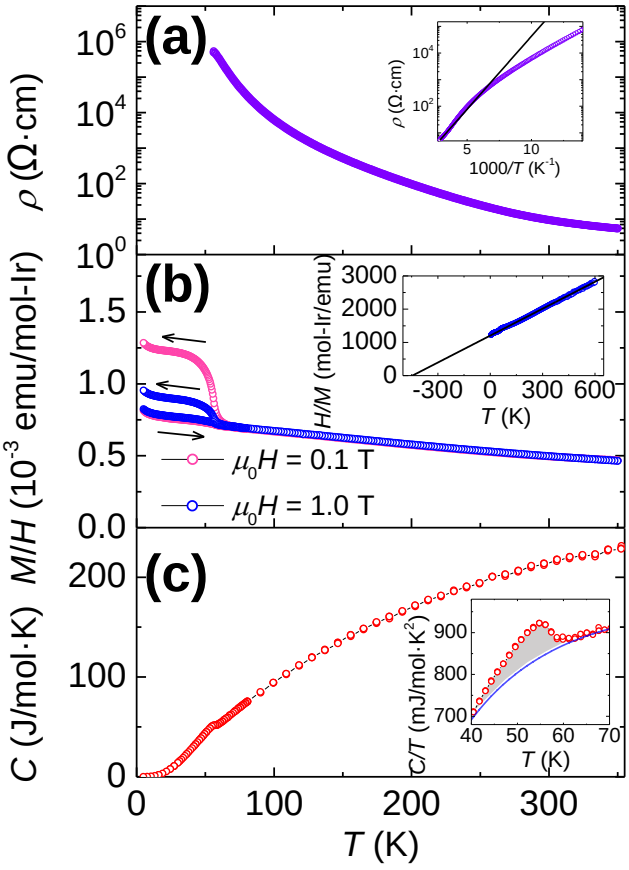

■ *Figure 4.7.* Temperature-dependent transport, magnetisation and specific heat measurements of $In_2Ir_2O_7$. (a) Resistivity as a function of temperature. The inset shows the Arrhenius plot of resistivity and the black line indicates the fit at high temperature. Below ~ 50 K, the resistance of $In_2Ir_2O_7$ sample is higher than the instrument limit. (b) Magnetic susceptibility M/H as a function of temperature for applied magnetic fields of 0.1 T and 1.0 T. The black arrows denote zero-field-cooling (→) and field-cooling (←) curves. The inset shows temperature dependence of inverse magnetic susceptibility. The black line indicates the Curie-Weiss fit. (c) Specific heat as a function of temperature. The inset shows the specific heat divided by temperature around the observed anomaly at T_m 55 K, where the blue line and the grey area correspond to the third-order polynomial fit and area used for estimation of entropy, respectively, which is discussed in the main text.

order.

The large ratio $f = |\theta_{\text{CW}}|/T_{\text{m}} \sim 8$ implies the presence of strong frustration, as expected from the frustrated pyrochlore lattice. Due to the lack of specific heat data from a non-magnetic reference sample (such as $In_2Pt_2O_7$ or $In_2Sn_2O_7$), it is not possible to accurately estimate the phonon contribution to the specific heat. However, we attempt to estimate the lattice contribution by fitting a third-order polynomial to C/T below and above T_{m}. We then subtract the obtained polynomial function from the C/T data and estimate the area of the specific heat peak at T_{m}, which amounts to released entropy of about $\sim 20\,\%$ of $R \ln 2(R \ln(2J_{\text{eff}} + 1))$ expected for the $J_{\text{eff}} = 1/2$ state (inset of Fig. 4.7(c)). The entropy release which is much smaller than the expected value implies that the magnetic correlation develops from higher temperatures but frustration prevents long-range order. The Curie-Weiss temperature of $\theta_{\text{CW}} \sim -450\,\text{K}$ implies that correlations start developing at temperatures of the order of 450 K and from that temperature the magnetic entropy is likely to be slowly released with cooling, and consequently the magnetic transition does not release 100 % of the expected entropy. We cannot estimate the entropy released outside of the transition at T_{m} as with the polynomial fit we exclude all magnetic contributions to the specific heat outside of T_{m}.

4.3.2 Reduced trigonal crystal field in $In_2Ir_2O_7$ despite larger IrO_6 distortion

In order to study the orbital states of $In_2Ir_2O_7$, we performed a RIXS measurement at the Ir L_3 absorption edge shown in Fig. 4.8(a). In addition to the elastic peak, we observe three clear features at 0.48(1) eV, 0.86(1) eV and 4.14 eV. The two sharp peaks located below 1 eV correspond to excitations within the t_{2g} manifold, while the one at 4.14 eV corresponds to excitations from the t_{2g} to e_g manifold. In the absence of distortion in an isolated IrO_6 octahedron, only one excitation peak from $J_{\text{eff}} = 3/2$ to $J_{\text{eff}} = 1/2$ would be observed within t_{2g} manifold. The presence of two sharp excitations implies the splitting of $J_{\text{eff}} = 3/2$ quartet into two Kramers doublets (ϵ_1 and ϵ_2 in Fig. 4.8(d)), as observed in other pyrochlore iridates [175, 212, 213]. The widths of the two low-energy peaks in the RIXS spectrum of $In_2Ir_2O_7$ ($\sim$ 200 meV) are significantly smaller than those of other reported pyrochlore iridates ($\sim$ 300 meV), likely reflecting the smaller bandwidth as identified in the band structure calculations shown below.

The energy difference of the two low-lying peaks, $\Delta E = E_2 - E_1$, represents the splitting of the $J_{\text{eff}} = 3/2$ manifold. We may ascribe the splitting to the trigonal crystal field originating from compression of IrO_6. As the strength of this trigonal field can be parameterised by the deviation of the x coordinate of O1 atom from the ideal value ($\Delta x = x - x_{\text{c}} = x - 0.3125$), the magnitude of splitting is expected to scale with Δx. In Fig. 4.8(c), ΔE for $In_2Ir_2O_7$ is compared with those for $Y_2Ir_2O_7$ and $Pr_2Ir_2O_7$ with smaller Δx. We find that ΔE does not

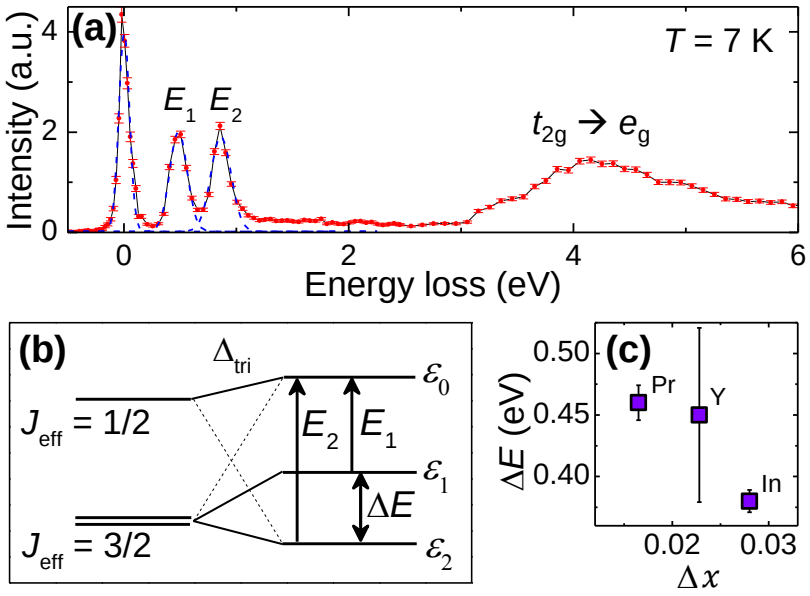

■ *Figure 4.8.* (a) Ir L_3-edge RIXS spectrum of $In_2Ir_2O_7$ polycrystalline sample at $T = 7$ K with incident energy $E_i = 11\,215$ eV. The Gaussian fits of the peaks are represented by a dashed blue line. The excitations labelled as E_1 and E_2 correspond to the ones depicted in (b). (b) The effect of trigonal compression of TM octahedron on the local electronic J_{eff} states producing three Kramers doublets (ϵ_0, ϵ_1 and ϵ_2) in the single ion anisotropy description. The $J_{eff} = 3/2$ quartet splits into two doublets, ϵ_1 and ϵ_2, and the ($J_{eff} = 1/2$)-derived state is ϵ_0. ϵ_0 and ϵ_2 are mixtures of the original $J_{eff} = 1/2$ and $J_{eff} = 3/2$ states. (c) The energy split $\Delta E = E_2 - E_1$ against Δx for $A_2Ir_2O_7$, where A = Pr [212], Y [175] and In.

depend on Δx appreciably and even decreases with increasing Δx. This implies that $In_2Ir_2O_7$, the pyrochlore iridate with the most distorted IrO_6 octahedra among the three compared compounds, experiences the smallest trigonal crystal field.

To describe the excitations observed below 1 eV and estimate the magnitude of λ_{SOC} and Δ_{tri}, we employed a standard Hamiltonian for a t_{2g}^5 configuration with Hund's coupling J_H, spin-orbit coupling λ_{SOC} and compressive trigonal field Δ_{tri}. We start by defining the on-site electron configuration of Ir^{4+}. The d^5 electron configuration is subject to an octahedral crystal field from the O_6 cage. Since the t_{2g}-e_g splitting (Δ_o) is of the order of ~ 4 eV and we expect $J_H < 1$ eV, we assume the $\Delta_o = 10\,Dq \gg J_H$ and exclude e_g orbitals. The five electrons reside in the t_{2g} manifold with a $L_{eff} = 1$, $S = 1/2$ configuration. For convenience, we then start with the LS coupling limit, which first gives the $|S = 1/2, L_{eff} = 1\rangle\ ^2P$ configuration as the only Hund multiplet. Next, λ_{SOC} splits the ^2P multiplet into $J_{eff} = 1/2$ doublet and $J_{eff} = 3/2$ quartet with $J_{eff} = 1/2$ as the lowest energy state. Finally, the trigonal crystal field Δ_{tri} lifts the degeneracy of $J_{eff} = 3/2$ states and mixes them with $J_{eff} = 1/2$ states, producing three

■ *Table 4.2.* Comparison of structural and electronic parameters for $A_2Ir_2O_7$, where A = Pr, Y and In. $r_{A^{3+}}$ is the ionic radius of A^{3+}, Δx represents the degree of the trigonal distortion of IrO_6 octahedra and $\Delta E = E_2 - E_1$ inferred from RIXS spectra. λ_{SOC} and Δ_{tri} are spin-orbit coupling and trigonal crystal field, respectively, in the case of $In_2Ir_2O_7$ obtained from the fitting of the Kanamori Hamiltonian to the RIXS data.

Compound	$r_{A^{3+}}$	Δx	ΔE (eV)	λ_{SOC} (eV)	Δ_{tri} (eV)
$Pr_2Ir_2O_7$ [175]	1.126	0.016 [214, 215]	0.46(2)	0.42	0.57
$Y_2Ir_2O_7$ [212]	1.019	0.0228 [216]	0.45(7)	0.43	0.56
$In_2Ir_2O_7$	0.92	0.028	0.38(1)	0.38	0.48

doublets as shown in Fig. 4.8(b). The energies of the three doublets depend on λ_{SOC} and Δ_{tri}:

$$\epsilon_1 = \Delta_{tri} - \frac{\lambda}{2}, \tag{4.3}$$

$$\epsilon_{0,2} = \frac{\Delta_{tri}}{2} + \frac{\lambda}{4} \pm \frac{1}{4}\sqrt{4\Delta_{tri}^2 + 4\Delta_{tri}\lambda + 9\lambda^2}, \tag{4.4}$$

where ϵ_0 corresponds to the ($J_{eff} = 1/2$)-derived state which mixes with that of $J_{eff} = 3/2$, ϵ_1 is the ($J_{eff} = 3/2$)-derived state which does not mix with $J_{eff} = 1/2$, and ϵ_2 is the ($J_{eff} = 3/2$)-derived state which is mixed with $J_{eff} = 1/2$, as shown with the dashed lines in Fig. 4.8(b). By fitting relevant parameters in H_{total} (section 2.3.1) to the observed peak positions, we obtain the values of $\lambda_{SOC} \sim 380$ meV and $\Delta_{tri} \sim |480$ meV| (compressive trigonal distortion).

In Table 4.2, Δ_{tri} for $In_2Ir_2O_7$ is smaller than those reported in $Pr_2Ir_2O_7$ and $Y_2Ir_2O_7$, as expected from the smaller ΔE inferred from RIXS (Fig. 4.8(a)). λ_{SOC} also appears to be the smallest for $In_2Ir_2O_7$. However, those values should be taken with caution, as reported RIXS spectra for $Pr_2Ir_2O_7$ [175] and $Y_2Ir_2O_7$ [212] exhibit broad, overlapping peaks below 1 eV, which should give larger peak position uncertainty in contrast to the well separated d-d excitations observed in $In_2Ir_2O_7$. Nevertheless, the lack of scaling of ΔE and the obtained Δ_{tri} with Δx implies that long-range trigonal crystal field originating from A^{3+} and Ir^{4+} cations contributes to the splitting of $J_{eff} = 3/2$ states.

▶ Limitations of the single ion t_{2g}^5 model

Despite the successful fitting of the single ion t_{2g}^5 model to the RIXS data of $In_2Ir_2O_7$, there exist several possible improvements to the fits. Exclusion of e_g states is acceptable when $10\,Dq \gg J_H$. In reality, $10\,Dq \sim 16J_H$ (reported $J_H \sim 0.25$ eV for d^4 iridate double perovskite [217]) which can induce mixing of t_{2g} and e_g states.

In addition, the observed RIXS spectra from powder samples capture $\boldsymbol{q}$-averaged d-d excitations. If significant dispersion of those excitations exists, the single ion model used here is not appropriate for extraction of λ_{SOC} and Δ_{tri}. However, the RIXS spectra of single crystal of $Eu_2Ir_2O_7$ (which we do not compare here due to conflicting reported structural

data [214, 215, 218, 219] likely due to known sample quality and stoichiometry issues [220]) do not show any appreciable momentum dependence of the the *d*-*d* excitations within the given resolution [212].

4.3.3 Nearly pure $J_{eff} = 1/2$ state in $In_2Ir_2O_7$

In order to clarify the combined effects of spin-orbit coupling, trigonal crystal field and intersite hopping on Ir 5*d* t_{2g} states, band structure calculations were performed for Mott-insulating $A_2Ir_2O_7$ for A = In, Lu and Y. $Y_2Ir_2O_7$ [216] has the least trigonally compressed IrO_6, while $Lu_2Ir_2O_7$ [219] and $In_2Ir_2O_7$ host nearly identical trigonal distortion. Neither Y^{3+} nor Lu^{3+} carry magnetic moments. The density of the Ir t_{2g} states (DOS) projected onto $J = 5/2$ ($J_{5/2}$) and $J = 3/2$ ($J_{3/2}$) states are shown in Fig. 4.9. For more detail on the results of the band structure calculations on $A_2Ir_2O_7$, visit Appendix B. Since the on-site Coulomb repulsion U is not incorporated, the calculations produce a metallic ground state for all three materials.

The pure $J_{eff} = 1/2$ wave function comprises only the $J_{5/2}$ states while $J_{eff} = 3/2$ wave function consists of both $J_{5/2}$ and $J_{3/2}$. Figure 4.9 shows that the states within ± 0.4 eV near E_F have $J_{eff} = 1/2$ character, while those below -0.4 eV are $J_{eff} = 3/2$ ones. Nonetheless, a sizeable $J_{3/2}$ weight near E_F is present, indicative of an admixture of the $J_{eff} = 3/2$ component to the $J_{eff} = 1/2$ states. Naïvely, one would expect the level of mixing of the $J_{eff} = 1/2$ and $J_{eff} = 3/2$ to be scaled by the degree of the trigonal compression of IrO_6 octahedra. Therefore, there should be more $J_{eff} = 3/2$, and consequently $J_{3/2}$, weight near E_F in $In_2Ir_2O_7$ and $Lu_2Ir_2O_7$ as compared to $Y_2Ir_2O_7$.

A comparable contribution of $J_{3/2}$ states appears in $Lu_2Ir_2O_7$ and $Y_2Ir_2O_7$, despite the larger distortion in the former. The $J_{eff} = 3/2$ weight around E_F is appreciably smaller in $In_2Ir_2O_7$ than not only that of $Y_2Ir_2O_7$, but also of $Lu_2Ir_2O_7$ with a comparable trigonal distortion, pointing to distinct formation of almost pure $J_{eff} = 1/2$ state in $In_2Ir_2O_7$. The t_{2g} bands of $In_2Ir_2O_7$ are narrower (~ 1.7 eV) than those of $Lu_2Ir_2O_7$ (~ 2.0 eV) despite a comparable magnitude of trigonal distortion and Ir-O-Ir angle. The origin of the contrast of the bandwidth and the orbital character between $In_2Ir_2O_7$ and $Lu_2Ir_2O_7$, despite nearly the same degree of trigonal distortion, has yet to be addressed. The intersite hopping and the covalency of the *A*-O bonds likely play an important role in fostering the ground state of pyrochlore iridates.

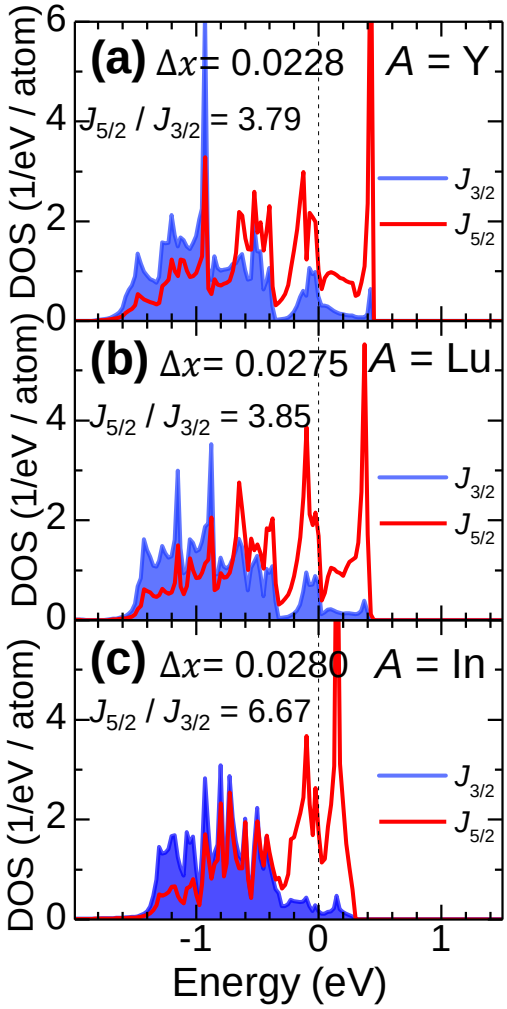

■ *Figure 4.9.* $J_{3/2}$ and $J_{5/2}$ resolved DOS for Ir t_{2g} bands in $A_2Ir_2O_7$ for A = (a) Y, (b) Lu and (c) In. The area beneath the curve of $J_{3/2}$-derived DOS is filled for clarity. The Fermi level E_F is indicated by dashed black lines. The ratio of the area under the $J_{5/2}$- and $J_{3/2}$-derived DOS curves within ±0.5 eV of E_F (±0.4 eV for A = In) is shown.

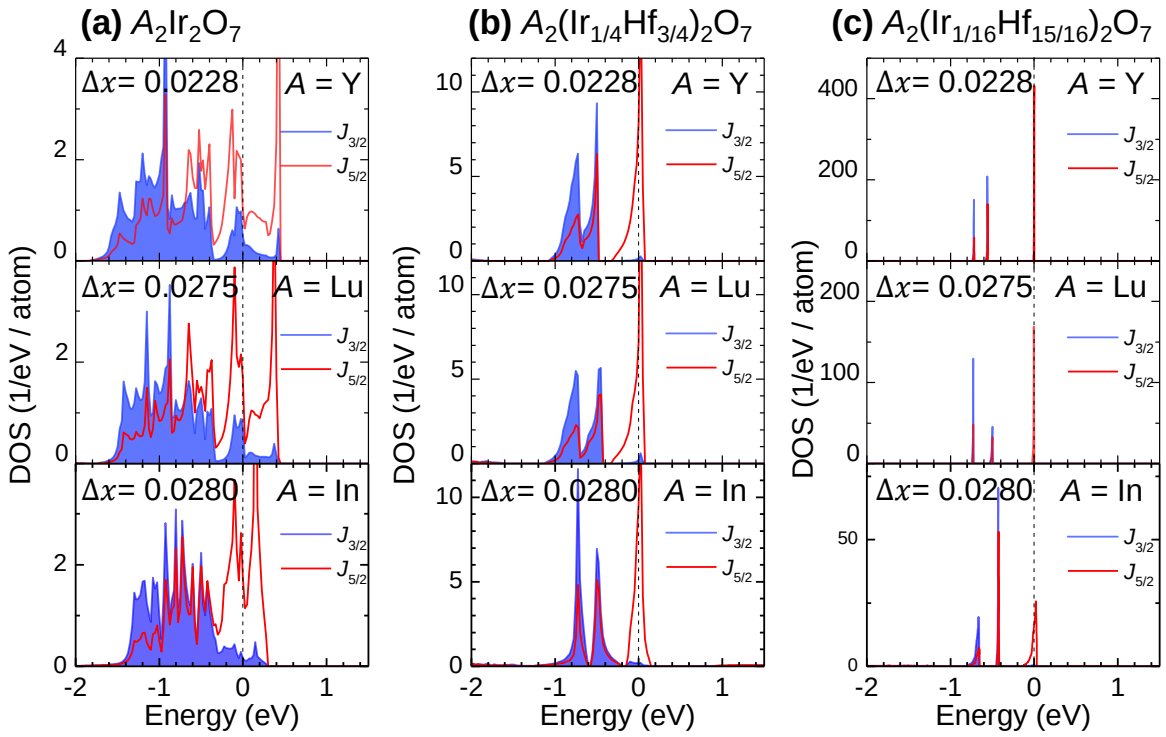

■ *Figure 4.10.* $J_{3/2}$ and $J_{5/2}$ resolved DOS for Ir t_{2g} bands for (a) $A_2Ir_2O_7$, (b) $A_2(Ir_{1/4}Hf_{3/4})_2O_7$ and (c) $A_2(Ir_{1/16}Hf_{15/16})_2O_7$. The top, middle and bottom panels correspond to A = Y, Lu and In, respectively. The area beneath the curve of $J_{3/2}$-derived DOS is filled for clarity. The Fermi level E_F is indicated by dashed black lines. The $J_{5/2}/J_{3/2}$ ratio discussed in the main text and shown in Fig. 4.11(a) was measured within (a) ±0.5 eV (±0.4 eV for A = In), (b) ±0.4 eV (±0.2 eV for A = In) and (c) ±0.2 eV.

4.4 Discussion

4.4.1 Influence of intersite hopping

To verify our hypothesis and to understand the effect of intersite hopping on the orbital character of Ir t_{2g} states, we performed band structure calculations for model pyrochlore iridates with suppressed Ir d-d hopping. Intersite hopping was reduced by replacing some of the Ir atoms by Hf atoms with $5d^0$ configuration, where the Hf $5d$ states are located at energies significantly higher than those of Ir (a difference of approximately $\sim$ 6 eV). This was achieved by reducing the symmetry of the $Fd\bar{3}m$ $A_2Ir_2O_7$ structure (with symmetry allowed displacements set to 0) and splitting the 16-fold Ir sites and replacing some of them by Hf atoms, hence selectively switching off intersite hopping for a certain neighbour rank. The neighbour rank was scaled by Ir-Ir distance. The calculations were performed without Coulomb U, and thus the metallic ground states were obtained.

First, we demonstrate the effect of gradual reduction of intersite hopping in the model

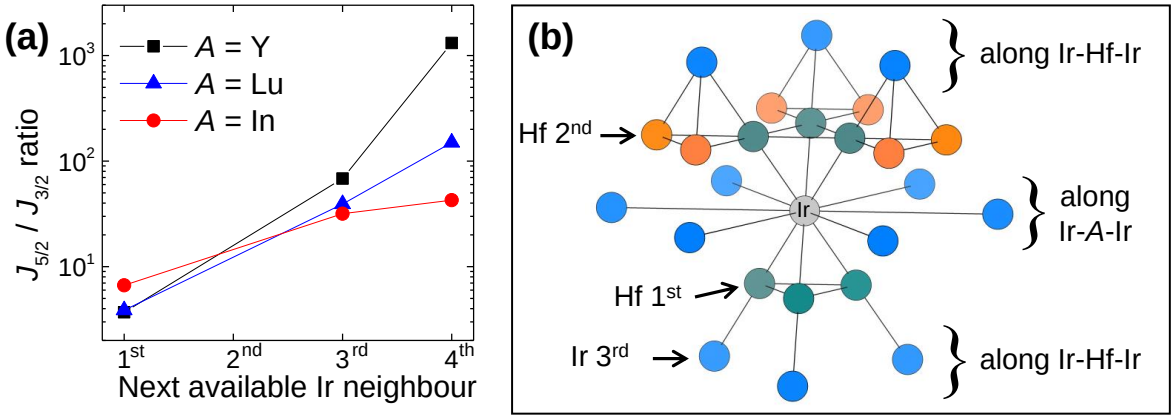

■ *Figure 4.11.* (a) Dependence of the $J_{eff} = 1/2$ character, expressed as a $J_{5/2}/J_{3/2}$ ratio, on the closest Ir neighbours available for intersite hopping: 1st ($A_2Ir_2O_7$), 3rd ($A_2(Ir_{1/4}Hf_{3/4})_2O_7$) and 4th ($A_2(Ir_{1/16}Hf_{15/16})_2O_7$). (b) A fragment of the $A_2(Ir_{1/4}Hf_{3/4})_2O_7$ trigonal unit cell showing Ir and Hf atoms only. The "central" Ir site is shown in grey, while the Hf 1st and 2nd neighbours are shown in dark cyan and orange, respectively. The Ir 3rd neighbours are shown in blue. There exist 12 possible paths between Ir 3rd neighbours: 6 via the Ir-Hf-Ir link and 6 via the Ir-*A*-Ir link, where *A* sites are not shown.

compounds with the experimentally observed trigonal compression of IrO_6 octahedra. We switch off 1st and 2nd neighbour hopping by replacing 3/4 of the Ir atoms by Hf atoms to obtain the lattice demonstrated in Fig. 4.11(b) with the chemical formula $A_2(Ir_{1/4}Hf_{3/4})_2O_7$ with the crystal symmetry reduced to trigonal. As a result, each Ir atom has only next-next-nearest (3rd) Ir neighbours. 3rd neighbours are connected via 12 paths: 6 via the Ir-Hf-Ir link within the neighbouring Ir-Hf tetrahedra and 6 via the Ir-*A*-Ir link through the *A* atoms forming a hexagon around the Ir site (Fig. 4.11(b)). The Ir 5*d* bands become narrow as compared to those of $A_2Ir_2O_7$ as shown in Fig. 4.10 (a) and (b). Three clear bands emerge: $J_{eff} = 1/2$ located between −0.4 eV and 0.2 eV for A = Y, Lu and within ±0.2 eV for A = In, as well as two ($J_{eff} = 3/2$)-derived bands located between −1 eV and −0.4 eV for A = Y, Lu and between −1 eV and −0.2 eV for A = In. As expected, the reduction of intersite hopping gives a band structure that resembles the single-ion picture shown in Fig. 4.8(b). Surprisingly, we observe a significant reduction in admixture of $J_{3/2}$ states (and hence $J_{eff} = 3/2$) near the Fermi level in all three model pyrochlore iridates $A_2(Ir_{1/4}Hf_{3/4})_2O_7$. In addition, Ir 5*d* bands are narrower for $In_2(Ir_{1/4}Hf_{3/4})_2O_7$ than for the other two compounds.

We reduce the intersite hopping even further by replacing additional Ir atoms with Hf atoms, such that there remains only one Ir atom out of sixteen in the original unit cell of the size of $Fd\bar{3}m$ with crystal symmetry be reduced to trigonal, giving a chemical formula $A_2(Ir_{1/16}Hf_{15/16})_2O_7$. Hopping from only 4th neighbours, which are at a distance of the lattice constant a to each other, is allowed. Naturally, the Ir 5*d* bands become narrower, and the states

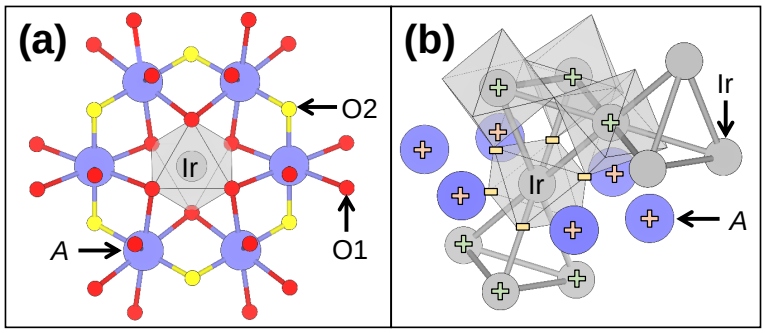

■ *Figure 4.12.* a) Bonding of AO_8 scalenohedrons to the IrO_6 octahedron. (b) Sources of trigonal crystal field acting on Ir atoms. Short-range trigonal crystal field originates from the O_6 anion cage, where compression stabilises a_{1g} orbitals. Long-range crystal field originates from the Ir^{4+} cations comprising the neighbouring Ir tetrahedra and the hexagon of A^{3+} cations. The former stabilises the a_{1g} states while the latter stabilises the e'_g states.

at the Fermi level preserve the $J_{eff} = 1/2$ character as depicted in Fig. 4.10(c). We estimate the "$J_{eff} = 1/2$"-ness by defining the ratio of the area under the curve of $J_{5/2}$- and $J_{3/2}$-derived DOS ($J_{5/2}/J_{3/2}$) in the region of the $J_{eff} = 1/2$ band. It is clear that the $J_{eff} = 1/2$-$J_{eff} = 3/2$ mixing is suppressed with the reduction of intersite hopping as shown in Fig. 4.11(a). This suggests that intersite hopping, rather than trigonal crystal field, controls the degree of $J_{eff} = 1/2$-$J_{eff} = 3/2$ hybridisation. We verify this by varying the degree of IrO_6 trigonal distortion of $A_2(Ir_{1/16}Hf_{15/16})_2O_7$ as discussed below.

4.4.2 Effect of short-range and long-range crystal field

The splitting of $J_{eff} = 3/2$ states does not scale with the degree of trigonal compression (Δx) of IrO_6 octahedra as shown in Fig. 4.8(c). Hozoi *et al.* discussed the importance of long-range crystal field, that is, crystal field originating from atoms further than the nearest-neighbour ligands, in addition to those of O^{2-} ions for the local electronic structure of $A_2Ir_2O_7$ [175]. Quantum chemistry calculations for clusters with undistorted IrO_6 octahedron revealed that the splitting of the $J_{eff} = 3/2$ states of ~ 0.2 eV remained [175]. This splitting has been attributed to long-range crystal field. Fig. 4.12(a) shows that each Ir site in $A_2Ir_2O_7$ is surrounded by a hexagon of positively charged A^{3+} cations. Those compete with the effect of the trigonal compression of IrO_6 octahedron, where the former stabilises the e'_g-type states, while the latter prefers the a_{1g}-type states. In addition, the Ir^{4+} cations form two triangular planes above and below the central Ir site, however those stabilise the a_{1g}-like orbitals similarly to the O^{2-} ligands. Therefore, the effect of trigonal crystal field from O^{2-} and Ir^{4+} ions competes with that originating from the A^{3+} ions as shown in Fig. 4.12(b).

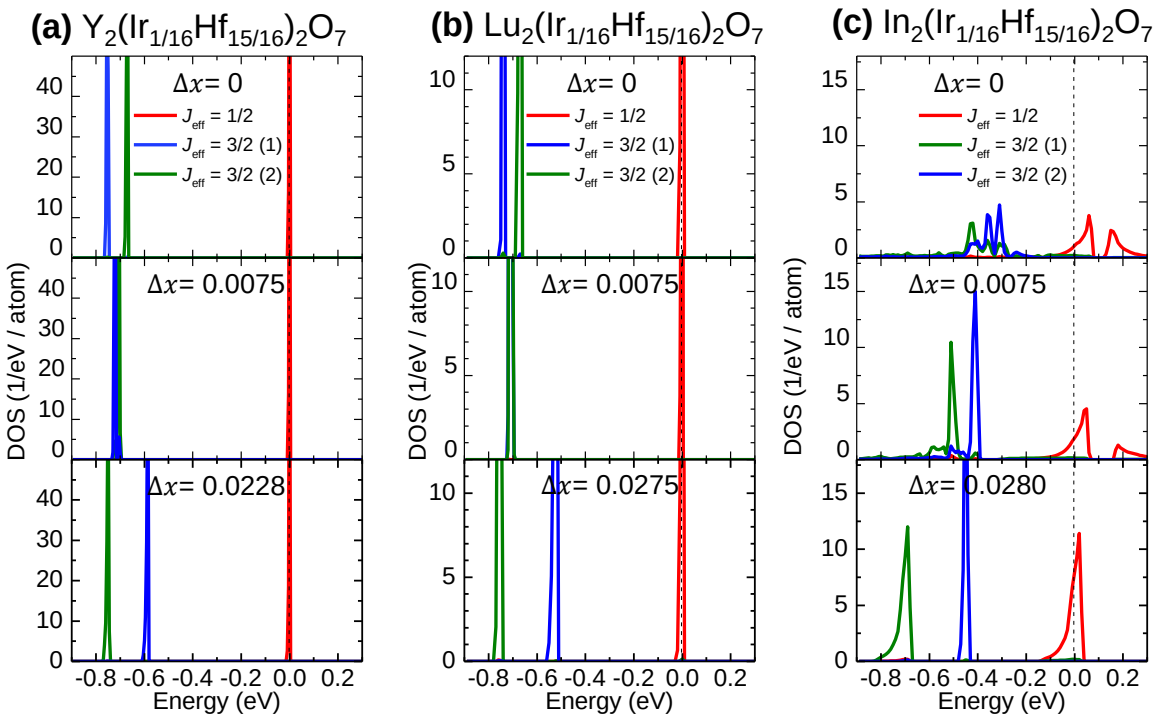

■ *Figure 4.13.* Calculated density of states for model (a) $Y_2(Ir_{1/16}Hf_{15/16})_2O_7$, (b) $Lu_2(Ir_{1/16}Hf_{15/16})_2O_7$ and (c) $In_2(Ir_{1/16}Hf_{15/16})_2O_7$ around E_F showing the t_{2g} states of Ir d-orbitals. The spin-orbit coupling is incorporated in the calculations, and the t_{2g} states are resolved into $J_{eff} = 1/2$ and 3/2 states. The calculation did not include Coulomb U. The Fermi level E_F is indicated by dashed black lines. The degree of trigonal distortion in IrO_6 octahedra is controlled by changing the position of O1 atom x and expressed as Δx. The Ir-O1 bond length is kept constant, and the lattice constant a is varied in order to accommodate the different distortions of IrO_6. The $J_{eff} = 3/2$ states with $J^z_{eff} = \pm 1/2$ and $\pm 3/2$ are shown in different colours.

In order to study the effect of these crystal fields in $In_2Ir_2O_7$, we performed band structure calculations with varying trigonal distortion of model pyrochlore iridates $A_2(Ir_{1/16}Hf_{15/16})_2O_7$ for A = In, Lu and Y with quenched hopping. The strength of crystal field from O^{2-} ions is controlled by changing the oxygen O1 position x, namely, the trigonal distortion of IrO_6 octahedra. The Ir-O1 distance was kept constant by varying the lattice constant a while changing the O1 position x. By suppressing hopping and varying the degree of the trigonal compression of the IrO_6 octahedron, we attempt to separate the impact of intersite hopping from that of trigonal crystal fields.

Fig. 4.13 shows the Ir 5d DOS near E_F of $_2(Ir_{1/16}Hf_{15/16})_2O_7$ for A = In, Lu and Y with varying IrO_6 distortion calculated with spin-orbit coupling. The DOS with the experimentally observed distortion (Δx) is also shown in Fig. 4.10(c). Ir t_{2g} orbitals are resolved into $J_{eff} = 1/2$ and 3/2 characters. In the top panels of Fig. 4.13(a) and (b), a clear splitting of $J_{eff} = 3/2$ bands

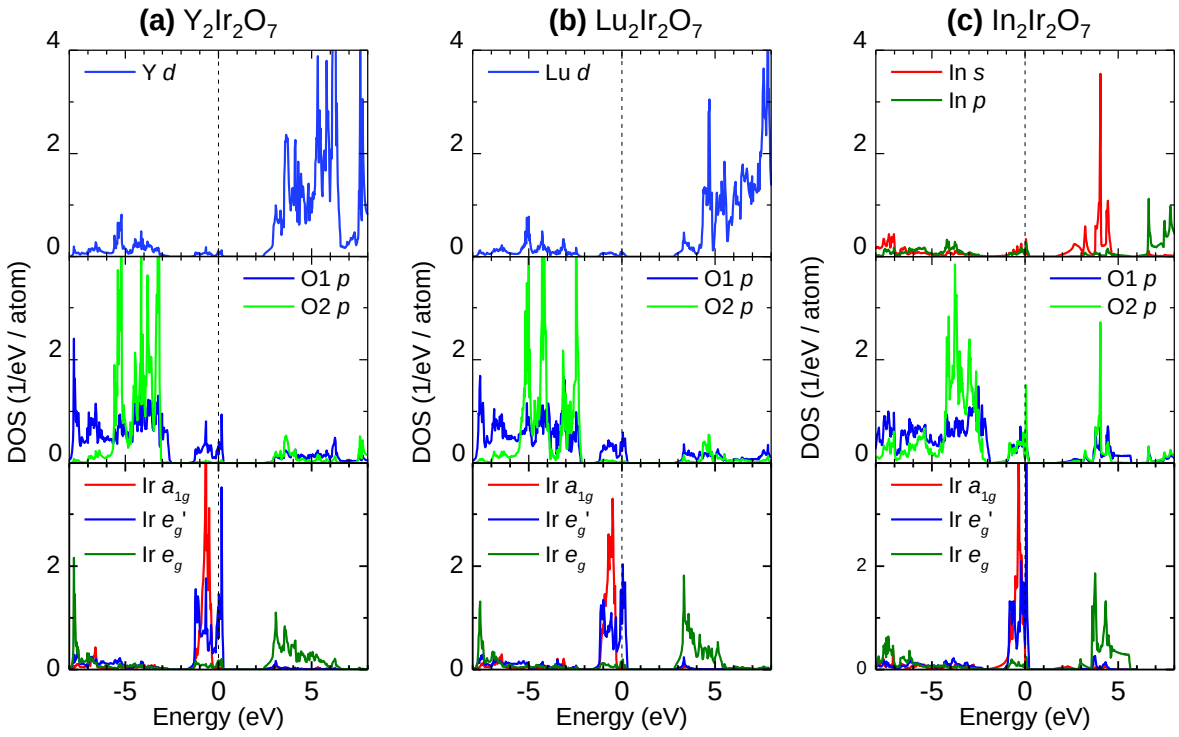

■ *Figure 4.14.* Densities of relevant atomic states calculated without spin-orbit coupling for (a) $Y_2Ir_2O_7$, (b) field into a_{1g} and e'_g. The Fermi level E_F is indicated by dashed black lines.

of about 0.1 eV is observed even for the undistorted A = Y and Lu model compounds. This evidences that the effect of crystal field originating from neighbouring cations is indeed not negligible [175]. Upon increasing the trigonal distortion, the splitting of $J_{eff} = 3/2$ states changes sign, goes through a minimum at around $\Delta x = 0.0075$ and gives splitting of about 0.15 eV and 0.2 eV for experimental values of distortion for A = Y and Lu model compounds, respectively (bottom panels of Fig. 4.13(a) and (b)). The splitting is enhanced by introducing the experimentally observed trigonal distortion. The crystal field from both oxygen atoms and neighbouring cations is operative in the splitting of the $J_{eff} = 3/2$ bands, but with a different sign. The influence of oxygen atoms is the dominant one in the experimental structure, as the least distorted $Y_2(Ir_{1/16}Hf_{15/16})_2O_7$ has the smallest splitting. We note that the splittings observed for experimental Δx is smaller than those observed in the RIXS experiment ($\Delta E \sim 0.4$ eV). This may point to the involvement of other mechanisms, such as the molecular orbital formation due to the Ir-Ir and Ir-O hybridisation, in the splitting of the $J_{eff} = 3/2$ manifold. The distinct DOS of $In_2(Ir_{1/16}Hf_{15/16})_2O_7$ will be discussed in the next section.

4.4.3 *A*-O bond-covalency-induced $J_{eff} = 1/2$ state

It appears that the intersite hopping is the dominant factor in mixing of the J_{eff} states and by reducing intersite hopping, a pure $J_{eff} = 1/2$ can be achieved. The band structure calculations with varying trigonal distortion evidence the influence of the trigonal crystal field, however that cannot account for the distinct nearly pure $J_{eff} = 1/2$ state in $In_2Ir_2O_7$ as compared to $Lu_2Ir_2O_7$. *A*-O covalency must be key for fostering the unique electronic structure of $In_2Ir_2O_7$ as discussed below.

In the top panels of Fig. 4.14, the DOS of atomic states originating from the *A* cations are shown. The empty Y 4*d* and Lu 5*d* states are located at energies above ~ 2.5 eV and do not show appreciable contribution at the Fermi level as their hybridisation with Ir 5*d* states is quite weak. Accordingly, the O2 2*p* states (O2 atoms coordinate *A* cations only) also do not emerge at the Fermi level. In contrast, the In 5*s* states are pushed to lower energies and are separated from E_F by ~ 1.5 eV. In addition, both In 5*s* and 5*p* states appear at E_F as well as O2 2*p* states, which is in the energy range of the Ir t_{2g} bands. This implies that there is significant hybridisation between the In-O and Ir-O networks in contrast to Y-O or Lu-O with Ir-O.

- Electronic structure of "virtual" $In_2Ir_2O_7$ with reduced trigonal distortion

  As discussed above, there is a sizeable hybridisation of In 5*s* and 5*p* states with O 2*p* states. In order to subtract the effect of the hybridisation on the Ir 5*d* states, we studied the electronic structure of virtual $In_2Ir_2O_7$ for which the crystal structure of $Y_2Ir_2O_7$ was used but with Y replaced by In. Therefore, the virtual $In_2Ir_2O_7$ has much reduced trigonal distortion as compared to the real $In_2Ir_2O_7$. The calculated band structures and orbital-resolved Ir 5*d* DOS near E_F for $Y_2Ir_2O_7$ and the virtual $In_2Ir_2O_7$ are shown in Fig. 4.15. In Fig. 4.15(c) the t_{2g} band becomes more dispersive likely due to the additional hopping path involving In atoms. Despite the equal trigonal distortion between the two compounds, the admixture of $J_{eff} = 3/2$ component to the $J_{eff} = 1/2$ state in the virtual $In_2Ir_2O_7$ is much smaller than that in $Y_2Ir_2O_7$. This fact points to the presence of another factor specific to In^{3+} ions. From our results so far, it appears that the Ir-O1-Ir bond bending scaled by trigonal distortion does not influence the mixing of J_{eff} states appreciably. Instead, the intersite hopping controls such hybridisation. For $In_2Ir_2O_7$, the hybridisation of In 5*s* and 5*p* states with the O1 2*p* states effectively weakens the hybridisation between Ir 5*d* and O1 2*p* states, reducing the hopping in the Ir-O1-Ir paths. This evidences that *A*-O covalency is key for stabilising the spin-orbital entangled $J_{eff} = 1/2$ state.

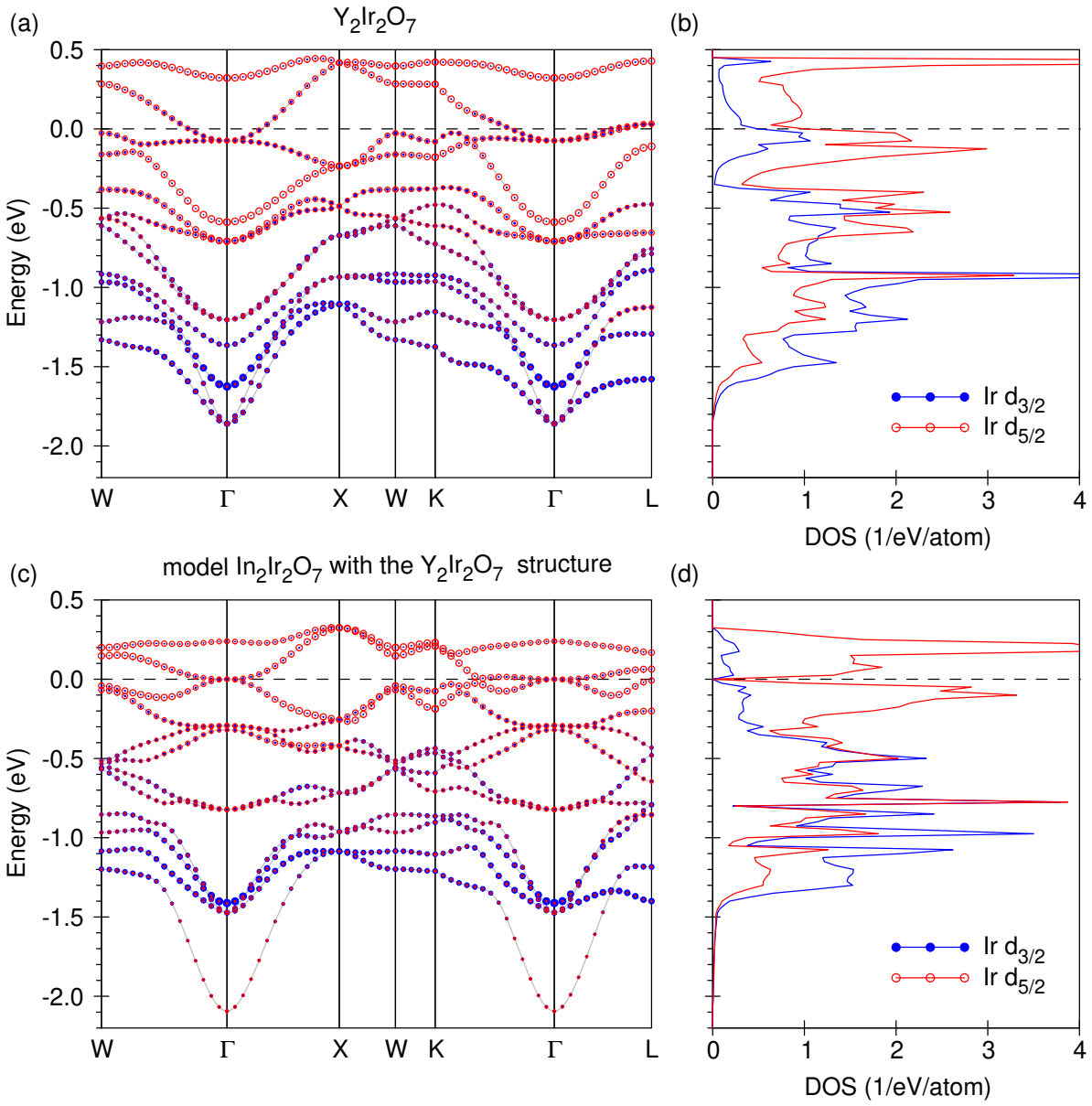

■ *Figure 4.15.* (a),(c) Calculated band structure and (b),(d) Ir 5*d* density of states resolved into $J = 5/2$ ($d_{5/2}$) and $J = 3/2$ ($d_{3/2}$) states for $Y_2Ir_2O_7$ and the virtual $In_2Ir_2O_7$, respectively. The Fermi level E_F is indicated by dashed black lines. Note that the $J_{eff} = 1/2$ state consists of pure $J = 5/2$ wave function and the $J_{eff} = 3/2$ has both $J = 5/2$ and $3/2$ components. This figure was created by Dr. Alexander Yaresko and is used here with his permission.

► Additional remarks

The importance of A-O covalency is further corroborated by the calculations for model pyrochlore iridates with reduced intersite hopping. In Fig. 4.10(c) the $J_{eff} = 1/2$ band in $In_2(Ir_{1/16}Hf_{15/16})_2O_7$ is broader (~ 0.2 eV) than those of A = Y, Lu (~ 0.01 eV). When Ir–Ir hopping is reduced, the In-O bond covalency and weak hybridisation with Ir-O network provide an extra hopping path between the remote Ir atoms in the super-cell lattice of model pyrochlore iridates. For $\Delta x = 0$, the Ir t_{2g} bands become broad as they hybridise strongly with In 5s and 5p states (top panel of Fig. 4.13(c)). When Ir–Ir hopping is only moderately reduced in Fig. 4.10(b), the bands of $In_2(Ir_{1/4}Hf_{3/4})_2O_7$ are the narrowest among the three compounds, implying that Ir-O-Hf-O-Ir hopping is the dominant hopping process which is disturbed by In-O hybridisation. Similarly, in real $A_2Ir_2O_7$ compounds the nearest neighbour Ir-O-Ir hopping dominates. The covalent In-O bond may also mask the effect of crystal field of In^{3+} ion acting on Ir atom.

Some of the pyrochlore iridates are reported to adopt the AIAO long-range magnetic order [189, 190]. The bifurcation of $\chi(T)$ between ZFC and FC curves implies the appearance of AIAO order in $In_2Ir_2O_7$ as well. The magnon dispersion observed in $Sm_2Ir_2O_7$ and $Er_2Ir_2O_7$ is consistent with AIAO order, however the momentum-dependence indicates smaller DM term and reduced magnon gap as compared to the pure $J_{eff} = 1/2$ model, possibly due to the admixture of the $J_{eff} = 3/2$ states [189] and vicinity to the MIT [190], respectively. $In_2Ir_2O_7$ should provide an ideal playground to investigate the magnetism of pure $J_{eff} = 1/2$ moment on a pyrochlore lattice. To confirm this, resonant elastic x-ray scattering (REXS) on single crystal $In_2Ir_2O_7$ would be an ideal tool.

4.5 Conclusion

Properties of pyrochlore iridates are expected to vary as a function of the A cation radius, and $In_2Ir_2O_7$, a Mott insulator with frustrated magnetism, seemingly adheres to this assumption. Its smallest A cation in the series produces the largest trigonal distortion and the smallest bandwidth, as observed in the band structure calculations, and manifested in the peak widths of the E_1 and E_2 excitations in RIXS. The single ion Hamiltonian appears satisfactory for modelling the intra-atomic spin-orbit excitons observed in RIXS spectrum of $In_2Ir_2O_7$, and shows that the splitting of the $J_{eff} = 3/2$ states does not depend solely on the degree of IrO_6 distortion. Instead, the crystal fields originating from the neighbouring cations also split the $J_{eff} = 3/2$ band, where the effect of O^{-2} and Ir^{4+} competes with that of A^{3+}. On the other hand, our series of band structure calculations capture the $J_{eff} = 1/2$ band character and show that the intersite hopping plays a central role in the mixing of the J_{eff} states, which

cannot be accounted for with the single-ion approach. $Y_2Ir_2O_7$ and $Lu_2Ir_2O_7$ can be viewed as semi-isolated Y/Lu-O and Ir-O networks, where intersite hopping and magnetic interactions take place on the Ir-O lattice. In contrast, the covalent In-O bonds in $In_2Ir_2O_7$ reduce the Ir-O hybridisation and suppress the inter-site hopping of Ir 5*d*-electrons and thus the orbital mixing, resulting in the nearly pure $J_{eff} = 1/2$ state. In addition, the covalent In-O bond might reduce the effective charge of In^{3+}, which likely affects the strength of the crystal field experienced by Ir^{4+}. Moreover, other mechanisms, such as correlation, Ir-Ir or Ir-O hybridisation in form of molecular orbital formation, could affect the electronic state of $In_2Ir_2O_7$.

The effects of inter-site orbital mixing and bond covalency, in addition to local structural distortion, need to be properly incorporated in order to understand the electronic structure of pyrochlore iridates. The importance of these factors should not be limited to pyrochlore iridates, and should be common in a wide variety of 5*d* and 4*d* transition-metal compounds with spatially extended *d*-orbitals. Those effects should be taken into account when designing materials hosting novel spin-orbit-entangled phases such as topological semimetals or quantum magnets.

Chapter 5

Ru_2O molecule formation in $In_2Ru_2O_7$

5.1 Introduction

As discussed so far, there has been substantial research activity in materials with t_{2g}^5 configuration hosting the spin-orbital entangled $J_{\text{eff}} = 1/2$ state in search for a Kitaev spin liquid, Weyl semimetal, superconductivity and more exotic phases. However, another platform for exotic electronic states may be realised with the t_{2g}^4 configuration found in ions such as Ru^{4+} which renders a non-magnetic $J_{\text{eff}} = 0$ singlet state. $4d$-based materials with t_{2g}^4 configuration, such as pyrochlore ruthenates, are discussed to be $S = 1$ magnets without orbital degeneracy due to large non-cubic crystal field. On the other hand, $Tl_2Ru_2O_7$ forms an exotic non-magnetic spin singlet state with orbital ordering, where the covalent Tl-O bonds might play a significant role in the ground state. We discovered a new pyrochlore ruthenate $In_2Ru_2O_7$ in which the interplay of spin-orbital entanglement, non-cubic crystal field and molecular orbital formation is tuned by In-O bond covalency.

In section 5.1, we discuss the predicted $J_{\text{eff}} = 0$ electronic state as well as molecular orbital formation observed in materials containing Ru^{4+} species. In section 5.2 we describe the methods used in this study. The new material pyrochlore ruthenate $In_2Ru_2O_7$ is presented in section 5.3, where we discuss its evolution of crystal structure and electronic properties on cooling from high temperatures in context of spin-orbital entanglement and molecular orbital formation. Finally, we discuss the role of the covalent In-O bonds in the stabilisation of the ground state of $In_2Ru_2O_7$ in section 5.4.

5.1.1 $J_{\text{eff}} = 0$ pseudospin and excitonic magnetism

The spin-orbital entangled $J_{\text{eff}} = 0$ pseudospin from the low spin t_{2g}^4 configuration, found in Ir^{5+} , Os^{4+} or Ru^{4+} ions, can be reached by starting from two limits, as shown in Fig. 5.1(a). If $\lambda_{\text{SOC}} \gg J_H$, the orbital l and spin s angular momenta combine for each electron individually, rendering a fully occupied $j_{\text{eff}} = 3/2$ quartet and an empty $j_{\text{eff}} = 1/2$ doublet and therefore a band insulator. The $j_{\text{eff}} = 3/2 \rightarrow j_{\text{eff}} = 1/2$ excitation is equal to $(3/2)\lambda_{\text{SOC}}$ (note that

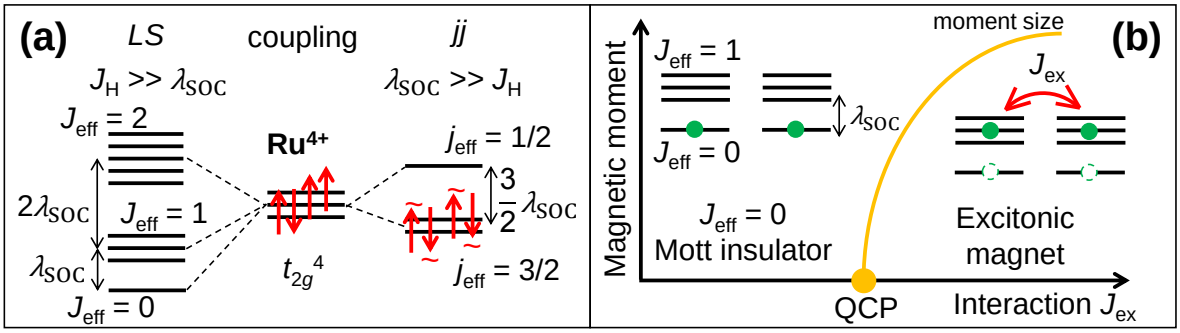

■ *Figure 5.1.* (a) The emergence of $J_{\text{eff}} = 0$ state in the t_{2g}^4 electron configuration in the *LS* (left) and *jj* (right) coupling limit. The arrow with ˜ symbol represents a pseudospin. (b) Magnetic moment as a function of the exchange interaction J_{ex} between $J_{\text{eff}} = 1$ pseudospins. QCP is quantum critical point.

$\lambda_{\text{SOC}} = \zeta/2s = \zeta$). If $\lambda_{\text{SOC}} \ll J_H$, the total orbital $L_{\text{eff}} = 1$ and spin $S = 1$ momenta combine and give a $J_{\text{eff}} = 0$ singlet, $J_{\text{eff}} = 1$ triplet and $J_{\text{eff}} = 2$ quintet (this is also shown in Fig. 1.8(a)). The $J_{\text{eff}} = 0 \longrightarrow J_{\text{eff}} = 1$ excitation is equal to λ_{SOC} (note that $\lambda_{\text{SOC}} = \zeta/2S = \zeta/2$). The $J_{\text{eff}} = 0$ state is magnetically inactive. In reality, no material locates strictly in the *jj* or *LS* coupling limit, however naïvely, the *LS* coupling might more accurately describe the $4d$ Ru^{4+} atom which is the focus of this chapter.

While the physics of a non-magnetic singlet state may seem unremarkable, new states of matter are expected to emerge via interactions between the upper-lying $J_{\text{eff}} = 1$ state separated by spin-orbit coupling λ_{SOC}. If the exchange interaction between the $J_{\text{eff}} = 1$ excited states is strong enough to overcome the gap, and the effective Zeeman splitting (due to internal exchange field from other sites) of the $J_{\text{eff}} = 1$ exceeds λ_{SOC}, a magnetically active ($J_{\text{eff}} = 1$)-derived state would be stabilised against $J_{\text{eff}} = 0$. This leads to a long-range magnetic order which is viewed as a bosonic condensation of $J_{\text{eff}} = 1$ triplet dubbed "excitonic magnetism" [50]. This is shown in Fig. 5.1(b), where for weak magnetic exchange between excited triplets (J_{ex}) a non-magnetic singlet state is stabilised, while beyond a critical value of J_{ex} condensation of the virtual $J_{\text{eff}} = 1$ levels takes place in the form of long-range magnetic order, where the moment size increases with J_{ex}. Between the two limits, a quantum critical point (QCP) is located. In the vicinity of QCP, where $\lambda_{\text{SOC}} \sim J_{\text{ex}}$, the magnetic condensate is expected to strongly fluctuate in phase and amplitude, where the latter is called the Higgs mode - a longitudinal spin-wave mode of "soft" spins [221].

The $J_{\text{eff}} = 0$ state is well established in $5d^4$ materials, for example iridate double perovskites Ba_2YIrO_6 and Sr_2MIrO_6 (M = Gd, Y) [217, 222] or osmate pyrochlore $Y_2Os_2O_7$ [223, 224], which show Van Vleck magnetism and no condensation of $J_{\text{eff}} = 1$ due to the large gap scaled by λ_{SOC}. Therefore, potential candidates for realising excitonic magnetism could be $4d$

analogues such as materials hosting Ru^{4+}, where λ_{SOC}, and hence the gap, should be reduced as compared to the exchange couplings between the excited states. Since in most materials the local cubic symmetry of RuO_6 octahedra is broken due to distortions, it is widely believed that the orbital moment is completely quenched and non-cubic crystal field dominates. For example, pyrochlore ruthenates are discussed to be a $S = 1$ magnet with strong trigonal distortion of the RuO_6 octahedra [225, 226]. Nevertheless, recently a layered perovskite Ca_2RuO_4 has been demonstrated to undergo an excitonic magnetic ordering, where a soft-moment amplitude (Higgs) mode, a hallmark of excitonic magnetism, has been identified [71] and the structure of the local excitations evidence the relevance of λ_{SOC} [72]. It is likely that other $4d^4$ ruthenates, such as pyrochlore $A_2Ru_2O_7$, also host excitonic magnetism.

5.1.2 Molecular orbital formation in ruthenates

Even though the J_{eff} pseudospin may remain relevant despite other perturbations in the materials discussed in chapter 1, this can often not be the case. While $4d^4$ materials serve as a promising platform for realisation of excitonic magnetism due to the smaller excitonic gap as compared to $5d^4$ analogues, a consequence arises: smaller λ_{SOC} may be less stable against other effects such as non-cubic crystal field, hybridisation or molecular orbital formation. There exist a number of ruthenates which become non-magnetic at low temperatures (Fig. 5.2(a)), where the transition to such a state is associated with the formation of low-dimensional network of Ru ions which form either a non-magnetic spin-singlet or molecular orbital such as dimers in honeycomb Li_2RuO_3 [161, 162] or 2-dimensional La_2RuO_5 [227, 228].

Honeycomb ruthenate Li_2RuO_3 undergoes a metal-to-insulator transition (MIT) at high temperatures with a simultaneous lattice distortion, where a herringbone pattern of dimers is formed on the initially almost regular honeycomb lattice [161, 162]. The dimers are discussed to form a spin singlet state or a molecular orbital formation involving σ-, π- and δ-type overlap of all three (t_{2g})-derived orbitals, giving six separated molecular orbitals which are then filled with eight electrons from two Ru^{4+} ions as shown in Fig. 5.2(b). Interestingly, according to pair distribution function (PDF) analysis of x-ray diffraction data, the Ru_2 dimers persist above the transition at $\sim 500\,\text{K}$, however the dimer crystal melts and the short Ru-Ru bonds are fluctuating [232].

Insulating pyrochlore ruthenates $A_2Ru_2O_7$ show long-range order [225, 226] (possibly a $J_{\text{eff}} = 1$ condensate as discussed above) and may seem resistant to molecular orbital formation, however there exists one unique member of the $A_2Ru_2O_7$ family. $Tl_2Ru_2O_7$, similarly to Li_2RuO_3, shows a sharp drop in $\chi(T)$ with decreasing temperature (Fig. 5.2(a)) and undergoes a MIT with a simultaneous structural transition from the cubic to an orthorhombic structure [233, 234] with a non-magnetic ground state confirmed by μSR [235]. However,

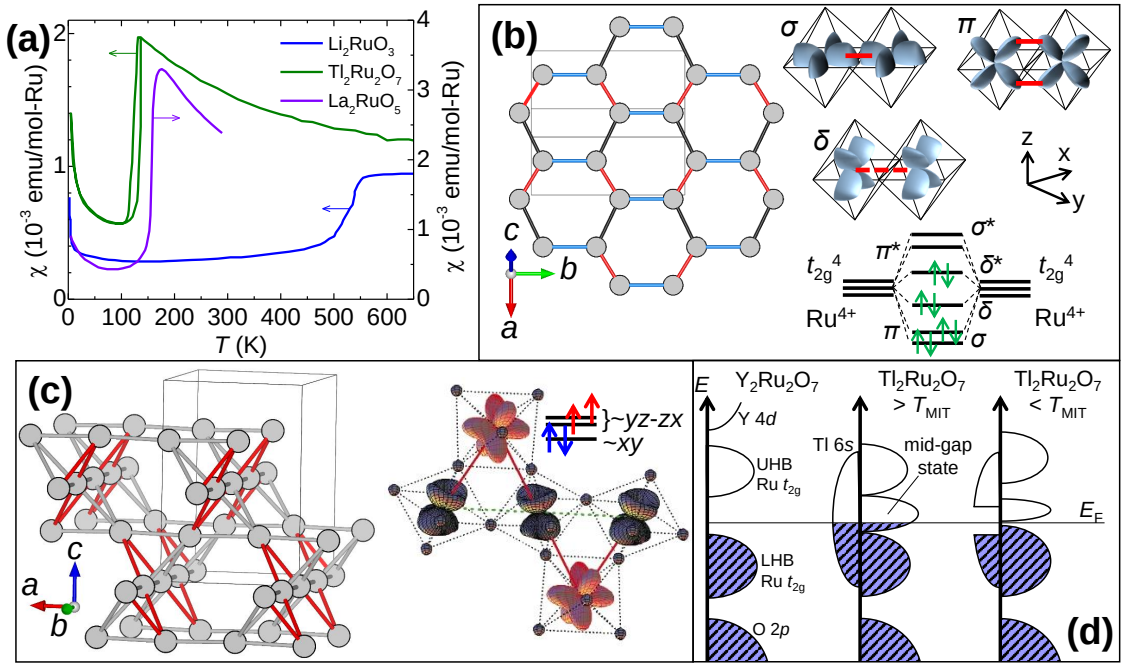

■ *Figure 5.2.* (a) Temperature dependent magnetic susceptibilities of powder samples of Li_2RuO_3 [161], $Tl_2Ru_2O_7$ [229] and La_2RuO_5 [227]. (b) Left: Li_2RuO_3 honeycomb lattice with the dimer bonds shown in red. Top: molecular orbital formation in Ru-Ru dimers in Li_2RuO_3 as a result of σ, π and δ overlap of d_{xy}, d_{yz-zx} and d_{yz+zx} orbitals. Right: the molecular orbital manifold with δ^* as the lowest occupied states. Taken after [161]. (c) Left: 1D zigzag chains (shown in red) on top of the Ru pyrochlore lattice. Right: within the 1D zigzag chains the $\sim d_{xy}$ orbitals do not overlap well. $\sim d_{yz}, d_{xz}$ orbitals overlap along the Ru-Ru bonds which are discussed to comprise the Haldane chain. Image adapted from Ref. [230]. (d) Simple schematic of electronic structures (LDA + U), from left to right: $Y_2Ru_2O_7$, $Tl_2Ru_2O_7$ above the structural transition and $Tl_2Ru_2O_7$ below the structural transition. Reproduced from Ref. [231].

the currently understood nature of its ground state is quite different to that of Li_2RuO_3. Instead of dimers, the low temperature structure comprises semi-isolated 1D zigzag chains on top of the Ru pyrochlore lattice as depicted in Fig. 5.2(c). The RuO_6 octahedra undergo tetragonal compression with the local z axes along short Ru-Ru bonds, resulting in orbital ordering, where the $\sim d_{xy}$ orbital is stabilised and filled with two electrons, while the d_{yz}- and d_{xz}-derived orbitals, which directly overlap along the short Ru-Ru bonds within the 1D chains, are partially filled. It has been argued that the non-magnetic 1D chain formation is associated with a Haldane chain [229], which is a $S = 1$ singlet state without dimerisation where each site participates in two valence bonds. While the validity of that interpretation of the ground state is under discussion, it is potentially a remarkable phenomenon as it would pose the first example of a Haldane chain formation on a 3D lattice.

5.1.3 Competition between phases in a new pyrochlore ruthenate tuned by *A*-O covalency

Complex ruthenium oxdes hosting Ru^{4+} serve as a platform for competition between various electronic phases, in particular J_{eff} magnetism and orbital ordering with spin singlet or molecular orbital formation. This competition can be tuned by spin-orbit coupling, non-cubic crystal field and inter-site hybridisation. An unprecedented electronic state can arise when Ru^{4+} is placed on a geometrically frustrated lattice, such as that of a pyrochlore structure. Therefore, we focus on pyrochlore ruthenates.

Insulating pyrochlore ruthenates $A_2Ru_2O_7$ show long-range order and are discussed to be $S = 1$ magnets due to the orbital moment quenching by strong trigonal crystal field [225, 226], while $Tl_2Ru_2O_7$ displays an exotic non-magnetic ground state. Up to date, the origin of the distinct behaviour of $Tl_2Ru_2O_7$ in comparison to other ruthenates is not clear, however theoretical evidence suggests that the role of Tl states should be important. Tl^{3+} is a *p*-block cation in contrast to Y or the lanthanides and the Tl-O bond has more covalent character than Y-O or Lu-O. As shown in Fig. 5.2(d), Y 4*d* states lie at substantially higher energies than Ru 4*d* or O 2*p* states and hence contribution of Y states near the Fermi level E_F should be negligible, effectively isolating the Ru-O network. Coulomb interaction, U, gaps out the partially filled Ru t_{2g} states producing a Mott insulator [236]. On the other hand, Tl 6*s* bands are in the vicinity of Ru 4*d* bands near E_F as well as O 2*p* bands and hence substantial hybridisation occurs between those. Such Tl-O hybridisation, as discussed in chapter 4, should affect the Ru-O hybridisation as well as the effective crystal field acting on Ru atoms. Moreover, on the basis of optical conductivity experiments, it has been discussed that such hybridisation results in self-doping of $Tl_2Ru_2O_7$ in form of charge transfer from the Tl-O to Ru-O reservoir, which produces mid-gap states (middle of Fig. 5.2(d)) resulting in a metallic state above the transition temperature T_{MIT} [231].

Below T_{MIT}, that is, in the low temperature state, it has been reported that Tl^{m+} ions (where $2 \lesssim m \lesssim 3$) undergo charge disproportionation into $Tl^{m-\delta}$ and $Tl^{m+\delta}$ [233], which is likely allowed by the comparable stability of Tl(I) and (III) oxidation states. This charge disproportionation was shown to gap the partially-filled antibonding band derived from Tl 6*s* and O2 2*p* states in LDA calculations [237], which is schematically shown on the right hand side of Fig. 5.2(d). Interestingly, a tight-binding model shows that when Tl atoms are returned to their high-symmetry ($Fd\bar{3}m$-derived) atomic positions, the gap closes, suggesting that the distortion of Ru atoms into the 1D zigzag chain is not the driving force behind the phase transition into the non-magnetic state in $Tl_2Ru_2O_7$ [237]. While Tl distortion-generated MIT scenario conflicts with the proposed mechanism of the Haldane gap opening within the Ru 1D zigzag chains, the role of Ru 4*d* electrons is not addressed, for which incorporation of

electron correlation should be necessary. In Ref. [229], LDA+U calculations with assumed antiferromagnetic order within the Ru 1D chains produces a large antiferromagnetic exchange within those. The role of Tl in the ground state formation of $Tl_2Ru_2O_7$ has not been further addressed in the last 20 years, and the issue of the nature of the ground state remains unresolved.

This importance of A-O covalency and its impact on spin-orbital entangled systems is discussed chapter 4. The A-O covalency plays an important role in $In_2Ir_2O_7$, where the hybridisation of In-O network with Ir-O network suppresses Ir-O-Ir intersite hopping and fosters a nearly pure $J_{\text{eff}} = 1/2$ band. Potentially, the In-O covalency could stabilise a spin-orbital entangled state in pyrochlore ruthenate. In addition, a new pyrochlore ruthenate with a covalent A-O bond could be an exciting platform for competition between exotic electronic phases. In light of the recent successful synthesis of $In_2Ir_2O_7$, we attempted and succeeded in the synthesis of a new pyrochlore ruthenate $In_2Ru_2O_7$. We found a unique molecular orbital formation on frustrated pyrochlore lattice, likely assisted by the structural instability due to A-O covalency.

5.2 Methods

5.2.1 Sample preparation

An unsuccessful solid state synthesis of $In_2Ru_2O_7$ at ambient pressure was reported over 30 years ago [238]. Due to the small size of In^{3+}, $In_2Ru_2O_7$ requires high pressure synthesis. The polycrystalline and single crystal samples of $In_2Ru_2O_7$ were obtained by a high-pressure synthesis technique described in section 2.1.2. For the polycrystalline samples, powders of In_2O_3 (Alfa Aesar, 99.994 % metal basis) and RuO_2 (Tanaka Kikinzoku, 76 wt.% Ru content) were mixed and ground in stoichiometric molar ratios and sealed in a Pt foil ampoule. The ampoule was heated at 1500 °C for 60 minutes under a pressure of 6 GPa. The exact same powder batches were used for x-ray and neutron diffraction, magnetic susceptibility and DSC measurements. Pieces of hard-pressed pellets of a different batch were used for resistivity and heat capacity measurements.

For single crystal samples, powders of In_2O_3 (Alfa Aesar, 99.994 % metal basis), RuO_2 (Tanaka Kikinzoku, 76 wt.% Ru content) and $InCl_3$ flux (Alfa Aesar, 99.99 % metal basis) were mixed and ground in a 2:4:1 molar ratio. Since $InCl_3$ is hygroscopic, the mixture preparation and loading into Pt ampoule was performed in a glove box under inert atmosphere. The ampoule was then heated at 1500 °C for 60 minutes under pressure of 8 GPa. After quenching the temperature and reaching ambient pressure, the obtained pellet was sonicated in a beaker

with deionised water in order to remove the water-soluble $InCl_3$ flux. Upon contact with water, the pressed-pellet disintegrated into powders of In_2O_3, RuO_2 and $In_2Ru_2O_7$ as well as black octahedron-shaped crystals. Single crystal samples were used in x-ray diffraction and magnetic susceptibility measurements only, as they were found to be extremely fragile.

The polycrystalline sample of reference material $Y_2Ru_2O_7$ was prepared with the same conditions as $In_2Ru_2O_7$, the only difference being Y_2O_3 (Alfa Aesar, 99.994 % metal basis) used for the powder precursor.

5.2.2 Single crystal x-ray diffraction and analysis

Crystals suitable for single-crystal x-ray diffraction were selected under high viscosity oil and mounted with grease on a loop made of Kapton foil (Micromounts^{TM}, MiTeGen, Ithaca, NY). Diffraction data were either collected with a SMART-APEX-II CCD X-ray diffractometer (Bruker AXS, Karlsruhe, Germany) equipped with a N-Helix low-temperature device (Oxford Cryosystems) [239] or with a SMART-APEX-I CCD X-ray diffractometer (Bruker AXS, Karlsruhe, Germany) equipped with Cryostream 700^{Plus} cooling/heating device (Oxford Cryosystems). Both cooling devices have temperature stability and accuracy of 0.2 K. The reflection intensities were integrated with the *SAINT* subprogram in the Bruker Suite software package [240]. For uniform handling of the data despite small size of the crystals and the twinning issue, multi-scan absorption corrections were applied using either *SADABS* [241] or *TWINABS* [242]. The structures were refined by full-matrix least-squares fitting with the *SHELXL* software package [243, 244] or with JANA2006 [245]. Jana2006 allows data setup and refinement for more than two twin operations involved.

5.2.3 Powder x-ray diffraction and analysis

Temperature dependent XRPD measurements were carried out both in Bragg-Brentano and Debye-Scherrer geometry. The former was used to obtain high-resolution data for monitoring the phase transition and indexing the powder patterns with Le Bail [246] or Pawley [247] method, while the latter was performed in order to obtain accurate reflection intensities for crystal structure Rietveld refinements. All XRPD analyses were performed using the programme TOPAS 6.0 [81].

- Debye-Scherrer geometry

XRPD data of the powdered $In_2Ru_2O_7$ sample were collected with a Stoe Stadi-P transmission diffractometer (primary beam Johann-type Ge(111) monochromator for Mo-$K\alpha_1$-radiation, Mythen-1K PSD) in Debye-Scherrer (DS) geometry with the sample sealed in a borosilicate glass capillary of 0.5 mm diameter (Hilgenberg, glass No. 14), which was spun during the

■ *Table 5.1.* Neutron scattering lengths b and cross sections σ for thermal neutrons. b is given in fm and σ is given in barns. Conc. is concentration. All values taken from Ref. [77] unless specified otherwise.

Isotope	Conc. (%)	b_{coh}	b_{inc}	σ_{coh}	σ_{inc}	σ_{tot}	σ_{abs}
In	—	$4.065 - 0.0539i$	—	2.08	0.54	2.62	193.8(15)
^{113}In	4.3	5.39	(+/−)0.017	3.65	0.000037	3.65	12.0(11)
^{115}In	95.7	$4.01 - 0.0562i$	−2.1	2.02	0.55	2.57	202(2)
Ru	—	7.03	—	6.21	0.4	6.6	2.56
O	—	5.803	—	4.232	0.0008	4.232	0.00019
^{16}O	99.762	5.803	0	4.232	0	4.232	0.0001
^{17}O	0.038	5.78	0.18	4.2	0.004	4.2	0.236
^{18}O	0.2	5.84	0	4.29	0	4.29	0.00016

measurement for better particle statistics. For heating and cooling of the sample, a cold N_2 gas blower (Oxford Cryostream 800, Oxford Cryosystems) was used. Heating and cooling was performed in 10 K steps using a rate of 2 K min^{-1}. The heating and cooling ramps were started at 303 K and the sample was heated up to 493 K and cooled down to 103 K. Each powder pattern was recorded for 3 h in the 2θ-range from 2 to 110°. Prior to each measurement, a delay time of 10 min was applied in order to allow thermal equilibration.

- Bragg-Brentano geometry

XRPD data of the powdered $In_2Ru_2O_7$ sample were collected on a laboratory powder diffractometer Bruker D8-Advanced in Bragg-Brentano (BB) geometry (primary Ge(111)-Johann-type monochromator for Cu-$K\alpha_1$-radiation, Lynx Eye detector). The sample was suspended in ethanol and put on a flat plate sample holder, where the solvent was slowly evaporated. For cooling of the sample a cooling chamber (PheniX, Oxford Cryosystems) was used. In order to avoid the condensation of ice, oxygen and nitrogen from the atmosphere, all measurements were performed in a high vacuum atmosphere ($p < 10^{-5}$ mbar). Heating and cooling was performed in 5 K steps using a rate of 2 K min^{-1}. The cooling and heating ramps were started at 30 K and the sample was cooled down to 23 K and heated up to 203 K. Each powder pattern was recorded for 12 h in the 2θ-range from 5 to 110°. Prior to each measurement, a delay time of 1 h was applied in order to allow thermal equilibration.

5.2.4 Time of flight neutron powder diffraction and analysis

For structural analysis and precise determination of positions of light oxygen atoms, the time of flight high resolution neutron powder diffraction technique was employed at high-resolution powder diffraction (HRPD) beamline at ISIS Neutron and Muon Source (Fig. 5.3).

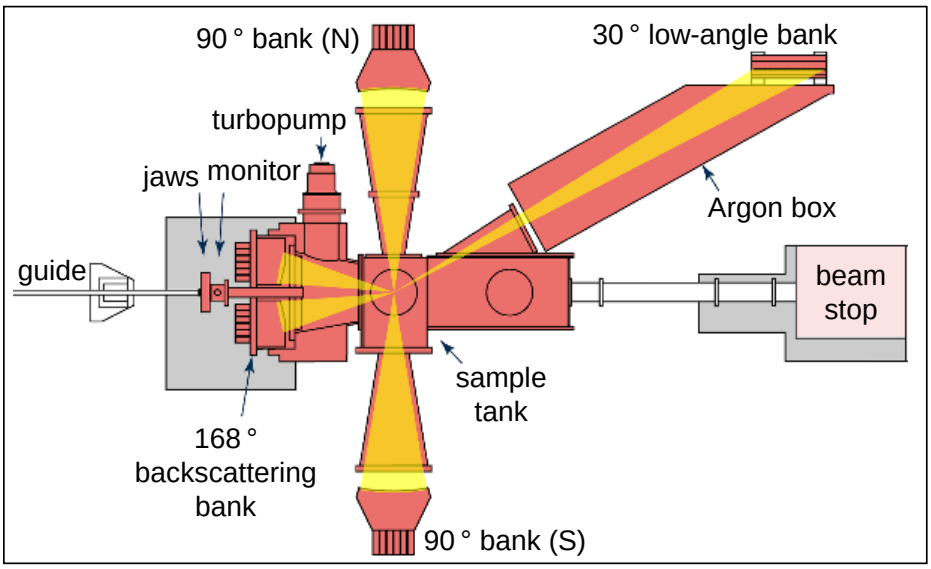

■ *Figure 5.3.* A schematic diagram of the HRPD instrument at ISIS. There are three sets of detector banks at $2\theta = 30°$, $90°$ and $168°$, where the latter is the highest resolution one. N and S correspond to north and south, respectively. The yellow areas depict the neutron beam scattered off the sample. Adapted and modified from Ref. [248].

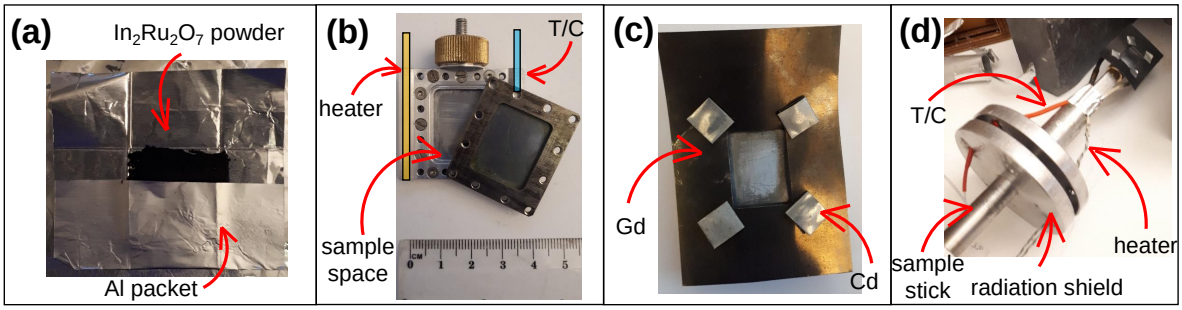

■ *Figure 5.4.* The sample holder used in the $In_2Ru_2O_7$ HRPD neutron diffraction experiment. (a) 0.591 g of polycrystalline sample of $In_2Ru_2O_7$ loaded into Al foil packet. (b) Flat plate sample can made of vanadium windows with aluminium alloy frame with the location of the heater and thermocouple (T/C) used for temperature control shown. (c) The Gd and Cd foil used to minimise background scattering in the back-scattering geometry. (d) The flat plate sample can mounted on the sample stick.

Since natural In has large absorption cross-section as shown in Table 5.1, a flat plate geometry was used to minimise neutron absorption (Fig. 5.4). The flat plate is made of two vanadium windows surrounded by an aluminium alloy frame which encloses the sample space. The polycrystalline sample was loaded into an aluminium (Al) foil packet in order to distribute the powder in the sample space evenly. Then, in order to minimise the scattering of neutrons of the whole flat plate in the back-scattering direction, a window made of gadolinium (Gd) foil fixed by screws covered with cadmium (Cd) foil, both strongly absorbing elements, were attached to the top of the flat plate. For temperature control, a closed cycle refrigerator (CCR) was employed, which uses helium gas from a helium compressor for achieving low temperatures. In Fig. 5.4(b) and (d), the positions of the heater and the temperature sensor (thermocouple, T/C) are shown. The neutron diffraction data were measured on cooling from 300 K down to 10 K in 10 K steps using cooling rate of 2.5 K min^{-1}, with a minimum count of 20 μAh per scan for determination of the unit cell temperature dependence and with longer counts at temperatures of interest for full structural solution. Prior to each measurement, a delay time of 10 min was applied in order to allow thermal equilibration. The collected neutron diffraction data was reduced, normalised and absorption-corrected using Mantid [158]. Some regions containing peaks from the sample environment, such as vanadium, aluminium and stainless steel, were removed from the data prior to analysis. Rietveld analysis of the neutron diffraction data was performed with the GSAS programme [80].

5.2.5 Structure determination

For identification of structural phases found in $In_2Ru_2O_7$ the following strategy was employed: (a) the symmetry (e.g. centring) and the unit cell dimensions were deduced from a diffraction pattern by performing Pawley or Le Bail fits, (b) subgroups of the parent pyrochlore structure $Fd\bar{3}m$ of the determined unit cell dimensions down to orthorhombic symmetry were identified, (c) candidate subgroups were tested using Pawley or Le Bail, and then Rietveld refinement, (d) the final (best fitting) models were tested for presence of higher symmetry than accounted for by using an online utility CheckCIF [249]. Indexing and structure solution was performed by Jürgen Nuss with single crystal x-ray diffraction. However since In and Ru atoms have similar atomic numbers and hence might be difficult to distinguish with x-ray scattering, neutron scattering was used for precise structure refinement including tracking positions of light O atoms.

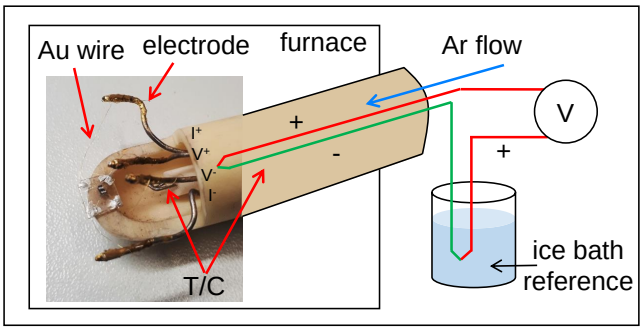

■ *Figure 5.5.* Schematic of the in-house resistivity equipment. A long alumina tube is placed into a furnace for reaching high temperatures. The 4-probe resistivity measurement setup is placed on the one end of the alumina tube which locates inside the furnace. The temperature is monitored with a type-R thermocouple with a cold junction. V indicates a voltmeter.

5.2.6 Resistivity at high temperatures

Resistivity measurements at temperatures above 350 K were performed using in-house equipment as shown in Fig 5.5. The high temperature was achieved with a tube furnace. Ar gas was flown through the furnace tube throughout the measurement. Temperature in the vicinity of the sample was monitored using a type-R thermocouple with a cold junction. The high temperature resistivity data is scaled against the low temperature resistivity data obtained with the PPMS via overlapping temperature regions of 300-350 K.

5.2.7 Resonant inelastic x-ray scattering

The temperature dependence of the electronic structure was investigated by measuring RIXS excitation spectra at the Ru L_3 edge at the P01 beamline at the PETRA-III synchrotron at DESY. The energy of the incident x-ray beam was tuned to 2838.5 eV ($2p_{3/2} \rightarrow 4d(t_{2g})$ excitation) by using a primary Si(111) two-bounce monochromator (cryogenically cooled) and a secondary four-crystal asymmetrical Si(111) channel-cut monochromator, which was then focused with a Kirkpatrick-Baez mirror. The scattering angle was fixed to 90° in horizontal scattering geometry. The scattered x-ray beam was analysed with a diced and spherically bent $SiO_2(10\bar{2})$ analyser. For more detail, see Ref. [250]. The total energy resolution, evaluated by the elastic scattering from GE varnish, was about 80 meV. The least squares fitting of the RIXS spectrum of $In_2Ru_2O_7$ at room temperature was performed using the method described in section 2.3.1.

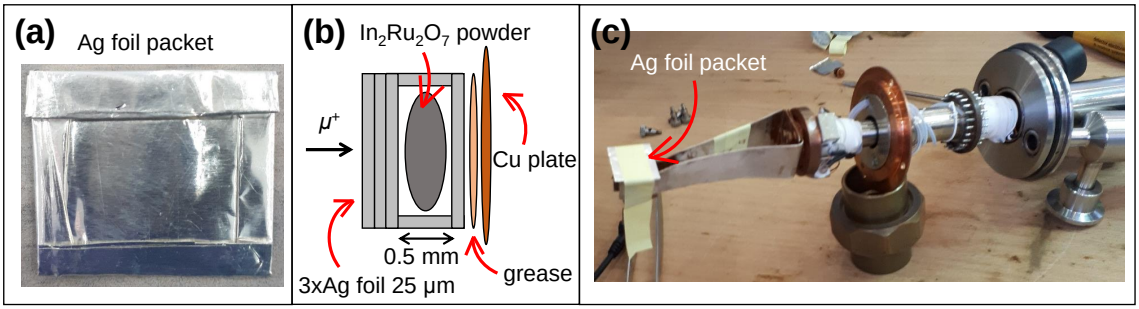

■ *Figure 5.6.* The sample holder used in the $In_2Ru_2O_7$ ZF-μSR experiment. (a) 0.75 g of polycrystalline sample of $In_2Ru_2O_7$ loaded into Ag foil (25 µm thickness) packet. (b) The sample mounting on top of the sample stick shown in (c). The Ag foil packet is wrapped three times in front of the sample. The Ag foil packed is then stuck to a Cu plate attached to the sample stick with grease. (c) The Ag foil packet mounted with tape on the sample stick.

5.2.8 Muon Spin Rotation

Muon Spin Rotation experiment on polycystalline $In_2Ru_2O_7$ was performed in zero field (ZF) setup by using the CHRONUS instrument at ISIS [251]. The sample was wrapped in a square Ag foil (25 µm thickness) packet. In order for the muons to stop inside the polycrystalline sample, three layers of Ag foil in front of the sample were used to slow muons down. The centre of asymmetry α was defined with a transverse-field (TF) measurement at 300 K:

$$A = \alpha \frac{N_F + N_B}{N_F - N_B}, \tag{5.1}$$

where A is the asymmetry, and N_F and N_B is the positron count in the forward and the backward scattering detector, respectively. The ZF data was collected on warming from 10 K to 300 K in 10 K steps with 20-50 million muon events per scan and then normalised and binned using WiMDA software [252].

5.2.9 Band structure calculations

The LDA band structure calculations were performed using the method described in section 2.5.1 and the crystal structures obtained from the neutron and x-ray diffraction experiments.

5.2.10 Energy Dispersive X-ray spectroscopy in the SEM mode

In order to establish the elemental composition of the newly synthesised compound, energy-dispersive x-ray (EDX) spectroscopy via scanning electron microscope (SEM) was employed.

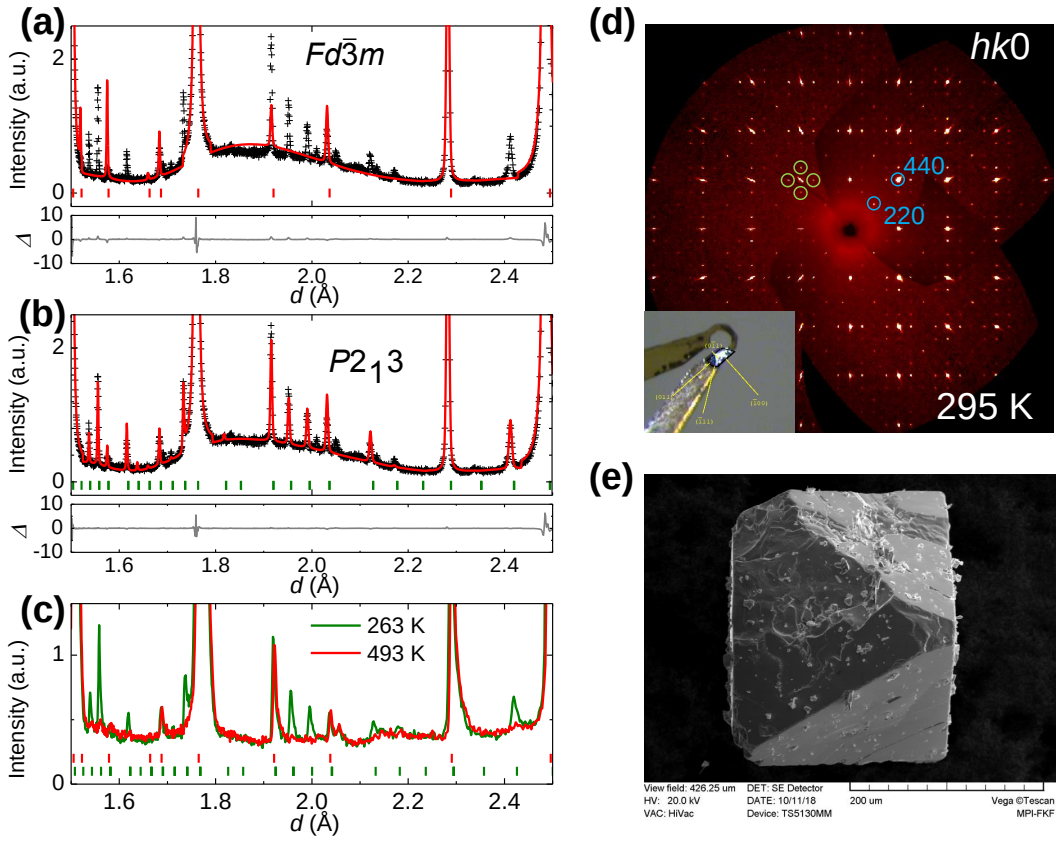

■ *Figure 5.7.* (a) and (b) show XRD patterns of polycrystalline $In_2Ru_2O_7$ measured at $T = 300\,K$ in BB geometry. The black crosses, red line and grey line represent the observed pattern, the Le Bail fit profile and the difference curve between the observed and calculated profiles, respectively. The red and green vertical bars represent $Fd\bar{3}m$ and $P2_13$ reflections, respectively. $Fd\bar{3}m$ space group cannot explain the the observed reflections, while $P2_13$ primitive cubic space group can explain the observed reflections. (c) XRD patterns of polycrystalline $In_2Ru_2O_7$ measured at $T = 300\,K$ in DS geometry at different temperatures. The F-centring forbidden peaks disappear above $\sim 450\,K$. (d) XRD pattern of $In_2Ru_2O_7$ crystal showing reflections in the $hk0$ reciprocal plane. The reflections circled in blue are indexed by the $Fd\bar{3}m$ space group, while the green ones are not and indicate a loss of F centring. At the bottom left, a photograph of the measured crystal with face indexing of a primitive cubic cell is shown. (e) SEM image of a $In_2Ru_2O_7$ octahedral crystal with surface damage visible.

5.3 Results

5.3.1 Weakly distorted pyrochlore lattice at room temperature

The XRD pattern from the polycrystalline sample of the product at room temperature indicates a pyrochlore-like structure, however numerous small peaks were observed which cannot not be indexed with the cubic pyrochlore structure with the space group $Fd\bar{3}m$ as shown in Fig 5.7(a). The additional peaks can be indexed by F-centring forbidden reflections and hence

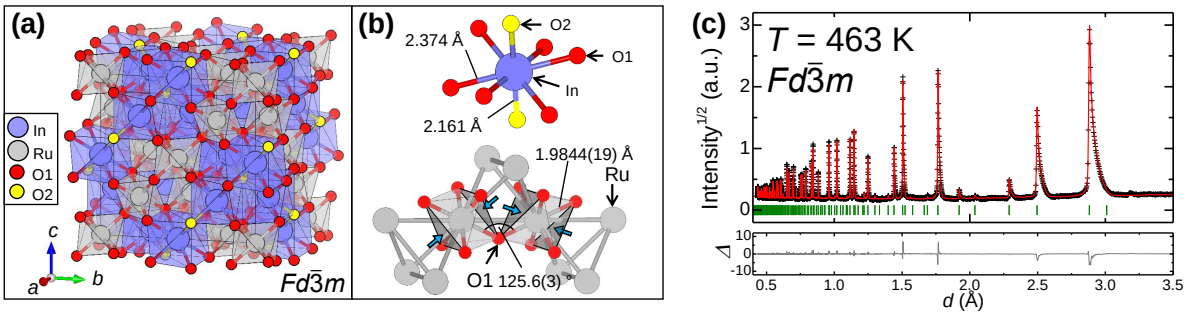

■ *Figure 5.8.* The crystal structure of $In_2Ru_2O_7$ in the $Fd\bar{3}m$ phase. The O2 atoms, which coordinate the In atoms only, are shown in yellow. (a) The $Fd\bar{3}m$ unit cell. (b) Top: the local environment of the In atom showing six long In-O1 and two short In-O2 bonds. Bottom: the local environment of Ru atoms on top of the pyrochlore lattice. The blue arrows indicate the direction of the trigonal compression. (c) Rietveld analysis of XRD pattern of polycrystalline $In_2Ru_2O_7$ measured at $T = 463$ K in DS geometry. The black crosses, red line and grey line represent the observed pattern, the calculated profile and the difference curve between the observed and calculated profiles, respectively. The green vertical bars represent $Fd\bar{3}m$ reflections.

the observed pattern can be accounted for with a primitive cubic cell such as $P2_13$ (Fig 5.7(b)). Single crystal XRD was attempted on $In_2Ru_2O_7$ crystals such as that depicted in Fig 5.7(e), however it was found that it comprises multiple domains (and thus was a polycrystal) and cannot be reasonably indexed. After crushing the crystal and measuring a piece of a size of $\sim 10\,\mu m$, a pattern shown in Fig 5.7(d) was observed, which also shows spots other than those accounted for by $Fd\bar{3}m$ symmetry, evidencing that the additional reflections observed in the polycrystalline pattern do not originate from an impurity and are intrinsic to $In_2Ru_2O_7$.

EDX elemental analysis of the crystal shown in Fig 5.7(e) shows atomic fractions of In, Ru and O of 16.6 %, 16.8 % and 66.6 %, respectively, indicating a In:Ru:O ratio of $\sim 2:2:8$, close to ideal $In_2Ru_2O_7$ pyrochlore. Furthermore, with increasing temperature, the additional peaks disappear above 450 K as shown in Fig 5.7(c) and the Rietveld analysis (Fig 5.8(c)) of the x-ray powder diffraction pattern shows that the product is a single phase of $In_2Ru_2O_7$ pyrochlore with $Fd\bar{3}m$ space group without any impurities within the instrumental resolution. $In_2Ru_2O_7$ has the smallest cubic lattice parameter $a = 9.982\,95(10)$ Å, the most trigonally compressed RuO_6 octahedra and the smallest Ru-O-Ru angle of 125.6(3)° among the reported pyrochlore ruthenates as shown in Fig 5.8(a) and (b). The refined structure parameters are shown in Table 5.2.

The distortion of $In_2Ru_2O_7$ below ~ 450 K is found to be a weak tetragonal one, as no primitive cubic structural model is found to fit the single crystal XRD pattern reasonably. The observed XRD pattern intensities in Fig 5.7(d) and the neutron diffraction pattern can be well explained with tetragonal non-centrosymmetric structure with space group $P4_12_12$, a

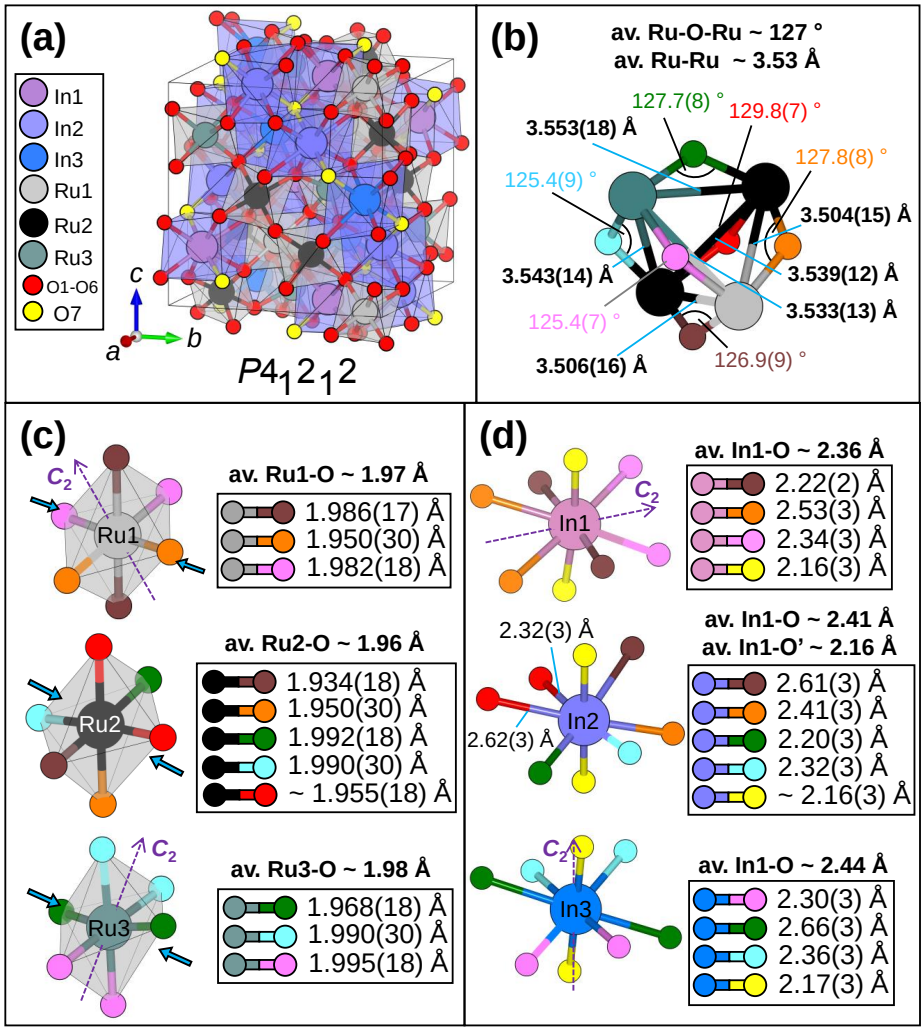

■ *Figure 5.9.* The crystal structure of $In_2Ru_2O_7$ in the $P4_12_12$ phase. The O2-derived (that is, O7) atoms, which coordinate the In atoms only, are shown in yellow. Other coloured atoms are O1-derived ones unless specified otherwise. Average (av.) bond lengths are indicated. The orientation of the C_2 axis on In and Ru sites is indicated by a purple dashed line. (a) The $P4_12_12$ unit cell. (b) The detail of the connectivity of the Ru-O network. (c) The local structure of the RuO_6 octahedra which deviate slightly from the high symmetry trigonally compressed octahedra found in the $Fd\bar{3}m$ phase. The blue arrows indicate the direction of the trigonal compression. (d) The local structure of the InO_8 scalenohedra. O and O' correspond to O1-derived and O2-derived atoms, respectively.

subgroup of $Fd\bar{3}m$ (Fig 5.9(a)), however with six nearly equally populated domains, meaning that the $In_2Ru_2O_7$ crystal is twinned. The tetragonal structure is pseudo-cubic as no clear splitting of $h00/00l$ or $hk0/h0l$ reflections in the powder high resolution neutron, x-ray and single crystal x-ray diffraction patterns was observed. The unit cell remains of approximately the same size with the unit cell parameters $a_t = 9.980\,26(19)$ Å, $c_t = 9.9808(4)$ Å. Both In and Ru sites, which are originally 16-fold in the cubic phase are split into two 4-fold and one 8-fold sites, while O1 splits into six sites (O1-O6) and O2 remains 8-fold (O7) (Table 5.2). The local symmetry of Ru1, Ru3, In1 and In3 site is C_2, while that of Ru2 and In2 is C_1. There remains one unique Ru tetrahedron as shown in Fig 5.9(b). In Fig 5.9(b) and (c) it appears that changes in the Ru-O network are not appreciable, since Ru-O bond length variance is of the order of ~ 3 %, the average Ru-O-Ru angle remains close ($\sim 127^\circ$) to the high symmetry value ($\sim 126^\circ$) and the RuO_6 octahedra deviate from the trigonally compressed geometry only marginally. On the other hand, the coordination environment around In atoms changes quite significantly as depicted in Fig 5.9(d). While the length of the (In-O2)-derived bonds coordinating In atoms only remain quite close to those found in the $Fd\bar{3}m$ phase in Fig 5.8(b), the In-O1 bonds disproportionate into three types of bonds: long (~ 2.6 Å), medium (~ 2.4 Å) and short (~ 2.3 Å). The modulation of the (In-O1)-derived bonds is of the order of 12 % in contrast to Ru-O bonds (~ 3 %).

5.3.2 Spin-orbital entangled singlet state in $In_2Ru_2O_7$ at room temperature

Above room temperature, polycrystalline $In_2Ru_2O_7$ shows an insulating behaviour in resistivity $\rho(T)$ as depicted in Fig 5.10(a). In Fig 5.10(e), the Arrhenius fit performed in the temperature region from 500 K to 450 K, that is, in the $Fd\bar{3}m$ phase, renders an activation energy of ~ 150 meV, which is comparable to that of other insulating ruthenates, such as pyrochlore $Lu_2Ru_2O_7$ [253] or layered perovskite Ca_2RuO_4 [225].

$In_2Ru_2O_7$ follows a Curie-Weiss-like temperature increase of magnetic susceptibility $\chi(T)$ on cooling as presented in Fig 5.10(b). The $Fd\bar{3}m \rightarrow P4_12_12$ structural transition at ~ 450 K does not produce any sizeable anomalies in $\rho(T)$ or $\chi(T)$ (Fig 5.10(a) and (b)), and should be of second order as evidenced by an absence of a pronounced peak in differential scanning calorimetry (DSC) at that transition temperature (Fig 5.10(c)). The lack of anomalies in physical properties across the $Fd\bar{3}m \rightarrow P4_12_12$ transformation suggests that no significant electronic change occurs.

To verify this hypothesis, scalar relativistic calculations were performed for $In_2Ru_2O_7$ $Fd\bar{3}m$ and $P4_12_12$ structural phases. First, we evaluate the DOS of the $Fd\bar{3}m$ structural phase shown in Fig 5.11(a)-(c). A metallic solution is obtained, suggesting that U is necessary to open a gap. Three distinct bands are produced between -8.5 eV and 5 eV. The states located

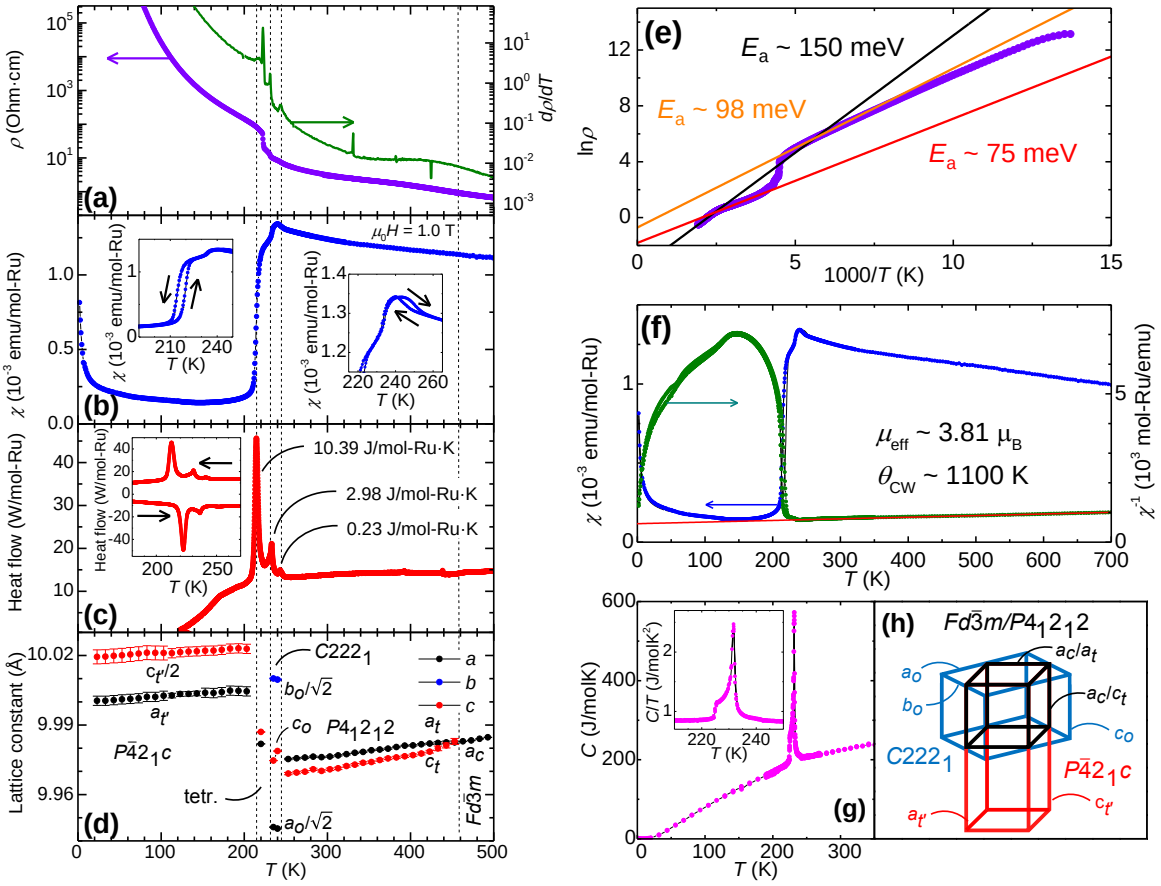

■ *Figure 5.10.* Temperature-dependent (a) resistivity $\rho(T)$ and the derivative of the resistivity $d\rho/dT$, (b) magnetic susceptibility $\chi(T)$, (c) heatflow determined with differential scanning calorimetry (DSC) and (d) the lattice parameters of an $In_2Ru_2O_7$ polycrystalline sample, obtained on cooling. In (a), below ~ 80 K, the resistance of $In_2Ru_2O_7$ sample is higher than the instrument limit. The insets of (b) show the thermal hysteresis of two transitions, where the black arrows denote the zero-field-cooling (→) and field-cooling (←) curves. In (c), the entropy release identified in the three separate first order phase transitions is indicated, and the inset shows both the heating (→) and cooling (←) DSC curves. In (d), *a*, *b* and *c* cubic, tetragonal and orthorhombic lattice parameters are scaled with respect to $Fd\bar{3}m$ lattice parameters with the relationship between the unit cells shown in (h). (e) The Arrhenius plots of $\rho(T)$ shown in (a) performed for $Fd\bar{3}m$, $P4_12_12$ and $P\bar{4}2_1c$ structural phases indicated by solid black, red and orange lines, respectively, with obtained thermal activation energies indicated. (f) The Curie-Weiss fit of $\chi(T)$ shown in (b) indicated by a red solid line. (g) Specific heat $C(T)$ of an $In_2Ru_2O_7$ polycrystalline sample. The inset shows specific heat divided by temperature around the multiple-transition region. (h) The relationship between the $Fd\bar{3}m$, $P4_12_12$, $C222_1$ and $P\bar{4}2_1c$ unit cells.

■ *Table 5.2.* Refined structural parameters of $In_2Ru_2O_7$ obtained at temperatures of 463 K and 300 K from x-ray and neutron diffraction patterns shown in Fig 5.8(c) and Fig 5.13(c), respectively. g and U_{iso} correspond to the site occupancy and the isotropic atomic displacement parameter, respectively. U_{iso} was constrained to be identical for the same elements residing on different Wyckoff sites. R_{wp} and χ^2 are refinement quality indices. a, b and c are unit cell parameters.

$T = 463$ K, $Fd\bar{3}m:2$ (No. 227), $Z = 8$. $R_{wp} = 0.0681$ and $\chi^2 = 1.99$ for 4 refined parameters. $a_c = 9.98295(10)$						
Atom	Site	x	y	z	g	U_{iso} (Å^2)
In	16d	1/2	1/2	1/2	1	0.0010(1)
Ru	16c	0	0	0	1	0.0010(1)
O1	48f	0.3409(4)	1/8	1/8	1	0.0166(10)
O2	8b	3/8	3/8	3/8	1	0.0166(10)
$T = 300$ K, $P4_12_12$ (No. 92), $Z = 8$. $R_{wp} = 0.0545$ and $\chi^2 = 3.166$ for 36 refined parameters. $a_t = 9.980\,26(19)$ Å, $c_t = 9.9808(4)$ Å						
Atom	Site	x	y	z	g	U_{iso} (Å^2)
In1	4a	0.1182(20)	0.8818(20)	3/4	1	0.0066(10)
In2	8b	0.1265(20)	0.3735(27)	0.2414(21)	1	=In1
In3	4a	0.3775(25)	0.6225(25)	−3/4	1	=In1
Ru1	4a	0.6214(11)	0.3786(11)	1/4	1	0.0039(4)
Ru2	8b	0.6241(13)	0.8726(10)	0.7583(11)	1	=Ru1
Ru3	4a	0.8709(13)	0.1291(13)	−1/4	1	=Ru1
O1	8b	0.9550(11)	0.4848(14)	0.3522(14)	1	0.00870(19)
O2	8b	0.5179(14)	0.7711(12)	−0.5796(13)	1	=O1
O3	8b	0.7181(13)	0.7559(19)	−0.3738(22)	1	=O1
O4	8b	0.9661(10)	0.0071(16)	0.8765(16)	1	=O1
O5	8b	0.9842(13)	0.2341(13)	−0.5898(14)	1	=O1
O6	8b	0.7101(12)	0.2567(16)	−0.8742(23)	1	=O1
O7	8b	0.0050(17)	0.7499(27)	0.6206(18)	1	=O1

between −8 eV and −2 eV are the (O 2p)-derived band. The band between −2 eV and 0.5 eV has predominantly Ru t_{2g} character, while the one located between 2 eV and 5 eV is the Ru e_g one. The O 2p states contribute significantly to all three bands and the weight of In 5s and band locates mostly near the (Ru e_g)-derived band. Both In 5s and 5p states have a significant contribution near the Fermi level, similarly to the case of $In_2Ir_2O_7$. The Ru t_{2g} states are split into a_{1g} and e'_g states due to trigonal distortion of RuO_6 octahedra and/or long-range trigonal crystal field discussed in chapter 4.

We proceed to comparison of the total scalar relativisc DOS of $In_2Ru_2O_7$ $Fd\bar{3}m$ and $P4_12_12$

structural phases. As shown in Fig 5.11(e), the volume of the primitive unit cell is four times smaller than that of the conventional unit cell for $Fd\bar{3}m$, and therefore the symmetry of high temperature $In_2Ru_2O_7$ was reduced to $P\bar{4}3m$ in order to produce equivalent volumes of the primitive unit cells, and hence first Brillouin zones, for the two structural phases (Fig 5.11(f)). In Fig 5.11(d), no significant difference is observed between the $Fd\bar{3}m$ and $P4_12_12$ structural phases except for a small shift of (O $2p$)-derived (Ru e_g / In s)-derived bands. This, combined with the observed physical properties, evidences that the $Fd\bar{3}m \rightarrow P4_12_12$ phase transition should not involve spin or orbital order involving Ru $4d$ electrons and could be rationalised by a lattice instability due to In-O geometry.

Since In^{3+} is non-magnetic, the magnetic response should originate from the Ru $4d$ electrons. The Curie-Weiss fit above 500 K shown in Fig 5.10(f) gives $\mu_{\text{eff}} \sim 3.8\mu_B$ and antiferromagnetic $\theta_{\text{CW}} \sim -1100$ K. The value of μ_{eff} exceeds that expected for $S = 1$, suggesting that spin-only moments cannot account for the electronic state of Ru^{4+}, or that $\chi(T)$ already deviates from the Curie-Weiss regime in the temperature range used for fitting.

In order to study the electronic structure of $In_2Ru_2O_7$, resonant inelastic x-ray scattering (RIXS) measurement at the Ru L_3 edge was performed and the result is shown in Fig. 5.12(a). At $T = 260$ K, in addition to the elastic peak, we observe six features at 53(17) meV, 276(4) meV, 394(34) meV, 700(18) meV, 1.01(2) eV and $\sim$ 3.5 eV. Large error bars for some of the peak positions are likely due to the considerable peak overlap. While the feature at 3.5 eV represents the excitations from the t_{2g} to e_g manifold, the ones below 1.5 eV correspond to excitations within the t_{2g} manifold. The $t_{2g} \rightarrow e_g$ excitation in $In_2Ru_2O_7$ has lower energy than those observed in $In_2Ir_2O_7$ and other pyrochlore iridates (Fig. 4.8(a)), which is expected due to the smaller spatial extension of the Ru $4d$ orbitals in the ruthenate. A minimum of five Voigt functions (excluding the elastic line) is required to describe the observed spectrum below 1.5 eV, and hence the t_{2g} multiplet excitations are labelled A_1, A_2, A_3, A_4 and A_5 as shown in Fig 5.12(a).

To describe the excitations observed below 1.5 eV, we employed a standard Hamiltonian for a t_{2g}^4 configuration with Hund's coupling J_{H}, spin-orbit coupling λ_{SOC} and compressive trigonal crystal field Δ_{tri}. The ideal trigonally compressed RuO_6 octahedron would have D_{3d} point symmetry as for the ideal pyrochlore lattice with $Fd\bar{3}m$ space group. In the distorted $P4_12_12$ phase at room temperature, the Ru site point symmetry is C_2 or C_i. However, distortions that deviate the RuO_6 octahedron away from D_{3d} point symmetry are relatively small, as the band structure calculations show that the Ru t_{2g} bands hold much of the a_{1g} and e_g character. Therefore, we initially neglect the additional distortions of the RuO_6 octahedron and consider the trigonal crystal field as the only non-cubic crystal field present.

We start by defining the on-site electron configuration of Ru^{4+}. The d^4 electron configura-

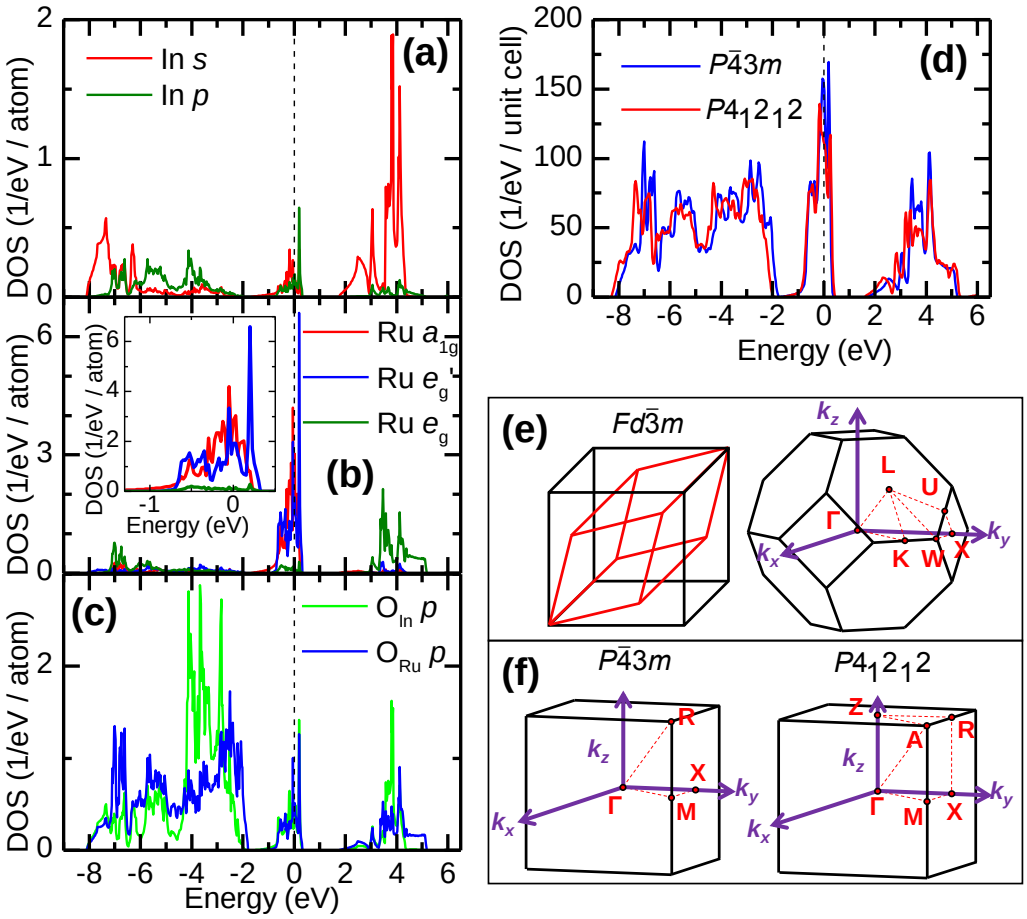

■ *Figure 5.11.* Calculated DOS for $In_2Ru_2O_7$ $Fd\bar{3}m$ and $P4_12_12$ structural phase without spin-orbit coupling. The Fermi level E_F is indicated by dashed black lines. (a) In 5*s* and In 5*p* states. (b) Ru 4*d* states with the t_{2g} manifold resolved into a_{1g} and e_g' characters in the trigonal coordinate system and the inset shows the Ru *d* states around the Fermi level. (c) O 2*p* states divided into O_{In} (O2) and O_{Ru} (O1) ones. (d) Total calculated DOS for $In_2Ru_2O_7$ in the $P\bar{4}3m$ (pseudo-$Fd\bar{3}m$ metrics) and $P4_12_12$ structural phases. (e) Left: The conventional and primitive unit cell of $Fd\bar{3}m$ shown in black and red, respectively. Right: The first Brillouin zone of the $Fd\bar{3}m$ structure. (f) Comparison of $P\bar{4}3m$ and $P4_12_12$ first Brillouin zones, where some high symmetry points, such as Γ, M and X, are equivalent between the two structures.

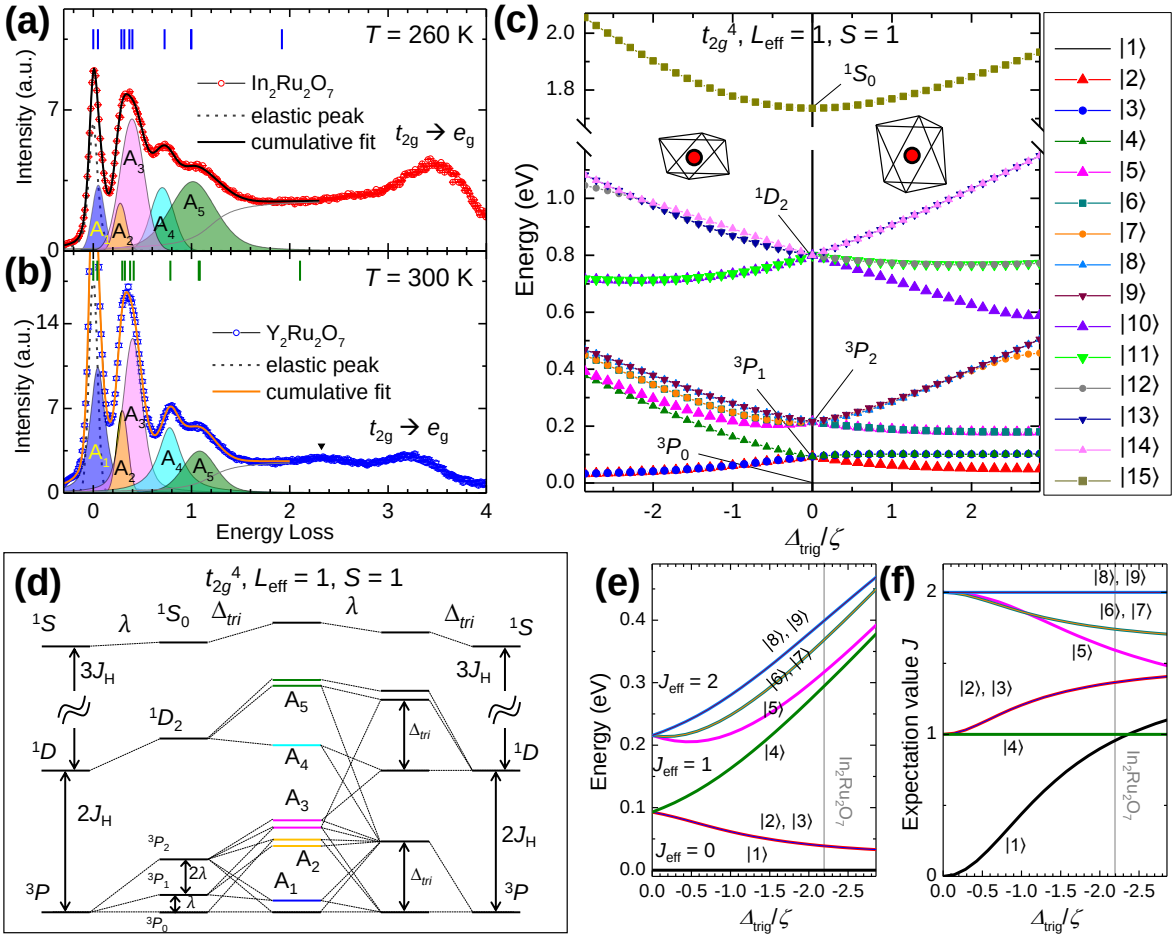

■ *Figure 5.12.* (a), (b): Ru L_3 edge RIXS spectra of $In_2Ru_2O_7$ (a) and (b) $Y_2Ru_2O_7$ polycrystalline samples with incident energy $E_i = 2839.2$ eV at $T = 260$ K (a) and 260 K (b). The dashed line shows the fitted elastic peak, while the peaks with the coloured area beneath the curve correspond to the excitations, which are schematically shown in (d). The grey line corresponds an arctangent function which represents the electronic continuum. All peaks were fitted with a Voigt profile. The blue (a) and green (b) ticks denote the energy levels obtained from the fitting discussed in the text. The black triangle in (b) marks an additional excitation. (c) Multiplet energy diagram for 15 states for t_{2g}^4 electronic configuration (labelled in order of energy) as a function of trigonal crystal field Δ_{tri}, where negative Δ_{tri} corresponds to compressive distortion. $J_{\text{H}} = 310$ meV and $\lambda_{\text{SOC}} = 70$ meV. (d) The *LS* coupling scheme of the t_{2g}^4 electronic configuration in the isolated ion description shown starting from two limits. Left: split by Hund's coupling J_{H}, then by spin-orbit coupling λ_{SOC} and finally by compressive Δ_{tri}. Right: split by Hund's coupling J_{H}, then by compressive trigonal crystal field Δ_{tri} and finally by spin-orbit coupling λ_{SOC}. The dashed lines indicate which states are mixed. The A_1, A_2, A_3, A_4 and A_5 coloured states correspond to the labelled excitations in (a) and (b). (e) A magnified region of (c) enclosing the lowest in energy 9 states ((^3P)-derived multiplet). The vertical grey line marks the Δ_{tri} value for $In_2Ru_2O_7$ obtained from fitting in (a). (f) The expectation value J as a function of compressive Δ_{tri} for the lowest in energy 9 states. The vertical grey line marks the Δ_{tri} value for $In_2Ru_2O_7$ obtained from fitting in (a).

tion is subject to an octahedral crystal field from the O_6 cage. Since the t_{2g}-e_g splitting (Δ_o) is of the order of $\sim 3.5\,\text{eV}$ and we expect $J_H < 1\,\text{eV}$, we assume the $\Delta_o = 10\,\text{Dq} \gg J_H$ and exclude e_g orbitals. The four electrons reside in the t_{2g} manifold with a $S = 1$ configuration. As $J_H > \lambda_{SOC}$, we then start with the *LS* coupling limit. First, Hund's rules render the ^3P configuration $|S = 1, L_{\text{eff}} = 1\rangle$ as the ground state, the ^1D configuration $|S = 0, L_{\text{eff}} = 2\rangle$ as the next excited state and the ^1S configuration $|S = 0, L_{\text{eff}} = 0\rangle$ as the highest energy state as depicted in Fig. 5.12(d). Second, λ_{SOC} splits the ^3P multiplet into $J_{\text{eff}} = 0$, 1 and 2 states with $J_{\text{eff}} = 0$ as the lowest energy state. Finally, the trigonal crystal field Δ_{tri} lifts the degeneracy and mixes the (^3P)-derived and (^1D)-derived states.

As shown in Fig. 5.12(c), for non-zero Δ_{tri}, the ground state remains a singlet, but is no longer a pure $J_{\text{eff}} = 0$ state because of mixture of other components. The $J_{\text{eff}} = 1$ triplet splits into a singlet and a doublet largely comprising $|J_{\text{eff}} = 1, J^z_{\text{eff}} = 0\rangle$ and $|J_{\text{eff}} = 1, J^z_{\text{eff}} = \pm 1\rangle$ states, respectively. The $J_{\text{eff}} = 2$ quintet splits into a singlet and two doublets largely comprising $|J_{\text{eff}} = 2, J^z_{\text{eff}} = 0\rangle$, $|J_{\text{eff}} = 2, J^z_{\text{eff}} = \pm 1\rangle$ and $|J_{\text{eff}} = 2, J^z_{\text{eff}} = \pm 2\rangle$ states, respectively. The higher-lying Hund's ^1D multiplet splits into two doublets and a singlet. For compressive Δ_{tri}, the doublet and the singlet states are stabilised in the ($J_{\text{eff}} = 1$)-derived and ($J_{\text{eff}} = 2$)-derived states, respectively, while within the ^1D multiplet one of the doublets is lowest in energy (left hand side of Fig. 5.12(c)).

In the large $\Delta_{\text{tri}}/\zeta$ limit, that is, when the trigonal crystal field is dominant (however $J_H > \Delta_{\text{tri}}$), the ^3P splits into a triplet and a sextet separated by Δ_{tri} (right side of Fig. 5.12(d)). Inclusion of SOC further splits these multiplets into the states smilar to those described later in this section and depicted in the centre of Fig. 5.12(d). Our band structure calculations of the room temperature $Fd\bar{3}m$ (and hence $P4_12_12$) phase without spin-orbit coupling shows a split of t_{2g} manifold into the a_{1g} and e_g states by trigonal crystal field and the energy difference between two manifolds is $\sim 200\,\text{meV}$ (Fig. 5.11(b) and (d)), therefore it is reasonable to assume that Δ_{tri} should be of the order of at least 100 meV to 200 meV. Under strong trigonal crystal field and without SOC, the energy of the first excitation should be of the order of Δ_{tri} (right side of Fig. 5.12(d)) and therefore it is not possible to explain the lowest energy peak of 53(17) meV or other peaks reasonably. This implies that the local electronic state at room temperature cannot be rationalised only with trigonal crystal field, and λ_{SOC} is necessary to be incorporated for understanding the local excitations. Indeed, for $\Delta_{\text{tri}}/\zeta \sim -2$, the multiplet in Fig. 5.12(c) matches the observed excitations reasonably.

By fitting the relevant parameters in H_{total} (section 2.3.1) to the observed peak positions, we obtain the energy level manifold marked in Fig. 5.12(e) and depicted in the centre of Fig. 5.12(d). The excitations observed at $T = 260\,\text{K}$ can be labelled in Fig. 5.12(a) as follows: A_1 is the excitation to the doublet derived from $J_{\text{eff}} = 1$ state, A_2 corresponds to the excitations

to two singlets, originating from $J_{\text{eff}} = 1$ and 2 manifold, and the A_3 is the excitation to the remaining two ($J_{\text{eff}} = 2$)-derived doublets. Finally, A_4 and A_5 correspond to the excitations to the (^1D)-derived states. The obtained values of $J_{\text{H}} \sim 310\,\text{meV}$, $\lambda_{\text{SOC}} \sim 70\,\text{meV}$ and $\Delta_{\text{tri}} \sim -300\,\text{meV}$ (compressive trigonal distortion) are similar to those reported in Ca_2RuO_4 with weak tetragonal distortion [72]. The magnitude of the non-cubic crystal field is larger in $In_2Ru_2O_7$ than that reported in Ca_2RuO_4 and can be rationalised by the strong trigonal compression of the RuO_6 octahedra. In addition, $|\Delta_{\text{tri}}|$ is smaller in $In_2Ru_2O_7$ than those found in the pyrochlore iridates shown in Table 4.2, which is consistent with the smaller Ru 4*d* orbitals in the pyrochlore ruthenate.

For the fitted parameters, the ground state remains a spin-orbital entangled singlet, however it is no longer the $J_{\text{eff}} = 0$ state. The singlet contains approximately 60 % of the $|J_{\text{eff}} = 0, J^z_{\text{eff}} = \pm 0\rangle$ state, while the remaining 40 % comprises the $|J_{\text{eff}} = 2, J^z_{\text{eff}} = \pm 0\rangle$ state, as evident from the expectation value $J \sim 1$ shown in Fig. 5.12(f). The good agreement of the RIXS spectrum with our theoretical model may imply that the approximations made so far, that is, exclusion of the e_g states and the additional distortion of RuO_6 octahedra in the $P4_12_12$ structural phase, are reasonable. The fitted Δ_{tri} is significantly larger than λ_{SOC}, however one can achieve the same multiplet structure by starting from both $\Delta_{\text{tri}} \gg \lambda_{\text{SOC}}$ and $\lambda_{\text{SOC}} \gg \Delta_{\text{tri}}$ limits.

To further justify the use of our simplified model, we compare the RIXS spectrum of $In_2Ru_2O_7$ to that of $Y_2Ru_2O_7$ with $Fd\bar{3}m$ symmetry, where only trigonal crystal field is acting on the t_{2g} manifold, as shown in Fig. 5.12(b). The RIXS spectrum of $Y_2Ru_2O_7$ at $T = 300\,\text{K}$ shows very similar features to that of $In_2Ru_2O_7$ except for slight differences in peak positions, intensities and profiles (which should be taken with caution due to peak overlap), and an additional feature at about 2.2 eV. The same fitting procedure as that used for $In_2Ru_2O_7$ gives values of $J_{\text{H}} \sim 345\,\text{meV}$, $\lambda_{\text{SOC}} \sim 70\,\text{meV}$ and $\Delta_{\text{tri}} \sim -310\,\text{meV}$. One could expect a significant difference in Δ_{tri} due to likely difference in the magnitude and/or sign of short- and long-range trigonal crystal field. Contrary to that expectation, Δ_{tri}, as well as λ_{SOC}, are quite similar between $In_2Ru_2O_7$ and $Y_2Ru_2O_7$ and J_{H} is significantly larger in the latter. This could be due to difference in inter-site hybridisation and bond-covalency of Y-O and In-O bonds.

The Curie-like behaviour of $\chi(T)$ in $In_2Ru_2O_7$ above room temperature can be attributed to two factors. The excitation between the ground state singlet to the lowest doublet is of the order of $\sim 500\,\text{K}$, and therefore sizeable contributions from the thermally-excited states should be present at high temperatures. In addition, considering the presence of long-range magnetic order in other pyrochlore ruthenates [254, 255], the magnetic exchange coupling may be strong enough compared to the magnetic excitation gap. The magnetic moments thus can originate from those residing on singlet-doublet Van Vleck transitions as well [50, 256].

- Limitations of the single ion t_{2g}^4 model

  Despite the successful fitting of the single ion t_{2g}^4 model on the RIXS data of $In_2Ru_2O_7$ and $Y_2Ru_2O_7$, there exist several possible improvements to the fits. Exclusion of e_g states is acceptable when $10\,\mathrm{Dq} \gg J_\mathrm{H}$. In reality, $10\,\mathrm{Dq} \sim 10 J_\mathrm{H}$ which can already induce mixing of t_{2g} and e_g states, additional splitting of multiplets due to cubic crystal field and modify the energy levels of the states. In addition, the pseudo-orthorhombic distortion of the RuO_6 octahedra in the $P4_12_12$ structural phase of $In_2Ru_2O_7$ should produce splitting of some multiplet levels. Finally, the hybridisation due to intersite hopping should also affect the multiplet structure, which has been discussed for $In_2Ir_2O_7$ in chapter 4. It is important to note that the peaks observed in RIXS spectra of both pyrochlore ruthenates are not well separated, and therefore fitted peak position, intensity and profile should be treated with caution.

5.3.3 Multiple phase transitions

The spin-orbit entangled singlet state is expected to display excitonic magnetism at low temperatures via the condensation of excited states. However, on cooling from 300 K, $In_2Ru_2O_7$ undergoes multiple structural phase transitions. First, at around 250 K a small hump with hysteresis in $\chi(T)$ (the right inset of Fig. 5.10(b)) and a kink in $\rho(T)$ (Fig. 5.10(a)) are observed. Simultaneously, $In_2Ru_2O_7$ becomes orthorhombic, adopting an $a_o \sim \sqrt{2}a_t$, $b_o \sim \sqrt{2}a_t$, $c_o \sim c_t$ unit cell with a space group $C222_1$ (relationship between unit cells shown in Fig. 5.10(h)) as evident from the reflections observed at 235 K in Fig. 5.13(b). Second, at about 230 K, $\chi(T)$ shows a moderate drop, while $\rho(T)$ exhibits a small jump. At that temperature, the diffraction peaks associated with the orthorhombic distortion vanish, implying that $In_2Ru_2O_7$ adopts a primitive tetragonal cell (possibly $P\bar{4}m2$ in Fig. 5.13(b)) with lattice parameters comparable to those of $P4_12_12$. As evident from DSC in Fig. 5.10(c), a total entropy of ~3 J/K·mol-Ru is released when crossing these two first order transitions, which could suggest partial quenching of orbital and/or spin degrees of freedom. The structures of those two phases are not solved yet and so far only the orthorhombic structure is indexed with the $C222_1$ space group. Therefore, the nature of the two intermediate phases is beyond the scope of this thesis.

Upon further cooling, a sharp drop of $\chi(T)$ down to a value of $\sim 2.5{\times}10^{-4}$ emu/mol-Ru is observed as shown in Fig. 5.10(b). Below 220 K, $\chi(T)$ exhibits nearly no temperature dependence, suggesting an emergence of a non-magnetic state or long-range antiferromagnetic order. The thermal hysteresis of $\chi(T)$ and a large peak in DSC with an entropy release as large as 10.39 J/K·mol-Ru suggest that the transition is of first order and involves quenching of spin and orbital degrees of freedom. Associated with the transition, $\rho(T)$ shows a discontinuous jump. Consequently, $In_2Ru_2O_7$ adopts a $P\bar{4}2_1c$ tetragonal unit cell with the c

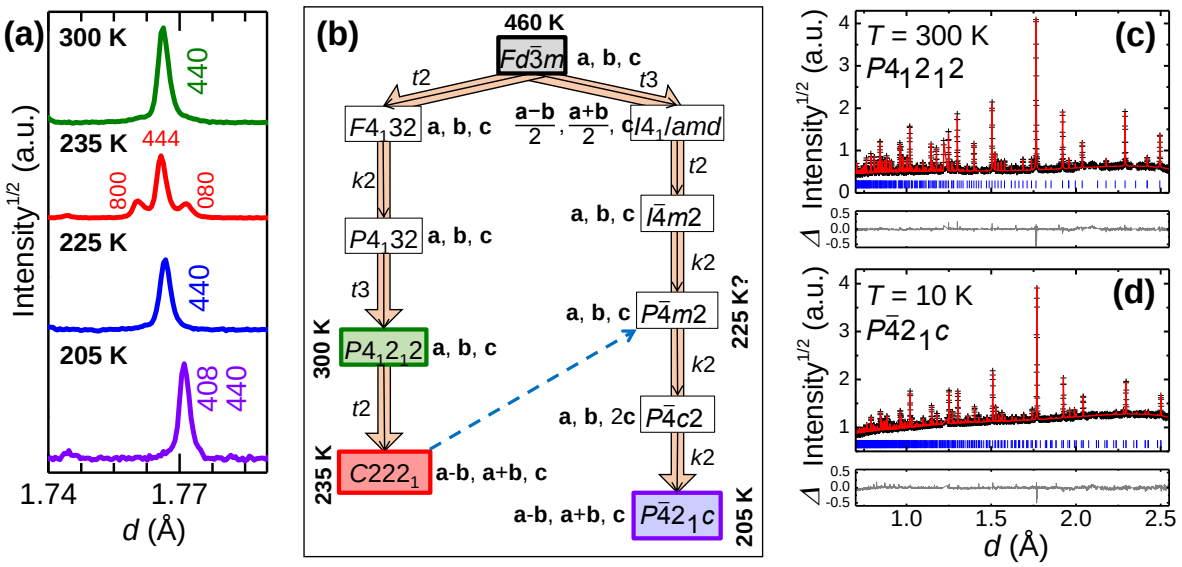

■ *Figure 5.13.* (a) Changes occurring with decreasing temperature around the 440 reflection observed in neutron diffraction powder patterns. (b) Group-subgroup relations between space groups found in all structural phases observed in $In_2Ru_2O_7$. Indices for group-subgroup relations are shown (e.g. $t2$, $k3$) as well as unit cell basis of a subgroup with respect to its supergroup. Orange arrows indicate transformations into subgroups, while the dashed blue arrow indicates that there is no group-subgroup relationship between the $C222_1$ and $P\bar{4}m2$ space groups. (c) and (d) show Rietveld analysis of the neutron diffraction powder patterns at $T = 300\,\mathrm{K}$ and $10\,\mathrm{K}$, where the black crosses, red line, grey line and blue ticks correspond to the observed pattern, the Rietveld fit profile, the difference curve between observed and calculated profiles and $In_2Ru_2O_7$ reflections, respectively. Structural parameters extracted from the depicted Rietveld plots are shown in Table 5.3.

unit cell parameter doubled as shown in Fig. 5.10(d) and (h), and seen in neutron diffraction pattern in Fig. 5.13(a) and (d). While the $Fd\bar{3}m \rightarrow P4_12_12 \rightarrow C222_1$ structural transitions obey the group-subgroup relationships, either $C222_1 \rightarrow$ primitive tetragonal or primitive tetragonal $\rightarrow P\bar{4}2_1c$ structural transition is likely to be violating Landau's postulate as shown in Fig. 5.13(b). However such a situation is allowed since, as evident from DSC (Fig. 5.10(c)), all structural transitions below 300 K are of first order. The details of the $P\bar{4}2_1c$ structural phase will be discussed in later sections.

As evident from $d\rho/dT$ in Fig. 5.10(a), the discontinuous jump occurs at a slightly higher temperature than the anomalies observed at $\sim 220\,\mathrm{K}$ in $\chi(T)$ and DSC. This could be due to the strain associated with the first order structural transition which might have a more severe effect on a pressed pellet with attached contacts used in the resistivity measurement in contrast to loose powder used in magnetic susceptibility measurement. In Fig. 5.10(g), the specific heat $C/(T)$ shows a broad, oddly shaped anomaly at $\sim 230\,\mathrm{K}$ which is consistent with the multiple first-order phase transitions in that temperature range. In addition, $C/(T)$ does

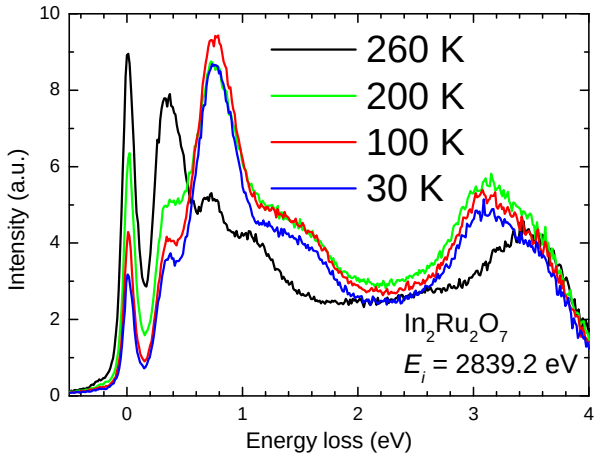

■ *Figure 5.14.* Ru L_3 edge RIXS spectra of $In_2Ru_2O_7$ polycrystalline sample with incident energy $E_i = 2839.2$ eV at $T = 260$ K, 200 K, 100 K and 30 K.

not show any other anomalies below 220 K. There are two anomalies in $d\rho/dT$ at $\sim$ 330 K and $\sim$ 430 K. The former anomaly is the temperature at which the low and high temperature resistivity data are combined resulting in a small offset. The latter could be linked to the $Fd\bar{3}m \rightarrow P4_12_12$ transition, or the crossover from an extrinsic charge gap to an intrinsic one at high temperatures.

We note that on cooling from high temperature across the multiple transitions, a total of $\sim 13.5\,\mathrm{J\,K^{-1}\,mol^{-1}}$-Ru is released. If one assumes that the ground state is a singlet, there should be no entropy to be released. However, it is likely that the higher-lying states are populated in the relevant temperature range $\sim$ 700 K and increase the entropy. The value inferred from DSC is rather close to the total entropy of Ru^{4+} $S = 1$, $L_{\mathrm{eff}} = 1$ electronic state of $R\ln((2L_{\mathrm{eff}} + 1)(2S + 1))$ of $\sim 18\,\mathrm{J\,K^{-1}\,mol^{-1}}$-Ru.

In addition, the RIXS spectra show drastic changes with decreasing temperature (Fig. 5.14). At 200 K, that is, below the sharp drop in $\chi(T)$, a large portion of the spectral weight appears to be transferred to higher energies, in particular 0.8 eV, suggesting that the local spin-orbital entangled singlet picture is no longer valid. Simultaneously, the $t_{2g} \rightarrow e_g$ shifts to lower energies energies which could be due to the occurring structural changes. In addition, the peak at $\sim$ 300 meV (excitations to ($J_{\mathrm{eff}} = 1$)-derived singlet and ($J_{\mathrm{eff}} = 2$)-derived states) shows a decrease in intensity as the temperature is lowered down to 30 K. This gradual decrease of intensity is not well understood and perhaps could be attributed to the cooling rate being insufficient for reaching thermal equilibrium at each measurement stage.

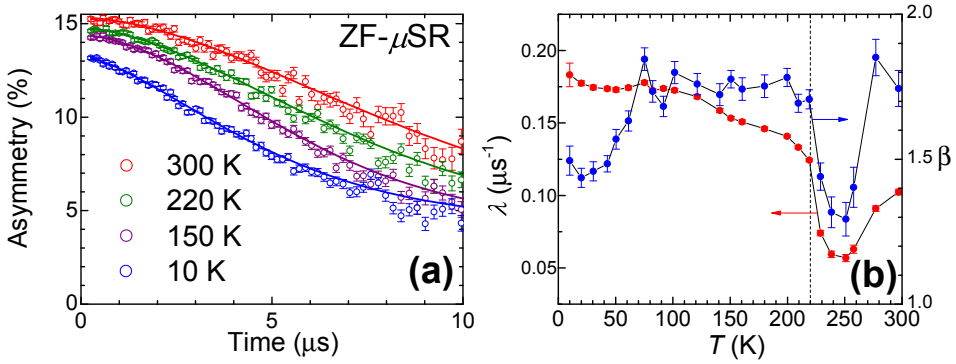

■ *Figure 5.15.* (a) Time evolution of ZF-μSR spectrum of $In_2Ru_2O_7$ polycrystalline sample at various temperatures obtained on warming. The solid lines show a stretched exponential fit of the data in the form $P_z(t) = Ae^{-(\lambda t)^\beta} + A_0$. (b) Temperature dependence of λ and β fitted with the stretched exponential. The dashed line marks the temperature of the sharp drop in $\chi(T)$.

5.3.4 Non-magnetic ground state

To identify the nature of the low temperature phase, we tracked the temperature dependence of ZF-μSR of polycrystalline $In_2Ru_2O_7$ sample. The time dependence of the muon asymmetry did not show an oscillation down to 10 K (Fig. 5.15(a)), which excludes the presence of long-range magnetic order and points to a non-magnetic state such a spin singlet or molecular orbital. Due to the lack of precise knowledge of the processes involved in the muon relaxation inside the $In_2Ru_2O_7$ polycrystalline sample, a general form of stretched exponential was used for fitting the muon relaxation:

$$P_z(t) = Ae^{-(\lambda t)^\beta} + A_0 \tag{5.2}$$

where $P_z(t)$ is the time-dependent asymmetry, A is the initial asymmetry, λ is the relaxation rate, β is the exponent and A_0 is the offset set to be identical in all temperature scans. The temperature dependence of λ and β is shown in Fig. 5.15(b) and it is evident that a sharp increase occurs in both λ and β below the transition temperature. This behaviour is similar to other compounds showing a non-magnetic spin singlet formation [235, 257–259], where an increase and then saturation of λ upon cooling across the magnetic transition corresponds to an opening of the magnetic excitation gap. One can fit the temperature dependence of λ by assuming fluctuating spins across the gap, and hence it is possible to extract the value of the gap [257]. However, in $In_2Ru_2O_7$, λ gradually increases with cooling below 220 K and β exhibits a sharp drop below 100 K. This is likely due to the glassy spin component appearing at around 150 K in $\chi(T)$ (Fig. 5.10(f)). This glassy component rendered such fitting ineffective. In addition, caution should be taken when dealing with stretched exponential fitting of μSR data, as λ and β are codependent.

5.3.5 Formation of Ru_2O trimers at low temperatures

To unveil the origin of the low temperature non-magnetic state, we investigated the structural changes occurring below 220 K. The single crystal x-ray diffraction, together with the powder neutron diffraction, showed that the crystal symmetry of $In_2Ru_2O_7$ is further reduced to the tetragonal space group $P\bar{4}2_1c$ with the doubling of the unit cell. At 10 K, the $P\bar{4}2_1c$ unit cell shown in Fig. 5.16(a) has lattice parameters of $a_{t'} = 10.004\,15(17)$ Å and $c_{t'} = 20.0148(5)$ Å and hosts four inequivalent 8-fold In as well as Ru sites with the pyrochlore lattice preserved (Table 5.3). The four Ru sites give rise to four types of Ru tetrahedra comprising exclusively Ru1 sites, two Ru2 and two Ru4 sites, exclusively Ru3 sites and all four Ru sites, respectively (Fig. 5.16(b)). Shown in Fig. 5.16(c), each RuO_6 octahedron is still approximately trigonally compressed, however the Ru-O bonds are subject to further modulation. RuO_6 octahedra undergo a "pseudo-tetragonal" compression, where two "axial" Ru-O bonds decrease in length, while the other four "equatorial" Ru-O bonds become elongated (Table 5.4). In addition, one of the axial Ru-O bonds becomes much shorter than the other ones by as much as 10 %, and those are Ru1-O11, Ru2-O6, Ru3-O4 and Ru4-O11 bonds shown in Fig. 5.16(c).

The O4, O6 and O11 atoms which are involved in a short Ru-O bond form another short Ru-O bond in the neighbouring RuO_6 octahedron, giving a short Ru-O-Ru link. In the high temperature cubic structure, those O atoms coordinate two Ru atoms and two In atoms simultaneously (Fig. 5.21(e)). In the $P\bar{4}2_1c$ structure, those O atoms are displaced much closer towards the Ru atoms, and effectively no longer coordinate the In atoms (Fig. 5.16(b) and (d)) and the In1-O4, In2-O6, In3-O11 and In4-O11 distances increase up to ~ 3 Å. As a result of this displacement, the Ru1-O11-Ru4, Ru2-O6-Ru2 and Ru3-O4-Ru3 angles are greatly enlarged and range from ~ 155 to 161°, while the average of Ru-O-Ru bonds angles along other directions remain close to the high symmetry value of $\sim 125°$ (Table 5.4). We find that while there are four inequivalent Ru sites, all of them participate in such short and large angle Ru-O-Ru geometry, which we call Ru_2O "trimers" (the oxygen atom in the trimer is denoted as O_t).

For clarity, Ru1-O11-O4, Ru2-O6-Ru2 and Ru3-O4-Ru3 trimers will be referred to as trimer 14, 2 and 3, respectively. The details of bond distances and bond angles are different for each trimer. Trimers 2 and 3 have C_2 point symmetry (C_2 axis parallel to the Ru-O-Ru plane), while trimer 14 has C_1 point symmetry, and there is twice as many 14 trimers as compared to 2 or 3. Trimers 2 and 3 orient in the $a + b$ and $a - b$ planes, respectively, and trimer 14 is oriented in the $b + c$ and $b - c$ planes. The Ru-Ru distance is the shortest within trimer 2, and the other two trimers have Ru-Ru distances comparable to other, "non-trimerised", Ru-Ru bonds (Fig. 5.16(b)), which implies that the Ru-Ru distance is not an important factor in the trimer formation. Despite the quantitative differences, the observed structural features are qualitatively the same among all trimers. The Ru_2O trimer units are effectively isolated from

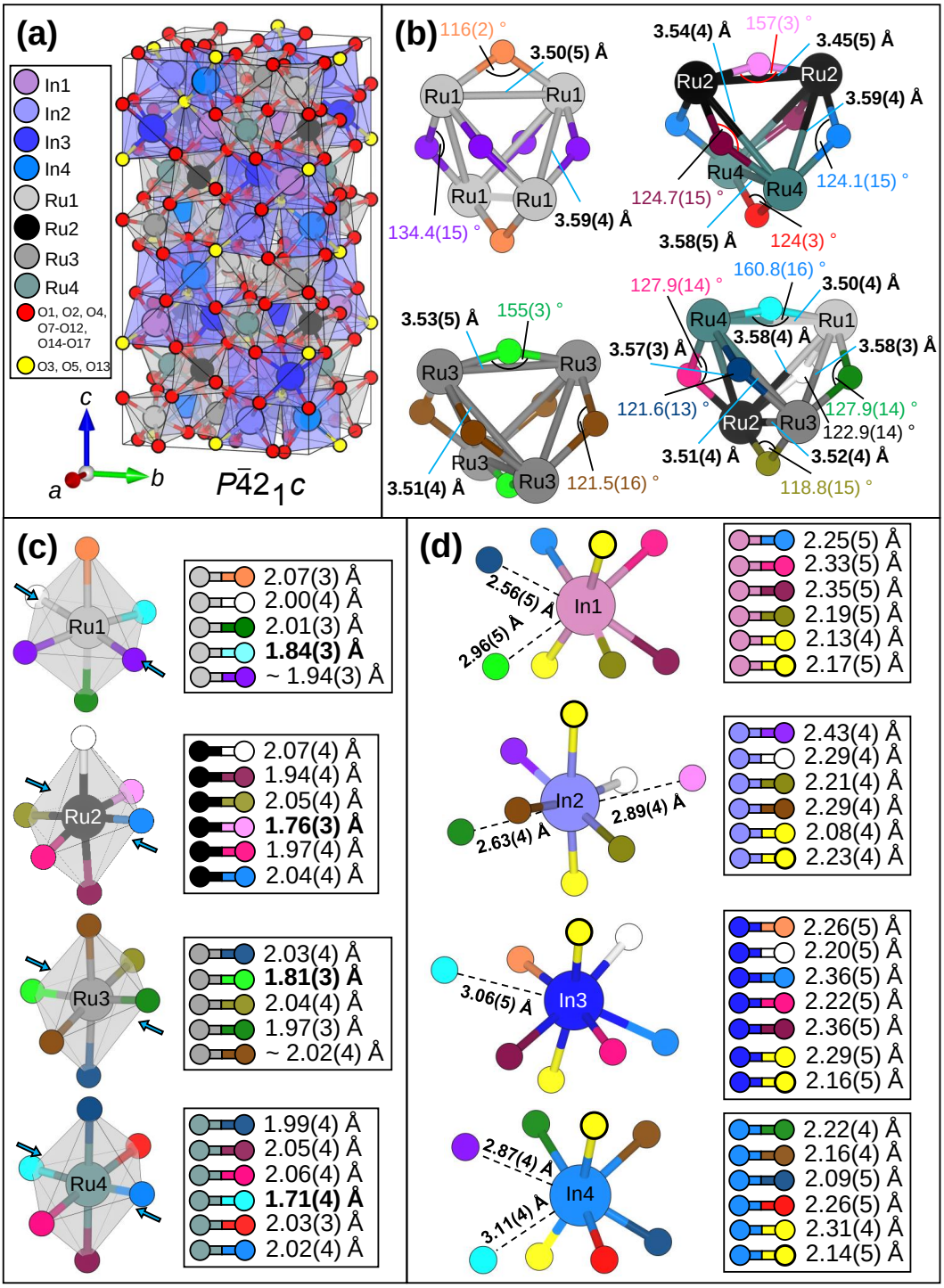

■ *Figure 5.16.* The crystal structure of $In_2Ru_2O_7$ in the $P\bar{4}2_1c$ phase. The O2-derived (that is, O3, O5 and O13) atoms, which coordinate the In atoms only, are shown in yellow. Other coloured atoms are O1-derived ones (all in different colours) unless specified otherwise. (a) The $P\bar{4}2_1c$ unit cell. (b) The detail of the connectivity of the Ru-O network. There are four types of Ru tetrahedra. (c) The local structure of the RuO_6 octahedra. The blue arrows indicate the direction of the trigonal compression axis. (d) The local structure of the InO_8 scalenohedra. The dashed lines between In and O atoms indicate that the O atom is displaced so far from the In atom that it is no longer considered to form a chemical bond with the In atom.

■ *Table 5.3.* Refined structural parameters of $In_2Ru_2O_7$ obtained at a temperature of 10 K from neutron diffraction pattern shown in Fig 5.13(d). g and U_{iso} correspond to the site occupancy and the isotropic thermal displacement parameter, respectively. U_{iso} was constrained to be identical for the same elements residing on different Wyckoff sites. R_{wp} and χ^2 are refinement quality indices. a, b, c are unit cell parameters.

$T = 10$ K, $P\bar{4}2_1c$ (No. 114), $Z = 16$. $R_{wp} = 0.0274$ and $\chi^2 = 5.810$ for 68 refined parameters.
$a_{t'} = 10.004\,15(17)$ Å, $c_{t'} = 20.0148(5)$ Å.

Atom	Site	x	y	z	g	U_{iso} (Å^2)
In1	8*e*	0.3700(34)	0.6429(35)	0.8068(19)	1	0.0028(15)
In2	8*e*	0.1395(30)	0.3619(30)	0.0681(15)	1	=In1
In3	8*e*	0.886(4)	0.8641(33)	0.1899(21)	1	=In1
In4	8*e*	0.6002(33)	0.8580(30)	0.0609(17)	1	=In1
Ru1	8*e*	0.8863(21)	0.1327(20)	0.0649(11)	1	0.0009(7)
Ru2	8*e*	0.6283(21)	0.8845(21)	0.3082(12)	1	=Ru1
Ru3	8*e*	0.3869(22)	0.3648(21)	0.9382(11)	1	=Ru1
Ru4	8*e*	0.1295(21)	0.3766(21)	0.8194(12)	1	=Ru1
O1	4*d*	0	1/2	0.8670(19)	1	0.0052(4)
O2	4*c*	0	0	0.1199(16)	1	=O1
O3	4*c*	0	0	0.2623(16)	1	=O1
O4	4*d*	1/2	1/2	0.9189(13)	1	=O1
O5	4*d*	0	1/2	0.0152(17)	1	=O1
O6	4*d*	1/2	0	0.3261(16)	1	=O1
O7	8*e*	0.4895(23)	0.2498(29)	0.8717(11)	1	=O1
O8	8*e*	0.2552(30)	0.4685(19)	0.8811(12)	1	=O1
O9	8*e*	0.5237(20)	0.7568(33)	0.3708(11)	1	=O1
O10	8*e*	0.7617(25)	0.7652(23)	0.2673(12)	1	=O1
O11	8*e*	0.7475(21)	0.1018(19)	0.1232(10)	1	=O1
O12	8*e*	0.2757(20)	0.2247(21)	0.9790(10)	1	=O1
O13	8*e*	0.7440(24)	0.7659(23)	0.1255(16)	1	=O1
O14	8*e*	0.5150(23)	0.2775(21)	0.9996(12)	1	=O1
O15	8*e*	0.5109(24)	0.7828(23)	0.2422(11)	1	=O1
O16	8*e*	0.0176(21)	0.1982(17)	0.0023(11)	1	=O1
O17	8*e*	−0.0066(25)	0.2825(23)	0.7586(11)	1	=O1

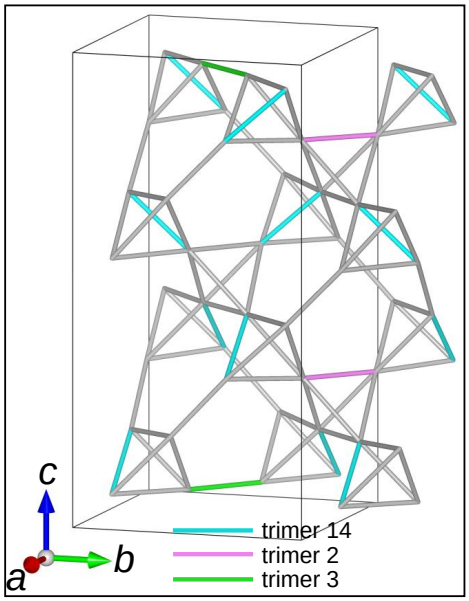

■ *Figure 5.17.* The trimer pattern adopted in the $P\bar{4}2_1c$ structural phase of $In_2Ru_2O_7$ with only Ru pyrochlore network shown. The blue, pink and green bonds denote the 14, 2 and 3 trimers, respectively.

■ *Table 5.4.* Structural features of the Ru-O network inferred from Table 5.3. z corresponds to the axial Ru-O bonds, while xy corresponds to the equatorial Ru-O bonds. For Ru-O-Ru bond angles, "trimer" refers to the shortest Ru-O-Ru links, while "long" refers all other Ru-O-Ru links in the four types of Ru tetrahedra where 1, 24, 3, and 1234 correspond to Ru tetrahedra comprising Ru1 sites only, two Ru2 and two Ru4 sites, Ru3 sites only, and Ru1, Ru2, Ru3 and Ru4 sites, respectively (Fig. 5.16(b)).

Average Ru-O bond lengths (Å)				
Orientation	$Ru1O_6$	$Ru2O_6$	$Ru3O_6$	$Ru4O_6$
z	1.89	1.87	1.89	1.87
xy	2.01	2.03	2.03	2.03
Average Ru-O-Ru bonds angles (°)				
Orientation	1	24	3	1234
trimer	161	157	155	161
long	128	130	133	130

the rest of Ru pyrochlore network because of much larger "inter-trimer" Ru-O bond lengths. Consequently, the original pyrochlore lattice of $In_2Ru_2O_7$ transforms into an arrangement of semi-isolated Ru_2O trimers as shown in Fig. 5.17.

5.3.6 Molecular orbital formation within the Ru_2O units at low temperatures

The trimer formation at low temperatures has a strong impact on the electronic structure as revealed by the band structure calculations without spin-orbit coupling. The partial DOS projected onto Ru 4*d* orbitals and O 2*p* orbitals are shown in Fig. 5.18. The calculated band structures for the $Fd\bar{3}m$ and $P4_12_12$ (Fig. 5.11(a)-(d)) structures are metallic when on-site Coulomb U is not incorporated, and both structural phases have slightly split Ru a_{1g} and e_g bands, produced by the trigonal crystal field. In contrast, the low temperature $P\bar{4}2_1c$ phase with Ru_2O trimers gives an insulating solution even without U. The trigonal coordinate system rationalised by trigonal compression of RuO_6 octahedra is no longer convenient, and instead Ru 4*d* states are resolved into d_{xy}, d_{xz}, d_{yz}, d_{z^2} and $d_{x^2-y^2}$ orbitals, where the local coordinates for each Ru site are defined such that the z axis points along the shortest RuO_t bond. Fig. 5.18 shows partial DOS relevant to (a) $Ru1O_6$, (b) $Ru4O_6$, (c) $Ru2O_6$ and (d) $Ru3O_6$ octahedra. Despite structural differences between the four RuO_6 octahedra, the relevant partial DOS produce qualitatively the same results. As shown in the middle panels of Fig. 5.18, the pseudo-tetragonal compression lowers the energy of d_{xy} and $d_{x^2-y^2}$ in the t_{2g} and e_g manifolds, respectively. The d_{xy} orbital is fully occupied, while the d_{xz} and d_{yz} orbitals are slightly mixed and split, yielding a small charge gap. The energy difference between the centroids of occupied and unoccupied t_{2g} manifolds is about 1 eV, which is close to the excitation of largest intensity observed at ~ 0.8 eV in the RIXS spectrum at $T = 30$ K shown in Fig. 5.14.

The presence of the charge gap can be attributed to the formation of molecular orbitals (MO) on the Ru_2O trimer units. The Ru_2O trimers have a noticeably large Ru-O_t-Ru angle of $\sim 160°$ which is close to the 180° bond geometry limit. Therefore, for simplicity, we consider a Ru_2O trimer with 180° bond geometry embedded in two corner-shared RuO_6 octahedra as depicted in Fig. 5.19(a) and (b). We fix the z axis parallel to the Ru-O-Ru bond and we incorporate the tetragonal compression (along z) which lowers the energy of d_{xy} and $d_{x^2-y^2}$ orbitals, rendering d_{xy} full and inactive. For the full Ru 4*d* orbital manifold, we consider both t_{2g}-p-t_{2g} and e_g-p-e_g hopping processes.

In the t_{2g}-p-t_{2g} hopping process shown in Fig. 5.19(a), Ru d_{xy} does not hybridise with O p states due to the orthogonal configuration and thus remains non-bonding. The d_{zx} and d_{yz} orbitals form an π-type overlap with O p_x and p_y orbitals, respectively. For both overlaps, one can consider three types of phase configurations: bonding (all in phase), antibonding (d in phase but p out of phase) and non-bonding (only one d and p in phase), which produce three molecular orbitals (MO). Those are indeed the solutions produced if one considers a simple Hamiltonian describing hopping in a "trilinear molecule" shown in Fig. 5.19(c). Similarly to Hückel's method [260], the used Hamiltonian does not contain any information other

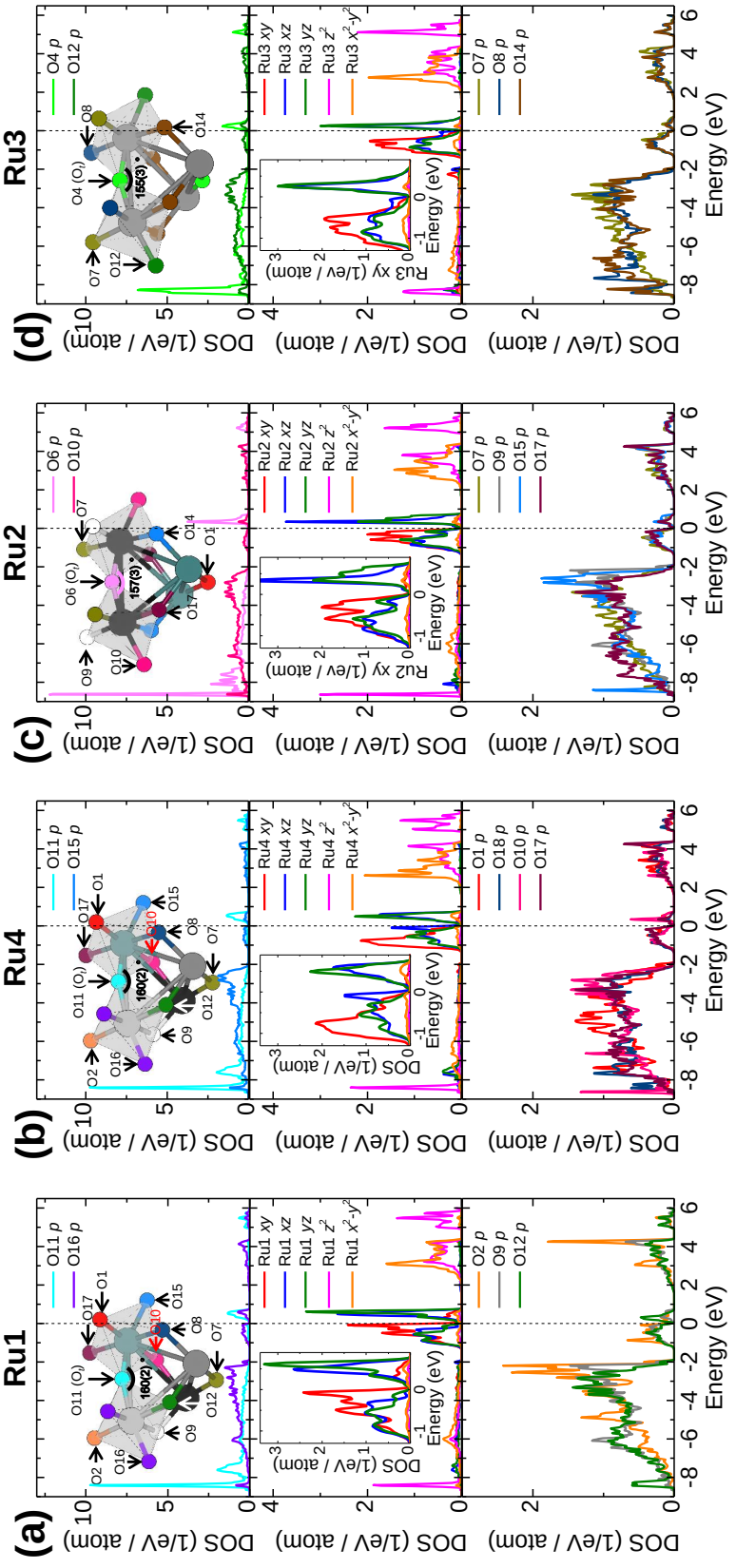

■ *Figure 5.18.* Density of states projected onto Ru *d* states and O *p* states in the $In_2Ru_2O_7$ $P\bar{4}2_1c$ structural phase corresponding to the four RuO_6 octahedra: (a) $Ru1O_6$, (b) $Ru4O_6$, (c) $Ru2O_6$ and (d) $Ru3O_6$. The Fermi level E_F is indicated by dashed black lines. Top panels show the contribution of the O atoms in the local Ru *z* axis, that is axial O *p* states. The middle panels show the Ru *d* states, where the *z* axis is fixed along the shortest Ru-O bond (that is, along (a) Ru1-O11, (b) Ru4-O11, (c) Ru2-O6 and (d) Ru3-O4). The bottom panel shows the contribution of the O atoms in the local Ru *xy* plane, that is equatorial O *p* states. For comparison of contributions between O axial and equatorial states, note the difference in scale between the top and bottom panels.

than the original atomic orbital energy and the hopping integral, and the resulting molecular orbitals can be described as a linear combination of the atomic orbitals. We can define our basis of atomic orbitals:

$$\phi_1 = p_x(p_y), \tag{5.3}$$

$$\phi_2 = d_{xz,1}(d_{yz,1}), \tag{5.4}$$

$$\phi_3 = d_{xz,2}(d_{yz,2}), \tag{5.5}$$

where ϕ_1, ϕ_2 and ϕ_3 describe the $p_x(p_y)$ and the two (1, 2) $d_{zx}(d_{yx})$ atomic orbitals. We consider hopping only between d and p orbitals, that is, the Hamiltonian matrix elements $H_{ij} \neq 0$ only if i, j are nearest neighbours (Fig. 5.19(c)). For example:

$$H_{31} = \langle \phi_3 \,|\, H \,|\, \phi_1 \rangle = t, \tag{5.6}$$

$$H_{32} = \langle \phi_3 \,|\, H \,|\, \phi_2 \rangle = 0, \tag{5.7}$$

where t is the hopping integral. We can then define the on-site energy for the p and d orbitals as E_p and E_d, respectively. Note that in this a simple approximation as we consider all hopping integrals and d orbital energies to be equivalent, which could be not the case. The Hamiltonian can be expressed as a matrix:

$$H = \begin{pmatrix} E_p & t & t \\ t & E_d & 0 \\ t & 0 & E_d \end{pmatrix} \tag{5.8}$$

Then, each of the created molecular orbitals ψ_i can be described as a linear combination of the atomic orbitals:

$$|\psi_i\rangle = a_i \,|\phi_1\rangle + b_i \,|\phi_2\rangle + c_i \,|\phi_3\rangle \,, \tag{5.9}$$

with the corresponding energies (eigenvalues of the Hamiltonian):

$$\epsilon_1 = E_d, \tag{5.10}$$

$$\epsilon_{2,3} = \frac{(E_p + E_d) \pm \sqrt{(E_p + E_d)^2 + 4(2t^2 - E_p E_d)}}{2}, \tag{5.11}$$

where ϵ_1 is the non-bonding MO located between the $\epsilon_{2,3}$ bonding and antibonding MOs in energy. For ruthenium oxide likely $E_d > E_p$, and so the bonding orbitals should be largely of oxygen character, while the antibonding orbitals are largely of ruthenium character (Fig. 5.19(c)). The e_g-p-e_g hopping process, namely σ-type d_{z^2}-p_z-d_{z^2} overlap, generates a similar result: there are three possible types of phase configurations, bonding, antibonding and non-bonding shown in Fig. 5.19(b), where the latter two are largely of d character.

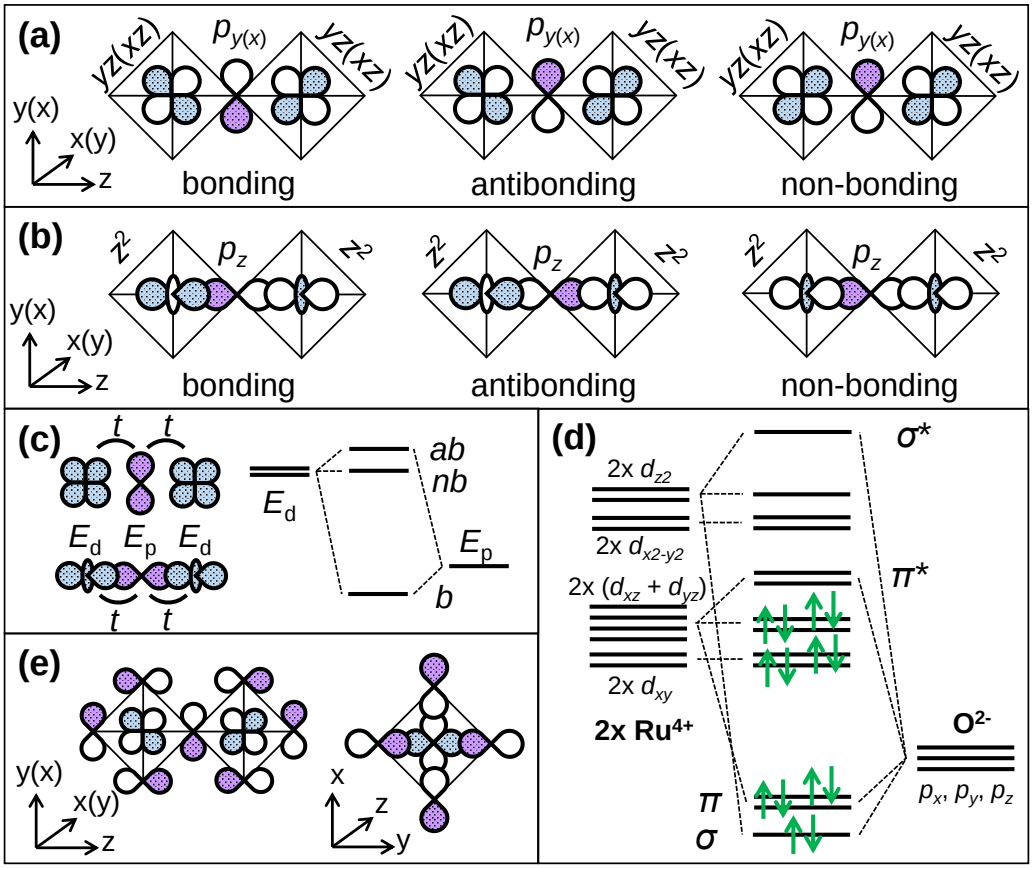

■ *Figure 5.19.* (a) π-type *d-p-d* orbital overlap in a 180° Ru-O-Ru bond geometry with two possible configurations: d_{yz}-p_y-d_{yz} and d_{xz}-p_x-d_{xz}. Three possible phase arrangements give bonding, antibonding and non-bonding molecular orbitals. (b) σ-type *d-p-d* orbital overlap in a 180° Ru-O-Ru bond geometry with d_{z^2}-p_z-d_{z^2}, which bonding, antibonding and non-bonding molecular orbitals. (c) Molecular orbital scheme for both (a) and (b). *ab*, *nb* and *b* denotes antibonding, non-bonding and bonding molecular orbitals, respectively. Note that in reality, E_d, E_p and t should not be equivalent for (a) and (b). (d) The total molecular orbital scheme including three O 2*p* orbitals and ten 4*d* orbitals from 2 Ru atoms. The d_{xy} and $d_{x^2-y^2}$ Ru orbitals are non-bonding and lower in energy due to pseudo-tetragonal compression (prior to molecular orbital formation). (e) Examples of other hopping processes generating additional hybridisation within RuO_6 octahedra. Left: bonding overlap with equatorial O *p* states of the configuration shown in (a). Right: bonding overlap of $d_{x^2-y^2}$ orbital with equatorial O p_x and p_y states.

From the above consideration, one would expect a total of eight manifolds to appear in the band structure, that is bonding, antibonding and non-bonding states from each π-type and σ-type overlap, as well as non-bonding d_{xy} and $d_{x^2-y^2}$ states depicted in Fig. 5.19(d). As the O_t atom is assumed to be no longer bonded to In atoms, it contributes its full six $2p$ electrons to the MO scheme, which together with four $4d$ electrons each from two Ru atoms gives a total of 14 electrons. As a result a band insulator is produced, where the highest (fully) occupied state in the Ru_2O unit is the non-bonding π MO, and the lowest energy excitation is that from the non-bonding π to the antibonding π^* state.

Despite the deviation of the Ru-O_t-Ru angle from 180° and additional distortions, those MO states are indeed observed in the calculated DOS of $In_2Ru_2O_7$ in the $P\bar{4}2_1c$ structure and the Fermi level locates between the π non-bonding and antibonding states (Fig. 5.19(d)) as shown in Fig. 5.18. The $d_{xz}(d_{yz})$-$p_x(p_y)$-$d_{xz}(d_{yz})$ hybridisation produces a broad bonding orbital stretching from -8 eV to -2 eV, a non-bonding orbital located between -1.5 eV and 0 eV just below the Fermi level E_F and an antibonding orbital located between 0 eV and 1 eV. The non-bonding d_{xy} orbital coincidentally overlaps with the π non-bonding states. As evident from top and middle panels of Fig. 5.18, the non-bonding π states are largely of Ru d character, while the antibonding states π have appreciable contribution from O_t p states.

Analogously, d_z^2-p_z-d_z^2 hybridisation produces bonding states manifested as a sharp peak at around -8 eV (top panels of Fig. 5.18), non-bonding states located between 2.5 eV and 4.5 eV and anti-bonding states located between 5 eV and 6 eV (middle panels of Fig. 5.18). The non-bonding $d_{x^2-y^2}$ orbital coincidentally overlaps with the σ non-bonding states. As evident from top and middle panels of Fig. 5.18, the σ bonding states have a strong contribution of the O_t p states, while the non-bonding and anti-bonding states comprise mostly the Ru d states. The σ-σ^* gap is of the order of $\sim$ 14 eV, while the π-π^* gap is smaller and about 5.5 eV, which is consistent with the difference in the strength of overlaps. The splitting of the e_g band due to formation of σ non-bonding and antibonding states is consistent with the broadening of the $t_{2g} \rightarrow e_g$ excitation observed in RIXS.

In the bottom panels of Fig. 5.18, p states of equatorial O atoms also show significant, and comparable to that of O_t, weight in bands between -8 eV and -2 eV (bonding π) as well as between 2 eV and 4.5 eV (non-bonding σ and $d_{x^2-y^2}$). This can be rationalised by not only deviations from the ideal Ru-O_t-Ru $\sim$ 180° geometry, but the additional hopping paths present within the RuO_6 units, for example between Ru d_{xz} and equatorial O p_x and p_z states, or between Ru $d_{x^2-y^2}$ and equatorial O p_x and p_y states as depicted in Fig. 5.19(e).

Incorporation of spin-orbit coupling does not show appreciable impact on the DOS of the $In_2Ru_2O_7$ $P\bar{4}2_1c$ structural phase. While the Ru d states appear to be affected as evident from shifts due to spin-orbital entanglement of the occupied states and unoccupied states, the gap

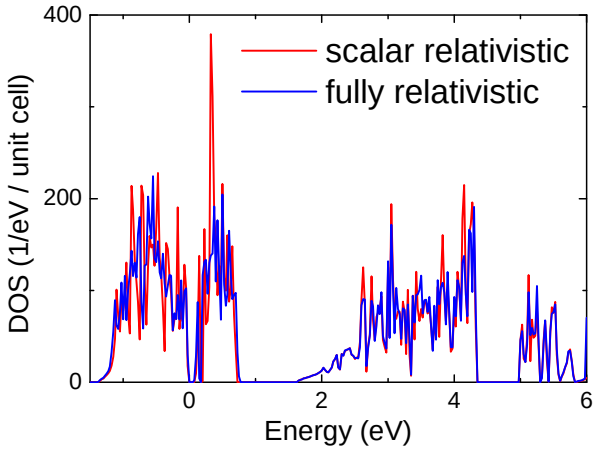

■ *Figure 5.20.* Comparison of the total calculated scalar-relativistic (without SOC) and fully relativistic (with SOC) DOS for $In_2Ru_2O_7$ in the $P\bar{4}2_1c$ structural phase.

remains robust (Fig. 5.20). Further details of the electronic structure might be affected upon incorporation of U, however bonding-antibonding split is likely the largest energy scale here, fostering trimerisation with molecular orbital formation in the non-magnetic ground state of $In_2Ru_2O_7$ produced by the strong structural distortion.

5.3.7 The role of the In-O network

This type of molecular orbital formation has never been observed in other pyrochlore ruthenates or other pyrochlore transition metal oxides. We argue that this unique feature of $In_2Ru_2O_7$ can be attributed to the nature of the In-O bonds. The A-site cation of pyrochlore oxides is coordinated by an anion scalenohedron comprising six O1 atoms and two O2 atoms as illustrated in Fig. 5.8(b). The O2 atom is located at the centre of a regular tetrahedron composed of A atoms. When the A-site cation is a rare-earth ion or Y^{3+}, the A-O bond is ionic and the high-symmetry coordination remains intact down to the lowest temperatures. In contrast, $In_2Ru_2O_7$ undergoes multiple structural transitions accompanied by drastic changes in the In-O network. In the cubic $Fd\bar{3}m$ structural phase above 450 K, the In-O2 bond-length (2.161 Å) is much shorter than that of In-O1 (2.374 Å) (Fig. 5.21(e)). The longer In-O1 bonds disproportionate into four slightly ($\sim$ 3 %) shorter bonds and two significantly longer ($\sim$ 10 %) bonds through the cubic to $P4_12_12$ tetragonal structural transition (Fig. 5.9(d)). Since the In 5s orbital locates close to the O 2p level, the In-O bonds are expected to have stronger covalent character compared with other A-O bonds of pyrochlore oxides.

In the low temperature $P\bar{4}2_1c$ structural phase below 220 K, the distortion of the In-O environment is further enhanced. Fig. 5.16(d) illustrates the In-O bonds around the four In

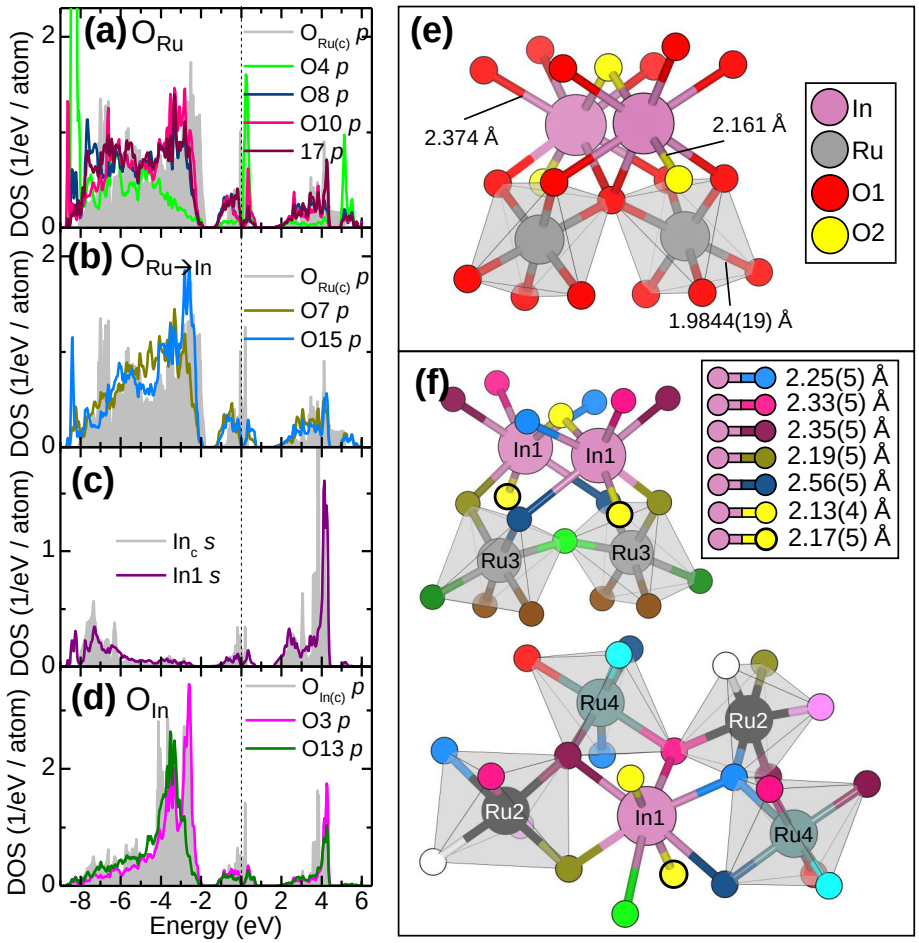

■ *Figure 5.21.* (a)-(d) Density of states projected onto In 5*s* states and O 2*p* states in $In_2Ru_2O_7$ $P\bar{4}2_1c$ structural phase corresponding to the $In1O_8$ scalenohedron. The grey states with the coloured area beneath the curve show the corresponding states in the $Fd\bar{3}m$ structural phase. (a) O 2*p* states of O atoms that remain bonded to Ru atoms. (b) O 2*p* states of O atoms that originate from O_{Ru} (O1) atoms in the $Fd\bar{3}m$ structural phase but move closer to In atoms. (c) In 5*s* states. (d) O 2*p* states of O atoms that originate from O_{In} (O2) atoms in the $Fd\bar{3}m$ structural phase. (e) The bonding of the InO_8 scalenohedra to the RuO_6 octahedra in the $Fd\bar{3}m$ structural phase. (f) The bonding of the InO_8 scalenohedra to the RuO_6 octahedra in the $P\bar{4}2_1c$ structural phase. Top: the O4 atoms bridging the two Ru3 atoms is no longer bonded to two In1 atoms. Bottom: In forms short In-O bonds with some of the O1-derived atoms.

sites. Some of the In-O bonds, which derive from the longer In-O1 bonds in the cubic phase (denoted as In-$O1_c$), become as long as $\sim$ 3 Å (In1-O4, In2-O6 and In3-O13 and In4-O13). Those involve the O_t atoms that comprise the Ru_2O trimer units: O4 (trimer 3) and O6 (trimer 2) atoms are released from two In1 (Fig. 5.21(f)) and In2 atoms, respectively, while the O13 atoms are released from In3 and In4 atoms (as the 14 trimer has no C_2 point symmetry). Effectively, the O4, O6 and O11 are no longer bonded to the In atoms and instead are strongly hybridised within the Ru_2O unit, contributing all their $2p$ electrons to the molecular orbitals.

In contrast, other (In-$O1_c$)-derived bonds shrink and become comparable to the (In-$O2_c$)-derived bond. The O atoms comprising those bonds are denoted $O_{Ru\rightarrow In}$. For example, In1-O7 and In1-O15 bond lengths are 2.19(5) Å and 2.25(5) Å, respectively, while the In1-O dumbbell bond lengths are 2.13(4) Å and 2.17(5) Å (Fig. 5.21(f)). Those shorter (In-$O1_c$)-derived bonds comprise mostly the equatorial (local xy plane) O atoms coordinating Ru atoms. In addition all In atoms except In3 have one additional longer (In-O1)-derived bond, such as In1-O8, In2-O12 and In4-O16. The short In-O bonds should have a strong covalent character, which in turn reduces the hybridisation between Ru $4d$ orbitals and O $2p$-orbitals of the equatorial O atoms. The suppressed d-p hybridisation enhances the isolation of Ru_2O molecular units from the rest of the lattice.

To further investigate the impact of the distortion on the In-O network, we asses the partial DOS projected onto In $5s$ orbitals and O $2p$ orbitals obtained with band structure calculation without spin-orbit coupling and compare them against those in the cubic phase as shown in Fig. 5.21(a)-(d). Fig. 5.21 depict partial DOS relevant to the $In1O_8$ scalenohedron, that is (a) O_{Ru} states ((In-$O1_c$)-derived bonds), (b) $O_{Ru\rightarrow In}$ states, (c) In s states and (d) O_{In} states (In-O dumbbell bonds). It appears that between -9 and -2 eV the O_{In} $2p$ states do not shift or broaden significantly in the $P\bar{4}2_1c$ as compared to $Fd\bar{3}m$ structural phase. On the other hand, in Fig. 5.21(a) and (b) the O $2p$ states shift to lower energies in the low temperature phase (Fig. 5.19(c)). While the $O_{Ru\rightarrow In}$ states show features similar to those of O_{Ru}, some of the DOS weight is transferred to higher energies, resembling the O_{In} states (Fig. 5.21(d)). In addition, the O15 $2p$ states shown in Fig. 5.21(b) contribute to the σ bonding states below -8 eV, however that can be rationalised by the fact that the O15 atom is an axial O atom in the $Ru4O_6$ octahedron, and hence quite likely participates in the σ-type hybridisation (top panels in Fig. 5.18). The changes occurring in the In and O bands do not seem to shed more light on the molecular orbital formation, however the subtle changes in the O bands corresponding to different types of In-O bonds do corroborate the bond disproportionation discussed above.

5.4 Discussion

The new pyrochlore ruthenate $In_2Ru_2O_7$ displays competition between a spin-orbital entangled singlet state and molecular orbital formation. Despite the largest trigonal distortion among the family of pyrochlore ruthenates, spin-orbit coupling λ_{SOC} is operative and produces a spin-orbital entangled singlet state at room temperature. Evidence of a similar singlet state in sister compound $Y_2Ru_2O_7$ implies that other pyrochlore ruthenates $A_2Ru_2O_7$ with trigonal distortion smaller than that found in $In_2Ru_2O_7$ also have a spin-orbital entangled state and their long-range magnetic ordering may represent an excitonic magnetic order. In contrast to those pyrochlore ruthenates, $In_2Ru_2O_7$ displays complex phase transitions and eventually becomes a non-magnetic insulator accompanied by a formation of molecular orbitals on the Ru_2O trimer units. The origin of multiple transitions below 250 K is not clear yet, and further structural analysis is required to unravel the nature of intermediate phases. As we observe substantial entropy release even above 220 K, we expect that the transitions at 235 K and 225 K should involve spin and orbital degrees of freedom, likely a precursor for the Ru_2O molecules.

Among the pyrochlore ruthenates, $Tl_2Ru_2O_7$ undergoes a metal-to-insulator transition and displays a non-magnetic ground state, similar to that of $In_2Ru_2O_7$, below 120 K [229]. The origin of non-magnetic state has been attributed to the formation of spin-singlet Haldane chain on the pyrochlore lattice within 1D Ru zigzag chains produced by lattice distortion. As Tl locates right below In in the periodic table, a similarly strong covalent *s-p* bond would be expected. The Tl-O bond covalency and disproportionation has indeed been addressed [231, 233, 237]. However, the influence of this covalency on the Ru 4*d* electronic states has not been fully explored.

Covalency effects in In-containing compounds however have been addressed in context of hybrid orbitals in indate spinels and metallic In long time ago in Ref. [261]. For instance, metallic In forms a FCC tetragonal lattice with $c/a > 1$ which is discussed to be induced by dsp^2 hybrid orbital formation. dsp^2 hybrid orbital is formed with In s, p_x, p_y and $d_{x^2-y^2}$ orbitals and favours square planar coordination (Fig. 5.22(b)). It is therefore believed that the tetragonal structure of In is induced by formation of strong covalent In bonds in the square lattice as shown in Fig. 5.22(a). A similar mechanism has been proposed in tetragonal ($c/a > 1$) spinels $CaIn_2O_4$ and $CdIn_2O_4$, where In occupies octahedral sites and forms similar hybrid orbitals to those of metallic In with O atom ligands coordinating the In atoms instead. The distortion of metallic In and indates is not driven by JT-instability discussed in chapter 1, and is a result of bond disproportionation due to bond covalency instead. It is likely that $In_2Ru_2O_7$ shows a similar mechanism, however the In 4*d* states do not locate in the vicinity of the 5*s* and 5*p* states and hence such dsp^2 hybridisation should not be relevant. Nevertheless, it

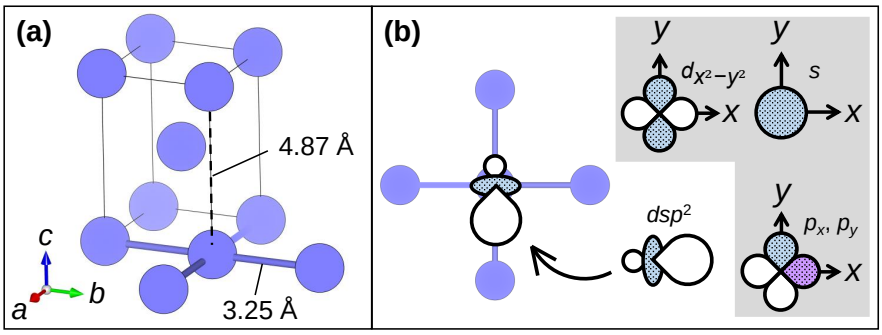

■ *Figure 5.22.* (a) Crystal structure of the metallic In with the short In-In bonds shown. (b) Possible explanation of the tetragonal distortion found in metallic In. The dsp^2 hybrid orbitals comprise In s, p_x, p_y and $d_{x^2-y^2}$ orbitals shown in the grey area. Each out of four dsp^2 hybrid orbitals is aligned with one of the In-In bonds.

is possible that some type of s-p hybrid orbital formation takes place in $In_2Ru_2O_7$, although it is not obvious what kind of bond geometry is preferred. The shortest In-O bonds in the $P\bar{4}2_1c$ $In_2Ru_2O_7$ structural phase form trigonal prismatic, octahedral, or square pyramid (all strongly distorted) coordinations around different In sites depending on the fixed In-O bond length limit. We are not aware of materials with partially filled d orbitals (magnetically active) that undergo a structural transition induced by bond disproportionation/hybrid orbital formation due to constituent magnetically inactive cation - ligand anion covalency effects. $In_2Ru_2O_7$ therefore appears as a first magnetic and spin-orbital entangled material that likely exhibits such a phenomenon.

In contrast to $In_2Ru_2O_7$, the $5d$ counterpart $In_2Ir_2O_7$ remains cubic down to the lowest temperature and spin-orbital entangled $J_{\text{eff}} = 1/2$ wave function is robust [170] (Chapter 4). In Fig. 5.23, a comparison of DOS in the $Fd\bar{3}m$ structure without spin-orbit coupling between the two compounds shows that the t_{2g} band is broader and the t_{2g}-e_g split is greater for $In_2Ir_2O_7$ as a consequence of more spatially extended $5d$ orbitals as compared to the Ru $4d$ orbitals. In addition, the O_{Ir} $2p$ bands below -2 eV locate at lower energy in $In_2Ir_2O_7$ (Fig. 5.23(d)). The O_{In} states of $In_2Ru_2O_7$ at around 4 eV are broadened compared with those of $In_2Ir_2O_7$, which could point to hybridisation of the In-O network with the Ru e_g states.

A more naïve rationalisation of the stark contrast between $In_2Ru_2O_7$ and $In_2Ir_2O_7$ involves the magnitude of spin-orbit coupling and d^5 electron count of Ir^{4+}. Firstly, spin-orbit coupling in $In_2Ir_2O_7$ is of the order of $\zeta \sim 0.4$ eV (while that of $In_2Ru_2O_7$ is ~ 0.15 eV) and is therefore larger than the non-cubic crystal field, likely fostering a more robust J_{eff} state against In-O lattice instability. Secondly, in the case of hypothetical Ir_2O molecular unit formation there would be two more electrons filling the molecular orbital manifold shown in Fig. 5.19(d), resulting in partial filling of the π^* antibonding orbitals and destabilisation of molecular

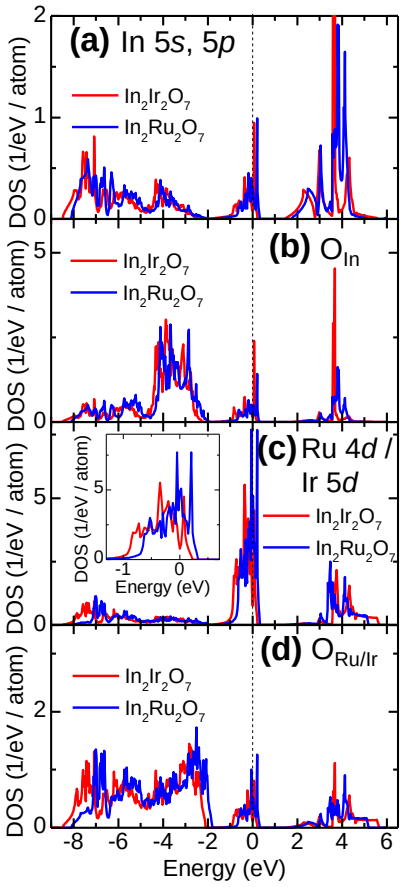

■ *Figure 5.23.* Calculated DOS for $In_2Ir_2O_7$ and $In_2Ru_2O_7$ $Fd\bar{3}m$ structural phases without spin-orbit coupling. The Fermi level E_F is indicated by dashed black lines. (a) In 4*s* and In 4*p* states. (b) O_{In} (O2) *p* states. (c) Ir 5*d* and Ru 4*d* states. (d) O_{Ir} and O_{Ru} (O1) *p* states.

orbital formation.

The competition between spin-orbital entanglement and molecular orbital formation has been seen in a number of 4*d* or 5*d*-based systems such as honeycomb-based iridates and ruthenates, particularly under pressure [103, 161, 162, 165, 167, 169] (see chapter 3). While spin-orbit coupling works to mix nearly degenerate t_{2g} orbitals to produce J_{eff} wave functions, strong inter-site hopping of specific t_{2g} orbitals may lead to a bonding and antibonding split of molecular orbitals, which lifts the degeneracy of t_{2g} manifold. A distinct feature in $In_2Ru_2O_7$ is that the molecular orbitals are formed with the involvement of the oxygen 2*p* electrons, namely induced by Ru 4*d*-O 2*p*-Ru 4*d* hopping through the corner-sharing connection, whereas the direct *d*-*d* hopping across the shared edges of the octahedra plays a crucial role in the honeycomb-based systems.

Orbital molecule formation is rare among $A_2B_2O_7$ magnetic pyrochlore oxides, while it is

common in AB_2O_4 spinels [41], which is likely due to "inconvenient" $\sim 130^\circ$ *B*-O-*B* angles in corner-sharing geometry in the former and easily favoured direct *d*-*d* hopping in the *B*-O_2-*B* edge-sharing geometry in the latter. In addition, Ru_2O trimer formation in $In_2Ru_2O_7$ is the first reported trimer molecule in 4*d* and 5*d* materials. So far, one pyrochlore oxide, $Y_2Mo_2O_7$ (Mo^{4+}, d^2), which exhibits spin glassy behaviour [262, 263], has been discussed to host disordered Mo_2 dimers [264]. The glassy behaviour has been attributed to freezing of one of the many degenerate dimer arrangements on the pyrochlore lattice, however it still remains under debate. Recently it has been proposed that the glassy behaviour can be attributed to freezing of one of the many degenerate 2-in-2-out Mo^{4+} magnetic moment (instead of dimer) arrangements, and the associated distortion occurs due to giant magnetoelastic coupling (lattice following spin) [265]. While $Y_2Mo_2O_7$ is a peculiar pyrochlore with Mo_2 dimers and structurally might be somewhat relevant here, its behaviour is rather different from that of $In_2Ru_2O_7$. The Mo_2 dimers are associated with short Mo-Mo bonds, where the Mo-O-Mo angle *decreases* to 116° as likely the bridging O atom is pushed away by the two Mo atoms moving closer to each other. The Mo-O-Mo angle is discussed to scale the magnetic exchange interaction that is related to the 2-in-2-out configuration [265]. In contrast, the Ru-Ru distances do not seem to play a significant role in $In_2Ru_2O_7$. Instead, the short Ru-O bonds and the Ru-O-Ru angle, which *increases* to $\sim 155^\circ$ along the short Ru-O bonds, lead to formation of non-magnetic Ru_2O trimers.

5.5 Conclusion

$In_2Ru_2O_7$ therefore offers a unique playground where subtle competition between spin-orbit coupling, crystal field, inter-site hopping and In-O bond covalency takes place. Despite the strong non-cubic crystal field, the spin-orbit coupling remains relevant and a spin-orbital entangled singlet state is stabilised. With decreasing temperature, the spin-orbital entangled state does not survive in $In_2Ru_2O_7$ due to the effect of In-O bond covalency on the Ru-O network. The In-O hybridisation induces distortion and disproportionation of covalent In-O bonds, which in turn generates formation of semi-isolated Ru_2O trimers. $In_2Ru_2O_7$ is the first 4*d* material with molecular orbital formation involving the O^{2-} anion, where spin-orbital entangled state magnetism is destroyed by the covalent *A*-O bond. This implies that covalent *A*-O bonds are an interesting player in competition with other interactions and can render different exotic electronic states depending on the selection of the crystalline lattice. Therefore, 4*d* materials with *A*-O bond covalency are a fascinating playground for exploring the competition between J_{eff}-pseudospin magnetism and molecular orbital formation.

Chapter 6

Conclusion

Transition metal compounds containing heavy 4*d* and 5*d* elements serve as a platform for exploration of novel electronic states. As spin-orbit coupling becomes large in those materials, novel states of matter have been predicted such as quantum magnet, Kitaev spin liquid, excitonic magnet, Weyl semimetal or topological Mott insulator. While spin-orbital entangled states can be stabilised in a variety of materials, other interactions are present on the same energy scale as spin-orbit coupling, such as correlation, intersite hopping or non-cubic crystal field. Therefore the class of heavy-transition-metal materials can stabilise or be tuned towards other exotic electronic states such as non-magnetic orbital molecule investigated here. Such tuning can be achieved by varying temperature, pressure or chemical substitution.

Here, we demonstrate that the $J_{\text{eff}} = 1/2$ magnetism in a Kitaev material β-Li_2IrO_3 can be destroyed by application of external pressure. At high pressures, β-Li_2IrO_3 forms short Ir–Ir bonds and exhibits a non-magnetic molecular orbital state along the dimers. Such competition between dimers and spin-orbital entangled magnetism seems to be a universal feature of Kitaev materials.

We also tested the stability of $J_{\text{eff}} = 1/2$ state against trigonal crystal field in pyrochlore iridates with large distortion. We found a new compound $In_2Ir_2O_7$, which is a unique pyrochlore iridate as it hosts a nearly pure $J_{\text{eff}} = 1/2$ state despite the non-cubic crystal field. Our band structure calculations indicate that intersite hopping plays a central role in mixing of the J_{eff} states, which is quite large in other pyrochlore iridates. However, what makes $In_2Ir_2O_7$ unique is the covalent *A*-O bond, which by hybridising with the Ir-O reservoir reduces the intersite hopping and $J_{\text{eff}} = 1/2$-$J_{\text{eff}} = 3/2$ hybridisation. Therefore, the covalent *A*-O bond is one possible recipe for stabilising a nearly pure spin-orbital entangled state.

Finally, we explored the interplay of spin-orbit coupling, non-cubic crystal field and *A*-O bond covalency in newly discovered pyrochlore ruthenate $In_2Ru_2O_7$. We find that at high temperatures, while the non-cubic crystal field splits and mixes the J_{eff} states, it fails to fully quench orbital moments, and a spin-orbital entangled singlet is rendered as the ground state. With decreasing temperatures however, $In_2Ru_2O_7$ undergoes several structural transitions which largely modify the electronic structure, and the spin-orbital entangled singlet does

not survive. The crystalline lattice strongly distorts, and some Ru-O-Ru angles increase from $\sim 125^\circ$ to nearly $\sim 160^\circ$, which brings the Ru-O-Ru link close to the 180° bond geometry. As a result, semi-isolated non-magnetic Ru_2O units form on the pyrochlore lattice, serving as a first example of a non-magnetic orbital molecule involving the O^{2-} anion on top of pyrochlore lattice. The distinct behaviour of $In_2Ru_2O_7$ as compared to other pyrochlore ruthenates is believed to be caused by the bond disproportionation of the covalent In-O network.

Several issues remain to be addressed for the materials studied here. First, it would be of interest to determine the magnetic order of $In_2Ir_2O_7$ in order to elucidate the influence of In-O bond covalency on the magnetic exchange couplings. For the case of new material $In_2Ru_2O_7$, many aspects still remain a mystery due to its complicated behaviour. The crystal and electronic structure of the observed intermediate phases is yet to be solved, and once determined it could shed light on the driving force of the ground state. Furthermore, the role of In-O covalency in the structural transitions is not entirely clear. In addition, the stark difference between $In_2Ir_2O_7$ and $In_2Ru_2O_7$ requires further explanation which could not be given here. It would be interesting to explore other new 4*d* and 5*d* magnetic pyrochlore or other materials comprising the In^{3+} atom, such as $In_2Mo_2O_7$ or $In_2Os_2O_7$. Materials containing other constituent non-magnetic *A* cations with covalent *A*-O bonds are also worthy of investigation.

This thesis demonstrates that transition metal compounds, where strong spin-orbit coupling competes with other electronic parameters, offer a plethora of exotic electronic phases. By selection of electron count, crystalline lattice and energy scales one can tune the ground state between spin-orbital entangled states, orbital ordering or orbital molecules. *A*-O covalency of constituent non-magnetic cation has been proven to be an important player in stabilisation of both spin-orbital entangled and orbital molecule phases. In particular, exploration of new compounds provides exciting new systems with a new story to tell and new questions to ask.

Appendix A

Structural aspects

Properties of TMOs largely depend on the arrangement and connectivity of the constituent atoms, that is, on the crystal structure comprising ligand anions, transition metal B and constituent cations A. Known crystal structures can be considered as arrangements of building blocks of simple metal oxide polyhedra, such as octahedra or tetrahedra. The ionic radius of O anion is larger ($\sim$ 1.3-1.4 Å) than that of transition metal cations ($\sim$ 0.5-1.2 Å) [266]. Therefore, one can consider first packing of the larger O anions, where the produced voids are then occupied by the smaller transition metal cations. The packing of highest efficiency is cubic closed packing (CCP, also known as face centred packing FCC) and hexagonal cubic packing (HCP). Many types of lattices can be derived from the FCC packing of O atoms which hosts octahedral and tetrahedral voids, as demonstrated in Fig. A.1(a).

If one fills all the octahedral voids, a rocksalt structure adopted by NaCl or CoO is produced (Fig. A.1(b)). In Fig. A.1(d), one can obtain the honeycomb structure from the rocksalt which is discussed in the next section. One can also modify the O FCC lattice in another way. If one replaces 1/4 of the O atoms by A atoms, 3/4 of all octahedral voids are annihilated. Then, by filling the remaining 1/4 of the octahedral voids with B one obtains ABO_3 perovskite as illustrated in Fig. A.1(e). If one then separates the 2D layers of octahedra in the ab plane, a layered perovskite is produced A_2BO_4 shown in Fig. A.1(f). Intermediate structures between the ABO_3 and A_2BO_4 exist with the generalised formula $A_{n+1}B_nO_{3n+1}$ dubbed the Ruddelsden-Popper series [267], where n denotes the number of single corner-sharing layers (for perovskite and layered perovskite $n = \infty$ and $n = 1$, respectively).

The famous frustrated spinel structure AB_2O_4 is also based on the O FCC lattice and is generated by filling 1/2 of the octahedral voids with B atoms and 1/8 of the tetrahedral voids with A as demonstrated in Fig. A.1(g). B cations form corner-sharing tetrahedrons, that is, the pyrochlore network, with edge-sharing B-O_2-B link. There is another famous pyrochlore network $A_2B_2O_7$ with corner-sharing B-O-B link, however, as discussed below, it has to be built from combined FCC and primitive cubic (CP) packing of cations and anions, respectively.

Another type of lattice is hyperkagome lattice $A_4B_3O_8$, which is a three-dimensional version of frustrated kagome lattice of B atoms consiting of corner-sharing triangles shown

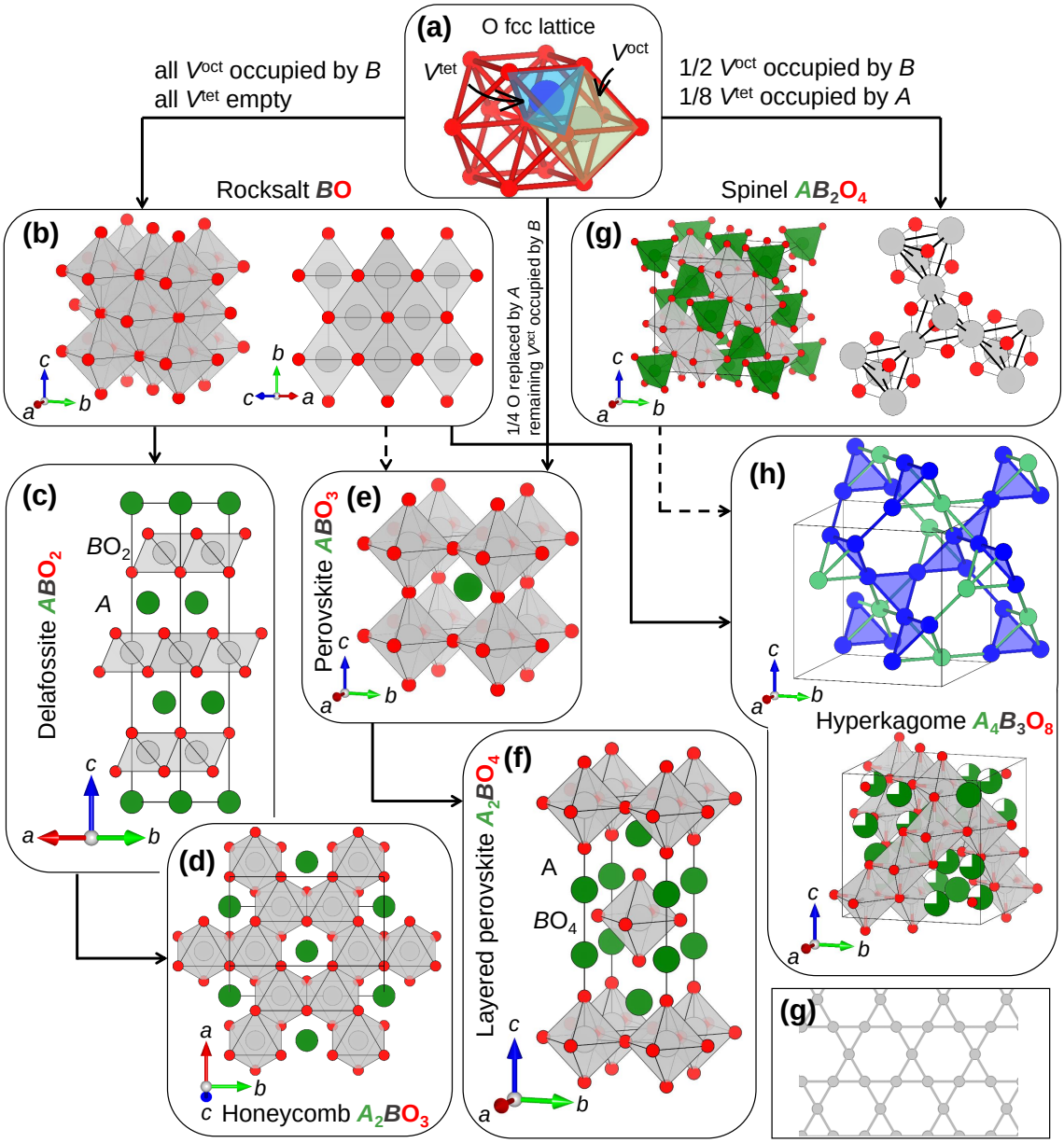

■ *Figure A.1.* Routes to various ternary oxide crystal structures (a) by filling octahedral (V^{oct}) and tetrahedral (V^{tet}) voids in an O anion FCC lattice with magnetic B and constituent A cations. (b) Rocksalt BO lattice obtained by filling all octahedral voids in (a). (c) The delafossite ABO_2 lattice obtained by replacing every other B layer along the (111) direction in (b) with A. (d) The honeycomb A_2BO_3 obtained by replacing 1/3 of B with A within the BO_2 layers in (c). (e) Perovskite ABO_3 structure can be generated by replacing 1/4 of the O anions forming the FCC lattice in (a) with constituent atoms A, which removed 3/4 of V^{oct}. The remaining V^{oct} are filled with B atoms. It can also be understood as a modification of the rocksalt structure, where every other B is removed in a checker board fashion, which leaves uncoordinated O atoms replaced by A atoms. (f) Layered perovskite A_2BO_4 structure, a two-dimensional version of the perovskite in (e). *Caption continued on the next page.*

■ *Figure A.1. Caption continued from the previous page.* (g) Left: Spinel AB_2O_4 structure obtained by filling 1/2 of octahedral voids with B and 1/8 of tetrahedral voids with A. A pyrochlore network with edge-sharing BO_6 octahedra intercalated by AO_4 tetrahedra is generated. Right: The B pyrochlore lattice (shown in thick black line) with B-O_2-B edge-sharing link shown. (h) Hyperkagome $A_4B_3O_8$ structure is a derivative of the rocksalt structure, as all A and B atoms occupy octahedral voids in (a). However, the hyperkagome network of B atoms can be seen as a modification of the pyrochlore network in the spinel in (g), where one of four B sites on each tetrahedron is replaced with A atom (top, hyperkagome network shown in dark blue). In addition, some A vacancy (bottom) is introduced. (h) The 2-dimensional kagome lattice, the parent of 3-dimensional hyperkagome lattice.

in Fig. A.1(g). The hyperkagome structure is a derivative of the rocksalt structure, however the network of B atoms can be understood as a pyrochlore lattice stripped of one atom in each tetrahedron as shown in Fig. A.1(h).

Honeycomb and hyperhoneycomb lattice

Honeycomb α-A_2BO_3 lattice is a superstructure of a rocksalt structure. In the parent rocksalt structure AO, the cations are arranged in face-centred cubic packing while the anions fill all the octahedral voids (or vice versa), corresponding to 4a and 4b Wyckoff sites in the $Fm\bar{3}m$ space group, respectively. Each cation is coordinated by six anions rendering edge-sharing AO_6 octahedra as shown in in Fig. A.2(a). The AO $Fm\bar{3}m$ structure has only one degree of freedom, the unit cell parameter. The honeycomb superstructure can be constructed by first introducing occupational disorder in the rocksalt via inserting a new cation A onto the 4a site, resulting in $A_{2/3}B_{1/3}O_2$ chemical formula. Subsequently, the disorder can be lifted in a number of ways [268].

In Fig. A.2(c), the B cation appears only in every other layer along the c axis. Within the $\sim AB_2$ layers, the A and B cations order such that they form inter-penetrating triangular and honeycomb lattices, respectively. As a result, the B sub-lattice form a semi-two-dimensional honeycomb lattice comprising edge-sharing BO_6 octaherda, where the honeycomb voids are occupied by the A cations and the layers are separated by the A cation. Such ordering reduces the symmetry from cubic $Fm\bar{3}m$ to monoclinic $C2/m$ with a monoclinic angle of $\beta \sim 110^\circ$ (Fig. A.2(b)). The lowering of symmetry to monoclinic gives many additional degrees of freedom as evident from split $C2/m$ sites in Table A.1, which results in distortions of the BO_6 octahedra and deviations from the ideal 90° bond geometry in real honeycomb materials.

Another way of lifting the disorder induced in Fig. A.2(a) is formation of an arrangement of A and B cations shown in Fig. A.2(d), where the B cations form a three-dimensional analogue of the honeycomb network called the hyperhoneycomb β-A_2BO_3. Similarly to the honeycomb, the reduction of symmetry allows distortions as evident from Table A.1. Each B cation has

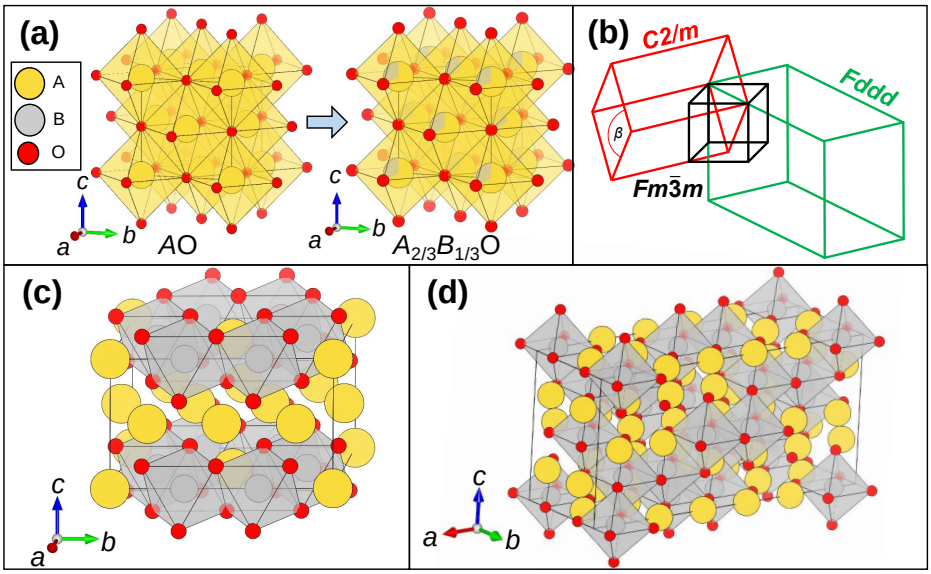

■ *Figure A.2.* (a) The crystal structure of *A*O rocksalt with space group $Fm\bar{3}m$ and $a \sim 5$ Å with occupational disorder. (b) The illustration of the unit cell transformation from rocksalt into honeycomb ($C2/m$) and hyperhoneycomb ($Fddd$) structures. (c) The honeycomb structure with only BO_6 octahedra shown. (d) The hyperhoneycomb structure with only BO_6 octahedra shown.

three *B* cation neighbours, and hence the local environment of the BO_6 octahedron in the hyperhoneycomb network is the same as that found in the honeycomb network.

Pyrochlore lattice

Cubic pyrochlore $A_2B_2O_7$ is a superstructure of a simple fluorite adopted by CaF_2 or ZrO_2. In the parent fluorite structure AO_2, the cations form face-centered cubic packing while the anions fill all the tetrahedral voids, corresponding to 4*a* and 8*c* Wyckoff sites in the $Fm\bar{3}m$ space group, respectively. Each cation is coordinated by eight anions rendering edge-sharing AO_8 scalenohedrons as shown in Fig. A.3(a). Like the rocksalt structure, the AO_2 $Fm\bar{3}m$ fluorite has only one degree of freedom, the unit cell parameter. One can introduce occupational disorder of *A* and *B* cations on the 4*a* site and oxygen vacancy in the 8*c* site depicted in Fig. A.3(a). One way of ordering the cations is *ABABAB*… pattern of alternating *A* and *B* chains which are stacked with a rotation of 90°, resulting in quadrupling of the unit cell into the space group $Fd\bar{3}m$ in Fig. A.3(a). The arrangement of *A* and *B* cations gives two inter-penetrating corner-sharing tetrahedral networks, known as the fully frustrated pyrochlore lattice (Fig. A.3(c)), which can be also viewed as layers of kagome and triangular lattices (Fig. A.3(b)). The 8*c* oxygen site splits into three sites: 8-fold O2, 8-fold vacancy V_O and 48-fold O1. O2 and V_O form dumbbell units O2-*A*-O2 and V_O-*B*-V_O on top of the original

■ *Table A.1.* Comparison of structural parameters of rocksalt, honeycomb and hyperhoneycomb.

Rocksalt AO, $Fm\bar{3}m$, $Z = 4$, $a_R \sim 5$ Å					
Atom	Site	x	y	z	g
A	$4a$	0	0	0	1
O	$4b$	1/2	1/2	1/2	1
Honeycomb α-A_2BO_3, $C2/m$, $Z = 4$ $a, c \sim (\sqrt{13/4})a_R$, $b \sim (3\sqrt{2}/2)a_R$, $\beta \sim 109°$					
Atom	Site	x	y	z	g
$A1$	$2a$	0	0	0	1
$A2$	$2d$	0	1/2	1/2	1
$A3$	$4h$	0	y	1/2	1
B	$4g$	0	y	0	1
O1	$4i$	x	0	z	1
O2	$8j$	x	y	z	1
Hyperhoneycomb β-A_2BO_3, $Fddd$, $Z = 16$ $a \sim (3\sqrt{2})a_R$, $b \sim (\sqrt{2})a_R$, $c \sim 2a_R$					
Atom	Site	x	y	z	g
$A1$	$16g$	1/8	1/8	z	1
$A2$	16dg	1/8	1/8	z	1
B	$16g$	1/8	1/8	z	1
O1	$16e$	x	1/8	1/8	1
O2	$32h$	x	y	z	1

scalenohedrons, reducing the coordination of the B cation from 8 to 6, which in reality is usually smaller than the A cation. The B cation is coordinated by O1 atom only, while the A cation is coordinated by six O1 atoms and two O2 atoms. If one maps the atomic positions in the $Fd\bar{3}m$ child structure from the $Fm\bar{3}m$ parent structure, the BO_6 octahedron is extremely trigonally compressed (Fig. A.4(a)). This extreme distortion is lifted by the new degree of freedom gained in the symmetry reduction, which is the O1 x fractional coordinate (Table A.2). Since the O1 atom coordinates both A and B atoms, $x = 3/8$ for an ideal AO_8 scalenohedron and $x = 5/16$ for an ideal BO_6 octahedron, and real pyrochlore materials adopt a value of x between the two, rendering both polyhedra inevitably distorted to some extent. For clarity, this distortion will be parameterised by the deviation from the ideal x_c value, Δx. We set $x_c = 5/16$ and $\Delta x = x - x_c = x - 5/16$.

The value $5/16 < x < 3/8$ reduces the trigonal compression of the BO_6 and increases the A-O1 bond length. As a result, the shorter A-O2 bonds form an anticrystoballite-like lattice

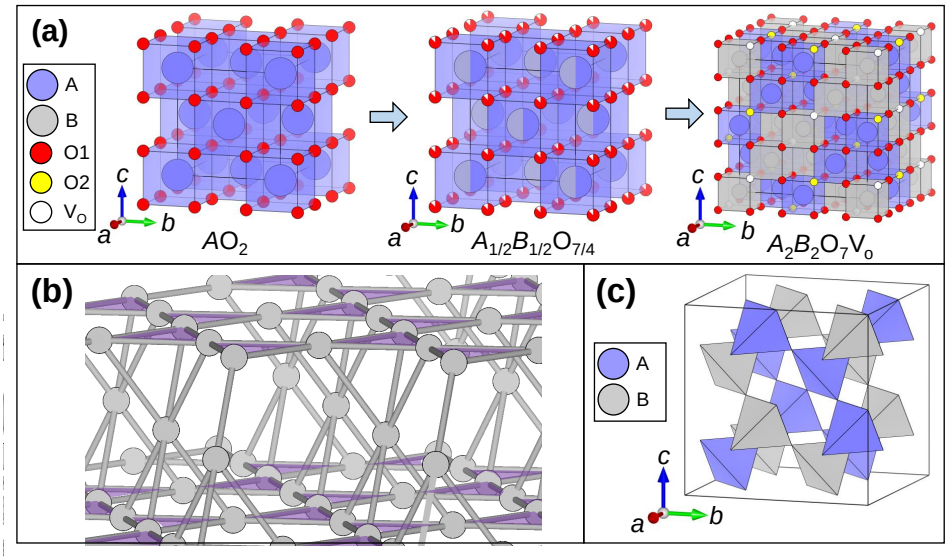

■ *Figure A.3.* (a) From left to right: the crystal structure of AO_2 fluorite with space group $Fm\bar{3}m$ and $a \sim 9.9884(4)$ Å, disordered fluorite with chemical formula $A_{1/2}B_{1/2}O_{7/4}$ with oxygen vacancy, ordering of the disordered fluorite results in $Fd\bar{3}m$ pyrochlore structure. (b) Pyrochlore lattice can be viewed alternating layeres of kagome (shown in purple) and triangular lattice. (c) Interpenetrating pyrochlore networks of A and B cations.

comprising O2-A-O2 dumbbell units as depicted in (Fig. A.4(b)). Effectively the $A_2B_2O_7$ can be viewed as a combination of a $B_2(O1)_6$ sub-lattice and $A_2(O2)$ sub-lattice. The $B_2(O1)_6$ network comprises corner-sharing trigonally compressed BO_6 octahedra, where the axis of trigonal compression is aligned with the local (111) axes of the B tetrahedra as shown in (Fig. A.4(c)).

Usually, the smaller the A cation, the less distortion the AO_8 polyhedron is able to accommodate, increasing x and hence increased trigonal compression of the BO_6 octahedron. The more trigonally compressed the BO_6 octahedron is, the smaller the B-O-B angle is. This is seen in the well-studied family of pyrochlore stanates $A_2^{3+}Sn_2^{4+}O_7$ (Fig. A.5). It appears that the A-O1 bond length is affected more than those of A-O2 and Sn-O1. The Sn-O1 bond length shows little variation with Δx and r_A, which is due to the counter-acting effects of shrinking lattice parameter and increasing trigonal compression.

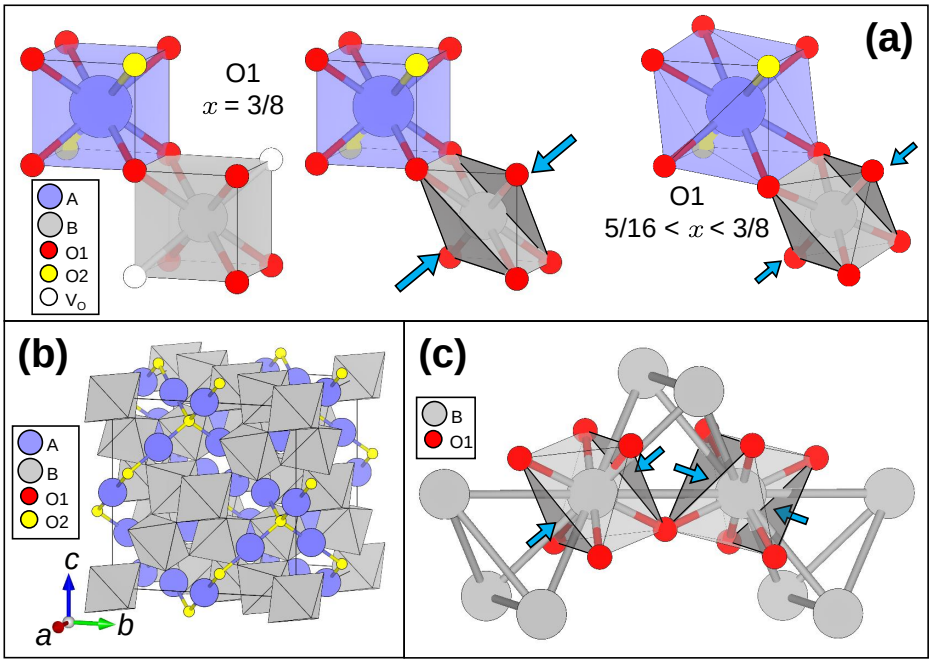

■ *Figure A.4.* (a) The AO_8 scalenohedron and BO_6 octahedron share edges. For the O1 position mapped from that of a disordered fluorite, the BO_6 octahedron is extremely trigonally compressed. As a result, O1 is displaced in order to reduce the trigonal compression of BO_6, which in turn distorts the AO_8 scalenohedron from the ideal cube. (b) The O2-*A*-O2 bonds form anticrystoballite-like network penetrating the hexagonal holes of the $B_2(O1)_6$ network. (c) The geometry of the $B_2(O1)_6$ network. The axis of the trigonal compression is aligned with the (111) direction of the *B* tetrahedra. For $x = 5/16$ and $x = 3/8$ the *B*-O-*B* angle is $\sim 141°$ and $\sim 109°$, respectively.

■ *Table A.2.* Comparison of structural parameters of fluorite and pyrochlore.

Fluorite AO_2, $Fm\bar{3}m$, $Z = 4$, $a_F \sim 5$ Å					
Atom	Site	x	y	z	g
A	4a	0	0	0	1
O	8c	1/4	1/4	1/4	1
Pyrochlore $A_2B_2O_7$, $Fd\bar{3}m$, $Z = 8$, $a \sim 2a_F$					
Atom	Site	x	y	z	g
A	16d	1/2	1/2	1/2	1
B	16c	0	0	0	1
O1	48f	$5/16 < x < 3/8$	1/8	1/8	1
O2	8b	3/8	3/8	3/8	1
V_O	8a	1/8	1/8	1/8	1

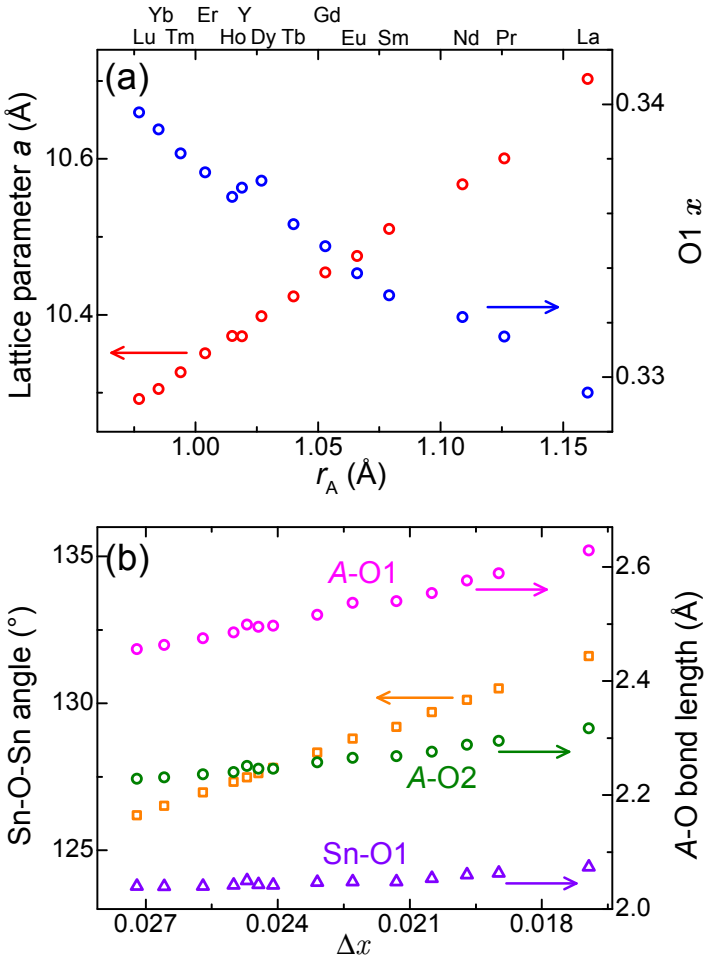

■ *Figure A.5.* (a) The structural properties of pyrochlore stanates $A_2^{3+}Sn_2^{4+}O_7$ as a function of (a) A^{3+} cation radius r_A and (b) Δx. (a) Increasing unit cell parameter a and decreasing O1 x fractional coordinate with decreasing r_A. (b) Decreasing A-O and Sn-O bond lengths and Sn-O-Sn angle with increasing Δx. The A-O1 bonds appear to be the most affected, while Sn-O1 bond lengths show little dependence on Δx, due to the combination of the effect of a and x. Structural parameters of $A_2^{3+}Sn_2^{4+}O_7$ adapted from Ref. [269].

Appendix B

Band structure calculations of pyrochlore iridates $A_2Ir_2O_7$

Here, more detailed results of LDA+SOC band structure calculations for pyrochlore iridates $A_2Ir_2O_7$ for A = Lu, In, Y and Pr are shown below in Fig. B.1 and Fig. B.2. The bandwidth and the weight of $J_{5/2}$ and $J_{3/2}$ is similar for A = Lu, Y and Pr. Therefore, it appears that the trigonal compression of IrO_6 and Ir-O-Ir angle have little effect on the bandwidth and the local electronic states. The DOS and band dispersion of $In_2Ir_2O_7$ is distinct from other pyrochlore iridates, as the hybridisation with In flattens out the t_{2g} bands around the Fermi level.

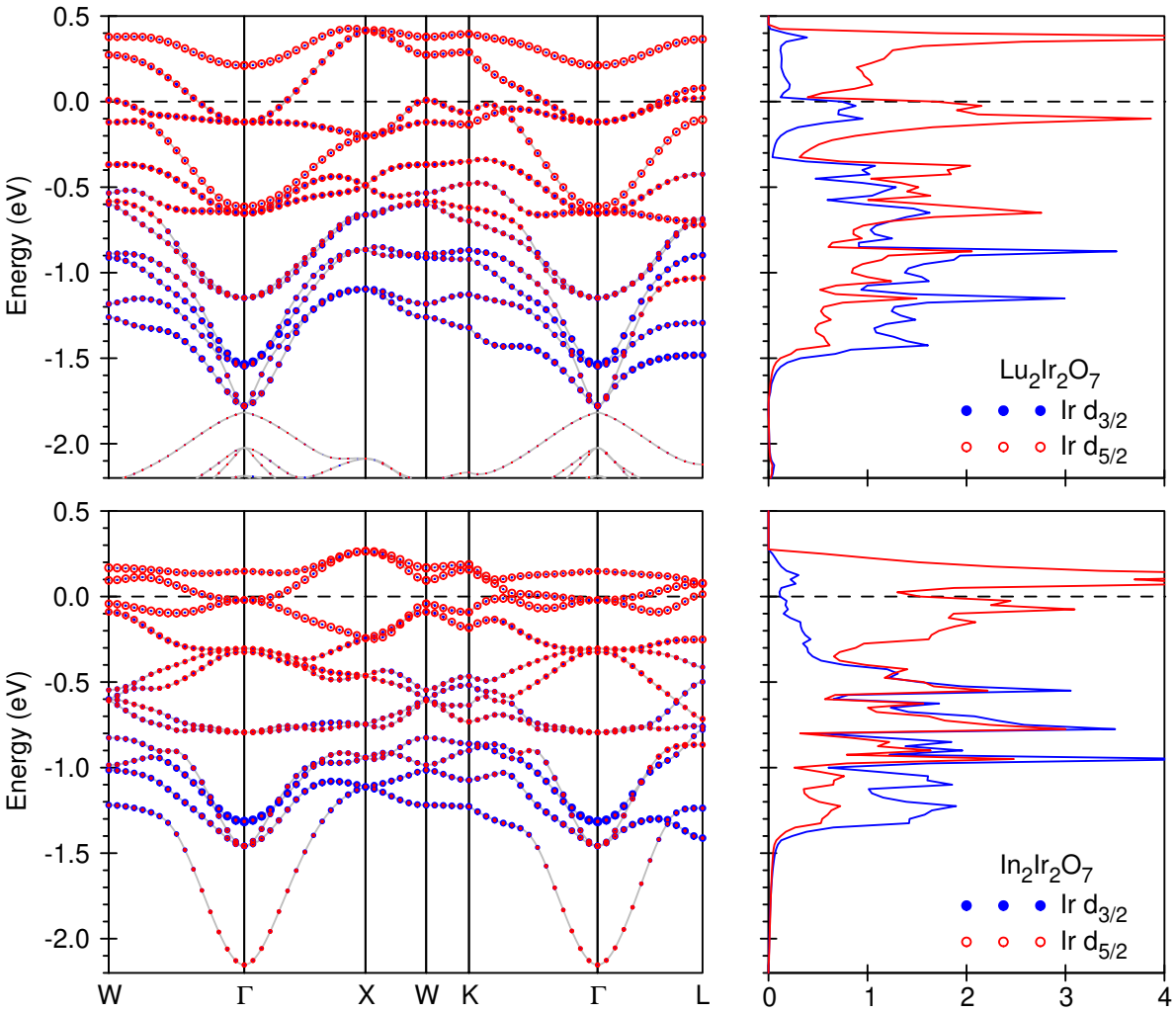

■ *Figure B.1.* Calculated band structure (left) and Ir 5*d* density of states (right) resolved into $J = 5/2$ ($d_{5/2}$) and $J = 3/2$ ($d_{3/2}$) states for $Lu_2Ir_2O_7$ (top) and $In_2Ir_2O_7$ (bottom). The Fermi level E_F is indicated by dashed black lines. Note that the $J_{eff} = 1/2$ state consists of pure $J = 5/2$ wave function and the $J_{eff} = 3/2$ has both $J = 5/2$ and $3/2$ components. This figure was created by Dr. Alexander Yaresko and is used here with his permission.

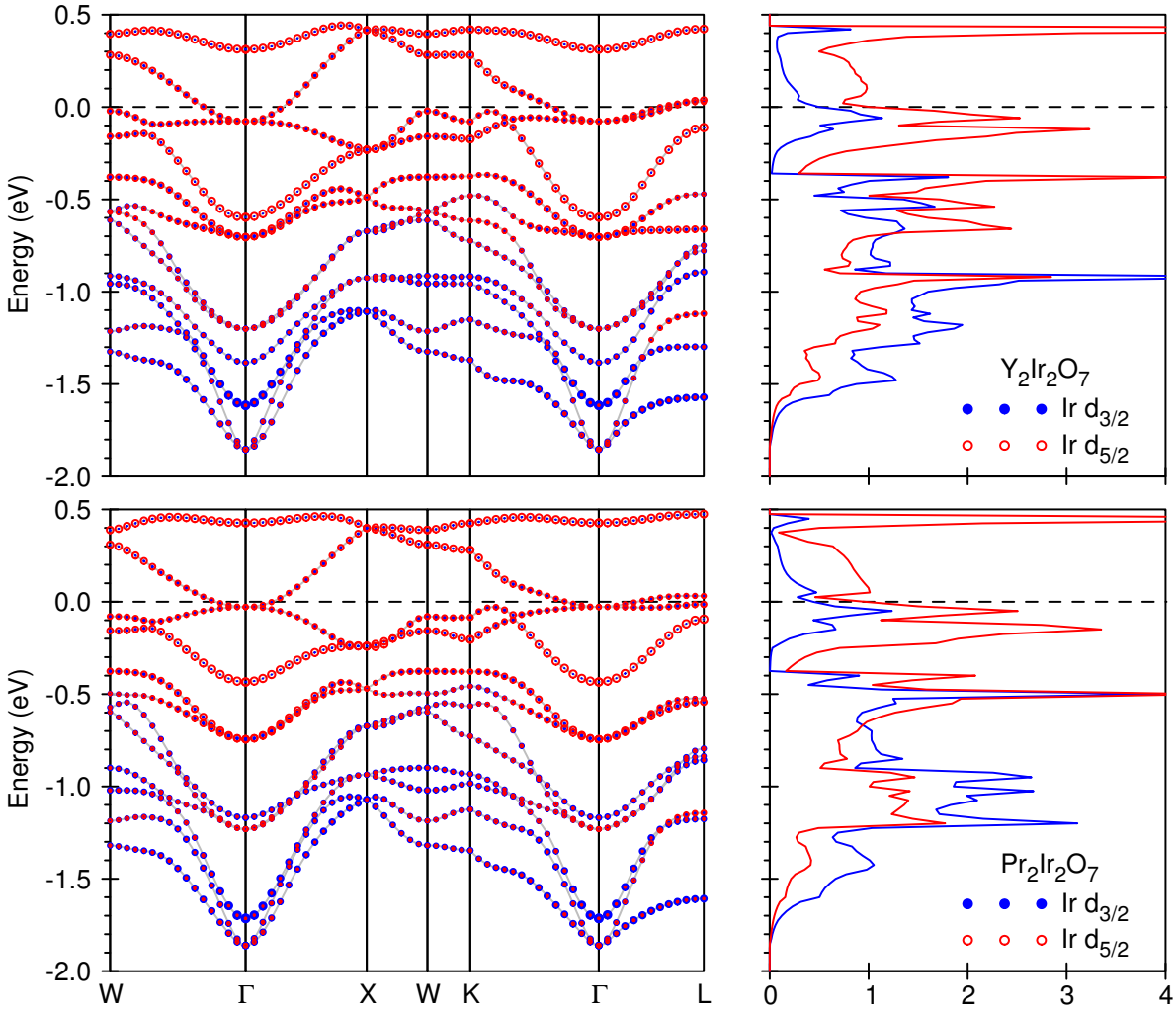

■ *Figure B.2.* Calculated band structure (left) and Ir 5*d* density of states (right) resolved into $J = 5/2$ ($d_{5/2}$) and $J = 3/2$ ($d_{3/2}$) states for $Y_2Ir_2O_7$ (top) and $Pr_2Ir_2O_7$ (bottom). Note that the $J_{\text{eff}} = 1/2$ state consists of pure $J = 5/2$ wave function and the $J_{\text{eff}} = 3/2$ has both $J = 5/2$ and $3/2$ components. This figure was created by Dr. Alexander Yaresko and is used here with his permission.

References

[1] J. G. Bednorz and K. A. Müller, "Possible high T_c superconductivity in the Ba-La-Cu-O system", Z. Physik B **64**, 189 (1986).

[2] F. J. Morin, "Oxides Which Show a Metal-to-Insulator Transition at the Néel Temperature", Phys. Rev. Lett. **3**, 34 (1959).

[3] A. P. Ramirez, "Colossal magnetoresistance", J. Phys.: Condens. Matter **9**, 8171 (1997).

[4] Y. Tokura and Y. Tomioka, "Colossal magnetoresistive manganites", J. Magn. Magn. Mater. **200**, 1 (1999).

[5] Y. Tokura, "Critical features of colossal magnetoresistive manganites", Rep. Prog. Phys. **69**, 797 (2006).

[6] S. Sachdev and B. Keimer, "Quantum criticality", Physics Today **64**, 29 (2011).

[7] B. Keimer, S. A. Kivelson, M. R. Norman, S. Uchida, and J. Zaanen, "From quantum matter to high-temperature superconductivity in copper oxides", Nature **518**, 179 (2015).

[8] A. J. Schofield, "Non-Fermi liquids", Contemp. Phys. **40**, 95 (1999).

[9] J. Hubbard, "Electron correlations in narrow energy bands", Proc. R. Soc. A **276**, 238 (1963).

[10] N. F. Mott, "The Basis of the Electron Theory of Metals, with Special Reference to the Transition Metals", Proc. Phys. Soc. A **62**, 416 (1949).

[11] N. F. Mott, *Metal-Insulator Transitions* (Taylor and Francis, London, 1990).

[12] J. B. Goodenough, *Magnetism and the Chemical Bond* (Interscience Publisher, New York, 1963).

[13] D. I. Khomskii, *Transition Metal Compounds* (Cambridge University Press, 2014).

[14] A. S. Bhalla, R. Guo, and R. Roy, "The perovskite structure – a review of its role in ceramic science and technology", Mater. Res. Innov. **4**, 3 (2000).

[15] K. I. Kugel and D. I. Khomskii, "The Jahn-Teller effect and magnetism: transition metal compounds", Sov. Phys. Usp. **25**, 231 (1982).

[16] J. Kanamori, "Superexchange interaction and symmetry properties of electron orbitals", J. Phys. Chem. Solids **10**, 87 (1959).

[17] J. B. Goodenough, "Theory of the Role of Covalence in the Perovskite-Type Manganites [La, *M*(II)]MnO_3", Phys. Rev. **100**, 564 (1955).

[18] J. B. Goodenough, "An interpretation of the magnetic properties of the perovskite-type mixed crystals $La_{1-x}Sr_xCoO_{3-\lambda}$", J. Phys. Chem. Solids **6**, 287 (1958).

[19] E. M. Wheeler, B. Lake, A. T. M. N. Islam, M. Reehuis, P. Steffens, T. Guidi, and A. H. Hill, "Spin and orbital order in the vanadium spinel MgV_2O_4", Phys. Rev. B **82**, 140406(R) (2010).

[20] S. Niitaka, H. Ohsumi, K. Sugimoto, S. Lee, Y. Oshima, K. Kato, D. Hashizume, T. Arima, M. Takata, and H. Takagi, "*A*-Type Antiferro-Orbital Ordering with $I4_1/a$ Symmetry and Geometrical Frustration in the Spinel Vanadate MgV_2O_4", Phys. Rev. Lett. **111**, 267201 (2013).

[21] H. Tsunetsugu and Y. Motome, "Magnetic transition and orbital degrees of freedom in vanadium spinels", Phys. Rev. B **68**, 060405(R) (2003).

[22] M. Reehuis, A. Krimmel, N. Büttgen, A. Loidl, and A. Prokofiev, "Crystallographic and magnetic structure of ZnV_2O_4", Eur. Phys. J. B **35**, 311 (2003).

[23] O. Tchernyshyov, "Structural, Orbital, and Magnetic Order in Vanadium Spinels", Phys. Rev. Lett. **93**, 157206 (2004).

[24] V. Pardo, S. Blanco-Canosa, F. Rivadulla, D. I. Khomskii, D. Baldomir, H. Wu, and J. Rivas, "Homopolar Bond Formation in ZnV_2O_4 Close to a Metal-Insulator Transition", Phys. Rev. Lett. **101**, 256403 (2008).

[25] J. Fujioka, T. Yasue, S. Miyasaka, Y. Yamasaki, T. Arima, H. Sagayama, T. Inami, K. Ishii, and Y. Tokura, "Critical competition between two distinct orbital-spin ordered states in perovskite vanadates", Phys. Rev. B **82**, 144425 (2010).

[26] B. Keimer, D. Casa, A. Ivanov, J. W. Lynn, M. v. Zimmermann, J. P. Hill, D. Gibbs, Y. Taguchi, and Y. Tokura, "Spin Dynamics and Orbital State in $LaTiO_3$", Phys. Rev. Lett **85**, 3946 (2000).

[27] G. Khaliullin and S. Maekawa, "Orbital Liquid in Three-Dimensional Mott Insulator: $LaTiO_3$", Phys. Rev. Lett **85**, 3950 (2000).

[28] H. F. Pen, J. van den Brink, D. I. Khomskii, and G. A. Sawatzky, "Orbital Ordering in a Two-Dimensional Triangular Lattice", Phys. Rev. Lett. **78**, 1323 (1997).

[29] M. Schmidt, W. I. Ratcliff, P. G. Radaelli, K. Refson, N. M. Harrison, and S. W. Cheong, "Spin Singlet Formation in $MgTi_2O_4$: Evidence of a Helical Dimerization Pattern", Phys. Rev. Lett. **92**, 056402 (2004).

[30] S. D. Matteo, J. Jackeli, C. Lacroix, and N. B. Perkins, "Valence-Bond Crystal in a Pyrochlore Antiferromagnet with Orbital Degeneracy", Phys. Rev. Lett. **93**, 077208 (2004).

[31] S. D. Matteo, G. Jackeli, and N. B. Perkins, "Valence-bond crystal and lattice distortions in a pyrochlore antiferromagnet with orbital degeneracy", Phys. Rev. B **72**, 024431 (2005).

[32] D. I. Khomskii, "Different Routes to Spin Gaps: Role of Orbital Ordering", Prog. Theor. Phys. Suppl. **159**, 319 (2005).

[33] S. V. Streltsov and D. I. Khomskii, "Unconventional magnetism as a consequence of the charge disproportionation and the molecular orbital formation in $Ba_4Ru_3O_{10}$", Phys. Rev. B **86**, 064429 (2012).

[34] J. P. Attfield, "Orbital molecules in electronic materials", APL Materials **3**, 041510 (2015).

[35] M. Imada, A. Fujimori, and Y. Tokura, "Metal-insulator transitions", Rev. Mod. Phys. **70**, 1039 (1998).

[36] P. G. Radaelli, Y. Horibe, M. J. Gutmann, H. Ishibashi, C. H. Chen, R. M. Ibberson, Y. Koyama, Y.-S. Hor, V. Kiryukhin, and S.-W. Cheong, "Formation of isomorphic Ir^{3+} and Ir^{4+} octamers and spin dimerization in the spinel $CuIr_2S_4$", Nature **416**, 155 (2002).

[37] O. A. Starykh, M. E. Zhitomirsky, D. I. Khomskii, R. R. P. Singh, and K. Ueda, "Origin of Spin Gap in CaV_4O_9: Effects of Frustration and Lattice Distortions", Phys. Rev. Lett. **77**, 2558 (1996).

[38] Y. Horibe, M. Shingu, K. Kurushima, H. Ishibashi, N. Ikeda, K. Kato, Y. Motome, N. Furukawa, S. Mori, and T. Katsufuji, "Spontaneous Formation of Vanadium "Molecules" in a Geometrically Frustrated Crystal: AlV_2O_4", Phys. Rev. Lett. **96**, 086406 (2006).

[39] A. J. Browne, S. A. J. Kimber, and J. P. Attfield, "Persistent three- and four-atom orbital molecules in the spinel AlV_2O_4", Phys. Rev. Mater. **1**, 052003(R) (2017).

[40] K. I. Kugel and D. I. Khomskii, "Crystal structure and magnetic properties of substances with orbital degeneracy", Zh. Eksp. Teor. Fiz. **64**, 1429 (1982).

[41] D. I. Khomskii and T. Mizokawa, "Orbitally Induced Peierls State in Spinels", Phys. Rev. Lett. **94**, 156402 (2005).

[42] R. Peierls, *Quantum Theory of Solids* (Oxford University Press, Oxford, 1955).

[43] R. Peierls, *More Surprises in Theoretical Physics* (Princeton University Press, Princeton, 1991).

[44] S. Sugano, Y. Tanabe, and H. Kamimura, *Multiplets of Transition-Metal Ions in Crystals* (Academic Press, New York, 1970).

[45] A. Abragam and B. Bleaney, *Electron Paramagnetic Resonance of Transition Ions* (Clarendon Press, Oxford, 1970).

[46] G. Chen, R. Pereira, and L. Balents, "Exotic phases induced by strong spin-orbit coupling in ordered double perovskites", Phys. Rev. B **82**, 174440 (2010).

[47] G. Chen and L. Balents, "Spin-orbit coupling in d^2 ordered double perovskites", Phys. Rev. B **84**, 094420 (2011).

[48] W. M. H. Natori, M. Daghofer, and R. G. Pereira, "Dynamics of a $j = 3/2$ quantum spin liquid", Phys. Rev. B **96**, 125109 (2017).

[49] M. G. Yamada, M. Oshikawa, and G. Jackeli, "Emergent SU(4) Symmetry in α-$ZrCl_3$ and Crystalline Spin-Orbital Liquids", Phys. Rev. Lett. **121**, 097201 (2018).

[50] G. Khaliullin, "Excitonic Magnetism in Van Vleck–type d^4 Mott Insulators", Phys. Rev. Lett. **111**, 197201 (2013).

[51] G. Jackeli and G. Khaliullin, "Mott Insulators in the Strong Spin-Orbit Coupling Limit: From Heisenberg to a Quantum Compass and Kitaev Models", Phys. Rev. Lett. **102**, 017205 (2009).

[52] X. Wan, A. M. Turner, A. Vishwanath, and S. Y. Savrasov, "Topological semimetal and Fermi-arc surface states in the electronic structure of pyrochlore iridates", Phys. Rev. B **83**, 205101 (2011).

[53] D. Pesin and L. Balents, "Mott physics and band topology in materials with strong spin–orbit interaction", Nat. Phys. **6**, 376 (2010).

[54] B. J. Kim, H. Ohsumi, T. Komesu, S. Sakai, T. Morita, H. Takagi, and T. Arima, "Phase-Sensitive Observation of a Spin-Orbital Mott State in Sr_2IrO_4", Science **323**, 1329 (2009).

[55] J. Matsuno, Y. Okimoto, Z. Fang, X. Z. Yu, Y. Matsui, N. Nagaosa, M. Kawasaki, and Y. Tokura, "Metallic Ferromagnet with Square-Lattice CoO_2 sheets", Phys. Rev. Lett. **93**, 167202 (2004).

[56] S. J. Moon, M. W. Kim, K. W. Kim, Y. S. Lee, J.-Y. Kim, J.-H. Park, B. J. Kim, S.-J. Oh, S. Nakatsuji, Y. Maeno, I. Nagai, S. I. Ikeda, G. Cao, and T. W. Noh, "Electronic structures of layered perovskite Sr_2MO_4 (M = Ru, Rh, and Ir)", Phys. Rev. B **74**, 113104 (2006).

[57] M. K. Crawford, M. A. Subramanian, R. L. Harlow, J. A. Fernandez-Baca, Z. R. Wang, and D. C. Johnston, "Structural and magnetic studies of Sr_2IrO_4", Phys. Rev. B **49**, 9198 (1994).

[58] G. Cao, J. Bolivar, S. McCall, J. E. Crow, and R. P. Guertin, "Weak ferromagnetism, metal-to-nonmetal transition, and negative differential resistivity in single-crystal Sr_2IrO_4", Phys. Rev. B **57**, R11039(R) (1998).

[59] B. J. Kim, H. Jin, S. J. Moon, J.-Y. Kim, B.-G. Park, C. S. Leem, J. Yu, T. W. Noh, C. Kim, S.-J. Oh, J.-H. Park, V. Durairaj, G. Cao, and E. Rotenberg, "Novel $J_{\text{eff}} = 1/2$ Mott State Induced by Relativistic Spin-Orbit Coupling in Sr_2IrO_4", Phys. Rev. Lett. **101**, 076402 (2008).

[60] P. A. Lee, N. Nagaosa, and X.-G. Wen, "Doping a Mott insulator: Physics of high-temperature superconductivity", Rev. Mod. Phys. **78**, 17 (2006).

[61] S. M. Hayden, G. Aeppli, R. Osborn, A. D. Taylor, T. G. Perring, S.-W. Cheong, and Z. Fisk, "High-energy spin waves in La_2CuO_4", Phys. Rev. **67**, 3622 (1991).

[62] J. Bertinshaw, Y. K. Kim, G. Khaliullin, and B. J. Kim, "Square Lattice Iridates", Ann. Rev. Condens. Matter Phys. **10**, 315 (2019).

[63] F. Wang and T. Senthil, "Twisted Hubbard Model for Sr_2IrO_4: Magnetism and Possible High Temperature Superconductivity", Phys. Rev. Lett. **106**, 136402 (2011).

[64] H. Watanabe, T. Shirakawa, and S. Yunoki, "Monte Carlo Study of an Unconventional Superconducting Phase in Iridium Oxide $J_{\text{eff}} = 1/2$ Mott Insulators Induced by Carrier Doping", Phys. Rev. Lett. **110**, 027002 (2013).

[65] Z. Y. Meng, Y. B. Kim, and H.-Y. Kee, "Odd-Parity Triplet Superconducting Phase in Multiorbital Materials with a Strong Spin-Orbit Coupling: Application to Doped Sr_2IrO_4", Phys. Rev. Lett. **113**, 177003 (2014).

[66] Y. K. Kim, O. Krupin, J. D. Denlinger, A. Bostwick, E. Rotenberg, Q. Zhao, J. F. Mitchell, J. W. Allen, and B. J. Kim, "Fermi arcs in a doped pseudospin-1/2 Heisenberg antiferromagnet", Science **345**, 187 (2014).

[67] H. Takagi, T. Takayama, G. Jackeli, G. Khaliullin, and S. E. Nagler, "Concept and realization of Kitaev quantum spin liquids", Nat. Rev. Phys. **1**, 264 (2019).

[68] Y. Okamoto, S. Niitaka, M. Uchida, T. Waki, M. Takigawa, Y. Nakatsu, A. Sekiyama, S. Suga, R. Arita, and H. Takagi, "Band Jahn-Teller Instability and Formation of Valence Bond Solid in a Mixed-Valent Spinel Oxide $LiRh_2O_4$", Phys. Rev. Lett. **101**, 086404 (2008).

[69] T. Takayama, A. Yaresko, A. Matsumoto, J. Nuss, K. Ishii, M. Yoshida, J. Mizuki, and H. Takagi, "Spin-orbit coupling induced semi-metallic state in the 1/3 hole-doped hyper-kagome $Na_3Ir_3O_8$", Sci. Rep. **4**, 6818 (2014).

[70] W. Witczak-Krempa, G. Chen, Y. B. Kim, and L. Balents, "Correlated Quantum Phenomena in the Strong Spin-Orbit Regime", Annu. Rev. Condens. Matter Phys. **5**, 57 (2014).

[71] A. Jain, M. Krautloher, J. Porras, G. H. Ryu, D. P. Chen, D. L. Abernathy, J. T. Park, A. Ivanov, J. Chaloupka, G. Khaliullin, and B. Keimer, "Higgs mode and its decay in a two-dimensional antiferromagnet", Nat. Phys. **13**, 633 (2017).

[72] H. Gretarsson, H. Suzuki, K. Hoon Kim, K. Ueda, M. Krautloher, B. J. Kim, H. Yavaş, G. Khaliullin, and B. Keimer, "Observation of spin-orbit excitations and Hund's multiplets in Ca_2RuO_4", Phys. Rev. B **100**, 045123 (2019).

[73] S. A. J. Kimber, C. D. Ling, D. J. P. Morris, A. Chemseddine, P. F. Henry, and D. N. Argyriou, "Interlayer tuning of electronic and magnetic properties in honeycomb ordered $Ag_3LiRu_2O_6$", J. Mater. Chem. **20**, 8021 (2010).

[74] C. R. Stanek, C. Jiang, B. P. Uberuaga, K. E. Sickafus, A. R. Cleave, and R. W. Grimes, "Predicted structure and stability of $A_4B_3O_{12}$ δ-phase compositions", Phys. Rev. B **80**, 174101 (2009).

[75] D. Walker, M. A. Carpenter, and C. Hitch, "Some simplifications to multianvil devices for high pressure experiments", American Mineralogist **75**, 1020 (1990).

[76] B. T. M. Wills and C. J. Carlile, *Experimental Neutron Scattering* (Oxford University Press, Oxford, 2009).

[77] V. F. Sears, "Neutron scattering lengths and cross section", Neutron News **3**, 29 (1992).

[78] H. M. Rietveld, "A profile refinement method for nuclear and magnetic structures", J. Appl. Cryst. **2**, 65 (1969).

[79] B. H. Toby, "*R* factors in Rietveld analysis: How good is good enough?", J. Appl. Phys. **21**, 67 (2001).

[80] B. H. Toby, "*EXPGUI*, a graphical user interface for *GSAS*", J. Appl. Cryst. **34**, 210 (2001).

[81] A. A. Coehlo, "TOPAS and TOPAS-Academic: an optimization program integrating computer algebra and crystallographic objects written in C++", J. Appl. Cryst. **51**, 210 (2018).

[82] K. Momma and F. Izumi, "*VESTA*: a three-dimensional visualization system for electronic and structural analysis", J. App. Crystallogr. **41**, 653 (2008).

[83] L. J. P. Ament, M. van Veenendaal, T. P. Devereaux, J. P. Hill, and J. van den Brink, "Resonant inelastic x-ray scattering studies of elementary excitations", Rev. Mod. Phys. **83**, 705 (2011).

[84] E. Collart, A. Shukla, F. Gélébart, M. Morand, C. Malgrange, N. Bardou, A. Madourib, and J.-L. Pelouardb, "Spherically bent analyzers for resonant inelastic X-ray scattering with intrinsic resolution below 200 meV", J. Synchrotron Rad. **12**, 473 (2005).

[85] J. P. Clancy, N. Chen, C. Y. Kim, W. F. Chen, K. W. Plumb, B. C. Jeon, T. W. Noh, and Y.-J. Kim, "Spin-orbit coupling in iridium-based 5*d* compounds probed by x-ray absorption spectroscopy", Phys. Rev. B **86**, 195131 (2012).

[86] M. A. Laguna-Marco, D. Haskel, N. Souza-Neto, J. C. Lang, V. V. Krishnamurthy, S. Chikara, G. Cao, and M. van Veenendaal, "Orbital Magnetism and Spin-Orbit Effects in the Electronic Structure of $BaIrO_3$", Phys. Rev. Lett. **105**, 216407 (2010).

[87] J. W. Kim, Y. Choi, J. Kim, J. F. Mitchell, G. Jackeli, M. Daghofer, J. van den Brink, G. Khaliullin, and B. J. Kim, "Dimensionality Driven Spin-Flop Transition in Layered Iridates", Phys. Rev. Lett. **109**, 037204 (2012).

[88] S. Boseggia, R. Springell, H. C. Walker, A. T. Boothroyd, D. Prabhakaran, D. Wermeille, L. Bouchenoire, S. P. Collins, and D. F. McMorrow, "Antiferromagnetic order and domains in $Sr_3Ir_2O_7$ probed by x-ray resonant scattering", Phys. Rev. B **85**, 184432 (2012).

[89] S. Boseggia, R. Springell, H. C. Walker, H. M. Rønnow, C. Rüegg, H. Okabe, M. Isobe, R. S. Perry, S. P. Collins, and D. F. McMorrow, "Robustness of Basal-Plane Antiferromagnetic Order and the $J_{\text{eff}} = 1/2$ State in Single-Layer Iridate Spin-Orbit Mott Insulators", Phys. Rev. Lett. **110**, 117207 (2013).

[90] K. Ohgushi, J. Yamaura, H. Ohsumi, K. Sugimoto, A. Takeshita S. Tokuda, H. Takagi, M. Takata, and T. Arima, "Resonant X-ray Diffraction Study of the Strongly Spin-Orbit-Coupled Mott Insulator $CaIrO_3$", Phys. Rev. Lett. **110**, 21721 (2013).

[91] A. Georges, L. de'Medici, and J. Mravlje, "Strong Correlations from Hund's Coupling", Ann. Rev. Condens. Matter Phys. **4**, 137 (2013).

[92] G. Van Rossum and F. L. Drake, *Python 3 Reference Manual* (CreateSpace, Scotts Valley, CA, 2009).

[93] M. W. Haverkort, M. Zwierzycki, and O. K. Andersen, "Multiplet ligand-field theory using Wannier orbitals", Phys. Rev. B **85**, 165113 (2012).

[94] M. McElfresh, *Fundamentals of Magnetism and Magnetic Measurements* (Quantum Design, 1994).

[95] G. A. Bain and J. F. Berry, "Diamagnetic Corrections and Pascal's Constants", J. Chem. Educ. **85**, 532 (2008).

[96] S. J. Blundell, "Spin-polarized muons in condensed matter physics", Contemp. Phys. **40**, 175 (1999).

[97] R. L. Garwin, L. M. Lederman, and M. Weinrich, "Observations of the Failure of Conservation of Parity and Charge Conjugation in Meson Decays: the Magnetic Moment of the Free Muon", Phys. Rev. **105**, 1415 (1947).

[98] U. von Barth and L. Hedin, "A local exchange-correlation potential for the spin polarized case. i", J. Phys. C **5**, 1629 (1972).

[99] P. Hohenberg and W. Kohn, "Inhomogeneous Electron Gas", Phys. Rev. **136**, B864 (1964).

[100] W. Kohn and L. J. Sham, "Self-Consistent Equations Including Exchange and Correlation Effect", Phys. Rev. **140**, A1133 (1965).

[101] O. K. Andersen, "Linear methods in band theory", Phys. Rev. B **12**, 3060 (1975).

[102] V. Antonov, B. Harmon, and A. Yaresko, *Electronic Structure and Magneto-Optical Properties of Solids* (Kluwer Academic Publishers, Dordrecht, 2004).

[103] T. Takayama, A. Krajewska, A. S. Gibbs, A. N. Yaresko, H. I. Ishii, H. Yamaoka, K. Ishii, N. Hiraoka, N. P. Funnell, C. L. Bull, and H. Takagi, "Pressure-induced collapse of the spin-orbital Mott state in the hyperhoneycomb iridate β-Li_2IrO_3", Phys. Rev. B **99**, 125127 (2019).

[104] A. Kitaev, "Anyons in an exactly solved model and beyond", Annals of Phys. **321**, 2 (2006).

[105] C. Nayak, S. H. Simon, A. Stern, M. Freedman, and S. D. Sarma, "Non-Abelian anyons and topological quantum computation", Rev. Mod. Phys. **80**, 1083 (2008).

[106] J. G. Rau, E. K.-H. Lee, and H.-Y. Kee, "Spin-Orbit Physics Giving Rise to Novel Phases in Correlated Systems: Iridates and Related Materials", Ann. Rev. Condens. Matter Phys. **7**, 195 (2016).

[107] S. M. Winter, A. A. Tsirlin, M. Daghofer, J. van den Brink, Y. Singh, P. Gegenwart, and R. Valenti, "Models and materials for generalized Kitaev magnetism", J. Phys. Condens. Matter **29**, 493002 (2017).

[108] S. Trebst, *Kitaev Materials*, (2017) arXiv:1701.07056, https://arxiv.org/abs/1701.07056.

[109] V. Todorova, A. Leineweber, L. Kienle, V. Duppel, and M. Jansen, "On $AgRhO_2$, and the new quaternary delafossites $AgLi_{1/3}M_{2/3}O_2$ syntheses and analyses of real structures", J. Solid State Rev. Mod. Phys **184**, 1112 (2011).

[110] J. H. Roudebush, K. A. Ross, and R. J. Cava, "Iridium containing honeycomb Delafossites by topotactic cation exchange", Dalton Trans. **45**, 8783 (2016).

[111] M. Abramchuk, C. Ozsoy-Keskinbora, J. W. Krizan, K. R. Metz, D. C. Bell, and F. Tafti, "Cu_2IrO_3: A New Magnetically Frustrated Honeycomb Iridate", J. Am. Chem. Soc. **139**, 15371 (2017).

[112] Y. Haraguchi, C. Michioka, A. Matsuo, K. Kindo, H. Ueda, and K. Yoshimura, "Magnetic ordering with an XY-like anisotropy in the honeycomb lattice iridates $ZnIrO_3$ and $MgIrO_3$ synthesized via a metathesis reaction", Phys. Rev. Mater. **2**, 054411 (2018).

[113] K. Kitagawa, T. Takayama, Y. Matsumoto, A. Kato, R. Takano, Y. Kishimoto, S. Bette, R. Dinnebier, G. Jackeli, and H. Takagi, "A spin–orbital-entangled quantum liquid on a honeycomb lattice", Nature **554**, 341 (2016).

[114] S. Mandal and N. Surendran, "Exactly solvable Kitaev model in three dimensions", Phys. Rev. B **79**, 024426 (2009).

[115] T. Takayama, A. Kato, R. Dinnebier, J. Nuss, H. Kono, L. S. I. Veiga, G. Fabbris, D. Haskel, and H. Takagi, "Hyperhoneycomb Iridate β-Li_2IrO_3 as a Platform for Kitaev Magnetism", Phys. Rev. Lett. **114**, 077202 (2015).

[116] Y. Singh, S. Manni, J. Reuther, T. Berlijn, R. Thomale, W. Ku, S. Trebst, and P. Gegenwart, "Relevance of the Heisenberg-Kitaev Model for the Honeycomb Lattice Iridates A_2IrO_3", Phys. Rev. Lett. **108**, 127203 (2012).

[117] A. Banerjee, C. A. Bridges, J.-Q. Yan, A. A. Aczel, L. Li, M. B. Stone, G. E. Granroth, M. D. Lumsden, Y. Yiu, J. Knolle, S. Bhattacharjee, D. L. Kovrizhin, R. Moessner, D. A. Tennant, D. G. Mandrus, and S. E. Nagler, "Single crystal growth from separated educts and its application to lithium transition-metal oxides", Sci. Rep. **6**, 35362 (2016).

[118] S. C. Williams, R. D. Johnson, F. Freund, S. K. Choi, A. Jesche, I. Kimchi, S. Manni, A. Bombardi, P. Manuel, P. Gegenwart, and R. Coldea, "Incommensurate counterrotating magnetic order stabilized by Kitaev interactions in the layered honeycomb α-Li_2IrO_3", Phys. Rev. B **93**, 195158 (2016).

[119] Y. Singh and P. Gegenwart, "Antiferromagnetic Mott insulating state in single crystals of the honeycomb lattice material Na_2IrO_3", Phys. Rev. B **82**, 064412 (2010).

[120] X. Liu, T. Berlijn, W.-G. Yin, W. Ku, A. Tsvelik, Y.-J. Kim, H. Gretarsson, Y. Singh, P. Gegenwart, and J. P. Hill, "Long-range magnetic ordering in Na_2IrO_3", Phys. Rev. B **83**, 220403(R) (2011).

[121] F. Ye, S. Chi, H. Cao, B. C. Chakoumakos, J. A. Fernandez-Baca, R. Custelcean, T. F. Qi, O. B. Korneta, and G. Cao, "Direct evidence of a zigzag spin-chain structure in the honeycomb lattice: A neutron and x-ray diffraction investigation of single-crystal Na_2IrO_3", Phys. Rev. B **85**, 180403(R) (2012).

[122] H. B. Cao, A. Banerjee, J.-Q. Yan, C. A. Bridges, M. D. Lumsden, D. G. Mandrus, D. A. Tennant, B. C. Chakoumakos, and S. E. Nagler, "Low-temperature crystal and magnetic structure of α-$RuCl_3$", Phys. Rev. B **93**, 134423 (2016).

[123] A. Biffin, R. D. Johnson, S. K. Choi, F. Freund, S. Manni, A. Bombardi, P. Manuel, P. Gegenwart, and R. Coldea, "Unconventional magnetic order on the hyperhoneycomb Kitaev lattice in β-Li_2IrO_3: Full solution via magnetic resonant x-ray diffraction", Phys. Rev. B **90**, 205116 (2014).

[124] A. Biffin, R. D. Johnson, I. Kimchi, R. Morris, A. Bombardi, J. G. Analytis, A. Vishwanath, and R. Coldea, "Noncoplanar and Counterrotating Incommensurate Magnetic Order Stabilized by Kitaev Interactions in γ-Li_2IrO_3", Phys. Rev. Lett. **113**, 197201 (2014).

[125] Jmol: an open-source Java viewer for chemical structures in 3D. http://www.jmol.org/.

[126] H. Gretarsson, J. P. Clancy, X. Liu, J. P. Hill, E. Bozin, Y. Singh, S. Manni, P. Gegenwart, J. Kim, A. H. Said, D. Casa, T. Gog, M. H. Upton, H.-S. Kim, J. Yu, V. M. Katukuri, L. Hozoi, J. van den Brink, and Y.-J. Kim, "Crystal-Field Splitting and Correlation Effect on the Electronic Structure of A_2IrO_3", Phys. Rev. Lett. **110**, 076402 (2013).

[127] A. Banerjee, C. A. Bridges, J.-Q. Yan, A. A. Aczel, L. Li, M. B. Stone, G. E. Granroth, M. D. Lumsden, Y. Yiu, J. Knolle, S. Bhattacharjee, D. L. Kovrizhin, R. Moessner, D. A. Tennant, D. G. Mandrus, and S. E. Nagler, "Proximate Kitaev quantum spin liquid behaviour in a honeycomb magnet", Nat. Mater. **15**, 733 (2016).

[128] S. H. Chun, J.-W. Kim, J. Kim, H. Zheng, C. C. Stoumpos, J. F. Malliakas C. D.and Mitchell, K. Mehlawat, Y. Singh, Y. Choi, T. Gog, A. Al-Zein, M. M. Sala, M. Krisch, J. Chaloupka, G. Jackeli, G. Khaliullin, and B. J. Kim, "Direct evidence for dominant bond-directional interactions in a honeycomb lattice iridate Na_2IrO_3", Nat. Phys. **11**, 462 (2015).

[129] G. van der Laan and B. T. Thole, "Local Probe for Spin-Orbit Interaction", Phys. Rev. Lett. **60**, 1977 (1988).

[130] B. T. Thole and G. van der Laan, "Branching ratio in x-ray absorption spectroscopy", Phys. Rev. B **38**, 3158 (1988).

[131] J. Chaloupka, G. Jackeli, and G. Khaliullin, "Zigzag Magnetic Order in the Iridium Oxide Na_2IrO_3", Phys. Rev. Lett. **110**, 097204 (2013).

[132] J. G. Rau, E. K.-H. Lee, and H.-Y. Kee, "Generic Spin Model for the Honeycomb Iridates beyond the Kitaev Limit", Phys. Rev. Lett. **112**, 077204 (2014).

[133] J. Chaloupka, G. Jackeli, and G. Khaliullin, "Kitaev-Heisenberg Model on a Honeycomb Lattice: Possible Exotic Phases in Iridium Oxides A_2IrO_3", Phys. Rev. Lett. **105**, 027204 (2010).

[134] I. Kimchi and Y.-Z. You, "Kitaev-Heisenberg-J_2-J_3 model for the iridates A_2IrO_3", Phys. Rev. B **84**, 097204 (2011).

[135] J. G. Rau and H.-Y. Kee, *Trigonal distortion in the honeycomb iridates: Proximity of zigzag and spiral phases in Na_2IrO_3*, (2014) arXiv:1408.4811, https://arxiv.org/abs/1408.4811.

[136] S. Bette, T. Takayama, K. Kitagawa, R. Takano, H. Takagi, and R. Dinnebier, "Solution of the heavily stacking faulted crystal structure of the honeycomb iridate $H_3LiIr_2O_6$", Dalton Trans. **46**, 15216 (2017).

[137] S. Bette, T. Takayama, V. Duppel, A. Poulain, H. Takagi, and R. Dinnebier, "Crystal structure and stacking faults in the layered honeycomb, delafossite-type materials $Ag_3LiIr_2O_6$ and $Ag_3LiRu_2O_6$", Dalton Trans. **48**, 9250 (2019).

[138] Y. Kubota, H. Tanaka, T. Ono, Y. Narumi, and K. Kindo, "Successive magnetic phase transitions in α-$RuCl_3$: XY-like frustrated magnet on the honeycomb lattice", Phys. Rev. B **91**, 094422 (2015).

[139] R. D. Johnson, S. C. Williams, A. A. Haghighirad, V. Singleton J.and Zapf, P. Manuel, I. I. Mazin, Y. Li, H. O. Jeschke, R. Valentí, and R. Coldea, "Monoclinic crystal structure of α-$RuCl_3$ and the zigzag antiferromagnetic ground state", Phys. Rev. B **92**, 235119 (2015).

[140] P. Lampen-Kelley, S. Rachel, J. Reuther, J.-Q. Yan, A. Banerjee, C. A. Bridges, H. B. Cao, S. E. Nagler, and D. Mandrus, "Anisotropic susceptibilities in the honeycomb Kitaev system α-$RuCl_3$", Phys. Rev. B **98**, 100403(R) (2018).

[141] J. A. Sears, M. Songvilay, K. W. Plumb, J. P. Clancy, Y. Qiu, Y. Zhao, D. Parshall, and Y.-J. Kim, "Magnetic order in α-$RuCl_3$: A honeycomb-lattice quantum magnet with strong spin-orbit coupling", Phys. Rev. B **91**, 144420 (2015).

[142] S.-H. Baek, S.-H. Do, K.-Y. Choi, Y. Kwon, A. U. B. Wolter, S. Nishimoto, J. van den Brink, and B. Büchner, "Evidence for a Field-Induced Quantum Spin Liquid in α-$RuCl_3$", Phys. Rev. Lett. **119**, 037201 (2017).

[143] K. A. Modic, T. E. Smidt, I. Kimchi, N. P. Breznay, A. Biffin, S. K. Choi, R. D. Johnson, R. Coldea, P. Watkins-Curry, G. T. McCandless, J. Y. Chan, F. Gandara, Z. Islam, A. Vishwanath, A. Shekhter, R. D. McDonald, and J. G. Analytis, "Realization of a three-dimensional spin–anisotropic harmonic honeycomb iridate", Nat. Comm. **5**, 4203 (2014).

[144] K. A. Modic, B. J. Ramshaw, J. B. Betts, N. P. Breznay, J. G. Analytis, R. D. McDonald, and A. Shekhter, "Robust spin correlations at high magnetic fields in the harmonic honeycomb iridates", Nat. Comm. **8**, 180 (2017).

[145] A. Ruiz, A. Frano, N. P. Breznay, I. Kimchi, T. Helm, I. Oswald, J. Y. Chan, R. J. Birgeneau, Z. Islam, and J. G. Analytis, "Correlated states in β-Li_2IrO_3 driven by applied magnetic fields", Nat. Comm. **8**, 961 (2017).

[146] R. Yadav, N. A. Bogdanov, V. M. Katukuri, S. Nishimoto, J. van den Brink, and L. Hozoi, "Kitaev exchange and field-induced quantum spin-liquid states in honeycomb α-$RuCl_3$", Sci. Rep. **6**, 37925 (2016).

[147] J. A. Sears, Y. Zhao, Z. Xu, J. W. Lynn, and Y.-J. Kim, "Phase diagram of α-$RuCl_3$ in an in-plane magnetic field", Phys. Rev. B **95**, 180411(R) (2017).

[148] Y. Kasahara, T. Ohnishi, Y. Mizukami, O. Tanaka, S. Ma, K. Sugii, N. Kurita, H. Tanaka, J. Nasu, Y. Motome, T. Shibauchi, and Y. Matsuda, "Majorana quantization and half-integer thermal quantum Hall effect in a Kitaev spin liquid", Nature **559**, 227 (2018).

[149] T. Yokoi, S. Ma, Y. Kasahara, S. Kasahara, T. Shibauchi, N. Kurita, H. Tanaka, J. Nasu, Y. Motome, C. Hickey, S. Trebst, and Y. Matsuda, *Half-integer quantized anomalous thermal Hall effect in the Kitaev material α-$RuCl_3$*, (2019) arXiv:2001.01899, `https://arxiv.org/abs/2001.01899`.

[150] E. Kin-Ho and Y.-B. Kim, "Theory of magnetic phase diagrams in hyperhoneycomb and harmonic-honeycomb iridates", Phys. Rev. B **91**, 064407 (2015).

[151] M. Majumder, R. S. Manna, G. Simutis, J. C. Orain, T. Dey, F. Freund, A. Jesche, R. Khasanov, P. K. Biswas, E. Bykova, N. Dubrovinskaia, L. S. Dubrovinsky, R. Yadav, L. Hozoi, S. Nishimoto, A. A. Tsirlin, and P. Gegenwart, "Breakdown of Magnetic Order in the Pressurized Kitaev Iridate β-Li_2IrO_3", Phys. Rev. Lett. **120**, 237202 (2018).

[152] H.-S. Kim, Y. B. Kim, and H.-Y. Kee, "Revealing frustrated local moment model for pressurized hyperhoneycomb iridate: Paving the way toward a quantum spin liquid", Phys. Rev. B **94**, 245127 (2016).

[153] R. Yadav, S. Rachel, L. Hozoi, J. van den Brink, and G. Jackeli, "Strain- and pressure-tuned magnetic interactions in honeycomb Kitaev materials", Phys. Rev. B **98**, 121107(R) (2018).

[154] L. S. I. Veiga, M. Etter, K. Glazyrin, F. Sun, C. A. J. Escanhoela, G. Fabbris, J. R. L. Mardegan, P. S. Malavi, Y. Deng, P. P. Stavropoulos, H.-Y. Kee, W. G. Yang, M. van Veenendaal, J. S. Schilling, T. Takayama, H. Takagi, and D. Haskel, "Pressure tuning of bond-directional exchange interactions and magnetic frustration in the hyperhoneycomb iridate β-Li_2IrO_3", Phys. Rev. B **96**, 140402(R) (2017).

[155] C. L. Bull, N. P. Funnell, M. G. Tucker, S. Hull, D. J. Francis, and W. G. Marshall, "PEARL: the high pressure neutron powder diffractometer at ISIS", High Pressure Res **36**, 493 (2016).

[156] F. Birch, "Finite Elastic Strain of Cubic Crystals", Phys. Rev. **71**, 809 (1947).

[157] S. Klotz, *Techniques in High Pressure Neutron Scattering* (CRC Press, Boca Raton, 2012).

[158] O. Arnold, J. C. Bilheux, J. M. Borreguero, A. Buts, S. I. Campbell, L. Chapon, M. Doucet, D. N., R. Ferraz Leal, G. M. A., V. E. Lynch, A. Markvardsen, D. J. Mikkelson, R. L. Mikkelson, R. Miller, K. Palmen, P. Parker, G. Passos, T. G. Perring, P. F. Peterson, S. Ren, M. A. Reuter, A. T. Savici, J. W. Taylor, R. J. Taylor, R. Tolchenov, W. Zhou, and J. Zikovsky, "Mantid—Data analysis and visualization package for neutron scattering and μSR experiments", Nucl. Instrum. Methods Phys. Res. A **746**, 156 (2014).

[159] A. C. Hannon, A. S. Gibbs, and H. Takagi, "Neutron scattering length determination by means of total scattering", J. Appl. Cryst. **51**, 854 (2018).

[160] D. Akobuije, W. J. Chijioke, A. Nellis, A. Soldatov, and I. F. Filvera, "The ruby pressure standard to 150 GPa", J. Appl. Phys. **98**, 114905 (2005).

[161] Y. Miura, Y. Yasui, M. Sato, N. Igawa, and K. K., "New-Type Phase Transition of Li_2RuO_3 with Honeycomb Structure", J. Phys. Soc. Jpn. **76**, 033705 (2007).

[162] Y. Miura, M. Sato, Y. Yamakawa, T. Habaguchi, and Y. Ono, "Structural Transition of Li_2RuO_3 Induced by Molecular-Orbit Formation", J. Phys. Soc. Jpn. **78**, 094706 (2009).

[163] A. W. Hull and W. P. Davey, "X-ray crystal analysis of 13 common metals", Phys. Rev. **17**, 571 (1921).

[164] H.-S. Kim and H.-Y. Kee, "Crystal structure and magnetism in α-$RuCl_3$: An *ab initio* study", Phys. Rev. B **93**, 155143 (2016).

[165] V. Hermann, M. Altmeyer, J. Ebad-Allah, F. Freund, A. Jesche, A. A. Tsirlin, M. Hanfland, P. Gegenwart, I. I. Mazin, D. I. Khomskii, R. Valentí, and C. A. Kuntscher, "Competition between spin-orbit coupling, magnetism, and dimerization in the honeycomb iridates: α-Li_2IrO_3 under pressure", Phys. Rev. B **97**, 020104 (2018).

[166] J. P. Clancy, H. Gretarsson, J. A. Sears, Y. Singh, S. Desgreniers, K. Mehlawat, S. Layek, G. K. Rozenberg, Y. Ding, M. H. Upton, D. Casa, N. Chen, J. Im, Y. Lee, R. Yadav, L. Hozoi, D. Efremov, J. van den Brink, and Y.-J. Kim, "Crystal-Field Splitting and Correlation Effect on the Electronic Structure of A_2IrO_3", npj Quantum Mater. **3**, 35 (2018).

[167] G. Bastien, G. Garbarino, R. Yadav, F. J. Martinez-Casado, R. Beltrán Rodríguez, Q. Stahl, M. Kusch, S. P. Limandri, R. Ray, P. Lampen-Kelley, D. G. Mandrus, S. E. Nagler, M. Roslova, A. Isaeva, T. Doert, L. Hozoi, A. U. B. Wolter, B. Büchner, J. Geck, and J. van den Brink, "Pressure-induced dimerization and valence bond crystal formation in the Kitaev-Heisenberg magnet α-$RuCl_3$", Phys. Rev. B **97**, 020104 (2018).

[168] M. A. McGuire, J. Yan, P. Lampen-Kelley, A. F. May, V. R. Cooper, L. Lindsay, A. Puretzky, L. Liang, S. KC, E. Cakmak, S. Calder, and B. C. Sales, "High-temperature magnetostructural transition in van der Waals-layered α-$MoCl_3$", Phys. Rev. Mat. **1**, 064001 (2017).

[169] L. S. I. Veiga, K. Glazyrin, G. Fabbris, C. D. Dashwood, J. G. Vale, H. Park, M. Etter, T. Irifune, S. Pascarelli, D. F. McMorrow, T. Takayama, H. Takagi, and D. Haskel, "Pressure-induced structural dimerization in the hyperhoneycomb iridate β-Li_2IrO_3 at low temperatures", Phys. Rev. B **100**, 064104 (2019).

[170] A. Krajewska, T. Takayama, R. Dinnebier, A. Yaresko, K. Ishii, M. Isobe, and H. Takagi, "Almost pure $J_{\text{eff}} = 1/2$ Mott state of $In_2Ir_2O_7$ in the limit of reduced intersite hopping", Phys. Rev. B **101**, 121101(R) (2020).

[171] K. Matsuhira, M. Wakeshima, R. Nakanishi, T. Yamada, A. Nakamura, W. Kawano, S. Takagi, and Y. Hinatsu, "Metal-Insulator Transition in Pyrochlore Iridates $Ln_2Ir_2O_7$ (Ln = Nd, Sm, and Eu)", J. Phys. Soc. Jpn. **76**, 043706 (2007).

[172] K. Matsuhira, M. Wakeshima, Y. Hinatsu, and S. Takagi, "Metal-Insulator Transitions in Pyrochlore Oxides $Ln_2Ir_2O_7$", J. Phys. Soc. Jpn. **80**, 094701 (2011).

[173] T. Kondo, M. Nakayama, R. Chen, J. J. Ishikawa, E.-G. Moon, T. Yamamoto, Y. Ota, W. Malaeb, H. Kanai, Y. Nakashima, Y. Ishida, R. Yoshida, H. Yamamoto, M. Matsunami, S. Kimura, N. Inami, K. Ono, H. Kumigashira, S. Nakatsuji, L. Balents, and S. Shin, "Quadratic Fermi node in a 3D strongly correlated semimetal", Nat. Comm. **6**, 10042 (2015).

[174] S. Nakatsuji, Y. Machida, Y. Maeno, T. Tayama, T. Sakakibara, J. van Duijn, L. Balicas, J. N. Millican, R. T. Macaluso, and J. Y. Chan, "Metallic Spin-Liquid Behavior of the Geometrically Frustrated Kondo Lattice $Pr_2Ir_2O_7$", Phys. Rev. Lett. **96**, 087204 (2006).

[175] L. Hozoi, H. Gretarsson, J. P. Clancy, B.-G. Jeon, B. Lee, K. H. Kim, V. Yushankhai, P. Fulde, D. Casa, T. Gog, J. Kim, A. H. Said, M. H. Upton, Y.-J. Kim, and J. van den Brink, "Longer-range lattice anisotropy strongly competing with spin-orbit interactions in pyrochlore iridates", Phys. Rev. B **89**, 115111 (2014).

[176] H. Shinaoka, S. Hoshino, M. Troyer, and P. Werner, "Phase Diagram of Pyrochlore Iridates: All-in–All-out Magnetic Ordering and Non-Fermi-Liquid Properties", Phys. Rev. Lett. **115**, 156401 (2015).

[177] S. Zhao, J. M. Mackie, D. E. MacLaughlin, O. O. Bernal, J. J. Ishikawa, Y. Ohta, and S. Nakatsuji, "Magnetic transition, long-range order, and moment fluctuations in the pyrochlore iridate $Eu_2Ir_2O_7$", Phys. Rev. B **83**, 180402(R) (2011).

[178] S. M. Disseler, C. Dhital, A. Amato, S. R. Giblin, C. de la Cruz, S. D. Wilson, and M. J. Graf, "Magnetic order in the pyrochlore iridates $A_2Ir_2O_7$ (A = Y, Yb)", Phys. Rev. B **86**, 014428 (2012).

[179] S. M. Disseler, C. Dhital, A. Amato, S. R. Giblin, C. de la Cruz, S. D. Wilson, and M. J. Graf, "Magnetic order and the electronic ground state in the pyrochlore iridate $Nd_2Ir_2O_7$", Phys. Rev. B **85**, 174441 (2012).

[180] H. Guo, K. Matsuhira, I. Kawasaki, M. Wakeshima, Y. Hinatsu, I. Watanabe, and Z. Xu, "Magnetic order in the pyrochlore iridate $Nd_2Ir_2O_7$ probed by muon spin relaxation", Phys. Rev. B **88**, 060411(R) (2013).

[181] R. Moessner and J. T. Chalker, "Properties of a Classical Spin Liquid: The Heisenberg Pyrochlore Antiferromagnet", Phys. Rev. Lett. **80**, 2929 (1998).

[182] B. Canals and C. Lacroix, "Pyrochlore Antiferromagnet: A Three-Dimensional Quantum Spin Liquid", Phys. Rev. Lett. **80**, 2933 (1998).

[183] T. Moriya, "Anisotropic Superexchange Interaction and Weak Ferromagnetism", Phys. Rev. **120**, 91 (1960).

[184] M. Elhajal, B. Canals, R. Sunyer, and C. Lacroix, "Ordering in the pyrochlore antiferromagnet due to Dzyaloshinsky-Moriya interactions", Phys. Rev. B **71**, 094420 (2005).

[185] G.-W. Chern, *Pyrochlore antiferromagnet with antisymmetric exchange interactions: critical behavior and order from disorder*, (2010) arXiv:1008.3038, https://arxiv.org/abs/1008.3038.

[186] T. Arima, "Time-Reversal Symmetry Breaking and Consequent Physical Responses Induced by All-In-All-Out Type Magnetic Order on the Pyrochlore Lattice", J. Phys. Soc. Jpn. **82**, 013705 (2013).

[187] S. Tardif, S. Takeshita, H. Ohsumi, J. Yamaura, D. Okuyama, Z. Hiroi, M. Takata, and T. Arima, "All-In–All-Out Magnetic Domains: X-Ray Diffraction Imaging and Magnetic Field Control", Phys. Rev. Lett. **114**, 147205 (2015).

[188] Z. Hiroi, J. Yamamura, T. Hirose, I. Nagashima, and Y. Okamoto, "Lifshitz metal-insulator transition induced by the all-in/all-out magnetic order in the pyrochlore oxide $Cd_2Os_2O_7$", APL Materials **3**, 041501 (2015).

[189] H. Sagayama, D. Uematsu, T. Arima, K. Sugimoto, J. J. Ishikawa, E. O'Farrell, and S. Nakatsuji, "Determination of long-range all-in-all-out ordering of Ir^{4+} moments in a pyrochlore iridate $Eu_2Ir_2O_7$ by resonant x-ray diffraction", Phys. Rev. B **87**, 100403 (2013).

[190] C. Donnerer, M. C. Rahn, M. M. Sala, J. G. Vale, D. Pincini, J. Strempfer, M. Krisch, D. Prabhakaran, A. T. Boothroyd, and D. F. McMorrow, "All-in–all-Out Magnetic Order and Propagating Spin Waves in $Sm_2Ir_2O_7$", Phys. Rev. Lett. **117**, 037201 (2016).

[191] S. H. Chun, B. Yuan, D. Casa, J. Kim, C.-Y. Kim, Z. Tian, Y. Qiu, S. Nakatsuji, and Y.-J. Kim, "Magnetic Excitations across the Metal-Insulator Transition in the Pyrochlore Iridate $Eu_2Ir_2O_7$", Phys. Rev. Lett. **120**, 177203 (2018).

[192] E. K.-H. Lee, S. Bhattacharjee, and Y. B. Kim, "Magnetic excitation spectra in pyrochlore iridates", Phys. Rev. B **87**, 214416 (2013).

[193] B. Yan and C. Felser, "Topological Materials: Weyl Semimetals", Ann. Rev. Condens. Matter Phys. **8**, 337 (2017).

[194] X. Yuan, C. Zhang, Y. Zhang, Z. Yan, T. Lyu, M. Zhang, Z. Li, C. Song, M. Zhao, P. Leng, M. Ozerov, X. Chen, N. Wang, Y. Shi, H. Yan, and F. Xiu, "The discovery of dynamic chiral anomaly in a Weyl semimetal NbAs", Nat. Comm. **11**, 1259 (2020).

[195] L. X. Yang, Z. K. Liu, Y. Sun, H. Peng, H. F. Yang, T. Zhang, B. Zhou, Y. Zhang, Y. F. Guo, M. Rahn, D. Prabhakaran, Z. Hussain, S.-K. Mo, C. Felser, B. Yan, and Y. L. Chen, "Weyl semimetal phase in the non-centrosymmetric compound TaAs", Nat. Phys. **11**, 728 (2015).

[196] B. Q. Lv, H. M. Weng, B. B. Fu, X. P. Wang, H. Miao, J. Ma, P. Richard, X. C. Huang, L. X. Zhao, G. F. Chen, Z. Fang, X. Dai, T. Qian, and H. Ding, "Experimental Discovery of Weyl Semimetal TaAs", Phys. Rev. X **5**, 031013 (2015).

[197] S.-Y. Xu, Y. Belopolski, D. S. Sanchez, C. Zhang, C. Chang, C. Guo, G. Bian, Z. Yuan, H. Lu, T.-R. Chang, P. P. Shibayev, M. L. Prokopovych, N. Alidoust, H. Zheng, C.-C. Lee, S.-M. Huang, R. Sankar, F. Chou, C.-H. Hsu, H.-T. Jeng, A. Bansil, T. Neupert, V. N. Strocov, H. Lin, S. Jia, and M. Z. Hasan, "Experimental discovery of a topological Weyl semimetal state in TaP", Sci. Adv. **1**, e1501092 (2015).

[198] W. Witczak-Krempa and Y. B. Kim, "Topological and magnetic phases of interacting electrons in the pyrochlore iridates", Phys. Rev. B **85**, 045124 (2012).

[199] W. Witczak-Krempa, A. Go, and Y. B. Kim, "Pyrochlore electrons under pressure, heat, and field: Shedding light on the iridates", Phys. Rev. B **87**, 155101 (2013).

[200] Y. Machida, S. Nakatsuji, Y. Maeno, T. Tayama, T. Sakakibara, and S. Onoda, "Unconventional Anomalous Hall Effect Enhanced by a Noncoplanar Spin Texture in the Frustrated Kondo Lattice $Pr_2Ir_2O_7$", Phys. Rev. Lett. **98**, 057203 (2007).

[201] Y. Machida, S. Nakatsuji, S. Onoda, T. Tayama, and T. Sakakibara, "Time-reversal symmetry breaking and spontaneous Hall effect without magnetic dipole order", Nature **463**, 210 (2010).

[202] F. F. Tafti, J. J. Ishikawa, A. McCollam, S. Nakatsuji, and S. R. Julian, "Pressure-tuned insulator to metal transition in $Eu_2Ir_2O_7$", Phys. Rev. B **85**, 205104 (2012).

[203] K. Ueda, J. Fujioka, Y. Takahashi, T. Suzuki, S. Ishiwata, Y. Taguchi, and Y. Tokura, "Variation of Charge Dynamics in the Course of Metal-Insulator Transition for Pyrochlore-Type $Nd_2Ir_2O_7$", Phys. Rev. Lett. **109**, 136402 (2012).

[204] H. Zhang, K. Haule, and D. Vanderbilt, "Metal-Insulator Transition and Topological Properties of Pyrochlore Iridates", Phys. Rev. Lett. **118**, 026404 (2017).

[205] A. B. Sushkov, J. B. Hofmann, G. S. Jenkins, J. Ishikawa, S. Nakatsuji, S. Das Sarma, and H. D. Drew, "Optical evidence for a Weyl semimetal state in pyrochlore $Eu_2Ir_2O_7$", Phys. Rev. B **92**, 241108 (2015).

[206] M. Nakayama, T. Kondo, Z. Tian, J. J. Ishikawa, M. Halim, C. Bareille, W. Malaeb, K. Kuroda, T. Tomita, S. Ideta, K. Tanaka, M. Matsunami, S. Kimura, N. Inami, K. Ono, H. Kumigashira, L. Balents, S. Nakatsuji, and S. Shin, "Slater to Mott Crossover in the Metal to Insulator Transition of $Nd_2Ir_2O_7$", Phys. Rev. Lett. **117**, 056403 (2012).

[207] K. Ueda, J. Fujioka, B.-J. Yang, J. Shiogai, A. Tsukazaki, S. Nakamura, S. Awaji, N. Nagaosa, and Y. Tokura, "Magnetic Field-Induced Insulator-Semimetal Transition in a Pyrochlore $Nd_2Ir_2O_7$", Phys. Rev. Lett. **115**, 056402 (2015).

[208] Z. Tian, Y. Kohama, T. Tomita, H. Ishizuka, T. H. Hsieh, J. J. Ishikawa, K. Kindo, L. Balents, and S. Nakatsuji, "Field-induced quantum metal–insulator transition in the pyrochlore iridate $Nd_2Ir_2O_7$", Nat. Phys. **12**, 134 (2016).

[209] K. Ueda, T. Oh, B.-J. Yang, R. Kaneko, J. Fujioka, N. Nagaosa, and Y. Tokura, "Magnetic-field induced multiple topological phases in pyrochlore iridates with Mott criticality", Nat. Comm. **8**, 15515 (2017).

[210] H. Okabe, M. Isobe, E. Takayama-Muromachi, A. Koda, S. Takeshita, M. Hiraishi, M. Miyazaki, R. Kadono, Y. Miyake, and J. Akimitsu, "Ba_2IrO_4: A spin-orbit Mott insulating quasi-two-dimensional antiferromagnet", Phys. Rev. B **83**, 155118 (2011).

[211] S. M. Disseler, "Direct evidence for the all-in/all-out magnetic structure in the pyrochlore iridates from muon spin relaxation", Phys. Rev. B **89**, 140413(R) (2014).

[212] J. P. Clancy, H. Gretarsson, E. K. H. Lee, D. Tian, J. Kim, M. H. Upton, D. Casa, T. Gog, Z. Islam, B.-G. Jeon, K. H. Kim, S. Desgreniers, Y. B. Kim, S. J. Julian, and Y.-J. Kim, "X-ray scattering study of pyrochlore iridates: Crystal structure, electronic, and magnetic excitations", Phys. Rev. B **94**, 024408 (2016).

[213] D. Uematsu, H. Sagayama, T. Arima, J. J. Ishikawa, S. Nakatsuji, H. Takagi, M. Yoshida, J. Mizuki, and K. Ishii, "Large trigonal-field effect on spin-orbit coupled states in a pyrochlore iridate", Phys. Rev. B **92**, 094405 (2015).

[214] J. N. Millican, R. T. Macaluso, S. Nakatsuji, Y. Machida, Y. Maeno, and J. Y. Chan, "Crystal growth and structure of $R_2Ir_2O_7$ (R = Pr, Eu) using molten KF", Mater. Res. Bull. **42**, 928 (2007).

[215] H. Takatsu, K. Watanabe, K. Goto, and H. Kadowaki, "Comparative study of low-temperature x-ray diffraction experiments on $R_2Ir_2O_7$ (R = Nd, Eu, and Pr)", Phys. Rev. B **90**, 235110 (2014).

[216] M. C. Shapiro, S. C. Riggs, M. B. Stone, C. R. de la Cruz, S. Chi, A. A. Podlesnyak, and I. R. Fisher, "Structure and magnetic properties of the pyrochlore iridate $Y_2Ir_2O_7$", Phys. Rev. B **85**, 214434 (2012).

[217] B. Yuan, J. P. Clancy, A. M. Cook, C. M. Thompson, J. Greedan, G. Cao, B. C. Jeon, T. W. Noh, M. H. Upton, D. Casa, T. Gog, A. Paramekanti, and Y.-J. Kim, "Determination of Hund's coupling in 5*d* oxides using resonant inelastic x-ray scattering", Phys. Rev. B **95**, 235114 (2017).

[218] C. L. Chien and A. W. Sleight, "Mössbauer effect studies of europium pyrochlores", Phys. Rev. B **18**, 2031 (1978).

[219] N. Taira, M. Wakeshima, and Y. Hinatsu, "Magnetic properties of iridium pyrochlores $R_2Ir_2O_7$(R = Y, Sm, Eu and Lu)", J. Phys. Condens. Matter **13**, 5527 (2001).

[220] A. W. Sleight and A. P. Ramirez, "Disappearance of the metal-insulator transition in iridate pyrochlores on approaching the ideal $R_2Ir_2O_7$ stoichiometry", Solid State Commun. **275**, 12 (2018).

[221] D. Pekker and C. M. Varma, "Amplitude/Higgs Modes in Condensed Matter Physics", Ann. Rev. Condens. Matter Phys. **6**, 269 (2015).

[222] T. Dey, A. Maljuk, D. V. Efremov, O. Kataeva, S. Gass, C. G. F. Blum, F. Steckel, D. Gruner, and T. Ritschel, "Ba_2YIrO_6: A cubic double perovskite material with Ir^{5+} ions", Phys. Rev. B **93**, 014434 (2016).

[223] Z. Y. Zhao, S. Calder, A. A. Aczel, M. A. McGuire, B. C. Sales, D. G. Mandrus, G. Chen, N. Trivedi, H. D. Zhou, and J.-Q. Yan, "Fragile singlet ground-state magnetism in the pyrochlore osmates $R_2Os_2O_7$ (R=Y and Ho)", Phys. Rev. B **93**, 134426 (2016).

[224] N. R. Davies, C. V. Topping, H. Jacobsen, A. J. Princep, F. K. K. Kirschner, M. C. Rahn, M. Bristow, J. G. Vale, I. da Silva, P. J. Baker, C. J. Sahle, Y.-F. Guo, D.-Y. Yan, Y.-G. Shi, S. J. Blundell, D. F. McMorrow, and A. T. Boothroyd, "Evidence for a $J_{\text{eff}} = 0$ ground state and defect-induced spin glass behavior in the pyrochlore osmate $Y_2Os_2O_7$", Phys. Rev. B **99**, 174442 (2019).

[225] S. Nakatsuji, S.-I. Ikeda, and Y. Maeno, "Ca_2RuO_4: New Mott Insulators of Layered Ruthenate", J. Phys. Soc. Jpn. **66**, 1868 (1997).

[226] M. Ito, Y. Yasui, M. Kanada, H. Harashina, S. Yoshii, K. Murata, M. Sato, H. Okumura, and K. Kakurai, "Neutron Diffraction Study of Pyrochlore Compound $R_2Ru_2O_7$ (R = Y, Nd) above and below the Spin Freezing Temperature", J. Phys. Soc. Jpn. **69**, 888 (2000).

[227] P. Khalifah, R. Osborn, Q. Huang, H. W. Zandbergen, R. Jin, Y. Liu, D. Mandrus, and R. J. Cava, "Orbital Ordering Transition in $La_4Ru_2O_{10}$", Science **297**, 2237 (2002).

[228] H. Wu, Z. Hu, T. Burnus, J. D. Denlinger, P. G. Khalifah, D. G. Mandrus, L.-Y. Jang, H. H. Hsieh, A. Tanaka, K. S. Liang, J. W. Allen, R. J. Cava, D. I. Khomskii, and L. H. Tjeng, "Orbitally Driven Spin-Singlet Dimerization in $S = 1$ $La_4Ru_2O_{10}$", Phys. Rev. Lett. **96**, 256402 (2006).

[229] S. Lee, J.-G. Park, D. T. Adroja, D. Khomskii, S. Streltsov, K. A. McEwen, H. Sakai, K. Yoshimura, V. I. Anisimov, D. Mori, R. Kanno, and R. Ibberson, "Spin gap in $Tl_2Ru_2O_7$ and the possible formation of Haldane chains in three-dimensional crystals", Nat. Mater. **5**, 471 (2006).

[230] Available at https://https://www.isis.stfc.ac.uk/Pages/Coupling-of-orbital,-spin,-and-lattice-degrees-of-freedom-in-Tl2Ru2O7.aspx.

[231] J. S. Lee, Y. S. Lee, K. W. Kim, T. W. Noh, J. Yu, T. Takeda, and R. Kanno, "Temperature-dependent self-doping effects on the metal-insulator transition of $Tl_2Ru_2O_7$", Phys. Rev. B **64**, 165108 (2001).

[232] S. A. J. Kimber, I. I. Mazin, J. Shen, H. O. Jeschke, S. V. Streltsov, D. N. Argyriou, R. Valentí, and D. I. Khomskii, "Valence bond liquid phase in the honeycomb lattice material Li_2RuO_3", Phys. Rev. B **89**, 081408(R) (2014).

[233] T. Takeda, M. Nagata, H. Kobayashi, R. Kanno, and Y. Kawamoto, "High-Pressure Synthesis, Crystal Structure, and Metal–Semiconductor Transitions in the $Tl_2Ru_2O_{7-\delta}$ Pyrochlore", J. Solid State Chem. **140**, 182 (1998).

[234] T. Takeda, R. Kanno, Y. Kawamoto, M. Takano, F. Izumi, A. W. Sleight, and A. W. Hewat, "Structure–property relationships in pyrochlores: low-temperature structures of $Tl_2Ru_2O_{7-\delta}$ ($\delta = 0.00$ and 0.05)", J. Mater. Chem. **9**, 215 (1999).

[235] M. Miyazaki, R. Kadono, K. H. Satoh, M. Hiraishi, S. Takeshita, A. Koda, A. Yamamoto, and H. Takagi, "Magnetic ground state of pyrochlore oxides close to metal-insulator boundary probed by muon spin rotation", Phys. Rev. B **82**, 094413 (2010).

[236] P. A. Cox, R. G. Egdell, J. B. Goodenough, A. Hamnett, and C. C. Naish, "The metal-to-semiconductor transition in ternary ruthenium (IV) oxides: a study by electron spectroscopy", J. Phys. C **16**, 6221 (1983).

[237] F. Ishii and T. Oguchi, "Electronic Band Structure of the Pyrochlore Ruthenium Oxides $A_2Ru_2O_7$ (A = Bi, Tl and Y)", J. Phys. Soc. Jpn. **69**, 526 (2000).

[238] A. Ehmann and S. Kemmler-Sack, "Systeme $Bi_{2-x}Ln_xRu_2O_7$ (Ln = Sm, Lu, Y, In)", Mater. Res. Bull. **20**, 437 (1985).

[239] G. Cakmak, J. Nuss, and M. Jansen, "LiB_6O_9F, the First Lithium Fluorooxoborate – Crystal Structure and Ionic Conductivity", Z. Anorg. Allg. Chem. **635**, 631 (2009).

[240] B. AXS, *Bruker suite*, version 2019/1 (Bruker AXS Inc., Madison, Wisconsin, USA, 2019).

[241] G. M. Sheldrick, *SADABS — Bruker AXS area detector scaling and absorption*, version 2014/5 (Bruker AXS Inc., Madison, Wisconsin, USA, 2012).

[242] G. M. Sheldrick, *TWINABS — Bruker AXS area detector scaling and absorption for twinned crystals*, version 2012/1 (Bruker AXS Inc., Madison, Wisconsin, USA, 2012).

[243] G. M. Sheldrick, "A short history of *SHELXL*", Acta Cryst. **A64**, 112 (2008).

[244] G. M. Sheldrick, "Crystal structure refinement with *SHELXL*", Acta Cryst. **C71**, 3 (2015).

[245] V. Petříček, M. Dušek, and L. Palatinus, "Crystallographic Computing System JANA2006: General features", Z. Kristallogr. **229**, 345 (2014).

[246] A. Le Bail, H. Duroy, and J. L. Fourquet, "*Ab-initio* structure determination of $LiSbWO_6$ by X-ray powder diffraction", Mater. Res. Bull. **23**, 447 (1988).

[247] G. S. Pawley, "Unit-cell refinement from powder diffraction scans", J. Appl. Phys. **14**, 357 (1981).

[248] Available at https://www.isis.stfc.ac.uk/Pages/Hrpd-technical-information.aspx.

[249] Available at https://checkcif.iucr.org/.

[250] H. Gretarsson, D. Ketenoglu, M. Harder, S. Mayer, F.-U. Dill, M. Spiwek, H. Schulte-Schrepping, M. Tischer, H. S. Wille, B. Keimer, and H. Yavas, "IRIXS: a resonant inelastic X-ray scattering instrument dedicated to X-rays in the intermediate energy range", J. Synchrotron Rad. **27**, 538 (2020).

[251] D. Tomono, T. Kawamata, Y. Hirayama, M. Iwasaki, I. Watanabe, K. Ishida, and T. Matsuzaki, "Progress in development of new μSR spectrometer at RIKEN-RAL", J. Phys. Conf. Ser. **225**, 012056 (2010).

[252] F. L. Pratt, "WIMDA: a muon data analysis program for the Windows PC", Physica B **289-290**, 710 (2000).

[253] A. Banerjee, R. Mishra, and Z. Singh, "The Lu–Ru–O System: Thermodynamic properties and impedance measurements of the pyrochlore $Lu_2Ru_2O_7$(s)", Solid State Ion. **201**, 42 (2011).

[254] M. Sato and S. Yoshii, "Studies on Metal-Insulator Transition of Pyrochlore Compound $Y_{2-x}Bi_xRu_2O_7$", J. Phys. Soc. Jpn. **68**, 3034 (1999).

[255] N. Taira, M. Wakeshima, and Y. Hinatsu, "Magnetic susceptibility and specific heat studies on heavy rare earth ruthenate pyrochlores $R_2Ru_2O_7$ (R = Gd–Yb)", J. Mater. Chem. **12**, 1475 (2002).

[256] J. Chaloupka and G. Khaliullin, "Highly frustrated magnetism in relativistic d^4 Mott insulators: Bosonic analog of the Kitaev honeycomb model", Phys. Rev. B **100**, 224413 (2019).

[257] K. Kojima, A. Keren, L. P. Le, G. M. Luke, B. Nachumi, W. D. Wu, Y. J. Uemura, K. Kiyono, S. Miyasaka, H. Takagi, and S. Uchida, "Muon Spin Relaxation and Magnetic Susceptibility Measurements in the Haldane System $(Y_{2-x}Ca_x)Ba(Ni_{1-y}Mg_y)O_5$", Phys. Rev. Lett. **74**, 3471 (1995).

[258] P. J. Baker, S. J. Blundell, F. L. Pratt, T. Lancaster, M. L. Brooks, W. Hayes, M. Isobe, Y. Ueda, M. Hoinkis, M. Sing, M. Klemm, S. Horn, and R. Claessen, "Muon-spin relaxation measurements on the dimerized spin-1/2 chains $NaTiSi_2O_6$ and TiOCl", Phys. Rev. B **75**, 094404 (2007).

[259] S. J. Blundell, T. Lancaster, P. J. Baker, W. Hayes, F. L. Pratt, T. Atake, D. S. Rana, and S. K. Malik, "Magnetism and orbitally driven spin-singlet states in Ru oxides: A muon-spin rotation study", Phys. Rev. B **77**, 094424 (2008).

[260] E. Hückel, "Die freien Radikale der organischen Chemie", Z. Physik **83**, 632 (1933).

[261] J. B. Goodenough and A. L. Loeb, "Theory of Ionic Ordering, Crystal Distortion, and Magnetic Exchange Due to Covalent Forces in Spinels", Phys. Rev. **98**, 391 (1955).

[262] J. Greedan, M. Sato, X. Yan, and F. Razavi, "Spin-glass-like behavior in $Y_2Mo_2O_7$, a concentrated, crystalline system with negligible apparent disorder", Solid State Commun. **59**, 895 (1986).

[263] M. J. P. Gingras, C. V. Stager, N. P. Raju, B. D. Gaulin, and J. E. Greedan, "Static Critical Behavior of the Spin-Freezing Transition in the Geometrically Frustrated Pyrochlore Antiferromagnet $Y_2Mo_2O_7$", Phys. Rev. Lett. **78**, 947 (1997).

[264] P. M. M. Thygesen, J. A. M. Paddison, R. Zhang, K. A. Beyer, K. W. Chapman, H. Y. Playford, M. G. Tucker, D. A. Keen, M. A. Hayward, and A. L. Goodwin, "Orbital Dimer Model for the Spin-Glass State in $Y_2Mo_2O_7$", Phys. Rev. Lett. **118**, 067201 (2017).

[265] A. Smerald and G. Jackeli, "Giant Magnetoelastic-Coupling Driven Spin-Lattice Liquid State in Molybdate Pyrochlores", Phys. Rev. Lett. **122**, 227202 (2019).

[266] R. D. Shannon, "Revised effective ionic radii and systematic studies of interatomic distances in halides and chalcogenides", Acta Cryst. **A32**, 751 (1976).

[267] S. N. Ruddlesden and P. Popper, "The compound $Sr_3Ti_2O_7$ and its structure", Acta Cryst. **11**, 54 (1958).

[268] G. C. Mather, C. Dussarrat, J. Etourneaub, and R. A. West, "A review of cation-ordered rock salt superstructure oxides", J. Mater. Chem. **10**, 2219 (2000).

[269] B. J. Kennedy, B. A. Hunter, and C. J. Howard, “Structural and Bonding Trends in Tin Pyrochlore Oxides”, J. Solid State Chem. **130**, 58 (1997).

Acknowledgements

First and foremost I would like to thank Prof. Hidenori Takagi, who kindly welcomed me into his Quantum Materials department at MPI and FMQ3 group at the University of Stuttgart. Prof. Takagi gave me an opportunity to work in a fantastic research environment, provided invaluable guidance throughout my Ph.D. project and introduced me to the exciting world of correlated materials.

I would also like to thank Prof. Thomas Schleid for accepting the role of co-examiner, and Prof. Andreas Köhn for chairing my examination. Thanks are due to Monika Carey at the Dean's office for her support and endless patience.

I would particularly like to thank Dr. Tomohiro Takayama, who supervised my Ph.D. project and was a fantastic mentor. Tomo taught me nearly everything... He was always incredibly kind and patient despite me asking stupid questions and often being resistant to his (correct) answers. He introduced me to chemistry and physics of correlated materials, conducting experiments in the lab he set up, giving scientific talks, writing papers and collaborating with other scientists. He guided me through my very first beamtimes at SPring-8 in Japan and ISIS in the UK. I wouldn't have made it through this Ph.D. project without Tomo and I am forever indebted to him.

I am very happy to have been a member of the FMQ3 Novel Quantum Materials group lead by Dr. Tomo Takayama. I would like to thank Marian Blankenhorn and Dr. Marco Polo Jimenez Segura, who not only welcomed me to the lab and helped with my project, but became my good friends. I'm grateful to Dr. Hajime Ishikawa and Dr. Minu Kim for sharing their solid state chemistry expertise. Dr. Andreas Rost provided me with help and guidance upon arrival at the University of Stuttgart which I appreciate very much. Dr. Makoto Yoshida, Daiki Shintani, Hangoo Lee, Laurenz Kruty, Tomo Soejima, Hana Soejima, Hiroto Takahashi and Jihuan Gu were also excellent colleagues who provided great company at the lab and at the office.

I owe a lot to all of Quantum Materials group members at MPI, who not only collaborated with me on this project, but made my work environment pleasant and my stay in Stuttgart enjoyable. I'm very thankful to Dr. Ulrich Wedig for his kindness and for helping me with organising a lot of things when arriving in Germany. Thanks are due to Dr. Alexander Yaresko for spending many hours trying to fill my empty head with electronic band structure (and sometimes ballet). Thank you Dr. George Jackeli for teaching me about spin-orbital models

and that all good things come from Georgia. I'm grateful to Dr. Jürgen Nuss for his fantastic work on single crystal XRD and sharing his expertise on crystallography, and to Dr. Sebastian Bette for his incredible XRD work on many of my powder samples. I have to especially thank the MPI high pressure lab members, Dr. Masahiko Isobe, Dr. Graham McNally, Frank Falkenberg, Uwe Engelhardt and Kersten Schunke, without whom high pressure synthesis would have not been possible. Thanks are also due to Sabine Prill-Diemer for conducting countless EDX experiments on my powders and crystals, and to Claus Mühle for his assistance with synthesis. I also appreciate the work of Kathrin Pflaum and Markus Dueller who were always happy to assist when I needed help. I'm very much indebted to the group secretaries, Sabine Paulsen, Ulrike Mergenthaler and Sabine Ost, who made sure I stayed out of trouble no matter how much I annoyed them. I also very much enjoyed the coffee breaks, meals, wine tastings and hiking trips with both Quantum Materials and FMQ3 members which kept me sane during this project...

Furthermore, I would like to thank Prof. Robert Dinnebier and Christine Stefani for their work on XRD, Dr. Reinhard Kremer and Eva Büchner for high temperature MPMS experiments as well as Dr. Alexander Boris and Ksenia Rabinovich for their hard work on measuring optical conductivity of my samples (which is sadly not a part of this thesis). Also thanks to Viola Duppel, Eva Büchner and Kathrin Küster for their contribution to this project.

A special thanks to beamline scientists at SPring-8 in Japan, Dr. Kenji Ishii, Dr. Hirofumi Ishii, Dr. Hitoshi Yamaoka and Dr. Nozomu Hiraoka, who put tremendous effort into the high pressure RIXS experiments. Thanks to Dr. Isao Watanabe and Dita Puspita Sari for their work on μSR experiments at ISIS. I'm very grateful to Dr. Joel Bertinshaw and Dr. Hlynur Gretarsson for introducing me to the P01 beamline at DESY in Hamburg.

I would also like to thank Dr. Alexandra Gibbs for not only sharing her expertise on neutron scattering during our experiments at ISIS, but also for her invaluable support and advice during my Ph.D. project.

Finally, I would like to thank my family and friends, and of course Henri, for their love and support.

The research presented in this thesis was funded and supported by Alexander von Humboldt Foundation and Max Planck Society.